

Characterization of Tensile and Fracture Properties of X52 Steel Pipes and Their Girth Welds

by

Meng Lin

A thesis submitted in partial fulfillment of the requirements for the degree of

Master of Science

in

Structural Engineering

Department of Civil and Environmental Engineering
University of Alberta

© Meng Lin, 2015

Abstract

Enbridge vintage Norman Wells Pipeline made of X52 steels has transported crude oil from Norman Wells, Northwest Territories (NWT) to Zama, Alberta since 1985. It is the first fully buried pipeline that traverses permafrost regions in Canada, and is often subjected to adverse geotechnical conditions. It is significant to investigate the resistance of the buried X52 steel pipeline in response to the imposed substantial stresses and strains caused by impacts and displacements from geotechnical instability.

In this thesis, tensile and fracture properties of X52 steel pipes and their girth welds are determined by small scale material tests. An original girth weld which was manufactured in 1980s and a new girth weld which was manufactured in 2013 are both studied and their material properties compared to the corresponding heat-affected zones and the pipe base metal. Tension tests are conducted to obtain stress-strain curves and determine the tensile properties of X52 pipe. The strain-hardening region of the true stress-strain curve is characterized into the empirical mathematical expressions otherwise known as the Hollomon equation and the Ramberg-Osgood equation. The stress-strain curve of X52 steel pipe is compared to curves obtained from higher grades of steel pipes and the comparison between the ductility of X52 steel pipe and other grades is discussed. Charpy V-notch impact tests are conducted to measure the energy required to fracture a V-notched specimen and determine the fracture properties of the pipe material. The decrease of the test temperature reduces the impact toughness and increases the probability of brittle fracture. The empirical correlation between the test CVN energy and the fracture toughness of X52 pipe is emphasized. Based on the test results, the tensile strain capacity of X52 pipe is predicted according to the empirical equation provided by CSA Z662-11. While the tensile strain capacity equations were developed based on tests conducted on higher grades of steel, the results of this work allowed the use of these equations to predict the amount of reduction of tensile strain capacity due to the presence of girth weld defects.

Acknowledgements

This research project is funded by Enbridge Pipeline Inc. I would like to appreciate Enbridge Pipeline Inc. for providing the research pipes, and Qualimet Inc. and Rejent Tool and Manufacturing Co. Ltd for manufacturing the specimens for the small scale tests.

I sincerely express my gratitude to my main supervisor Dr. Samer Adeeb and co-supervisor Dr. J. J. Roger Cheng for their guidance and assistance throughout the project. I am particularly inspired by Dr. Samer Adeeb with his great patience and valuable advices to complete this thesis. I would like to acknowledge Dr. Millan Sen from Enbridge Pipeline Inc., who provided the research direction and significant support for the project. I would also like to thank Dr. Driver Robert, Dr. Marwan El-Rich, Dr. Carlos Cruz Noguez and Dr. Mustafa Gul who taught me academic knowledge in the course work.

Special thanks to Greg Miller and Cameron West of I.F. Morrison Structural Engineering Laboratory, and Bernice Faulkner and Dave Waege of the Mechanical Engineering Machine Shop, Dr. Jason Carey and Garrett Melenka for the technical assistance during the small scale tests.

I wish to express my appreciations to my fellow graduate students Celal Cakiroglu and Muntaseer Kainat for their support in the project. I also wish to thank Arlene Figley for her assistance during my M.Sc. program. Lastly, I would like to acknowledge my parents for their love and encouragement during my time at University of Alberta.

Table of Contents

<i>Chapter</i>	<i>Page</i>
Abstract	ii
Acknowledgements	iii
Table of Contents	iv
List of Tables	viii
List of Figures	ix
List of Symbols and Abbreviations	xii
1. Introduction	1
1.1 Background and Problem Statements	1
1.2 Objective of Thesis	6
1.3 Organization of Thesis	8
2. Literature Review	9
2.1 Introduction to Pipelines	9
2.1.1 Failures of Pipelines.....	9
2.1.2 External Loading Effects on Pipelines.....	18
2.1.3 Internal Pressure Effects on Pipelines.....	23
2.1.4 Specification and Grades of Pipes	27
2.2 Mechanical Properties of Steel	30
2.2.1 Strength.....	30
2.2.2 Ductility	31
2.2.3 Toughness.....	33
2.2.4 Stiffness.....	35
2.2.5 Other Properties	36
2.3 Weldability of Steel.....	37
2.4 Stress-Strain Curve of Steel.....	39
2.4.1 Divisions of Stress-Strain Curve.....	39
2.4.2 Engineering and True Stress and Strain	41

2.3.3 Yielding Phenomenon	43
2.4.4 Strain Hardening, Strain Aging, and Bauschinger Effect	46
2.5 Fracture	50
2.5.1 Characterization of Fracture	50
2.5.2 Fracture Mechanics	53
2.5.2.1 Stress-intensity Factor and Fracture Modes.....	54
2.5.2.2 Linear Elastic Fracture Mechanics and Elastic-Plastic Fracture Mechanics	55
2.5.2.3 Fracture Toughness Parameters	56
2.5.2.4 Variables to Fracture Toughness	59
2.5.2.5 Variables to Fracture Toughness	62
3. Tension Test	66
3.1 Introduction to Tension Test.....	66
3.2 Objective	66
3.3 Test Methodology	67
3.4 Test Specimens and Grips	68
3.4.1 Design of Specimens.....	68
3.4.2 Design of Grips	70
3.5 Test Equipment and Setup.....	71
3.5.1 Selection of Loading Range.....	71
3.5.2 Selection of Extensometer	72
3.5.3 Calibration and Alignment.....	72
3.6 Test Procedures	74
3.7 Test Result and Analysis	75
3.7.1 Summary of Experimental Tensile Properties	76
3.7.2 Representative Curves	82
3.7.2.1 Average Curve	82
3.7.2.2 Mathematical Equations.....	83
3.7.2.3 Comparison of the Representative Curves.....	87

3.7.3 Comparison between the Curves	89
3.8 Conclusion of Tests	94
3.9 Variability of Test Results	97
4. Charpy V-notch Impact Test.....	98
4.1 Introduction to CVN Test.....	98
4.2 Objective	100
4.3 Test Specimens and Test Temperature	101
4.4 Test Methodology	103
4.4.1 Test Methodology and Test Machine	103
4.4.2 Measurement of Ductility	104
4.4.2.1 Percentage of Shear Fracture	104
4.4.2.2 Lateral Expansion	104
4.5 Test Results and Analysis.....	106
4.6 Conclusion of Tests	109
4.7 Variability of Test Results	111
4.8 Comparison with Higher Grades of Steel Pipes for CVN Tests Results	112
4.9 Correlation with Fracture Toughness.....	117
4.9.1 Fracture Toughness Parameters	117
4.9.2 Restrictions of Fracture Toughness Test	119
4.9.3 Correlation between CVN Energy and Fracture Toughness	121
4.9.4 Comparison with Higher Grades of Steel Pipes for Fracture Toughness Tests Results.....	125
5. Prediction of Tensile Strain Capacity.....	129
5.1 Introduction to Strain-based Design	129
5.2 Comparison of X52 to Higher Grades of Steel Pipes	131
5.3 Prediction of the Tensile Strain Capacity.....	134
5.3.1 Introduction of CSA Z662-11 Equations	134
5.3.2 Calculation of Tensile Strain Capacity.....	136
5.3.3 Effects of Defect Size on the Tensile Strain Capacity	139

5.3.4 Limitation of CSA Z662-11 Equations	141
6. Summary, Conclusion, and Future Direction.....	144
6.1 Summary	144
6.2 Conclusion	146
6.3 Future Directions	149
References	150
Appendix A - Measurement of Ductility	164
Appendix B - Design of test specimens.....	167
Appendix C - Test Stress-Strain Curves	169
Appendix D – ϵ_{crit} affected by Defect Size	179

List of Tables

<i>Table</i>	<i>Page</i>
2.1 Tensile requirements from standards	29
3.1 Numbers of tension test specimens.....	69
3.2 Tensile properties obtained from the standard tension tests	77
3.3 Assumed properties from power law equations	86
3.4 Tensile properties of X52 pipe (longitudinal direction).....	96
3.5 Tensile properties of X52 pipe (circumferential direction).....	96
4.1 Numbers of Charpy V-notch impact test specimens	102
4.2 Results obtained from CVN impact tests at room temperature	107
4.3 Results obtained from CVN Impact tests at lower temperature	108
4.4 CVN and tension tests results of API X52, X65, X70, and X80 pipe steels.....	114
4.5 Correlations between CVN and K_{IC} , J_{IC} , δ_{IC}	124
4.6 Fracture toughness test and tension results of API X52, X65, X70, X80 and X100 pipe steels.....	128
5.1 Comparison of different grades of steel pipes	133
5.2 Results from tension test.....	136
5.3 Determination of ε_t^{crit} for a surface-breaking defect.....	137
5.4 Determination of ε_t^{crit} for a buried defect	137
A.1 Measurement of reduction of area and elongation for longitudinal rectangular tension specimens.....	165
A.2 Measurement of reduction of area and elongation for circumferential round tension specimens.....	166

List of Figures

<i>Figure</i>	<i>Page</i>
1.1 Canadian primary energy production and their proportion in 2012	4
1.2 Enbridge liquid pipeline systems	4
1.3 Girth weld	5
2.1 Photos of common pipe failure	11
2.2 Comparison of average failure rate per 100 km of pipelines in UK for steel, cast iron and ductile iron pipes	14
2.3 Canadian provincial crude oil and natural gas production and their proportions in 2013	15
2.4 Numbers of Alberta pipelines incidents and the proportion of failure causes between 1990-2012.....	17
2.5 An example of frost heave and thaw settlement	19
2.6 Landslides	22
2.7 Longitudinal stress, hoop stress and radial stress on a cylindrical pipe.....	24
2.8 Free ends and capped ends on a pipe	25
2.9 Stress in free ends and capped ends conditions	25
2.10 The relationship between σ_r/σ_h and D/t or P_o/P_i	25
2.11 Material toughness	34
2.12 Butt weld and fillet weld.....	38
2.13 Typical stress-strain curves for a steel specimen	41
2.14 Comparison of true and engineering stress-strain curves	43
2.15 Yielding plateau due to Lüder bands.....	45
2.16 Determination of the yield strength in gradual yielding	45
2.17 An engineering stress-strain curve showing strain hardening.....	48
2.18 An engineering stress-strain curve showing strain aging.....	49
2.19 An engineering stress-strain curve showing Baushinger effect and hysteresis loop	49
2.20 Engineering stress-strain curve for ductile fracture and brittle fracture	52
2.21 Appearance of a typical ductile fracture and brittle fracture during uniaxial tension test.....	52

2.22	The sequence of how tensile fracture is formed for a ductile steel specimen.....	53
2.23	The three basic fracture modes	54
2.24	Loading and unloading of nonlinear elastic and elastic-plastic materials	55
2.25	Crack blunting and crack-tip opening displacement.....	56
2.26	Ductile crack growth.....	56
2.27	Effects of specimen thickness on fracture toughness K	60
2.28	Effects of specimen thickness on fracture surface	60
2.29	Schematic CTOD versus temperature transition curve for structural steels	62
2.30	Fracture toughness test specimens.....	63
2.31	Clamped single edge notch tension specimens.....	65
3.1	A rectangular tension test specimen.....	68
3.2	A round tension test specimen	68
3.3	Location and orientation of specimens machined from the pipe	69
3.4	Design of grips	70
3.5	MTS test machine (1000kN capacity) and extensometer (50mm gage length).....	73
3.6	MTS test machine (40kN capacity) and extensometer (10mm gage length).....	73
3.7	Photos of fracture of a rectangular specimen.....	81
3.8	Photos of fracture of a round specimen	82
3.9	Average points to create a representative curve of longitudinal base metal	83
3.10	An example of how to determine parameters in Hollomon and Ramberg-Osgood equations	85
3.11	Comparison of average curve, power curves, and quasi-static curve of longitudinal base metal.....	87
3.12	Comparison of the longitudinal new HAZ and base metal.....	90
3.13	Comparison of the circumferential new weld, HAZ and base metal	91
3.14	Comparison of the circumferential old weld, HAZ and base metal	91
3.15	Comparison of the circumferential new and old girth weld metal.....	92
3.16	Comparison of the circumferential new and old HAZ.....	92
3.17	Comparison of the longitudinal and circumferential base metal	93
3.18	Comparison of the longitudinal and circumferential new HAZ	93
4.1	CVN and cleavage fracture versus temperature curve.....	99

4.2 Design and photos of a subsize CVN specimen	101
4.3 Chapy impact test machine	103
4.4 Examples of fracture appearance	105
4.5 CVN energy versus temperature data for X52 steel pipe.....	110
4.6 CVN energy versus temperature curve for API X65 steel pipe	115
4.7 CVN energy versus temperature curve for API X65 and X70 steel pipes.....	115
4.8 CVN energy versus temperautre curve for API X70 and X80 steel pipes.....	116
4.9 CVN versus temperature curve for impact loading and slow bend loading	122
4.10 Standard CT specimen in the CL direction and nonstandard curved SENB specimen in the CR direction.....	126
5.1 Comparison of true stress-strain curves of different grades of pipe	132
5.2 A planar defect in the pipe wall.....	135
5.3 Longitudinal tensile strain capacity as a function of two surface-breaking defect parameters ξ and η	139
5.4 ϵ_t^{crit} as a function of two buried defect parameters and a constant buried defect parameter (a) ξ or $2c/t=6$; (b) η or $2a/t=0.3$; (c) ψ or $d/t=0.3$	140
5.5 ϵ_t^{crit} as a function of CTOD based on constant $\lambda=0.75$, $\xi=6$, $\eta=0.3$, $\psi=0.3$	143
B.1 Design of rectangular tension test specimen	167
B.2 Design of round tension test specimen.....	167
B.3 Design of subsize CVN test specimen	168
B.4 MTS end tab grip with right-hand thread.....	168
B.5 Assembly of tension test specimen, grips and fixtures.....	168
C.1 Stress-strain curves of base metal.....	169
C.2 Stress-strain curves of weld metal.....	172
C.3 Stress-strain curves of HAZ	174
D.1 ϵ_t^{crit} for surface-breaking defects	179
D.2 ϵ_t^{crit} for buried defects	179

List of Symbols and Abbreviations

Latin symbols

a	Crack length or depth of a fracture toughness test specimen
a_0	Original crack length
A	Cross-sectional area
A_f	Cross-sectional area at fracture
A_0	Original cross-sectional area
ΔA	Reduction of cross-sectional area
b	Crack remaining ligament ($b = w - a$)
b_0	Original crack remaining ligament ($b_0 = w - a_0$)
B	Thickness of a fracture toughness test specimen
w	Width of a fracture toughness test specimen
$^{\circ}\text{C}$	Degrees Celsius
D	Outer diameter of the pipe
E	Young's modulus (Modulus of elasticity)
E_{sh}	Strain hardening modulus
G	Shear Modulus (Modulus of rigidity)
G	Energy release rate
G_{Ic}	Plain strain fracture toughness characterized by G
L_f	Gauge length at fracture
L_0	Original gauge length
ΔL	Change in gauge length
J	J - integral (a line or surface integral that encloses the crack tip from one crack surface to the other)
J_c	Value of J at fracture instability before stable tearing crack extension
J_{Ic}	Plane strain fracture toughness characterized by J - integral (at the initiation of ductile cracking)
J_{el}	Elastic component of J ($J_{el} = G$)
J_{pl}	Plastic component of J

J_u	Value of J at fracture instability after stable tearing crack extension
K	Bulk Modulus
K	Strength coefficient of Hollomon equations
K	Stress intensity factor
K_c	Plane stress fracture toughness characterized by K -factor
K_I	Mode I (opening) stress intensity factor
K_{Ic}	Plane strain fracture toughness characterized by K - factor
K_{II}	Mode I (in-plane shear) stress intensity factor
K_{III}	Mode III (out-of-plane shear) stress intensity factor
K_{Id}	Fracture toughness from dynamic loading rate
n	Strain hardening exponent of Hollomon equations
n_{RO}	Strain hardening exponent of Ramberg-Osgood equations
P or P_i	Internal pressure
P_o	External pressure
r	Inner radius of the pipe
t	Thickness of pipe wall
T_s	Temperature shift in Barsom & Rolfe Correlation
Y	Factor that depends on geometry of the specimen and the mode of loading

Greek Symbols

γ	Shear strain
δ	Crack-tip opening displacement (CTOD)
δ_c	CTOD at fracture instability without significant stable tearing crack extension
δ_{Ic}	Plane strain fracture toughness characterized by CTOD (at the initiation of ductile cracking)
δ_u	Value of CTOD at fracture instability after stable tearing
ε_{eng}	Engineering strain
ε_{true}	True strain
ε_t^{crit}	Longitudinal tensile strain capacity
ε_e	Elastic strain

ε_p	Plastic stain
ε_f	True fracture strain
ε_h	Hoop strain
ε_L	Longitudinal strain
ε_r	Radial strain
ε_u	Uniform strain (based only on the strain up to maximum load)
ε_{ult}	Ultimate elongation (numerically equal to the engineering strain at fracture)
η	Ratio of defect height to pipe wall thickness ($\eta = a/t$ for surface-breaking defects, $\eta = 2a/t$ for buried defects)
λ	Ratio of yield strength to tensile strength ($\lambda = Y/T$)
ξ	Ratio of defect length to pipe wall thickness ($\xi = 2c/t$)
σ_{eng}	Engineering stress
σ_{true}	True Stress
σ_h	Hoop stress
σ_L	Longitudinal stress
σ_r	Radial stress
σ_{TS}	Ultimate tensile strength
σ_{Tsd}	Dynamic ultimate tensile strength
σ_Y	Effective yield strength or flow strength, defined as the average of the 0.2% offset yield strength and ultimate tensile strength ($\sigma_Y = \frac{\sigma_{YS} + \sigma_{TS}}{2}$)
σ_{YS}	Yield strength
σ_{Ysd}	Dynamic yield strength
τ	Shear stress
ν	Poisson's ratio
ψ	Ratio of defect depth to pipe wall thickness ($\psi = d/t$)

Abbreviations

API	American Petroleum Institute
ASM	American Society for Metals
ASME	American Society of Mechanical Engineers

ASTM	American Society of Testing and Materials
AWWA	American Water Works Association
CVN	Charpy V-notch impact energy
CSA	Canadian Standard Association
CTOD	Crack-tip opening displacement
DBTT	Ductile-brittle transition temperature
FTP	Fracture transition plastic
HAZ	Heat-affected zone
HSS	High strength steel
ISO	Organization for Standardization
LYS	Lower yield strength
MTS	Material testing systems
NDT	Nondestructive testing
NPS	Nominal pipe size or diameter base on inches
NSS	Normal strength steel
PSL	Product specification levels
SMYS	Specified minimum yield strength
USE	Upper shelf energy
UYS	Upper yield strength
YPE	Yield point elongation

1. Introduction

1.1 Background and Problem Statements

Pipelines are currently regarded as the safest, most efficient and environmentally friendly method of transporting energy resources from remote places of production to the places of consumption to fuel the lives of people. Canada is abundant in energy resources, and the primary productions are crude oil and natural gas, which consisted of 41% and 34% respectively of the total domestic energy production in 2012 (Natural Resources Canada; 2014). Other energy productions, such as coal, hydroelectricity, natural gas liquids (NGLs), nuclear power and other renewables, and their respective proportion are shown in Fig. 1.1. Most current energy pipelines are constructed of coated steel to resist corrosion. In Alberta, steel pipelines consisted of about 86% of total energy pipelines (Alberta Energy Regulator; 2013).

Some energy production places such as Subarctic regions are often characterized by a harsh climate and difficult terrain and subjected to various kinds of adverse geotechnical events. For example, the Norman Wells, located in the Sahtu region of the Northwest Territories, is an abundant source of crude oil. The Norman Wells pipeline, as the first fully buried pipeline that traverses permafrost regions in Canada, has been operated by Enbridge Pipelines Inc. since 1985 (Burgess et al., 2010; Pederson et al., 2010). The pipeline is a 540 miles (869 km) of NPS 12 inch pipeline transporting crude oil from Norman Wells, Northwest Territories (NWT) to Zama, Alberta, with a capacity of 50,000 barrels per day. Nominal Pipe Size (NPS) is a widely used non-dimensional designator for diameter based on inches. Fig 1.2 shows the routes of liquid pipelines owned by Enbridge Pipelines Inc. in Canada. The route circled at the top of the map is the Norman Wells to Zama pipeline in the northern regions. The pipeline was constructed over two winter seasons between 1983 and 1985 and has been in operation since April 1985. The effects of permafrost terrain on the pipeline construction and operation and the soil-pipeline interaction should be particularly monitored and studied. In particular, the effects of slope instability, frost heave, and thaw settlement should be investigated. Pipelines buried out of sight beneath the

ground can be subjected to undesirable geotechnical conditions, imposing substantial external stresses and strains caused by impacts and displacements from geotechnical instability. The imposed loads on buried pipelines may be axial tensile or bending depending on the direction of external load with respect to the pipe axis. Both the external loading and internal pressure effects should be carefully considered for anticipating the potential failures and analyzing the resistance of the pipelines.

Most structural engineers in the past emphasized the issue of local buckling and wrinkles at the compression side of the pipe which is subjected to the substantial bending stresses. However, it has recently been realized that the issue of fractures and leaking at the tension side of the pipe may be as severe especially if a crack is present at tension side of the pipe walls. Failure in such cases could be catastrophic with the potential consequence of explosions in the case of gas pipelines and environmental effects in the case of liquid pipelines. In addition, many researches at present have been conducted to investigate high strength steel (HSS) pipes, such as X80 and X100, rather than normal strength steel (NSS) pipes, such as X60 and X70. This is due to the current increase of the use of HSS pipes in Canada. Hillenbrand and Kalwa (2002) indicated that an engineering project using HSS pipes instead of NSS pipes would cost less because the weight of required pipes would reduce. At the University of Alberta, many researches were conducted for normal and high strength steel pipes. For example, Cheng et al. (2004), Sen (2006) and Ahmed (2010) researched local buckling behaviors of cold bend pipes made of NSS steels. Cold bends are required if the orientation of the pipeline routes are changed in order to accommodate the terrain. Full scale pressurized test were conducted in response of the applied in-plane bending and axial tension. The tension side failure of pressurized NSS pipes under bending was investigated by Cakiroglu et al. (2012, 2014) in numerical analysis. They discovered that the increase of internal pressure would change the failure mode from the buckling at the compression side to the fracture at the tension side. The value of internal pressure equal to or more than 67% of specified minimum yield strength (SMYS) of the pipe would cause the tension side failure in their numerical bending tests on a defect free pipe. Neupane (2012) and Fathi (2012) researched the buckling resistance of high strength steel pipes and discovered that the anisotropic behavior is significant in high strength steel pipes and it has

great effects on buckling response. The anisotropic behaviors is determined by the stress-strain curves obtained from specimens machined in the longitudinal or circumferential direction, and the curves show the great difference in magnitude and shape. The circumferential stress-strain curve generally lies over the longitudinal stress-strain curve, and the circumferential yield stress is higher than the longitudinal yield stress. The circumferential stress-strain curve has a distinct yield point in the yielding region while the longitudinal stress-strain curve does not have this feature.

On the other hand, few researches were conducted for the lower strength steel pipes. To understand the stress-strain behavior of the vintage X52 steel pipes becomes the major focus of this thesis. The research X52 steel pipes were provided by Enbridge Pipelines Inc. from Norman Well pipeline. The investigation of the tensile strain capacity of the pressurized Norman Wells pipes of grade X52 steels in response to the applied axial tensile and bending loadings have been conducted by Enbridge Pipelines Inc. and the University of Alberta since 2012. The full investigation includes both small scale material tests and full scale pressurized tests. In this thesis, small scale material tests are carefully performed to understand the tensile and fracture properties of X52 steel pipes and their girth welds. A series of tension tests are conducted to obtain stress-strain curves and determine the tensile properties of the pipe material, such as the Young's modulus, the yield strength, the tensile strength, the elongation and so on. A series of Charpy V-notch impact tests are conducted to measure the energy required to fracture a V-notched specimen and determine the fracture properties of the pipe material, such as the impact toughness and estimated fracture toughness according to the empirical correlations. The longitudinal tensile strain capacity of the pipe is predicted based on the equations provided in CSA Z662-11. The reduction of the tensile strain capacity caused by girth weld defects is generally studied. The experimental results and their further discussions will contribute to understanding the current material conditions of the buried vintage X52 pipes and their girth welds manufactured in the 1980s.

The researched X52 pipe has an actual outer diameter of 12.75 in (324 mm) and actual wall thickness of 0.27 inch (6.86 mm). There is an existed girth weld manufactured in 1980s on

the pipe walls and is labeled as “old” girth weld. To better understand the current conditions of this original girth weld, a new girth weld was manufactured in 2013 and labeled as “new” girth weld. The photos of the two girth welds are shown in Fig. 1.3.

Canadian primary energy production, by source, 2012

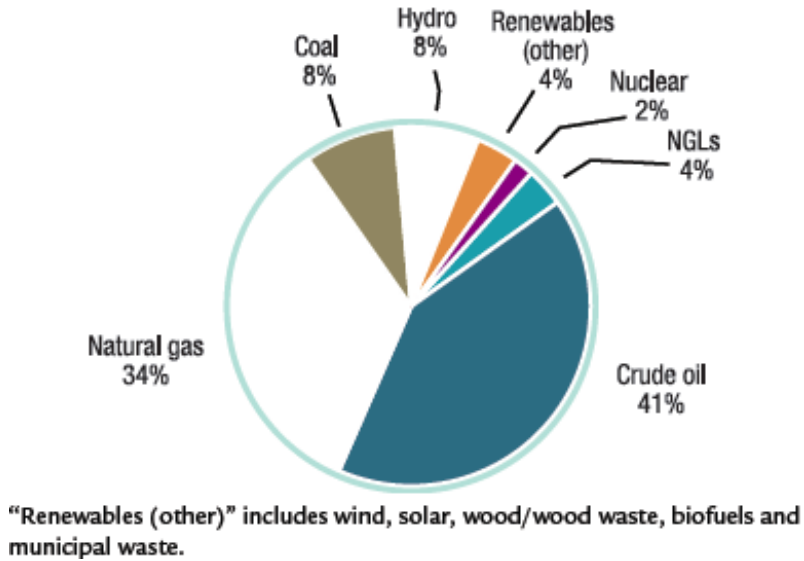


Fig. 1.1 Canadian primary energy production and their proportion in 2012 (From Natural Resources Canada, 2014)

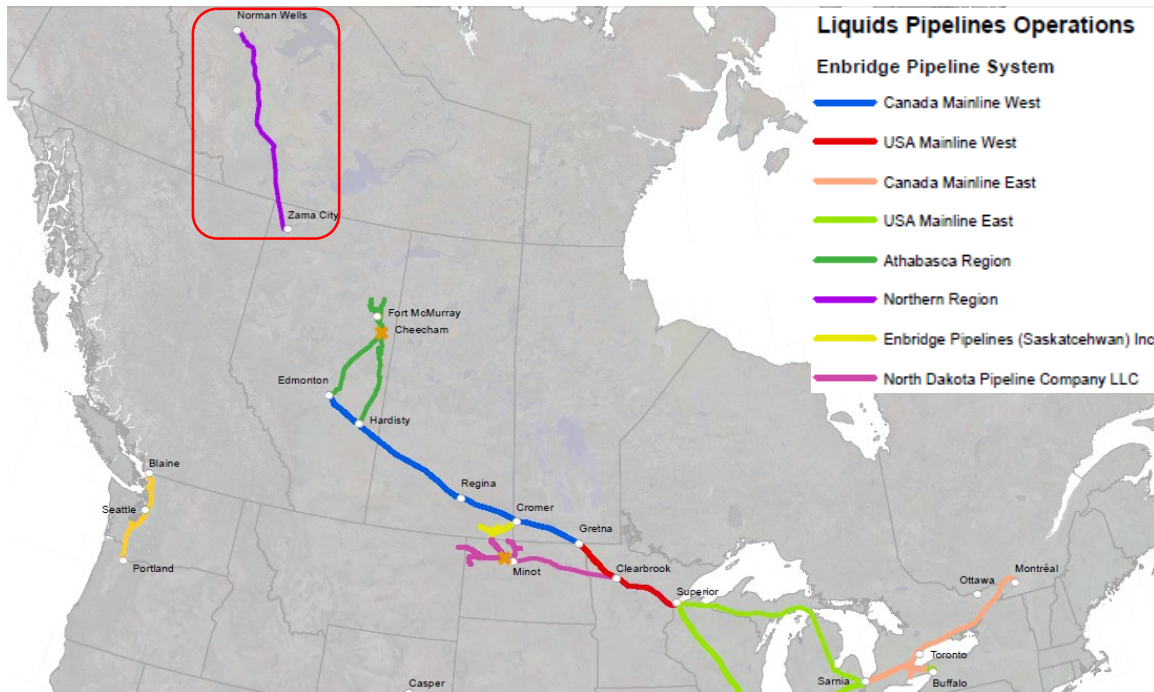


Fig. 1.2 Enbridge liquid pipeline systems (From Enbridge Inc., 2014, Map # 113-2014-2)



(a)



(b)

Fig. 1.3 Girth weld (a) “old” girth weld; (b) “new” girth weld

1.2 Objective of Thesis

The objective of this thesis is to investigate the tensile and fracture properties of vintage Norman Wells X52 steel pipes and their girth welds by conducting experimental small scale material tests. The test results are carefully analyzed and the longitudinal tensile strain capacity is predicted according to CSA Z662-11. The motivation is to utilize the code equations for X52 steel pipes.

First of all, a comprehensive and detailed literature work is completed to understand the main failures of pipelines and mechanical properties of steel materials. The tensile properties are carefully reviewed by studying a typical stress-strain curve obtained from a ductile steel specimen. The fracture properties are studied by measuring the fracture toughness in fracture mechanics.

Secondly, small scale tension tests are conducted to determine the tensile properties of the X52 pipe and girth welds. In tension tests, specimens machined from the base metal, the weld metal, and the heat-affected zone (HAZ) are all tested and compared through both engineering and true stress-strain curves. The elastic deformation properties (Modulus of Elasticity), the strength properties (yield strength and tensile strength), and the ductility properties (elongation and reduction of cross-sectional area) of pipe specimens are determined. Strain-hardening region of the true stress-strain curve obtained from each specimen is particularly characterized into the empirical mathematical expressions known as the Hollomon equation and the Ramberg-Osgood equation.

Thirdly, a series of Charpy V-notch impact tests are conducted to measure the energy required to fracture a CVN specimen and understand the fracture properties of X52 pipe and girth welds. In CVN impact tests, specimens machined with a V-notch from the base metal, the weld metal, and the heat-affected zone (HAZ) are all tested at room temperature and a lower temperature. The impact toughness and the ductility of the pipe specimens are directly determined by observed CVN energy values and fracture surfaces measurements. By cooling specimens to a specific lower temperature, the temperature effects on material resistance to impact strikes are discussed. An important further discussion of the

experimental CVN energy values is to empirically correlate them with fracture toughness parameters, such as plane-strain stress intensity factor (K_{Ic}), J - integral value (J_{Ic}), or critical crack-tip opening displacement (δ_{Ic}). The requirements and assumptions for the validity of the correlations between parameters are carefully investigated. A comparison with higher grade of API X-grade steel pipes for CVN tests and fracture toughness tests results are discussed to better understand the obtained results of the research X52 steel pipe.

Lastly, the strain-based design in pipelines is investigated. The stress-strain behaviors of different X- grade steel pipes (X52, X60, X65, X80 and X100) are studied from the stress-strain curves. The magnitude and shape of the curves are emphasized to understand the difference between low and high strength steels. Based on experimental results, the tensile strain capacity of X52 pipe is predicted according to the empirical equation provided by CSA Z662-11. The reduction of the tensile strain capacity caused by a surface-breaking defect or a buried defect is studied. The limitation and validity of the equations are discussed.

1.3 Organization of Thesis

Chapter 1 introduces the pipelines systems in Canada, particularly Norman Wells pipelines, explains the reason for investigating the tensile and fracture behaviors of X52 steel pipes and their girth welds, and states the objectives and the organization of this thesis.

Chapter 2 consists of a comprehensive and detailed literature review on the main failures of pipelines caused by internal pressure and external loadings, mechanical properties of steel materials, characterization of a typical steel stress-strain curve, and introduction to fracture mechanics.

Chapter 3 discusses the experimental setup and methods of the tension tests, the results of tensile properties of X52 pipe specimens, and the mathematical expression of the obtained stress-strain curves.

Chapter 4 discusses the experimental setup and methods of the Charpy V-notch impact tests, the results of fracture properties of X52 steel pipe specimens, the empirical correlation between experimental CVN energy values and the fracture toughness parameters, and the comparison between the research X52 steel pipe and higher grade of API X-grade steel pipes for CVN and fracture toughness test results.

Chapter 5 introduces the strain-based design, discuss the comparison between low and high strength X-grade steel pipes from their stress-strain curves and discuss the prediction of tensile strain capacity of X52 steel pipes based on experimental material properties and a selected defect sizes according to the CSA empirical equations.

Chapter 6 summarizes the results of the tension and CVN impact tests, concludes the tensile and fracture properties of X52 steel pipes and their girth welds, predicts the tensile strain capacity of the X52 steel pipes, and recommends the direction for future work.

2. Literature Review

This chapter includes a comprehensive and detailed literature review on the topics of failures of pipelines and the mechanical properties of steel materials. In particular, a typical stress-strain curve and fracture toughness in fracture mechanics are carefully studied to understand the tensile and fracture properties of the material.

2.1 Introduction to Pipelines

Since pressurized steel pipelines are buried out of sight beneath the ground, they are often prone to a variety of potential threats caused by both internal pressure and external loadings. The external loadings include both the loads and displacements from geotechnical instability and often impose substantial axial tensile or bending stresses and strains on pipelines. It is significant to understand the common failures of pipelines and their reasons, analyze the stresses and strains produced by either internal or external loadings and anticipate the resistance of the pipelines.

2.1.1 Failures of Pipelines

The pressurized pipelines often fail when the stress in the pipe wall material exceed a critical failure criterion, and consequently pipelines lose their products either by leak or rupture. A variety of reasons may threaten the pipes. For example, improper pipe manufacturing may produce material defects; improper joint connection may produce stress concentration and cause joint leak; corrosion and contamination may cause localized corrosion pitting or wall thinning over a large area; excessive internal pressure and external forces may result in buckling, tensile failure, or other types of failure; heating or cooling pipes beyond the specified temperature range may change pipe dimensions and material properties, and produce tensile or compressive stresses (Cassa, 2005). The common failures and their reasons for water pipelines and energy pipelines are both investigated to have an overall understanding of pipelines.

In general, the common crack failure modes associated with all pressurized pipelines are blow out, circumferential cracking, longitudinal split, ductile rupture, and joint leak (Makar,

Desnoyers & McDonald, 2001; Cassa, 2005; Water Services Association of Australia, 2012). Blow out is commonly caused by corrosion pitting and wall thinning. Corrosion pitting is shown by a localized small hole. As the pipe resistance to internal pressure is reduced by wall thinning to some extent, internal liquid blows the remaining thin wall, and the failure occurs. The size of blow out depends on pipe material. Circumferential cracking is commonly caused by external bending forces or tensile forces due to soil movements, and mostly occurs in small diameter pipes. A circumferential crack propagates partly or fully around the circumference of the pipe. Longitudinal split is commonly caused by internal pressure when it surges at the time of pump starts, corrosion pitting or manufacturing defects, and mostly occurs in large diameter pipes. Longitudinal splits propagate along the length of the pipe, and the length varies from short to full length of the pipe. Full-length splits on the opposite sides of the pipe are able to cause the entire top of the pipe to break off.

Blow out, circumferential cracking, and longitudinal split are typically brittle failures, and mostly common in cast iron pipes. However, steel pipes usually experience ductile failure. Ductile rupture and tearing of the pipe wall are commonly caused by corrosion. As pipe wall thickness is reduced, pipe material tears due to the ductility and then an opening in the pipe wall is induced. Anti-corrosion coating is usually applied on the external surface of pipes to effectively avoid corrosion. Failure occurs not only on the pipe base, but also at the joints, such as the location of girth weld. Girth weld defects will be the potential threats. In addition, improper joint connection or use of non-elastomeric seal joints, such as lead or lead compound, may cause internal liquid to leak out through the joints, especially when the operating pressure is high (Water Services Association of Australia, 2012). This type of failure mode is common in both cast iron pipes and steel pipes. Some photographs of above common failure modes on water pipelines are illustrated in Fig. 2.1 (Water Services Association of Australia, 2012).



(a)



(b)



(c)



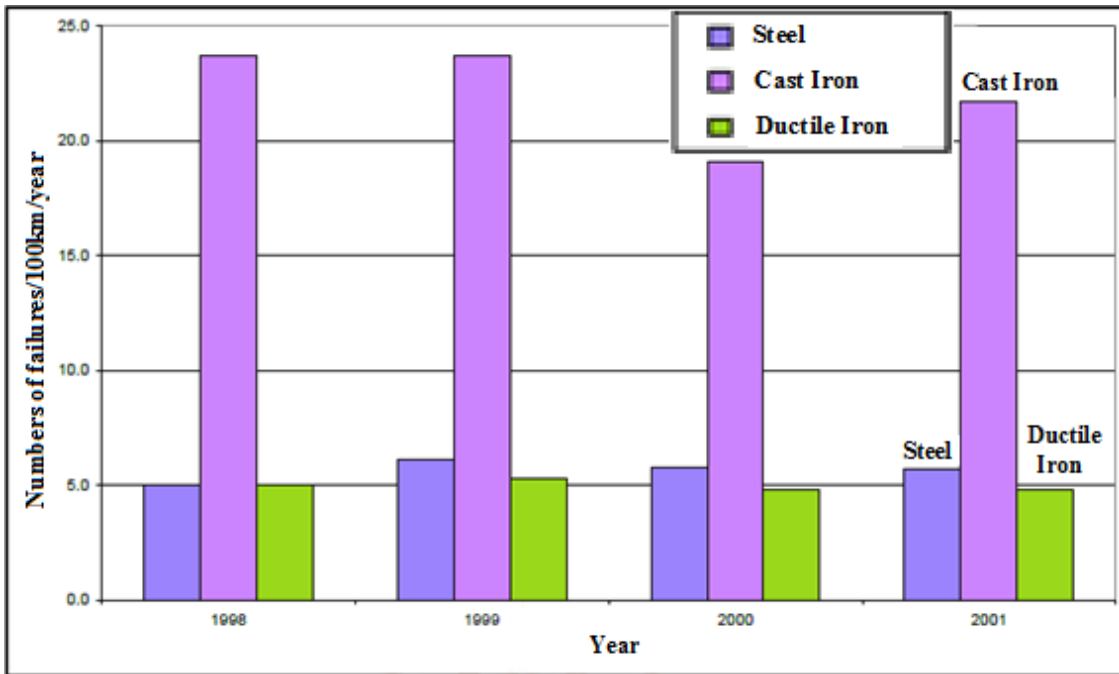
(d)



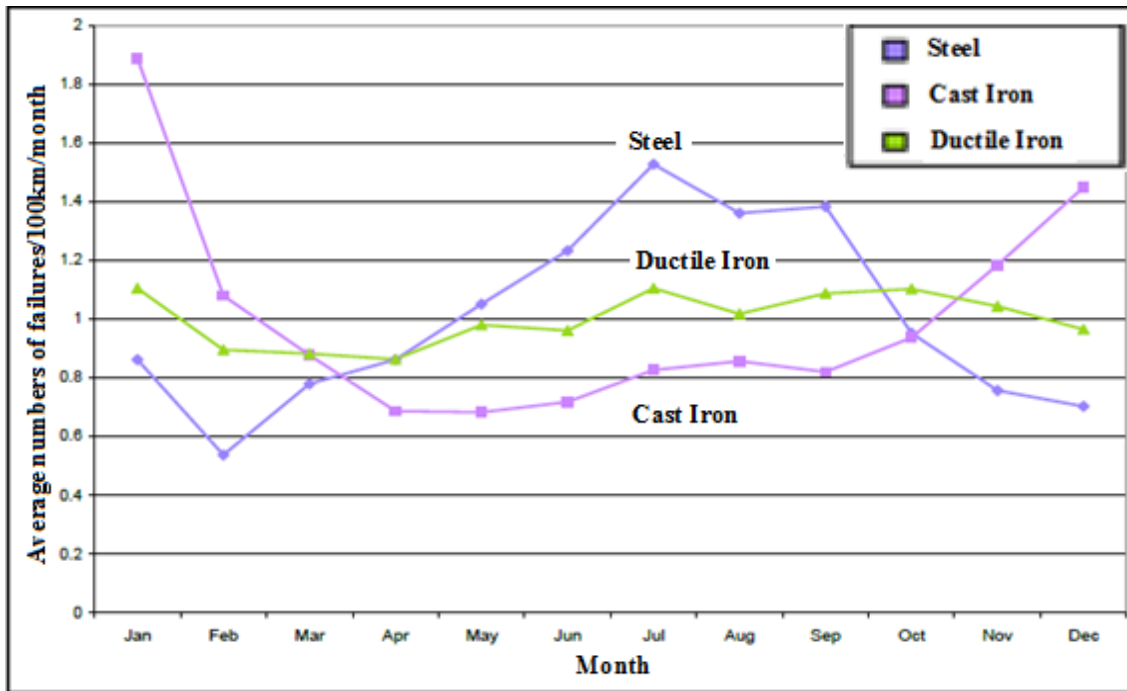
(e)

Fig. 2.1 Photos of common pipe failure (a) pin hole (corrosion pit) on a ductile iron pipe; (b) blow out on a ductile iron pipe; (c) circumferential cracking on a cast iron pipe; (d) longitudinal split on a cast iron pipe; (e) ductile rupture (pipe wall tearing) on a steel pipe. (From Water Services Association of Australia, 2012)

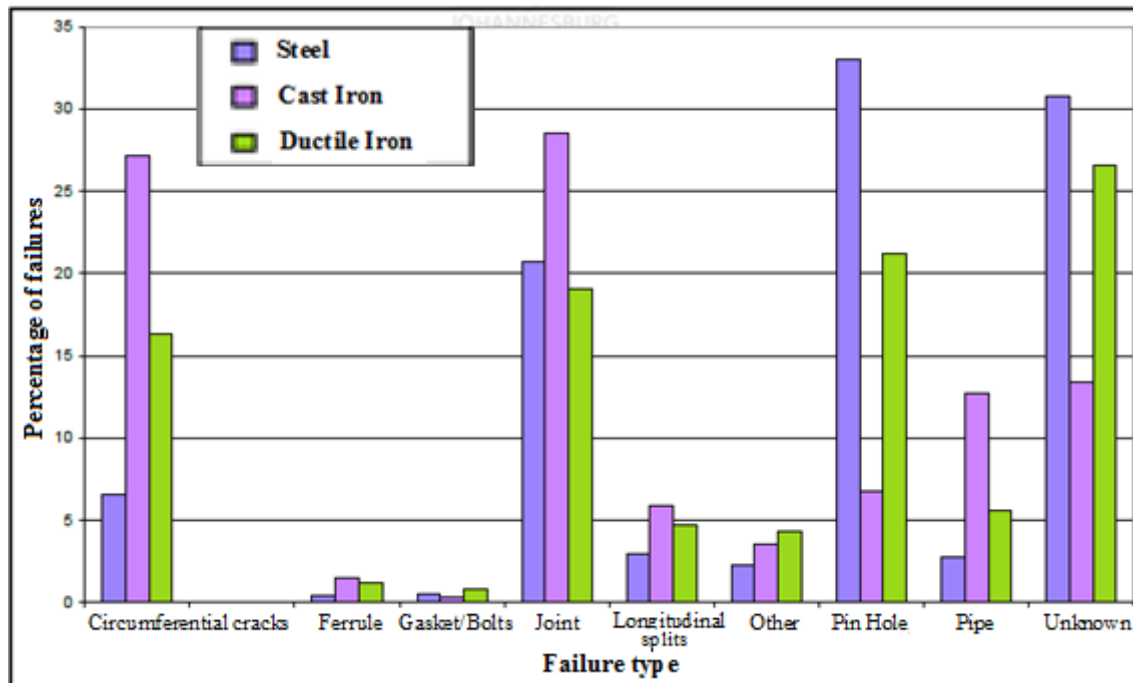
The failure of water pipelines was investigated by the UK Water Industry Research in 2005 (Cassa, 2005). They compared the failure rate of steel pipes, cast iron pipes, and ductile pipes per 100 km of pipeline, the monthly trends of failure rates over a year, and their most common type of failures. The failure rate is a measure of the overall annual pipeline performance and is computed by dividing the total recorded numbers of failures from all utilities for a particular pipeline over a year by the total length of this pipeline, and had the unit of failures/100km/year in this research. Fig. 2.2 (a) illustrates the average failure rate per 100 km of pipelines in the UK for these three types of materials in the years from 1998 to 2001. The figure shows that steel pipes and ductile iron pipes are more reliable, and fail less than cast iron pipes. Fig. 2.2 (b) illustrates the average failure rate per 100 km of pipelines in each month over a year for the three types of materials. The data for each month was summarized in the years from 1990 to 2002. The figure shows that steel pipes fail more during the summer months from June to September, cast iron pipes fail more during the winter months from November to February, and ductile iron pipes do not show obvious difference between months. The failure of steel pipes in the summer may be caused by the thaw settlement. Fig. 2.2 (c) illustrates the percentage of common failure types in the UK for the three types of materials in the years from 1990 to 2002. The main failures of steel pipes are corrosion pin holes, joint failures, and other unknown failures, the main failures of cast iron pipes are circumferential cracking and joint failures, and the main failures of ductile pipes are corrosion pin holes, circumferential cracking, joint failures, and other unknown failures.



(a)



(b)



(c)

Fig. 2.2 Comparison of average failure rate per 100 km of pipelines in the UK for steel, cast iron and ductile iron pipes (a) average failure rate between 1998-2001; (b) average failure rate over a year; (c) percentage of failure types between 1990-2002 (Adapted From Cassa, 2005, pp. 2-21~2-22)

The data of Canadian energy pipelines were reported by Natural Resources Canada (2014). Among all provinces in Canada, Alberta produced the predominant amount of crude oil and natural gas, which were 76% and 74% of each total domestic production in 2013. The proportions made by other provinces are shown in Fig. 2.3. Alberta Energy Regulator (2013) collected data for energy pipelines in Alberta from January 1, 1990 to December 31, 2012 and reported the failure rate of pipeline per 1000km per year. According to the failure statistics, the main causes for pipelines failures (hits, leaks, and rupture) were internal corrosion, external corrosion, construction damage, earth movements (slope movement, heaves, or settlements), joint failures, overpressure failures, pipe failure (stress corrosion cracking, fatigues, or mechanical damage), valve/fitting failures (seal blowouts and packing leaks), weld failure (seam rupture or sulphide stress cracking at the girth weld), and damage by others (third-party excavation or interference). Fig. 2.4 illustrated the numbers of incidents for two primary energy pipelines (crude oil and natural gas pipelines)

and a water pipeline from 1990 to 2012 and the proportion of causes for these three pipelines failures. During 23 years, 538 incidents were recorded for crude oil pipeline and its failure rate was about 23 per year, 5484 incidents were recorded for natural gas pipeline and its failure rate was about 238 per year, and 4245 incidents were recorded for water pipeline and its failure rate was about 185 per year. It is worth noting that the most important failure cause was internal corrosion, which was responsible for 21.2% of total crude oil pipeline failures, 53.2% of total natural gas pipeline failures, and 57.1% of total water pipeline failures. In general, the water content and erosive constituents (mud or sand) will increase the corrosivity. Before the crude oil is transported, it is processed, and water and sediments are removed. The transported oil will be less corrosive than the raw oil. For this reason, the number of internal corrosion failures was the least for crude oil pipeline, but the most for water pipeline. For natural gas pipeline, a large number of pipelines carried raw gas which contains some amounts of water, H₂S, and CO₂. Since 1990, some types of internal corrosion protection have been applied on water pipeline surface to reduce the number of internal corrosion failures, and it dropped from 330 per 1000 km in 1990 to 120 per 1000km in 2012. The external corrosion is the second important cause, which was responsible for 12.6% of total crude oil pipeline failures, 11.7% of natural gas pipeline failures, and 6.5% of total water pipeline failures. The external corrosion was not related to the transported production, but depended on the pipe coating and external soil conditions.

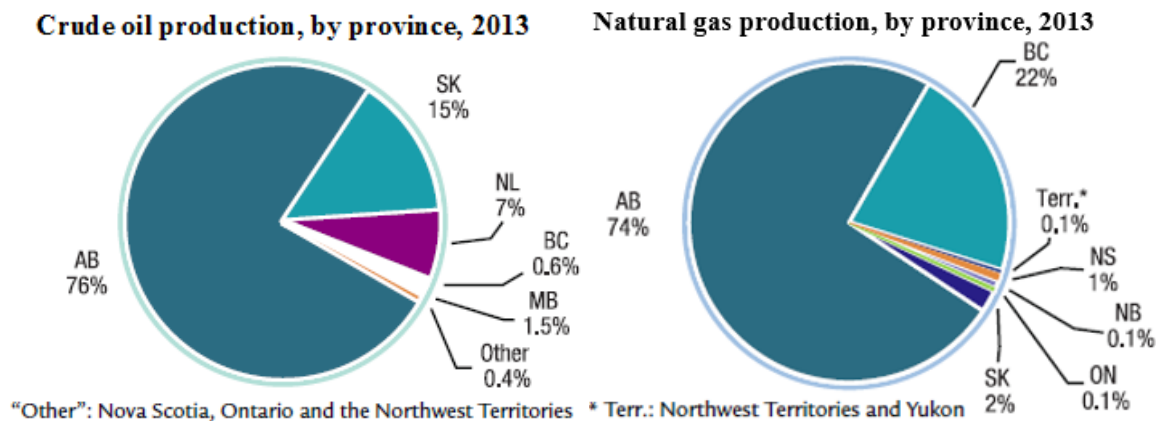
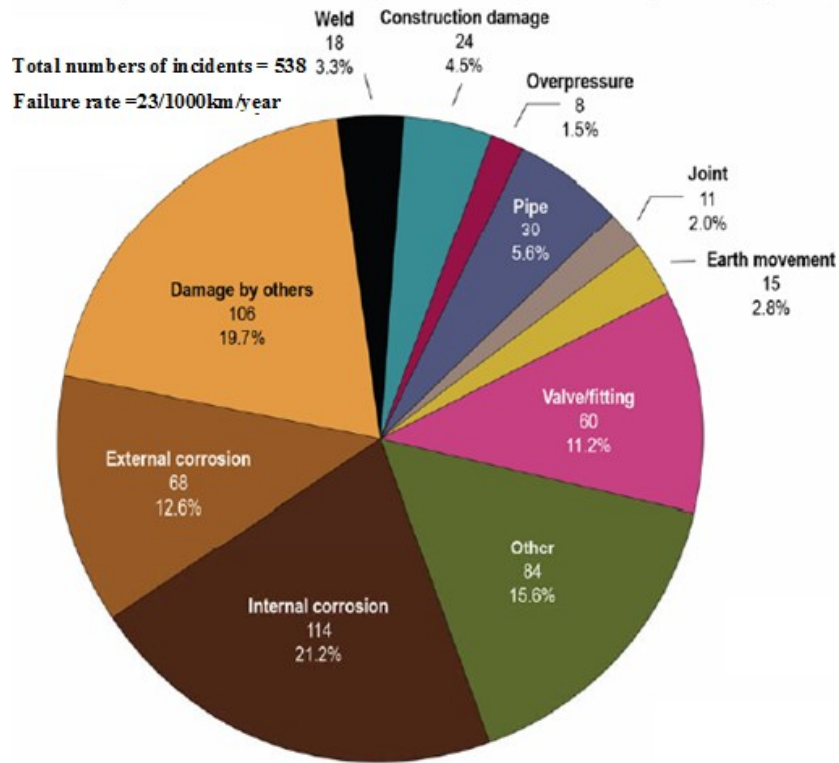


Fig. 2.3 Canadian provincial crude oil and natural gas production and their proportions in 2013. (From Natural Resources Canada, 2014)

Crude oil pipeline incidents by cause for all years combined

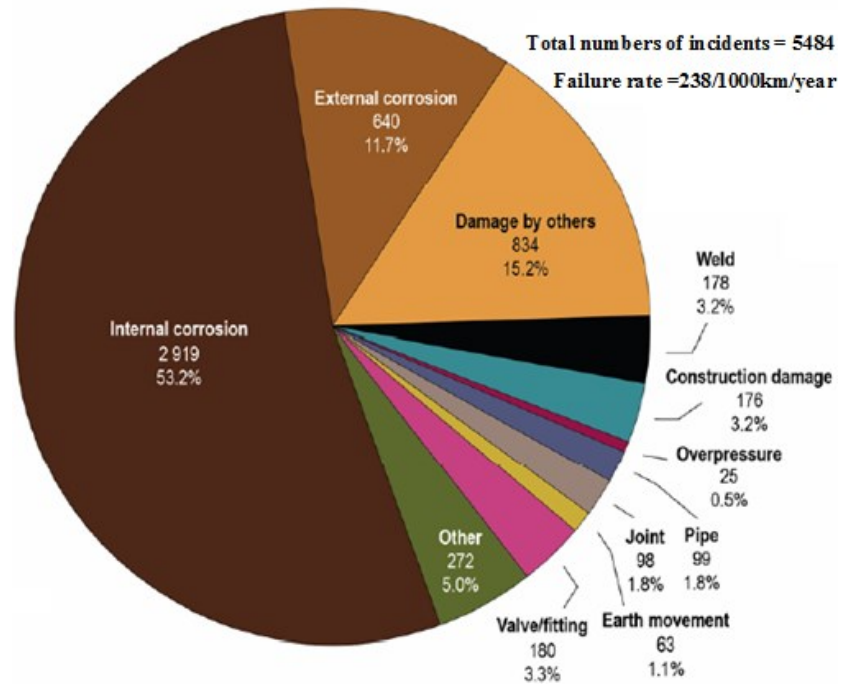
January 1, 1990, to December 31, 2012 (hits, leaks, and ruptures, excludes pressure tests)



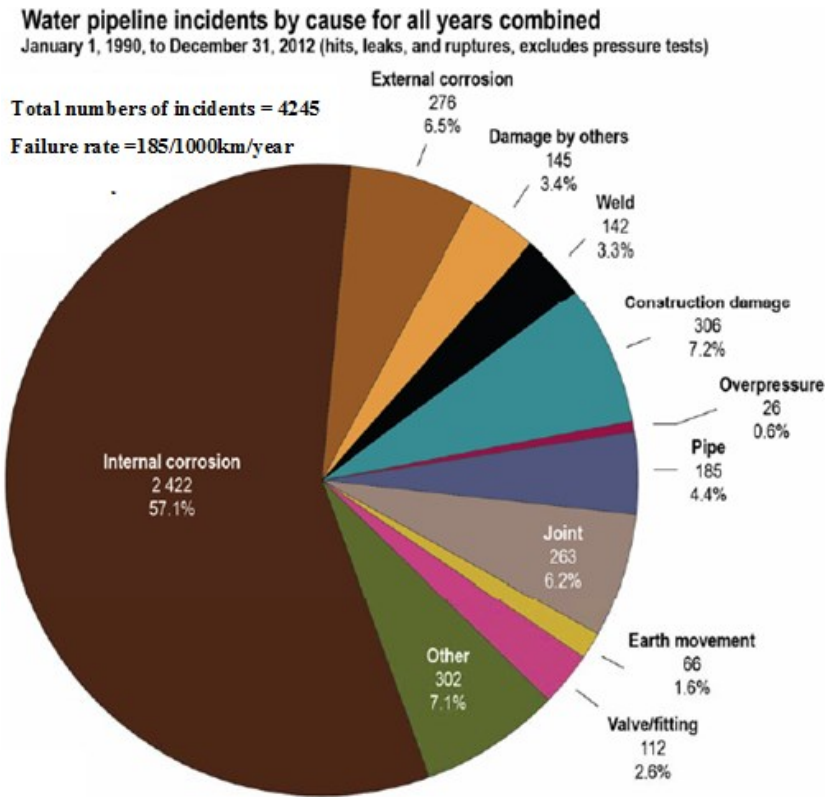
(a)

Natural gas pipeline incidents by cause for all years combined

January 1, 1990, to December 31, 2012 (hits, leaks, and ruptures, excludes pressure tests)



(b)



(c)

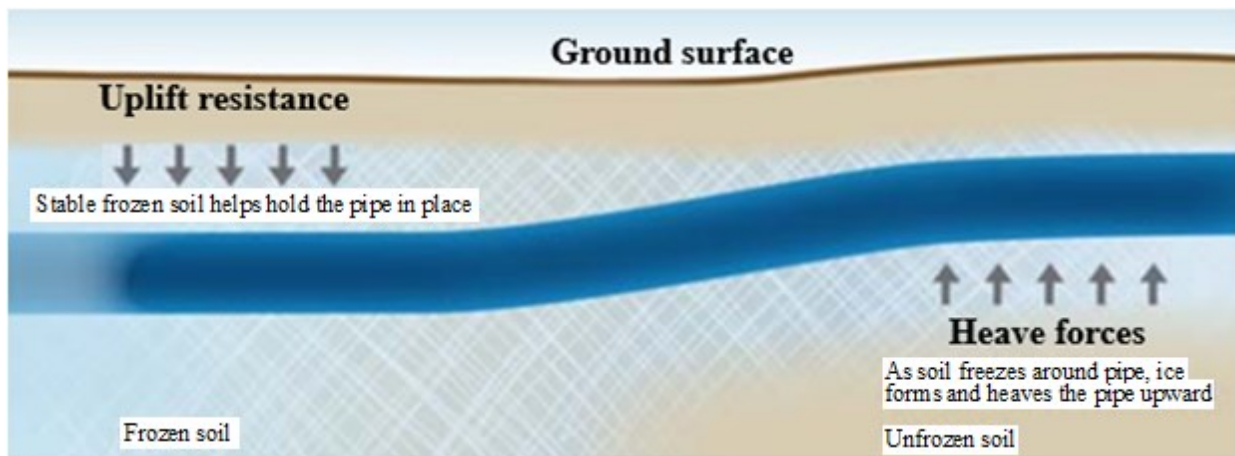
Fig. 2.4 Numbers of Alberta pipelines incidents and the proportion of failure causes between 1990 – 2012 (a) crude oil pipeline; (b) natural gas pipeline; (c) water pipeline (From Alberta Energy Regulator, 2013)

2.1.2 External Loading Effects on Pipelines

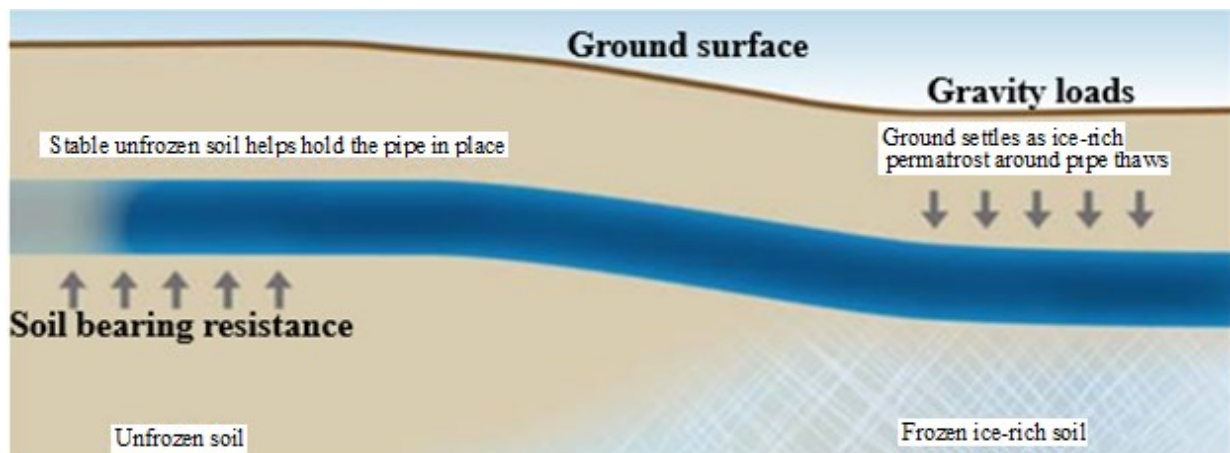
Pipelines are prone to various geotechnical events because they usually transverse regions with harsh climate and difficult terrain. Such events may pose serious threats to pipelines buried out of sight beneath the ground, as a form of imposing substantial external stresses and strains caused by impact and displacement from geotechnical instability. Some common examples of external threats and how they affect the pipelines buried beneath the ground were described by Muhlbauer (2004).

Soil movements are believed to be the main and most common potential threats to buried pipelines (Muhlbaue, 2004). Soil movements impose external forces and displacements on pipelines. Such imposition can be sudden which results in immediate failures to pipelines, or gradual over a period of years which results in substantial stresses and strains on the pipelines. Based on whether a slope is involved or not, soil movements can be generally categorized by soil sliding or soil volume change. Soil sliding is termed as slope instability or landslides, which is described by unstable mass-downslope movements imposing unfavorable external forces of gravity and displacements on pipelines. The common phenomena include soil slides, rock slides, mudflows, avalanches and creep, which can be triggered by various reasons. Soil volume change is caused by differential temperature and the moisture content, which results in shrinkage, swelling, and settlement. Shrinkage and swelling are often seen in high expansive clays, which ruin the pipe coating and generate stresses on the pipe walls. Not embedding pipelines directly in such expansive soils is a practical way to effectively avoid such risk. In cold regions, seasonal frost heave and thaw settlement are often seen as water in the ground freezes and thaws, which result in a considerable displacement of the ground on the buried pipeline. In the winter, the unfrozen frost-susceptible soil expands due to freezing, which produces upward displacement of the ground and heave forces on the buried pipeline (Bai, 2014; Nixon, Sortland, & James, 1990). As shown in Fig. 2.5 (a), the pipe section around the unfrozen soil moves upward due to the frost heave, while its ambient pipe section resist this movement due to the uplift resistance of the stable frozen soil. In the summer, the soil sinks due to the thawing of frozen soil, which produces downward displacement and gravity load of the ground on the buried pipeline. Significant settlement results in considerable external bending and shear

stresses and strains on the pipeline (Muhlbauer, 2004; Bai, 2014). As shown in Fig. 2.5 (b), the pipe section around the initial frozen soil moves downward due to the thaw settlement, while its ambient pipe section resists this movement due to the bearing resistance of the stable unfrozen soil. If possible, pipelines should be buried below the frost line to effectively avoid such risk (Muhlbauer, 2004). However, pipelines sometimes have to transverse sensitive discontinuous permafrost regions in which frost heave and thaw settlement usually occur.



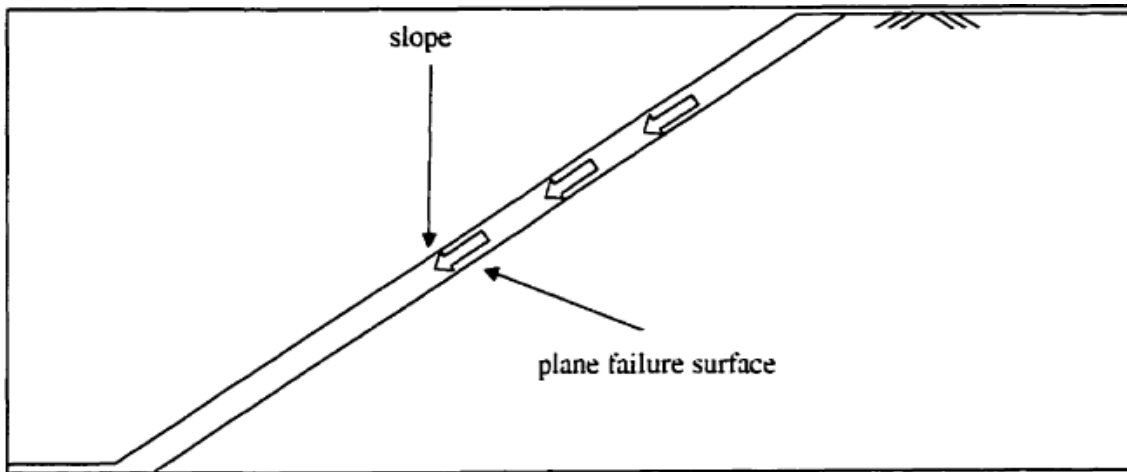
(a)



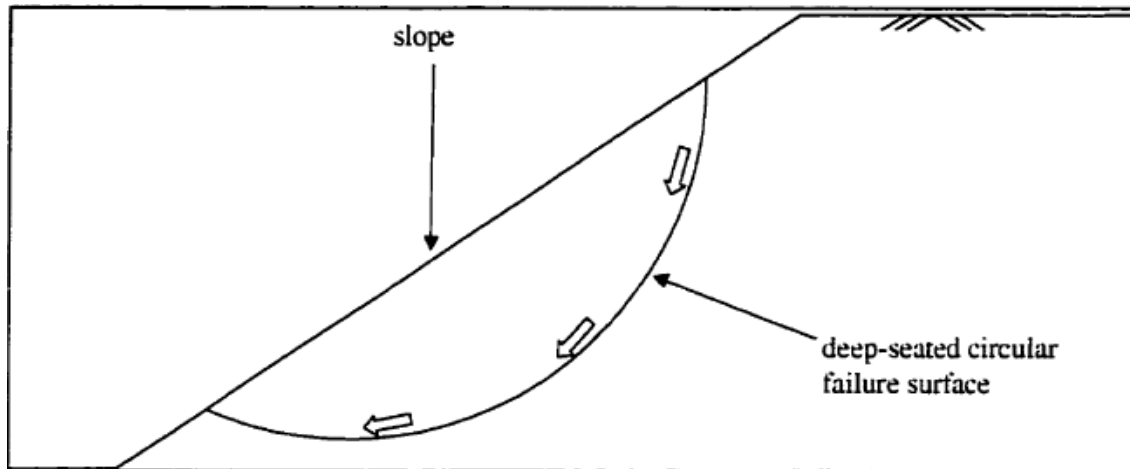
(b)

Fig. 2.5 An example of (a) frost heave and (b) thaw settlement (Adapted from White, 2013, pp.2-3)

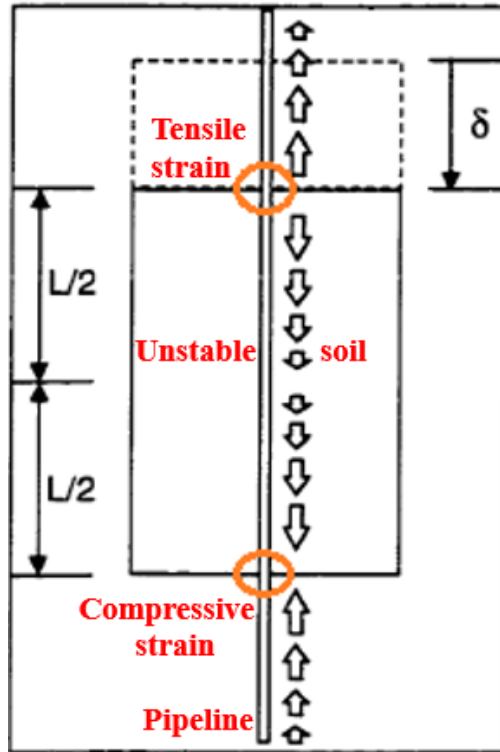
The imposed stresses and strains on buried pipelines may be axial or bending, which is determined by the relative soil movement with respect to the pipe axis. The soil-pipeline interaction due to various types of landslides were carefully investigated by Chen (1999). Landslides are typically characterized by various types, including planar landslides and deep-seated landslides. As shown in Fig. 2.6 (a), a planar landslide is described by a sliding surface parallel to the slope surface, such as the longitudinal landslide and transverse landslide. The longitudinal landslide occurs when soil moves parallel to the pipe axis, while the transverse landslide occurs when soil moves perpendicular to the pipe axis. As shown in Fig. 2.6 (b), a deep-seated landslide is described by a sliding surface resembling arcs of circles. It usually produces both longitudinal and transverse forces on buried pipelines. The effects of the longitudinal landslide and the transverse landslides on pipelines were described in details. As shown in Fig. 2.6 (c), the unstable soil moves δ and tends to push the pipeline down the slope; as a result, the adjacent stable soil resists downward movement and generates upward stresses on the pipeline. The potential failure of the pipeline occurs near the interface between unstable and stable soil (Arya, n.d.). The accumulated axial tensile strains may cause tensile failure and fracture while the axial compressive strains may cause local buckling and wrinkles. As shown in Fig. 2.6 (d), as the adjacent stable soil resists pipeline down the slope, the flexural bending strains are induced on pipeline. High bending strains are accumulated at the interface between unstable and stable soil (Arya, n.d.). However, axial tensile strains caused by axial stretching of the pipelines are predominant. Even at the interface, the tensile stress is higher than the bending stress (Chen, 1999). The potential failure of the pipeline is attributed to axial stretching and flexural bending.



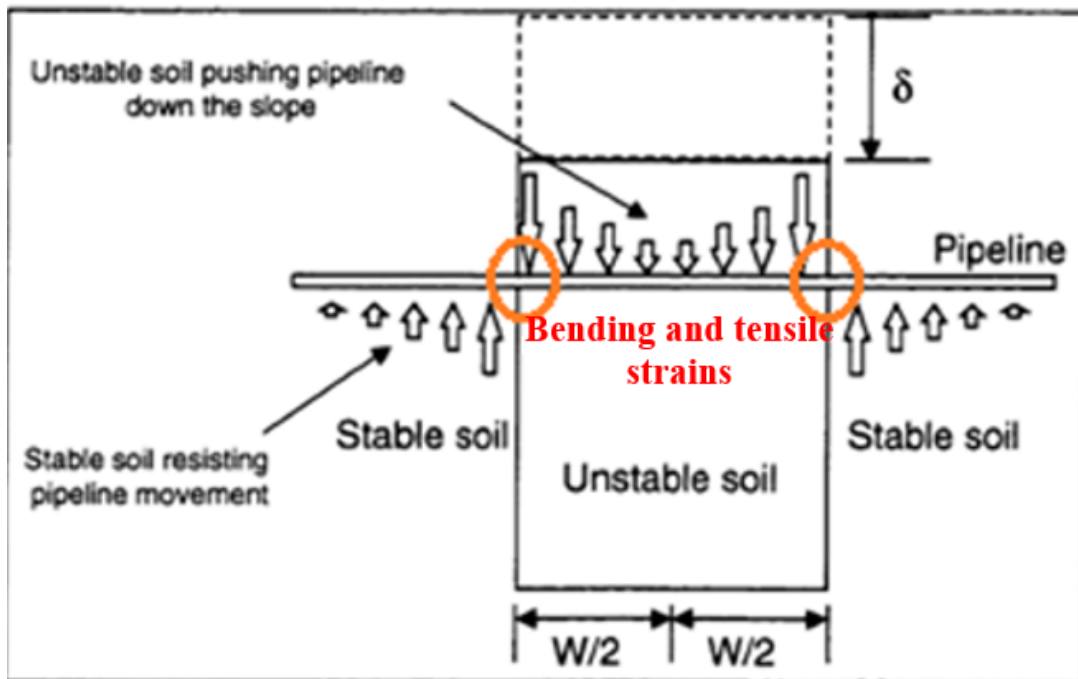
(a)



(b)



(c)



(d)

Fig. 2.6 Landslides (a) planner landslide; (b) deep-seated landslide; (c) longitudinal landslide; (d) transverse landslide (Adapted from Chen, 1999, pp.14,43,45)

2.1.3 Internal Pressure Effects on Pipelines

In this section, the stresses and strains caused by internal pressure on pipelines are carefully reviewed. For a thin walled cylindrical pipe, the internal pressure produces three mutually perpendicular principal stresses on the pipe walls, which are the longitudinal stress (σ_L), the hoop stress (σ_h), and radial stress (σ_r). As shown in Fig. 2.7, the longitudinal stress, also called the axial stress, acts along the direction which is parallel to the longitudinal axis of the pipe; the hoop stress, also called circumferential stress, acts circumferentially in a direction which is perpendicular to the axis of pipe; the radial stress acts along the radial direction which is perpendicular to the pipe wall (Sharma, n.d.). Among these three states of stresses, the hoop stress is the highest stress for an internally pressurized cylindrical pipe, and it should not exceed the maximum allowable stress that the pipe is able to withstand. If it exceeds, the pipe wall thickness should be increased to avoid failure (Lee, J., Rainey, W., & Brunner, M., 1998). Barlow's formula gives a simple and widely used method to calculate the hoop stress, but it only applies to the thin walled pipe under internal pressure without any external pressure. Lee et al. (1998) discovered that the radial stress to hoop stress ratio σ_r/σ_h is less than 0.1 when the pipe wall thickness to diameter ratio t/D is less than 0.05 if only the internal pressure is applied. As a result, for the thin walled pipe ($t/D < 0.05$), the very small radial stress can be negligible. From the theoretical viewpoint, the radial stress varies from the pressure P_i on the inner surface to pressure zero on the outer surface, but it is negligibly small compared to the longitudinal stress and hoop stress for the thin walled pipe (Clemens; 2005). Therefore, the stress state for an element of a thin walled internally pressurized pipe is usually regarded as a biaxial stress state rather than a tri-axial stress state. Lee et al. (1998) also mentioned that the radial stress cannot be negligible for the thick walled pipe or when external pressure is applied. As shown in Fig. 2.10, the radial stress to hoop stress ratio σ_r/σ_h increases significantly as the external pressure to internal pressure ratio P_o/P_i increases.

Consider an infinitely long free section of a thin walled pipe under the effect of an internal pressure P , shown in Fig. 2.8 (a). The longitudinal strain is regarded as zero because the infinite long pipe is theoretically not able to extend or contract in the longitudinal direction. The resisting stress is the hoop stress. From Fig. 2.9 (a), the equilibrium of the applied

force owing to the internal pressure and the resisting force owing to the hoop stress can be obtained and expressed by $P \cdot DL = \sigma_h \cdot 2Lt$. After conversion, the hoop stress is expressed by $\sigma_h = \frac{PD}{2t}$, which is known as the Barlow's formula. The outside diameter rather than the inside or the mean diameter is widely used in the formula because it results in the maximum hoop stress and a conservative result in the stress assessment. Consider a long section of a thin walled pipe with capped ends under the effect of the internal pressure P , shown in Fig. 2.8 (b). The resisting stresses is both the hoop stress and the longitudinal stress. From Fig. 2.9 (b), the equilibrium of the applied force owing to the internal pressure and the resisting force owing to the longitudinal stress can be obtained and expressed by $P \cdot \frac{\pi D^2}{4} = \sigma_L \cdot \pi Dt$. After conversion, the longitudinal stress is expressed by $\sigma_L = \frac{PD}{4t}$. In summary, the longitudinal stress (σ_L), the hoop stress (σ_h), and the radial stress (σ_r) caused by internal pressure are expressed below.

$$\sigma_L = \frac{PD}{4t}; \sigma_h = \frac{PD}{2t}; \sigma_r \approx 0 \text{ if } D \gg t \text{ because } \sigma_L, \sigma_h \gg \sigma_r$$

(σ_r varies from P on the inter surface to 0 on the outer surface)

where

P is internal pressure

D is pipe outer diameter

t is pipe wall thickness

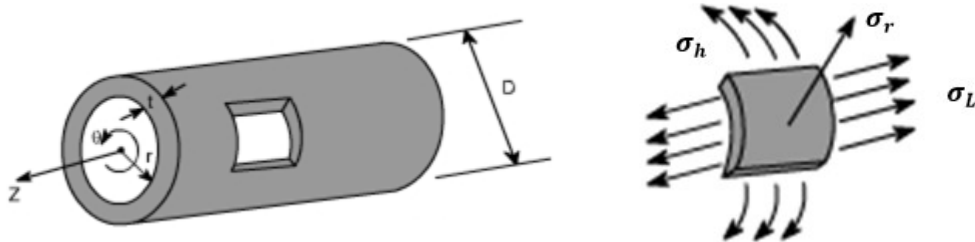


Fig. 2.7 Longitudinal stress (σ_L), hoop stress (σ_h) and radial stress (σ_r) on a cylindrical pipe (From Sharma, n.d., Lecture 15)

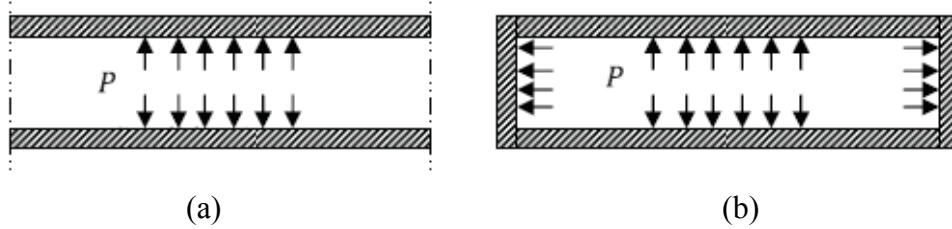


Fig. 2.8 (a) Free ends and (b) capped ends on a pipe (From Adeeb, 2011, p.265)

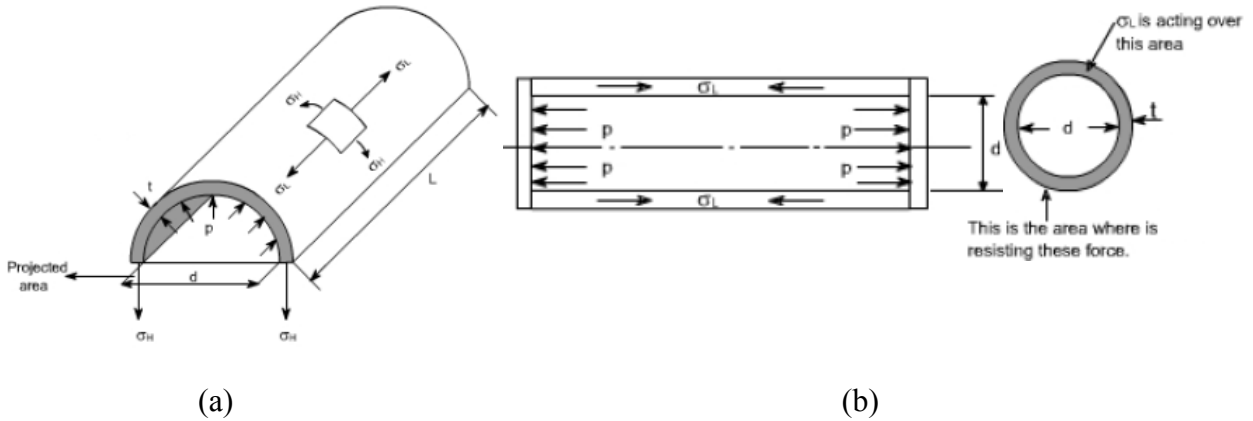


Fig. 2.9 Stress in free ends and capped ends conditions (a) Hoop stress; (b) hoop and longitudinal stress (From Sharma, n.d., Lecture 15)

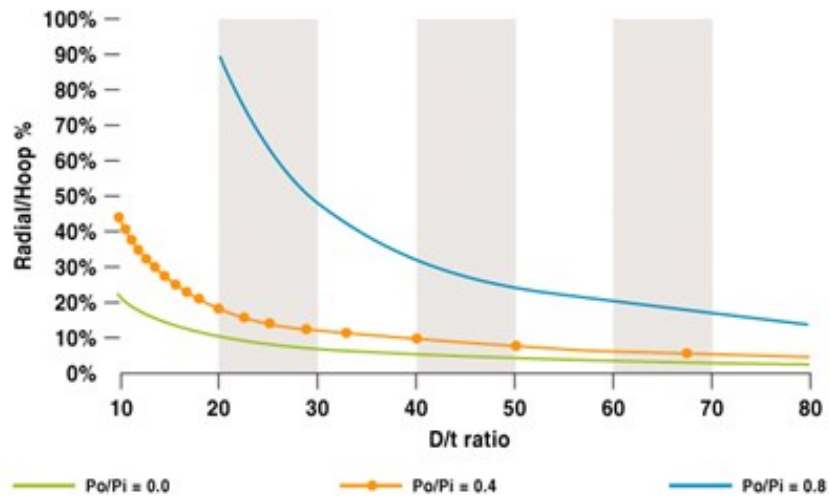


Fig. 2.10 The relationship between radial stress to hoop stress ratio σ_r/σ_h and pipe diameter to wall thickness ratio D/t or external pressure to internal pressure ratio P_o/P_i (From Lee, Rainey & Brunner, 1998)

The relationship between the stress and the strain prior to the elastic limit is generally described by Hooke's law, expressed by $\sigma = E\varepsilon$. If an element is subjected to a uniaxial tensile stress in one direction, it will extend in the force direction and deform in the other two perpendicular directions according to the value of Poisson's ratio. The strain in the force direction is expressed by $\varepsilon_1 = \frac{\sigma_1}{E}$ and the strain in the other perpendicular directions are expressed by $\varepsilon_2 = \varepsilon_3 = -\nu \frac{\sigma_1}{E}$, where E is the young's modulus and ν is Poisson's ratio, defined as the negative ratio of the lateral strain to the longitudinal strain. If an element is subjected to three mutually perpendicular stresses, the strain in each direction is the accumulation of combined effects of three directions, which are expressed by $\varepsilon_1 = \frac{\sigma_1}{E} - \nu \frac{\sigma_2}{E} - \nu \frac{\sigma_3}{E}$, $\varepsilon_2 = \frac{\sigma_2}{E} - \nu \frac{\sigma_1}{E} - \nu \frac{\sigma_3}{E}$ and $\varepsilon_3 = \frac{\sigma_3}{E} - \nu \frac{\sigma_1}{E} - \nu \frac{\sigma_2}{E}$ (Clements, 2005).

As a result, in the case of thin walled cylindrical pipes with capped ends under the effect of internal pressure only, the resultant strains including the longitudinal strain ε_L , the hoop strain ε_h , and the radial strain ε_r can be calculated below, with the assumption that $\sigma_r = 0$. The Poisson's ratio ν is commonly taken as 0.3 for steel pipes. Therefore, the results show the positive values of the longitudinal strain and the hoop strain but the negative value of the radial strain. The internal pressure expands the pipe in both length direction (longitudinal) and diameter direction (hoop) but contracts the pipe in the wall thickness direction (radial).

$$\begin{aligned}\varepsilon_L &= \frac{\sigma_L}{E} - \nu \frac{\sigma_h}{E} - \nu \frac{\sigma_r}{E} = \frac{PD}{4tE} (1 - 2\nu) \\ \varepsilon_h &= \frac{\sigma_h}{E} - \nu \frac{\sigma_L}{E} - \nu \frac{\sigma_r}{E} = \frac{PD}{4tE} (2 - \nu) \\ \varepsilon_r &= \frac{\sigma_r}{E} - \nu \frac{\sigma_L}{E} - \nu \frac{\sigma_h}{E} = \frac{PD}{4tE} (-3\nu)\end{aligned}$$

where

P is internal pressure

D is pipe outer diameter

t is pipe wall thickness

E is modulus of elasticity

ν is Poisson's ratio

In the case of infinitely long thin walled cylindrical pipes under the effect of internal pressure only, the longitudinal strain can be regarded as zero because the pipe cannot expand or contract in the longitudinal direction. With the assumption that $\sigma_r = 0$, the longitudinal strain and stress have following relationship.

$$\varepsilon_L = \frac{\sigma_L}{E} - \nu \frac{\sigma_h}{E} = 0 \Rightarrow \sigma_L = \nu \sigma_h = \nu \frac{PD}{2t}$$

In this case, the hoop and radial strains are given by:

$$\varepsilon_h = \frac{\sigma_h}{E} - \nu \frac{\sigma_L}{E} = \frac{PD}{2tE} (1 - \nu^2)$$

$$\varepsilon_r = -\nu \frac{\sigma_L}{E} - \nu \frac{\sigma_h}{E} = \frac{-\nu PD}{2tE} (1 + \nu)$$

2.1.4 Specification and Grades of Pipes

Pipeline systems are standardized in many pipe standards or specifications, such as API Spec 5L (2012) and CSA Z245.1 (2014). The American Petroleum Institute (API) Specification 5L adheres to the International Organization for Standardization ISO 3183 and identifies two basic product specification levels (PSL), which are PSL 1 and PSL 2. They represent different levels of standard technical requirements for seamless or welded steel pipes. PSL 1 is a standard quality for line pipe, while PSL 2 contains additional quality for chemical composition, mechanical properties, and testing requirements. The Charpy V-notch impact test is required for PSL 2 pipe. If the pipe outer diameter is equal to or smaller than 508mm, the fracture appearance should exhibit more than 85% shear area based on 0 °C or a lower test temperature. The absorbed CVN energy should be more than 27 J for pipe grade equal to or lower than X70, but more than 40 J for pipe grade higher than X70. Pipe grades covered by API Spec 5L include A25, A, B, and X-grade from X42 to X70 for PSL 1 pipes, and X-grade from X42 to X120 for PSL 2 pipes. The grade is commonly designated by a letter followed by a number. Take pipe grade of X52 (L360) for an example, which is the research object of this thesis. The letter X represents the chemical composition of the material and the number 52 or 360 is numerically equivalent to the specified minimum yield strength (SMYS) in inch-pound (ksi) units or SI (MPa) units. The tensile requirements of X52, X60, X65, X80 and X100 pipes are provided in API Spec 5L (2012) and shown in Table 2.1. This is the foundation of the following comparison in Chapter 5

between low strength steel pipe (X52), normal strength steel pipe (X60 and X65), and high strength steel pipe (X80 and X100).

Canadian Standards Association (CSA) Z245.1 identifies three categories for pipe according to the requirements for proven pipe body notch toughness properties. Category I pipe does not have notch toughness requirements, Category II pipe has notch toughness requirements in form of both energy absorption and fracture appearance, and Category III pipes has notch toughness requirements in form of only energy absorption. For Category II pipe, if the outer diameter is smaller than 457mm, the absorbed energy from a full size specimen in the Charpy V-notch impact test should be equal to or higher than 27 J, while if the outer diameter is larger than 457mm, the absorbed CVN energy should be higher than 40 J and drop-weight tear tests would be better used. The fracture appearance in either test should exhibit more than 60% shear area. For Category III pipe, the absorbed CVN energy should be equal to or higher than 18 J. Pipe grades covered by the CSA Z245.1 include grades from 241 to 483 for sour service and grades from 241 to 825 for other than sour service. Pipe grades covered by CSA Z245.1 can be considered as equivalents to pipe grades covered by API Spec 5L, which is shown in Table 2.1. The yield strength of most grade of pipe is determined at 0.5% total strain, while it is determined by 0.2% offset for grades higher than X90 or L625 in API Spec 5L, and for grades higher than Grade 690 in CSA Z245.1. In addition, the maximum limit of Y/T ratio in the table applies for pipe with outer diameter larger than 323.9 mm in API Spec 5L, while larger than 355.6 mm in CSA Z245.1.

Table 2. 1 Tensile requirements from standards

API Spec 5L/ ISO 3183								CSA Z245.1					
Pipe Grade	PSL 1 Pipe		PSL 2 Pipe					Pip Grade	Category I, II, III Pipes				
	Yield Strength MPa (ksi)	Tensile Strength MPa (ksi)	Yield Strength MPa (ksi)		Tensile Strength MPa (ksi)		Y/T Ratio		Yield Strength MPa		Tensile Strength MPa		Y/T Ratio
	min	min	min	max	min	min	max		min	max	min	max	max
L360 or X52	360 (52.2)	460 (66.7)	360 (52.2)	530 (76.9)	460 (66.7)	760 (110.2)	0.93	Grade 359	359	530	455	760	0.93
L415 or X60	415 (60.2)	520 (75.4)	415 (60.2)	565 (81.9)	520 (75.4)	760 (110.2)	0.93	Grade 414	414	565	517	760	0.93
L450 or X65	450 (65.3)	535 (77.6)	450 (65.3)	600 (87.0)	535 (77.6)	760 (110.2)	0.93	Grade 448	448	600	531	760	0.93
L555 or X80			555 (80.5)	705 (102.3)	625 (90.6)	825 (119.7)	0.93	Grade 550	550	690	620	830	0.93
L690 or X100			690 (100.1)	840 (121.8)	760 (110.2)	990 (143.6)	0.97	Grade 690	690	825	760	970	0.93

2.2 Mechanical Properties of Steel

Metallic pipe is generally made of steel. Steel is a ferrous metallic material that consist almost entirely of iron (Fe), and a small amount of principal alloying elements such as carbon (C) and manganese (Mn), and many other elements (Drive, 2013). API Spec 5L (2012) clearly specifies chemical composition for X-grades steel pipes. For example, an X52 PSL 1 pipe contains maximum 0.28% C and 1.4% Mn, while an X52 PSL 2 pipe contains maximum 0.24% C and 1.4% Mn. The chemical composition has a significant effect on the mechanical properties of a material. In general, by increasing the content of carbon, the material's strength and hardness increase, but ductility, toughness and even weldability decrease, and manganese has similar but less effect (Drive, 2013). Not only the chemical composition, but also the steelmaking process can affect the material properties of a finished steel pipe. For examples, properties may be affected by heat treatment involving reheating and subsequent cooling of the steel. The mechanical properties of a material are usually determined by the reaction to the applied loadings, such as tension, compression, bending, shear, and torsion. Most materials are anisotropic, but steels are regarded as isotropic exhibiting same elastic behaviors in all directions. The mechanical properties of a material are independent of the geometric dimensions, but are often affected by temperature, rate of loadings, or other external interferences. The most common properties of structural steels are carefully reviewed below, such as the strength, the ductility, the toughness, and the stiffness.

2.2.1 Strength

The strength of material is usually the primary concern, which indicates the maximum stress that a material is able to resist before failure or before developing appreciable plastic deformation. Steel materials are widely used because of their relatively high tensile strength measured by the yield strength (σ_{YT}) and the ultimate tensile strength (σ_{TS}). As mentioned above, the standard API Spec 5L identified a specified minimum yield strength and a specified minimum tensile strength for different pipe grades. However, the actual strength of a particular pipe specimen is usually measured by its stress versus strain curves by conducting a standard tension test according to standard ASTM E8/E8M-11.

The yield strength is the stress at the yield point and that is when the material begins to deform permanently (Davis, 2004; Roylance, 2008). Prior to the yield point, the deformation is fully recovered upon removal of the load and the material returns its original shape. Theoretically, the steel material may exhibit a perfectly plastic deformation response when yielding, with a dramatic increase in strain but not a noticeable increase in stress. This behavior is translated into as a long and comparatively flat yielding plateau in a stress vs. strain curve. The yield strength can be determined by the upper yield strength, the lower yield strength, or the mean yield strength during the yield point elongation. However, sometimes the material does not show a well-defined yielding point, but yields gradually. In this case, either the offset method (offset=0.2%) or the extension-under-load method (EUL=0.5%) can be used to determine the yield strength according to the standard. The yield strength is determined at a plastic strain equals to 0.2% or at a total strain equals to 0.5%.

The ultimate tensile strength is the maximum stress that the material is subjected to before it breaks, and it corresponds to the highest point on a stress vs. strain curve (Davis, 2004; Roylance, 2008). The strain that corresponds to the ultimate yield strength is called the uniform strain (ϵ_u) For ductile steel pipes, the yield strength is more important than the ultimate tensile strength because the material develops the permanent plastic deformation after the yield strength is reached. However, for other brittle material pipes, such as cast iron pipes, the ultimate tensile strength is very important because the material does not have obvious yield point before sudden fracture.

2.2.2 Ductility

Steel is a ductile material with desirable ductility. Ductility is a measure of the ability that a material can be plastically deformed between the onset of yielding and final fracture in response to an applied tensile force. When a specimen is stretched to fail, its ductility can be measured by the elongation or the reduction of area at fracture location and both of them are expressed as a percentage. After fracture, the final distance between two gauge marks (L_f) and cross-sectional area of necking location (A_f) are measured. The elongation is obtained by dividing the change in gauge length (ΔL) by the original gauge length (L_0).

The fracture gauge length (L_f) is measured by putting two fractured pieces of specimen back together. The elongation is numerically equal to the engineering strain at fracture (ϵ_{ult}). The reduction of area is obtained by dividing the reduction of cross-sectional area (ΔA) by the original cross-sectional area (A_0). The fracture cross sectional area is measured based on the minimum thickness (t_f) and width (w_f). The expressions of these two ductility parameters are shown below (Davis, 2004).

$$\text{Elongation} = \frac{\Delta L}{L_0} = \frac{L_f - L_0}{L_0}; \text{Reduction of area} = \frac{\Delta A}{A_0} = \frac{A_0 - A_f}{A_0} = \frac{A_0 - (t_f \cdot w_f)}{A_0}$$

Obviously, the ductility is a geometric property rather than a material property, because it depends on the dimensions of the reduced section of the specimen. The total extension of the test specimen consists of both the uniform elongation prior to necking and localized elongation after necking begins. The uniform elongation is not only determined by material properties, but also the effect of specimen size and shape on the development of the necking. The calculated percent elongation contributed by localized extension depends on the selection of gauge length. Measuring a specimen with a shorter gauge length or a longer gauge length will lead to the value of the elongation being higher or lower. Therefore, appropriate determination of various material's ductility should be measured by uniform standard geometric specimens. A standard gauge length of 200 mm or 50mm in a standard tension test is often used (Kulak & Grondin, 2010). In general, a higher value of elongation and higher value of reduction of area indicate a good ductility. The large plastic deformation on a stress-strain curve is the primary advantage of a ductile material like steel, because in practical applications, the large plastic deformation occurring before failure provides a useful warning before the complete failure. On the contrary, a brittle material like cast iron, brings about more safety concern because it breaks sharply without plastic deformation. Notice that the ductility may be reduced for some reasons such as poor design or imperfect fabrication, in this case, a ductile steel can also fail in a brittle manner. Therefore, it is important to understand a material's plasticity to predict when and how it fails. The ductility also relates to the yield strength. Generally, a higher grade of steel pipe such as a modern X80 pipe is more brittle and less ductile than a lower grade of steel pipe such as a vintage X52 pipe.

2.2.3 Toughness

Toughness is a measure of the ability of a material to absorb large amount of energy to deform plastically without fracture. The material toughness is described by the total area under the stress-strain curve in a uniaxial tensile test and has units of energy per volume (Bhushan, 2013).

$$\text{Toughness} = \int_0^{\epsilon_f} \sigma d\epsilon$$

It indicates the amount of mechanical energy per unit volume that can be exerted on a material before fracture, and is equal to the material slow energy absorption up to failure. Fig. 2.11 compares the stress-strain curve of a high strength steel, a medium strength steel and a low strength steel, and shows that the medium strength steel exhibits the highest toughness (NDT Resource Centre). This indicates that high toughness depends on a good balance of high strength and high ductility. At room temperature, X52 steel is a tough material and tends to fail in a ductile manner – stable fracture after yielding. However, if steel loses its toughness for some reasons, it may change to fail in a brittle manner – unstable and sudden fracture. The reasons that influence the toughness of steel material maybe the rate of loading, the temperature, and the notch effect (Billingham et al., 2003; NDT Resource Centre). The toughness decreases as the rate of loading increases, as the temperature decreases, and as a notch or crack is present. The notch effect is related to the distribution of stress. When the applied loading generates a triaxial tension stress state adjacent to the notch, the region near the notch tip deform plastically as the yield stress is reached. However such deformation may be restricted by the surrounding regions which remains elastic, and then the material fails in a brittle manner and thus exhibits lower toughness. These triaxial constraints against plastic strains are most often seen in a thick section rather than a thin section. As a result, impact toughness, notch toughness, and fracture toughness are often studied to understand the material toughness properties.

The impact toughness measures the ability of a material to absorb energy during fracture when subjected to a high rate impact loading. The notch toughness measures the ability of a material to absorb energy when a sharp notch is present. The fracture toughness measures the ability of a material to resist crack formation and propagation. The Charpy V-notch

impact test is usually conducted to measure the impact toughness and notch toughness, as the form of energy required to fracture a notched specimen at a particular temperature and loading rate. The fracture toughness test is usually conducted to measure the fracture toughness, determined by one of the toughness parameters, such as the stress-intensity factor (K), J integral (J), and crack-tip opening displacement ($CTOD$ or δ). They can be measured by a critical single point value, such as plain strain fracture toughness characterized by K -factor (K_{Ic}), J -integral (J_{Ic}) and crack-tip opening displacement (δ_{Ic}) or in a resistance curve (R -curve) where a toughness parameter ($K, J, CTOD$) is plotted against the crack extension (Anderson,2005).

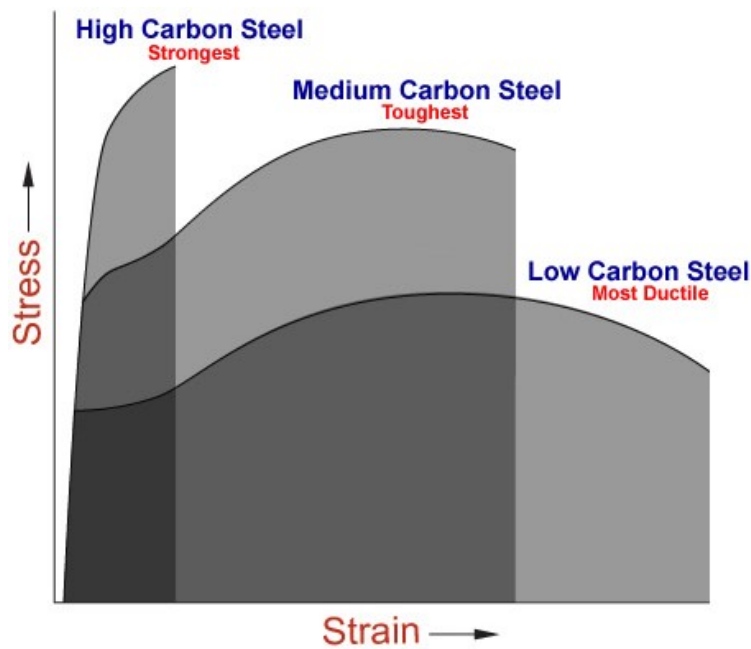


Fig. 2.11 Material toughness (From “Toughness” in Nondestructive Testing (NDT) Resource Centre)

2.2.4 Stiffness

Stiffness is the rigidity of a structure to resist changes in shape, such as bending, stretching, and twisting (Baumgart, 2000; Gere & Goodno, 2012). It is a measure of the amount of load (or stress) required to produce a unit deformation (or unit strain), which can be shown by $k = F/\delta$ in Hooke's law, and has units of N/mm (Roylance, 2008; Gere & Goodno, 2012). Its complementary concept is flexibility (Wenham, 2001). Stiffness is usually characterized by the elasticity or elastic modulus, but they are not the same. Stiffness is a property of the structure, and is influenced by the material properties and geometry. The elasticity is the property of the material, and indicates the ability of the elastic material recovering back to its original configuration after the removal of the external load (Baumgart, 2000). To be more specific, if an elastic member is subjected to a small external force, the internal forces of atoms resist the deformation and the material exhibits elastic deformation. After the removal of the external force, the material returns to its original shape. However, if the material is subjected to a stress higher than the yield strength, planes of atoms slide over one another and the material exhibits plastic deformation, which is non recoverable after the stress is removed (Kailas, n.d.). It is important to control the amount that a structural member deforms in response to the applied force.

In general, the stiffness is usually characterized by the Young's modulus (E), shear modulus (G), bulk modulus (K) and Poisson's ratio (ν) (Leppin, Shercliff, Robson & Humphreys, n.d.; Roylance, 2008). The Young's modulus or the modulus of elasticity (E) is a common measure of the axial stiffness. The higher the value of the Young's modulus, the stiffer the material is. It can be defined as the ratio of the applied normal stress ($\sigma = F/A$) to the resultant normal strain ($\epsilon = \Delta L/L$) for elastic deformation in uniaxial tension or compression. Obeying Hooke's law, it has an expression of $E = \frac{\sigma}{\epsilon}$, and a unit of pressure (MPa or psi). It can be experimentally derived from the slope of the initial straight line on a stress vs. strain curve in a uniaxial tensile test. If a material is isotropic like steel, young's modulus is identical in all directions; otherwise, it varies depending on the direction of the applied force. Poisson's ratio (ν) is another important elastic property relating to the stiffness. When a material is stretched elastically in direction y , it usually contracts in other two perpendicular direction x and z . Such effect can be measured by the Poisson's ratio,

which is the negative ratio of lateral strain ($\varepsilon_x = \frac{\Delta x}{x}$ or $\varepsilon_z = \frac{\Delta z}{z}$) to the axial strain ($\varepsilon_y = \frac{\Delta y}{y}$) in the direction of the force, expressed as $\nu = -\frac{\varepsilon_x}{\varepsilon_y}$ or $\nu = -\frac{\varepsilon_z}{\varepsilon_y}$. The shear modulus or modulus of rigidity (G) is defined as the ratio of the shear stress ($\tau = F/A$) to the shear strain ($\gamma = \tan\theta = \theta$) for elastic deformation in shear, expressed as $G = \frac{F/A}{\Delta x/h} = \frac{\tau}{\tan\theta} = \frac{\tau}{\gamma}$. ($\Delta x \ll h \Rightarrow \tan\theta = \theta = \gamma$). The bulk modulus (K) is defined as the ratio of increase of pressure ($\Delta p = F/A$) to the relative decrease of volume ($\varepsilon_V = \Delta V/V$) for elastic deformation in hydrostatic pressure, expressed as $K = \frac{F/A}{\Delta V/V} = \frac{\Delta p}{\varepsilon_V}$.

For isotropic materials, these four elastic properties Young's Modulus (E), shear modulus(G), bulk modulus (K) and Possion's ratio(ν) are all related and their interrelation are shown below (Leppin, Shercliff, Robson & Humphreys, n.d.; Roylance, 2008).

$$\nu = \frac{E}{2G} - 1 = \frac{3K - E}{6K}$$

At room temperature, these four elastic properties are constant for steel material. In the absence of detailed information, the values of these properties can be generally assumed as: $E=200$ GPa, $G=77$ GPa, $K=160$ GPa, $\nu=0.3$. However, in order to accurately determine the properties, a uniaxial tensile test is usually conducted to measure the Young's modulus and Possion's ratio. A sensitive extensometer is required to measure the elastic axial strains, and strain gages are required to measure elastic lateral strains (Davis, 2004).

2.2.5 Other Properties

Hardness is a property that closely related to the strength. It is usually determined by the measure of the ability of a material to resist penetration of an indenter. For steel materials, the hardness increases as the carbon content increases (Driver, 2013).

Corrosion resistance is used to describe the material resistance to corrosion when a structural member is exposed to the weather. Pipe coating is usually required to protect steel pipes from corrosion (Kulak & Grondin, 2010)

2.3 Weldability of Steel

Weldability indicates the level of ease by which a material can be welded (Driver, 2013). A good weldability insures the adequate strength and toughness of the weld and heat affected zone. As described in steelConstruction. info, welding is an important process of fabricating steel pipes and the most common way is arc welding. An electric arc is used to produce intense heat to melt the base metal at the joint, and a separate filler material, working as a consumable electrode, is usually added in fusion. After cooling and solidification, a metallurgical bond - weld metal is created. If the filler matches the chemical composition of the base metal, the weld metal is described as “matching” weld metal, which has similar mechanical properties to the base metal, particularly in strength; if the filler matches the chemical composition of a metal with lower/ higher material properties than the base metal, then the weld metal is described as “undermatching/overmatching” weld metal, respectively (steelConstruction. info, “welding”). The region in the base metal close to the weld metal is called the heat-affected zone (HAZ), which has not been melted, but its mechanical properties have been alternated by the heat from welding. The main types of welds are butt welds (groove welds) and fillet welds, which are shown in Fig. 2.12. A weld can be welded with full penetration or partial penetration (steelConstruction. info, “welding”). The full penetration has a strength the same as that of the base metal, while the partial penetration has less strength because of its smaller cross sectional area than that of the base metal. A fillet weld is easier to manufacture, but is less effective to restore the strength than a butt weld.

All steels are weldable, but the quality and cost of welds are different. A low carbon steel usually has a better weldability than a high carbon steel. This is due to the higher possibility that a high carbon steel crack in weld metal or HAZ during cooling after welding. A preheated or post-heated treatment is necessary for a high carbon steel to create quality joints (Driver, 2013). Generally, the weldability increases as the carbon content decreases or more accurately as the carbon equivalent (CE) decreases. Following equation is the international expression of CE for a pipe with a minimum 0.12% Carbon composition, provided by API Spec 5L (2012):

$$CE = C + \frac{Mn}{6} + \frac{Cr + Mo + V}{5} + \frac{Ni + Cu}{15}$$

Where: carbon (C), manganese (Mn), chromium (Cr), molybdenum (Mo), vanadium (V), nickel (Ni), copper (Cu).

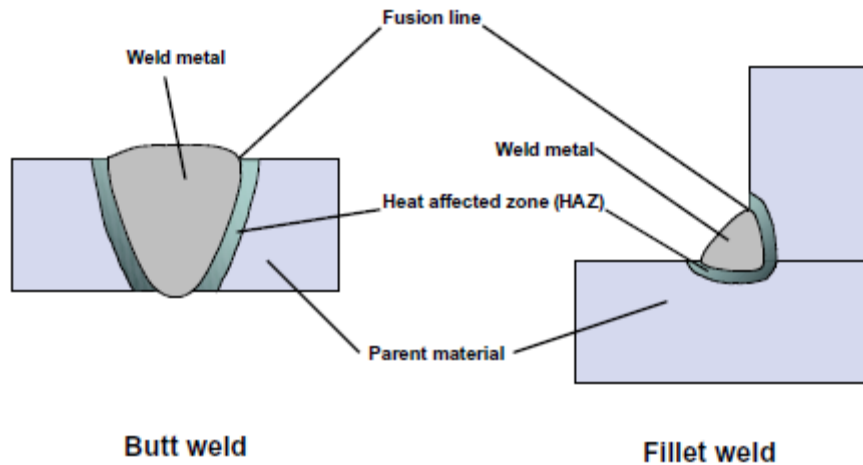


Fig. 2.12 Butt weld and fillet weld (From steelCounstruction. info, “Welding”)

2.4 Stress-Strain Curve of Steel

The stress-strain curve is a property of the material and according to the Standard ASTM E8/E8M-11, it can be obtained in a uniaxial test where a specimen is subjected to uniaxial tensile force until fracture, and its force-deformation curve can be directly obtained from the test. Simply dividing the force and deformation data by the cross sectional area and the original length respectively, the stress-strain curve is produced. Independence of the specimen dimensions is the primary strength of studying a stress-strain curve rather than studying a force-deformation curve. A stress-strain curve only depends on the inherent material behaviors of the specimen, and is used to demonstrate many important properties, such the elastic deformation properties (Young's modulus), strength properties (yield strength and tensile strength), ductility properties (elongation and reduction of area) and other characteristics (strain-hardening and necking) (Holt, 2000). The general shape and magnitude of a typical stress-strain curve of steel and its important features are reviewed below.

2.4.1 Divisions of Stress-Strain Curve

A typical example of an engineering stress-strain curve of a steel material specimen loaded in tension was given by Adeeb (2012) and shown in Fig. 2.13. The curve is divided into four regions, including the elastic region, the yielding region, the strain-hardening region, and the necking region. The most important features in the four regions on the curve were described by many researchers and summarized below. In the elastic region (curve OAB), the stress and strain has linear relationship until the proportional limit (point A) is reached, and has slightly nonlinear relationship afterwards up to the elastic limit (point B). The proportional limit is defined as the stress at which the linearity of the curve ceases, and the elastic limit is defined as the stress at which the plastic deformation begins. However, it may be sometimes difficult to distinguish these two limits on the curve because the clear difference depends heavily on the accuracy and sensitivity of the measurement to small strains, and as a result, considering two limits at the same point is acceptable (Kulak and Grondin, 2010). The initial linear relationship of the stress (σ) and the strain (ϵ) obeys Hooke's law, expressed as $\sigma = E\epsilon$. The strain in this region is equal to the elastic strain (ϵ_e), and slope of the initial linear curve is equal to Young's modulus (E). In the yielding

region (curve BC), the specimen begins to yield and deform plastically from the elastic limit (point B). Low and medium strength steel specimens usually exhibit a well-defined yield point, followed by a relatively long and flat yielding plateau (Kulak and Grondin, 2010). This phenomenon is accompanied by a considerable increase in strain and non-appreciable increase in stress. The yield strength can be measured by the upper yield stress, lower yield stress, or mean yield stress during the yield point elongation. However, high strength steel specimens usually show gradual yielding, the yield strength can be measured by the stress corresponding to 0.2% plastic strain or 0.5% total strain. In the strain-hardening region (curve CDE), the stress increases as the plastic strain increases with a slope (E_{sh}) lower than previous slope (E) in the elastic region, and eventually reaches to the ultimate tensile strength (σ_{TS}) at the uniform elongation (ϵ_u) just prior to the necking. The strain hardening is very common in ductile steels. The reason for this phenomenon was described by Juneja (2010). Dislocations within the atomic and crystal structure is generated by plastic deformation. As the dislocation density is higher, the dislocation movements may be obstructed by other stationary dislocations and grain boundaries. In order to overcome such obstruction, a higher force is required. Therefore the load capacity of a material is increased by plastic deformation. If the stress is removed and later reapplied at point D, the paths of unloading and reloading are parallel to the path of the initial loading with an offset by the residual strain. The specimen behaves elastically with the slope E upto a yield stress at point D which is higher than the previous yield stress at point B. In this region, the cross sectional area decreases as the specimen elongates, but the volume of the specimen remains constant (Dieter, 2000; Moosbrugger, 2002). In the necking region (curve EF), the specimen necks and the cross-section area decreases rapidly with a reduction of the applied load until the final rupture of the specimen occurs. After strain hardening, the volume of the specimen does not remain constant anymore. A weaker location of the specimen is certainly formed where the extent of reduction of the cross sectional area is greater than the growth of elongation (Dieter, 2000; Moosbrugger, 2002). As a result, the necking begins at this weaker location in which further elongation is concentrated. Also, due to the slower elongation growth, the required force to elongate the specimen decreases, shown by the sudden drop of the curve. The stress and strain at fracture are termed as the failure stress and elongation at fracture respectively.

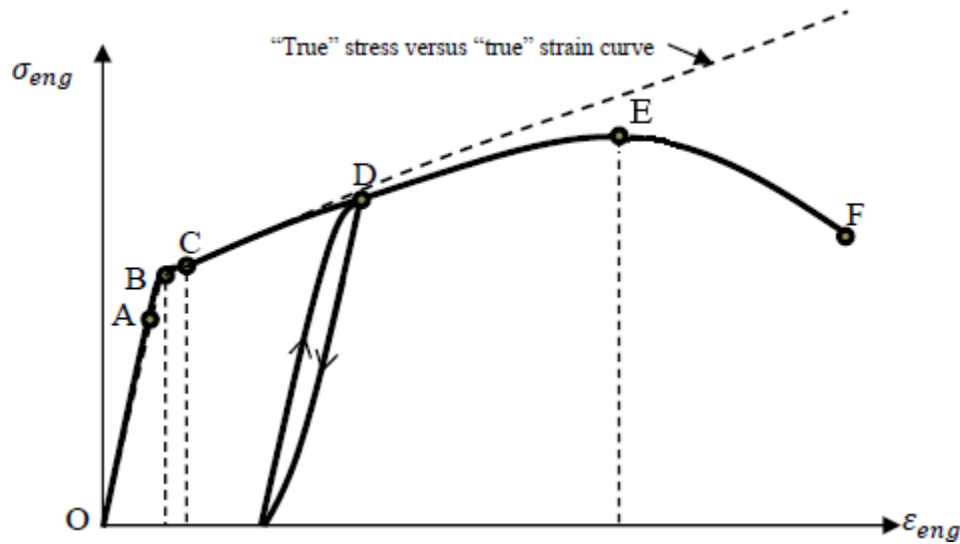


Fig. 2.13 Typical stress-strain curves for a steel specimen. (From Adeeb, 2012, “Plasticity”)

2.4.2 Engineering and True Stress and Strain

The definition of engineering and true stress and strain and their relationships were described by Holt (2000) and Dieter (2000). Stress is defined as the amount of the applied force on a given cross-sectional area, and has units of pressure, usually expressed as thousand pounds per square inch (ksi) or megapascals (MPa). Strain is defined as the change per unit length in an original linear dimension, and has no units, or expressed as inch per inch (in/in) or millimeter per millimeter (mm/mm). In a uniaxial tensile test, the typical measure of stress and strain are engineering stress and strain, which can be easily calculated from experimental force and deformation data. The engineering stress (σ_{eng}) is calculated as the ratio of applied force (F) to the original cross section area (A_0). The engineering strain is calculated as the ratio of nominal change in length (ΔL) to the original gauge length (L_0). The engineering stress-strain curve is frequently used, but they do not indicate how the material truly behave under the uniaxial tensile stress because engineering stress and strain are related to the original dimensions. In fact, as the specimen is extended by the stress, the cross sectional area decreases due to necking and do not maintain the original dimension. Therefore, a true stress-strain curve based on actual dimensions is preferred for practical use. The true stress (σ_{true}) is calculated as the ratio of the applied force (F) to the instantaneous cross section area (A). The true strain (ϵ_{true}) is calculated by

the integral of the incremental true strain ($d\varepsilon$) over a period of time, and the incremental strain is the ratio of incremental change in length (dl) to instantaneous gauge length (l). Assumed that the volume (V) is constant and the deformation is uniform under the tensile force, the true stress and strain can be converted from engineering stress and strain. All relationships and conversions between engineering and true stress and strain are expressed below.

$$\sigma_{eng} = \frac{F}{A_0}$$

$$\varepsilon_{eng} = \frac{\Delta L}{L_0} = \frac{L - L_0}{L_0}$$

$$\sigma_{true} = \frac{F}{A} = \frac{F}{A_0} \cdot \frac{A_0}{A} = \sigma_{eng}(1 + \varepsilon_{eng})$$

$$\varepsilon_{true} = \int_{L_0}^L d\varepsilon = \int_{L_0}^L \frac{dl}{l} = \ln\left(\frac{L}{L_0}\right) = \ln(1 + \varepsilon_{eng})$$

$$V = LA = L_0A_0 \Rightarrow \frac{A_0}{A} = \frac{L}{L_0} = 1 + \varepsilon_{eng}$$

The above conversions between true and engineering stress and strain are only valid when the deformation is isochoric (volume preserving) and when the deformation is uniform along the gauge length, in other words, just before the necking happens. After necking begins, both cross-sectional area and elongation at the location of the neck should be directly measured to calculate the accurate true stress and strain. As shown in Fig. 2.14, for the same material, the engineering and true stress-strain curves match each other before yielding, but diverge largely after yielding as the strain increase. The engineering stress-strain curve falls down after the ultimate tensile strength is reached while the true stress-strain curve continues to increase until final fracture. The engineering stress-strain curve is identical in shape to the force-deformation curve but only with different magnitude due to dimensions. During the formation of a neck, a complex tri-axial stress state is produced and the radial stress and hoop stress would raise the longitudinal stress required to cause the plastic flow (Dieter, 2000; Moosbrugger, 2002). Therefore, after necking happens, the calculated true stress based on the minimum cross-sectional area at the neck should be corrected for the tri-axial stress state effect because the calculated values are higher than those really needed for causing the plastic

flow. In the absence of useful information for the tri-axial stress state effect, the calculated true fracture stress is usually erroneous and useless.

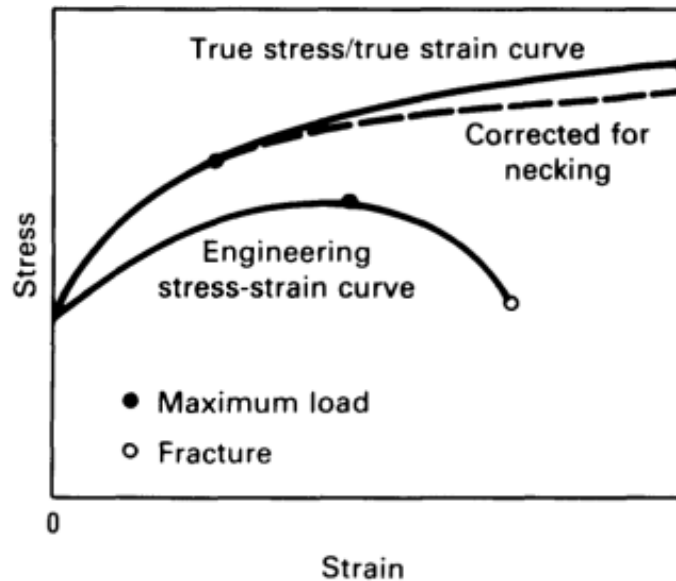


Fig. 2.14 Comparison of true and engineering stress-strain curves. (From Dieter, 2000, ASM Handbook Volume 8, pp.102)

2.3.3 Yielding Phenomenon

Most steels show either a well-defined yield point followed by the yielding plateau or gradual yielding. The yield strength is usually defined as a stress where a small amount of plastic deformation occurs, such as offset yield strength (offset=0.2%), extension-under-load yield strength (EUL=0.5%), and upper yield strength or lower yield strength (Holt, 2000). The first two types of yield strength is designed for a material showing gradual yielding, while the later one type of yield strength is designed for a material showing yielding plateau. As mentioned earlier, low and medium strength steel specimens usually show yielding plateau due to the localized yielding (Kulak & Grondin, 2010). The yielding begins from a definite yield point, followed by slightly fluctuated lower stresses as elongation increases. The initial maximum stress at yield point is termed as the upper yield strength (UYS), the subsequent minimum stress is termed as the lower yield strength (LYS), and the region between the onset of yielding and the onset of the strain hardening is termed as yield point elongation (YPE). The plastic deformation during the yielding is not homogeneous but concentrated in several discrete narrow zones, which are called Lüder

bands. This phenomenon was described by Dieter (2000) and is shown in Fig. 2.15. At the upper yield point, a discrete band appears at a local stress concentration, inclined at approximately 45° to the tensile axis. The load drops to the lower yield point due to the formation of the band. Then as the specimen is elongated, the band propagates along the length of the specimen and causes the yield point elongation. The yielding plateau can be measured by an autographic device using the autographic diagram method introduced in ASTM E8/E8M-11. The yield strength may be determined by the upper yield strength, the lower yield strength, or the mean strength during the yield point elongation, but the lower yield strength provides the most conservative value. The measured yield strengths are usually affected by the testing speed, the test machine stiffness, and how axially the force is applied to the specimen. For example, the off-axial force (bending force) with a slow testing speed is able to suppress the peak of UYS, and therefore another type of yielding may be produced, shown by a long and flat yielding plateau without a distinction between UYS and LYS (ASTM E8/E8M-11). High strength steel specimens usually show gradual yielding (Kulak & Grondin, 2010). In the absence of a well-defined yield point, the yield strength is usually defined as a stress that corresponds to a specified small amount of plastic strain, often 0.2% plastic strain or 0.5% total strain. These two definitions of yield strength are more commonly used, because they are unified and less affected by sensitivity of the measurement. Offset yield strength (offset=0.2%) is determined by the offset method, which is described by drawing a straight line (mn) parallel to the initial linear portion of the curve (OA) with a specified offset of 0.2% (0m), which equates a plastic strain of $\varepsilon_p=0.2\%$. Offset yield strength is the stress at the intersection (point r) between the straight line and the curve. Extension-under-load yield strength (EUL=0.5%) is determined by extension-under-load method, which is described by drawing a straight normal line (mn) at a specified extension of 0.5% (0m), which equates a total strain of $\varepsilon_T=\varepsilon_e + \varepsilon_p=0.5\%$. Extension-under-load yield strength is the stress at the intersection (point r) between the straight line and the curve. These two methods were included in standard ASTM E8/E8M-11) and shown in Fig. 2.16.

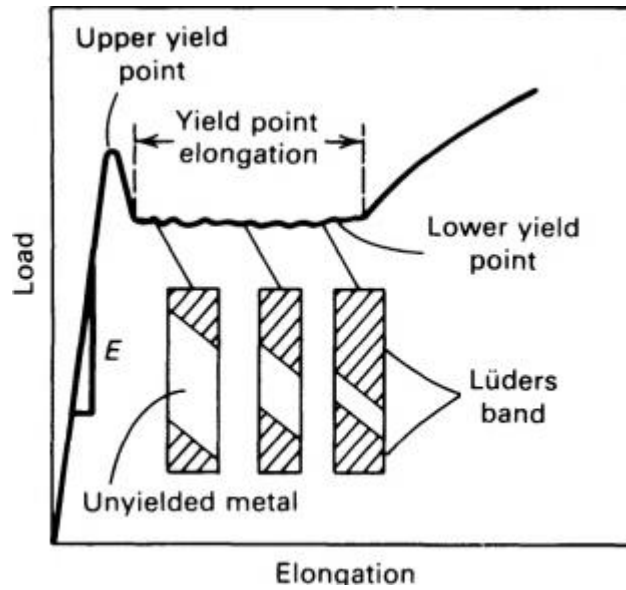


Fig. 2.15 Yielding plateau due to Lüder bands (From Dieter, 2000, ASM Handbook Volume 8, pp100)

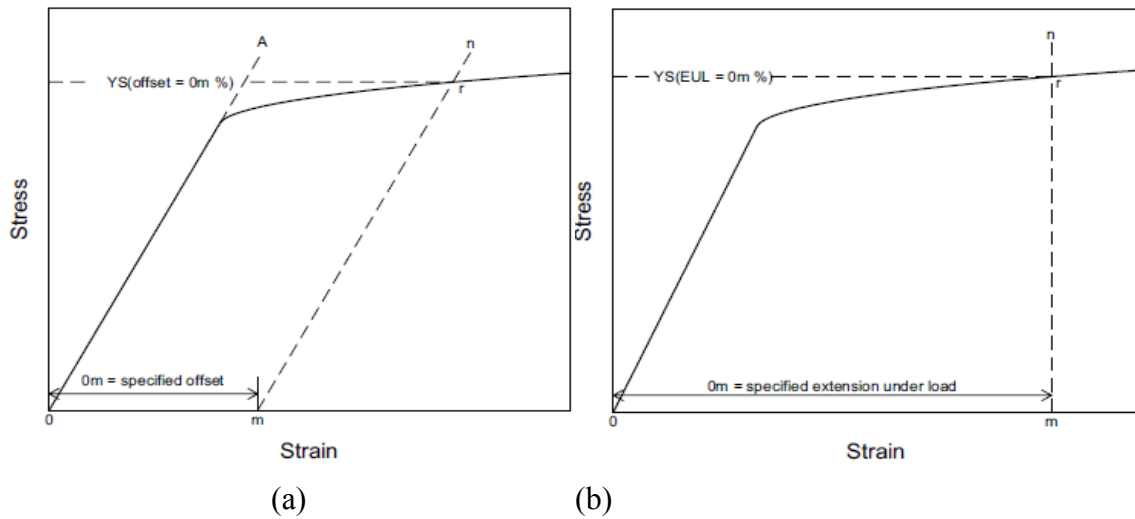


Fig. 2.16 Determination of the yield strength in gradual yielding (a) the offset method; (b) the extension-under-load method (Adapted from ASTM E8/E8M-11, pp. 16-17)

2.4.4 Strain Hardening, Strain Aging, and Bauschinger Effect

The influences of the strain hardening, the strain aging, and the Bauschinger effect were investigated by many researchers in the past years by loading and unloading a test specimen in tension or compression and producing an engineering stress-strain curve. If a test specimen is loaded in uniaxial tensile stress less than the elastic limit, then unloaded and immediately reloaded in the same direction, its paths of unloading and reloading are identical to the path of the initial loading. After unloading, the specimen returns to its original shape and the deformation is fully recovered. However, if a steel test specimen is loaded in uniaxial tensile stress more than the elastic limit, then unloaded and immediately reloaded in same direction, its paths of unloading and reloading are parallel to the path of the initial loading but with an offset by the residual strain. After unloading, the deformation is unrecoverable, and a permanent plastic strain remains. The path of immediate reloading develops elastically with the slope E upto the point where the unloading begins and follows the virgin curve. The loading and unloading paths are shown by arrows in Fig. 2.17 which is taken from Brockenbrough and Johnston (1981). The increase of the yield strength is caused by the strain hardening due to the increase of the plastic deformation, which was explained by Juneja (2010). Dislocations within the atomic and crystal structure is generated by plastic deformation. As the dislocation density is higher, the dislocation movements may be obstructed by other stationary dislocations and grain boundaries. In order to overcome such obstruction, a higher force is required. Therefore the load capacity of a material is increased by plastic deformation. In comparison with the new reloading curve and the virgin curve, the yield strength increases but the tensile strength remains same.

The strain aging is defined to describe the increase of strength and the reappearance of the yielding phenomenon, and is sensitive to temperature and time (Baird, 1963; Lu, 1990). If a test specimen is loaded in uniaxial tensile stress more than the elastic limit, then unloaded and loaded in the same direction after aging for several days at room temperature or several hours at a higher aging temperature, the yielding phenomenon returns at a higher yield point. The path of reloading develops elastically with the slope E upto a yield point beyond the virgin curve. The loading and unloading paths are shown by arrows in Fig. 2.18 which

is taken from Brockenbrough and Johnston (1981). In comparison with the new reloading curve after strain aging and the virgin curve, both of the yield strength and tensile strength increases but the ductility decreases. An atmosphere of carbon and nitrogen atoms is formed along the length of dislocation during the aging, and the diffusion of carbon and nitrogen atoms impedes the movement of the subsequent dislocation caused by plastic deformation and contributes to material strengthening or hardening and ductility losing (Baird, 1963; Lu, 1990). The effects of strain hardening or strain aging should be considered when dealing with a specimen machined from a location at which the material may have been plastically deformed and thus the properties measured in the test would be greatly different from those measured from virgin material (Holt, 2000). The process of pipeline coating induces high temperature on the pipeline steel which has a strain aging effect (Yoo, et al., 2008; Okatsu, et al., 2008).

The Bauschinger effect is named after the German engineer Johann Bauschinger, who first defined it in 1860. This phenomenon is associated with the change of the direction of the stress and the strain, resulting in the lower yield strength on reloading. If a test specimen is initially loaded in a tensile stress more than the elastic limit then unloaded, its path of unloading is parallel to the path of initial loading with an offset by the residual strain. Then if the specimen is immediately reloaded with a compressive stress, the elastic limit in compression will be lower than the previous elastic limit, and the path of compressive reloading has a very different shape compared to the path of initial tensile loading. This shape of response curve is similar if the sequence of applying the tensile stress and the compressive stress switch. This is because the compressive yield strength is theoretically equal to the tensile yield strength. The Bauschinger effect is influenced by the previous history of the plastic deformation as well. Again, when dealing with a specimen machined from a location at which the material may have been plastically deformed, the properties measured in the test would be greatly different from those measured from virgin material. An example of Bauschinger effect on an engineering stress-strain curve of a round A36 steel specimen was given by Holt (2000) and shown in Fig. 2.19. The specimen is initially loaded to 0.01 tensile strain, then unloaded and reloaded to 0.01 compressive strain, and secondly unloaded and reloaded to 0.01 tensile strain again. It is noticed that the specified

0.01 exceeds the elastic limit and the plastic strain is present. The path of initial tensile unloading-compression reloading-compression unloading-second tension loading constitutes a typical hysteresis loop. The reduced yield strength by Bauschinger effect when reloading is reversed is an indication of anisotropic plastic behavior. The reduced yield strength by Bauschinger effect may also occur when the reloading and initial loading is in the same direction (Lubahn and Felgar, 1961; Lubliner, 2008). However, if a material exhibits isotropic plastic behavior, it may not show Bauschinger effect and the yield strength keeps constant even when the reloading is reversed (Adeeb, 2012). Neupane (2012) and Fathi (2012) showed that the anisotropic behavior observed in pipeline steels can be attributed to the past history of the manufacturing process in which the expansion process of the pipeline causes an increase in the yield strength in the circumferential direction and a decrease in the yield strength in the longitudinal direction.

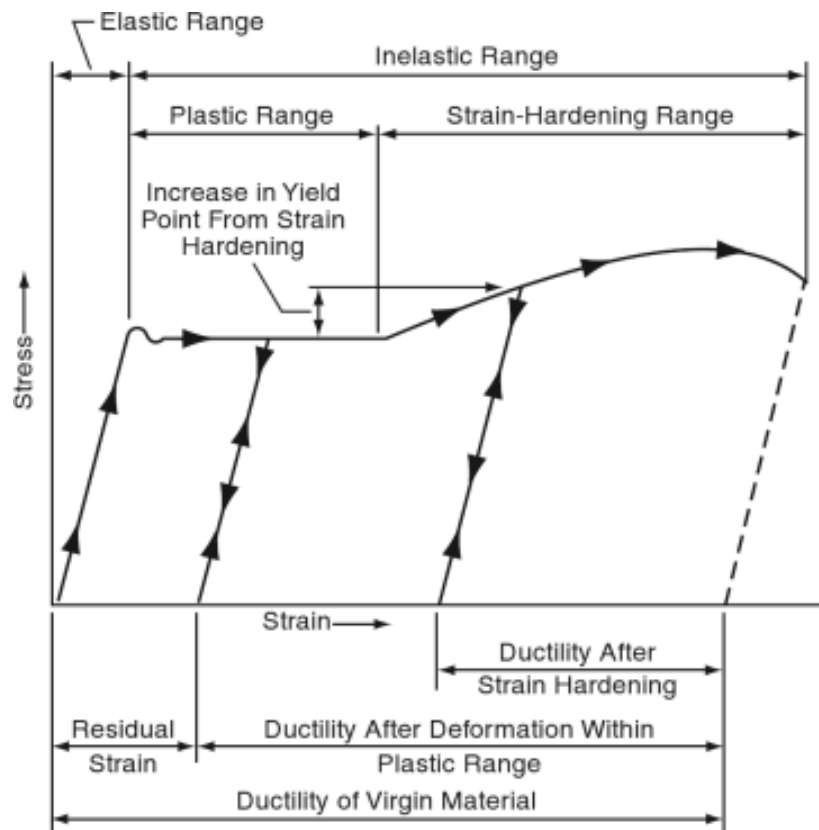


Fig. 2.17 An engineering stress-strain curve showing strain hardening (From Brockenbrough and Johnston, 1981, USS steel design manual, pp.18)

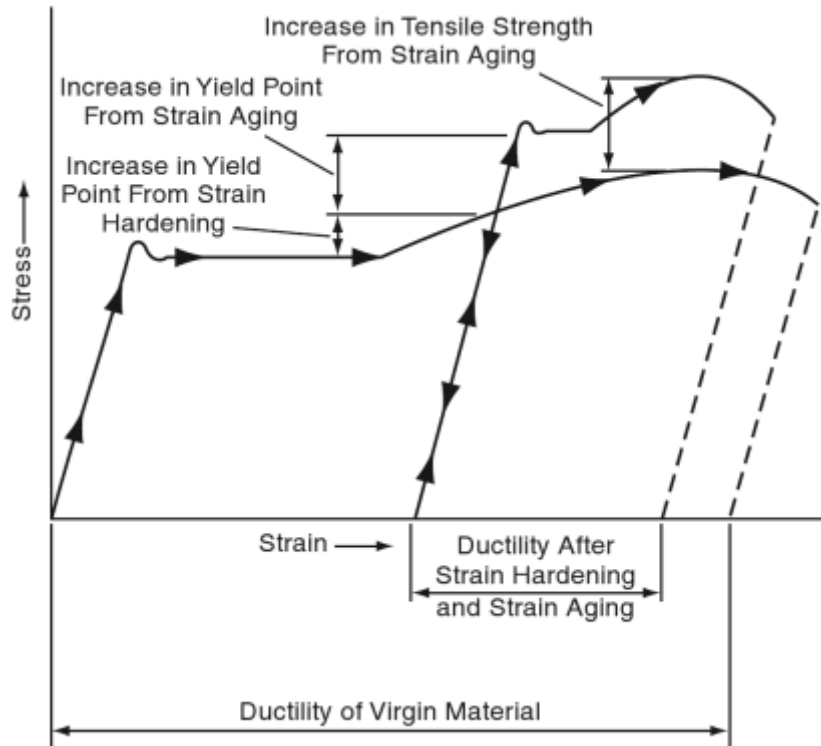


Fig. 2.18 An engineering stress-strain curve showing strain aging (From Brockenbrough & Johnston, 1981, USS steel design manual, pp.19)

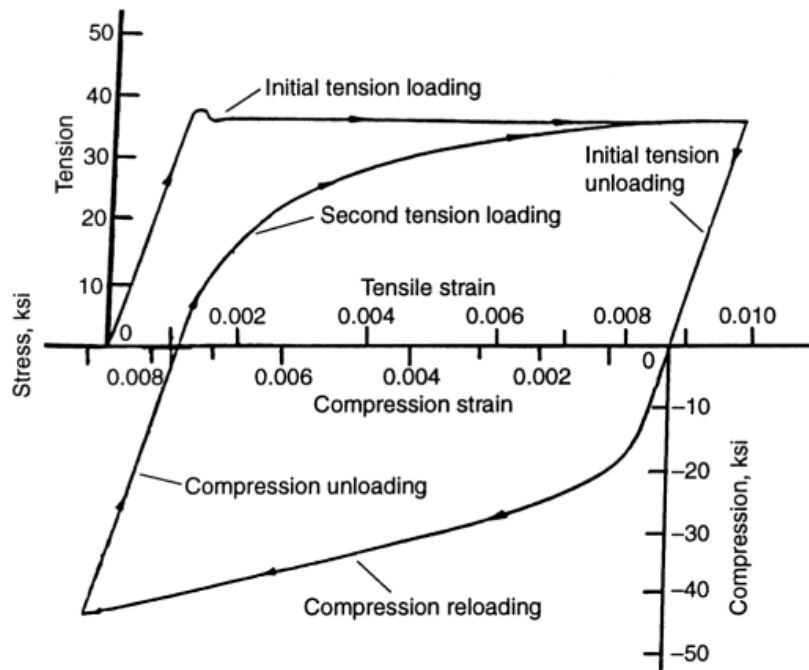


Fig. 2.19 An engineering stress-strain curve showing Baushinger effect and hysteresis loop. (From Holt, 2000, ASM Handbook Volume 8, pp.128)

2.5 Fracture

2.5.1 Characterization of Fracture

The ultimate failure of materials is fracture, which can be described by the separation of a structural body in response to the applied stress (Bhushan, 2013). The fracture behaviors and characterizations have been investigated by many researchers and are summarized below (Kerlins and Phillips, 1987; Davis, 2004; Askeland and Phule, 2006; Kailas, n.d.). The general process of a fracture can be described by the crack formation followed by the crack propagation (Bhushan, 2013; Kailas, n.d.).

There are many viewpoints to characterize fracture of metals (Kailas, n.d.). Based on the strain during the fracture, fracture can be characterized by ductile fracture or brittle fracture. Ductile fracture is described by tearing a specimen slowly and stably and extensive plastic strains are generated during the crack formation and propagation, while brittle fracture is described by breaking a specimen rapidly and unstably and little plastic strains are observed during the crack formation and propagation. Based on the crystallographic structure, fracture can be characterized by shear fracture or cleavage fracture. Shear fracture is caused by shear stress on slip plane inclined at 45° to the applied tensile stress, while cleavage fracture is caused by tensile stress normal to cleavage plane. Based on the fracture appearance, gray and fibrous surface is caused by shear fracture while bright and granular surface is caused cleavage fracture. Based on the path of crack propagation, intergranular fracture is described by crack propagating along the grain boundaries while transgranular fracture is described by crack propagating through the grains. In reality, most metals does not exhibits 100% shear fracture or 100% cleavage fracture but a mixture mode of fracture, which is usually measured by the percent shear fracture or percent ductility.

A typical fracture appearance of a ductile steel specimen, such as X52 steel, in response to the uniaxial tensile stress is a dimpled cup-and-cone fracture with a relative separation between the interior fibrous and flat zone and the exterior shear-lip. The fracture begins at the central interior zone due to normal (cleavage) fracture and ends at the exterior shear-lip zone due to shear fracture. The sequence of how a cup-and-cone fracture is formed is shown in Fig. 2.22 and explained below (Askeland and Phule, 2006; Davis, 2004; Kailas,

n.d.). As a ductile steel specimen is elongated in tension to some extent, necking occurs and small microvoids are generated in the interior of the specimen due to the triaxial tensile stresses caused by geometrical changes. Then microvoids grow and coalesce to form a big internal crack. The crack spreads outward perpendicular to the tensile stress and later rapidly propagates to the edge of the specimen at 45° to the tensile stress. Shear lips are formed by shear stress in the final stage. Shear lips around the periphery of the neck contribute to one piece of the fracture surface in the form of a cup shape and the other piece of fracture surface in the form of a cone shape.

A large amount of energy is expended during the extensive plastic deformation and localized necking and an important failure warning is given prior to the final ductile fracture. Therefore, ductile materials are usually governed by yield or ultimate strength. However, by changing the temperature or the geometric constraints which raise the stress, the fracture mode can be altered. Ductile materials may fail in brittle fracture under the low temperature or with strict geometric constraints. The brittle fracture surface is predominated by bright and granular flat zone without apparent shear lips. Cracks propagate rapidly from the center to periphery and their path are shown by radial ridges on the surface. Very small amount of energy is expended in the absence of extensive plastic deformation and necking. No failure warning is given since the brittle fracture is sudden. A comparison of a typical ductile fracture appearance and a typical brittle fracture appearance during a tension test is shown in Fig. 2.21 (Davis, 2004). A material failing in ductile or brittle fracture depends on the material toughness, which as mentioned earlier is described by the total area under the engineering stress-strain curve in a uniaxial tensile test, and shown in Fig. 2.20. Toughness indicates how much amount of energy per unit volume can be done on a material without causing the fracture, and is equal to material slow energy absorption up to failure (Bhushan, 2013). In general, ductile materials have higher toughness than brittle materials.

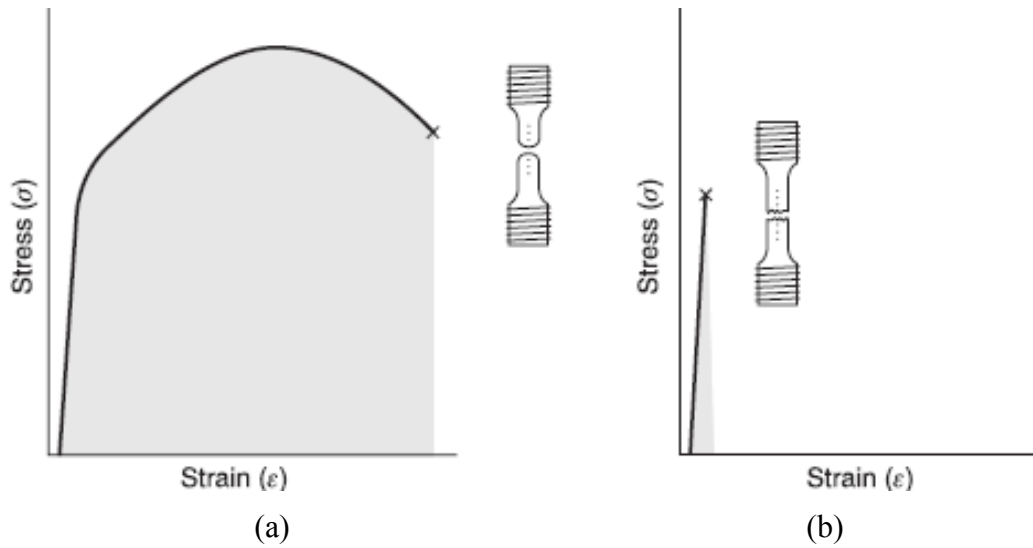


Fig. 2.20 Engineering stress-strain curve for (a) ductile fracture and (b) brittle fracture (From Bhushan, 2013, pp.63)

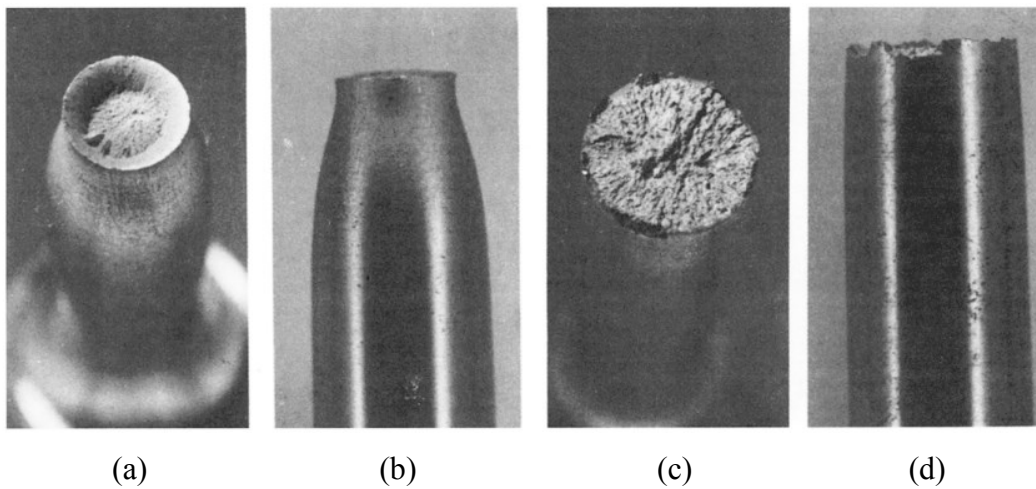


Fig. 2.21 Appearance of a typical (a)(b) ductile fracture and (c)(d) brittle fracture during uniaxial tension test (From Davis, 2004)

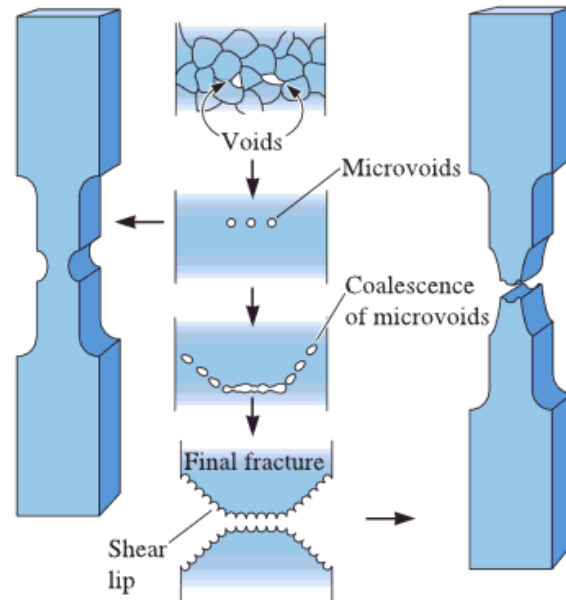


Fig. 2.22 The sequence of how tensile fracture is formed for a ductile steel specimen (From Askeland and Phule, 2006, pp.231)

2.5.2 Fracture Mechanics

The traditional approach and fracture mechanics approach for the structural design and material selection were identified in the past and described by many researchers, such as Anderson (2005) and Czicho, Saito and Smith (2006). The traditional approach is the design of the strength of materials. The yield or tensile strength of a material is usually measured in a tension test to indicate the material resistance to the applied stress. However, the fracture mechanics approach adds crack size as a new parameter, and measure the fracture toughness of a material rather than its strength properties. The fracture toughness measures the ability of a material to resist crack formation and propagation, and can be directly measured by a fracture toughness as the form of a toughness parameter ($G, K, J, CTOD$ or δ) or indirectly measured by a CVN impact test as the form of energy required to fracture a notched specimen. Prefabricating a crack or notch to produce the stress concentration and extreme condition in the vicinity of crack-tip to measure the fracture toughness of a material is very important (Bhushan, 2013). It is because cracks have great possibility to be formed in the process of the manufacture of the structures or during the operational service (Czicho, Saito and Smith, 2006; NDT Resource Centre).

2.5.2.1 Stress-intensity Factor and Fracture Modes

The fundamental principle of fracture mechanics approach is to characterize the stress and strain field in the vicinity of crack tip by a single toughness parameter, such as the stress-intensity factor (K). The crack begins to grow when the stresses adjacent to the crack tip reaches to the material fracture toughness, which is characterized the by stress-intensity factor (K). A subscript is usually given to the stress-intensity factor to denote the one of three basic modes of loading applied to the crack, which are opening mode (denoted by K_I), in-plane shear mode (denoted by K_{II}), and out-of-plane shear mode (denoted by K_{III}). As shown in Fig. 2.23, opening mode is the condition in which a tensile stress is normal to the plane of the crack; in-plane shear (sliding) mode is the condition in which a shear stress is parallel to the plane of the crack and perpendicular to the crack front; out-of plane shear (tearing) mode is the condition in which a shear stress is parallel to the plane of the crack and crack front. The stress-intensity factor (K) is a function of the applied stress, the size of the crack and the constraint effect of the specimen geometry, which can be generally expressed by (Anderson, 2005; Czicho, Saito and Smith, 2006)

$$K_{(I,II,III)} = Y\sigma\sqrt{\pi a}$$

where

$K_{(I,II,III)}$ is the stress intensity factor related to each mode of loading ($MPa\sqrt{m}$)

σ is the applied remote stress (MPa)

a is the crack length (m)

Y is a factor that depends on geometry of the specimen and the mode of loading

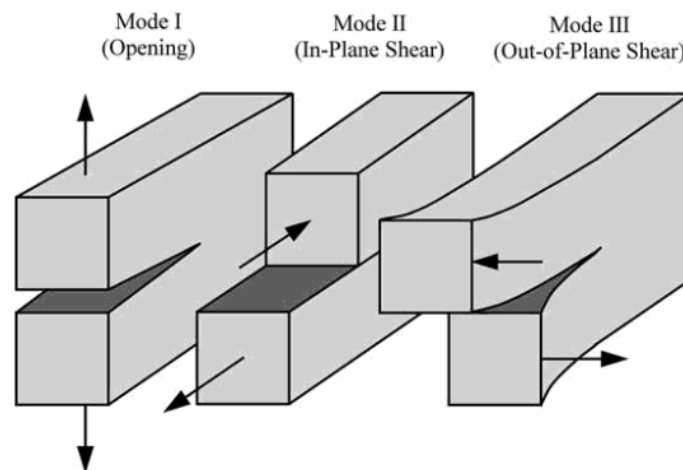


Fig. 2.23 The three basic fracture modes (From Anderson, 2005, pp.43)

2.5.2.2 Linear Elastic Fracture Mechanics and Elastic-Plastic Fracture Mechanics

Fracture mechanics is usually subdivided in two categories, which are linear elastic fracture mechanics and elastic-plastic fracture mechanics, and the theory for the first category is the basis of both categories (Anderson, 2005; Czicho, Saito and Smith, 2006). Linear elastic fracture mechanics applies to materials whose crack tip is surrounded and dominated by linear elastic deformation or with small scale plastic deformation (small scale yielding). The theory is valid for isotropic and linear elastic materials. A sharp crack (or blunts with limited plasticity) is formed at the crack tip and then the crack propagates rapidly. The failure is predominantly cleavage fracture or brittle fracture. Elastic-plastic fracture mechanics applies to materials whose crack tip is surrounded by a large scale plastic deformation (large scale yielding). The theory is valid for both the nonlinear elastic materials and elastic-plastic materials if unloading is not provided. Their loading paths are identical but the unloading paths are different. As shown in Fig. 2.24, The unloading of the nonlinear elastic material follows original loading path while the unloading of the elastic-plastic steel materials follows the path that is parallel to the linear loading path with a slope equal to Young's modulus (Anderson, 2005). Fig. 2.25 and Fig. 2.26 shows the crack-tip opening displacement and the development of a ductile crack growth and (Anderson, 2005). As the cracked specimen is loaded, the microvoids initiate and then develop to voids. As the initial sharp crack blunts with large scale of plasticity at the crack tip, voids continue to grow and eventually coalesce with the main crack. Due to the ductile crack growth, the specimen is torn slowly and stably.

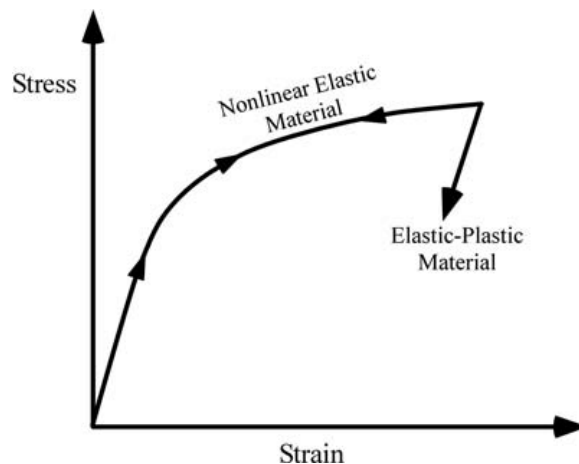


Fig. 2.24 Loading and unloading of nonlinear elastic and elastic-plastic materials (From Anderson, 2005, pp.108)

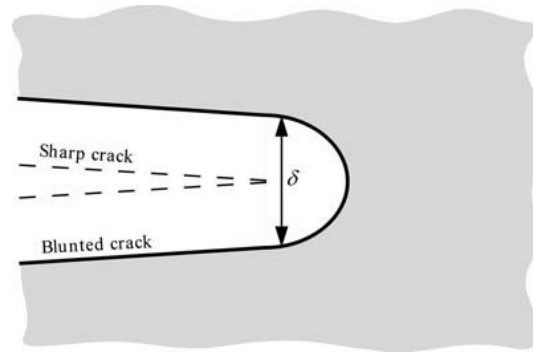


Fig. 2.25 Crack blunting and crack-tip opening displacement (From Anderson, 2005, pp.104)

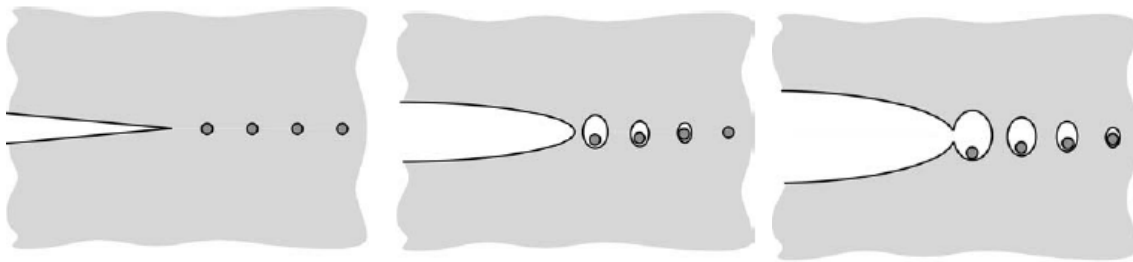


Fig. 2.26 Ductile crack growth (From Anderson, 2005, pp.232)

2.5.2.3 Fracture Toughness Parameters

Fracture toughness can be characterized by a fracture toughness parameter in a fracture toughness test, such as the stress-intensity factor (K), the energy release rate (G), the J integral (J), and the crack-tip opening displacement ($CTOD$ or δ). They can be measured by a single point value of fracture toughness under the plain strain conditions, such as K_{Ic} , G_{Ic} , J_{Ic} and δ_{Ic} , or an entire resistance curve (R -curve) where a parameter (K , G , J , δ) is plotted against the crack extension (Anderson, 2005). In linear elastic fracture mechanics, fracture toughness is determined at the point of instability which is close to the crack initiation and is usually characterized by plain strain fracture toughness characterized by K - factor (K_{Ic}) or characterized by the energy release rate (G_{Ic}). The material resistance beyond the crack initiation is small and thus the measurement is not required (Zhu & Joyce, 2012). The energy release rate (G) is an indication of the energy required to grow the crack, and it is related to the stress-intensity factor (K_I) based on crack tip constraints, given below (Anderson, 2005).

$$G = \frac{K_I^2}{E'}$$

where

$$E' = E \text{ under plane stress condition}$$

$$E' = \frac{E}{(1-\nu)^2} \text{ under plane strain condition}$$

In the elastic-plastic mechanics, fracture toughness is determined by an entire R -curve, such as J - R curve or δ - R curve, which describes the continuous process of slow and stable crack tearing. Due to the requirement of a single point value of fracture toughness in many methods and applications, J_{Ic} or δ_{Ic} is usually deduced from the R -curve at the onset of ductile crack growth, which is shown at a point on the curve whose slope changes dramatically (Zhu & Joyce, 2012; Anderson, 2005). J_{Ic} or δ_{Ic} indicates elastic-plastic initiation toughness, and this toughness is still measured under plane strain conditions. J -integral is a measure of the energy required to grow the crack and can be mathematically expressed as a line or surface integral that encloses the crack tip from one crack surface to the other (Kocak et al., 2006). It describes the local stress-strain field in the vicinity of the crack tip. $CTOD$ or δ is the displacement at the original crack tip (Fig. 2.25). Both elastic and plastic components of these two elastic-plastic parameters should be considered. Note that their elastic components can be determined in linear elastic fracture mechanics. The elastic component J -integral is equal to the elastic energy release rate and is related to the stress-intensity factor for linear elastic mode I loading (Anderson, 2005).

$$J_{el} = G = \frac{K_I^2}{E'}$$

The relationship between the J -integral and the crack tip opening displacement is given based on a constraint factor (m) and effective yield strength (σ_Y). API 579-1/ASME FFS-1 (2007) takes 1.4 as an approximate value of m in the absence of detailed information. The effective yield strength is the average of the static yield strength and ultimate tensile strength.

$$J = m \cdot \sigma_Y \cdot \delta$$

Based on the theoretical relationship between fracture toughness parameters in linear elastic fracture mechanics, an “equivalent K_{Ic} ” value can be derived from J_{Ic} or δ_{Ic} value in the limit of small scale yielding under plane strain conditions (API 579-1/ASME FFS-1, 2007).

$$K_{Ic} = \sqrt{\frac{J_{Ic} \cdot E}{1-\nu^2}} = \sqrt{\frac{m \cdot \sigma_Y \cdot \delta_{Ic} \cdot E}{1-\nu^2}}$$

where

K_{Ic} , J_{Ic} , and δ_{Ic} are plane strain fracture toughness characterized by stress-intensity factor K ($MPa\sqrt{m}$), J -integral (kJ/m^2), and crack-tip opening displacement (mm)

E is Young’s modulus at the temperature of interest (MPa)

ν is Poisson’s ratio in the elastic range and is normally taken as 0.3 for steels

m is the conversion constant, taken as 1.4 in the absence of detailed information

σ_Y is effective yield strength, which is equal to $\frac{\sigma_{YS} + \sigma_{TS}}{2}$ (MPa)

The above relationships are based on the plane strain conditions. For plane stress conditions in linear elastic fracture mechanics, an “equivalent K_c ” value can be derived from J_c or δ_c value as well, and shown below (Anderson, 2005).

$$K_c = \sqrt{J_c \cdot E} = \sqrt{m \cdot \sigma_Y \cdot \delta_c \cdot E}$$

where

K_c , J_c , and δ_c are plane stress fracture toughness characterized by stress-intensity factor K ($MPa\sqrt{m}$), J integral (kJ/m^2), and by crack-tip opening displacement (mm)

2.5.2.4 Variables to Fracture Toughness

The variables that influence the toughness of steel material are the rate of loading, the temperature, and the notch effect. The toughness decreases as the rate of loading increases, as the temperature decreases, and as a notch or crack is present (NDT Resource Centre). The notch effect is related to the distribution of stress at crack tip, which is influenced by loading mode and specimen geometric conditions, such as dimensions and ratio of crack depth to specimen width (Zhang et al., 2010; Wang et al., 2012).

In the study of geometric conditions of specimens, the specimen thickness plays an important role in measuring the fracture toughness by altering the crack-tip constraints, stress state conditions and fracture behaviors. Fig. 2.27 indicates that fracture toughness characterized by stress intensity factor K decreases as the specimen thickness increases (NDT Resource Centre). The curve is obtained under the opening mode of loading. A thicker specimen tends to produce the triaxial stress state which results in more crack tip constraints and less crack tip yielding, and increases the possibility of brittle fracture and decreases fracture toughness; however, a thin specimen tend to produce the biaxial stress state which results in less crack tip constraints and more crack tip yielding, and increase the possibility of ductile fracture and increases fracture toughness (Zhu and Joyce, 2012). Once the thickness of the specimen exceeds a critical value, fracture toughness decreases to a lower bound constant value K_{Ic} , called the critical plane-strain stress intensity factor. K_{Ic} is a true material property which indicates the resistance of a material to crack propagation under the plane strain condition, and is independent of the loading and geometric conditions (Wang et al. 2012). The plane strain condition is a triaxial stress state which constrains strains in the thickness direction (z -direction) and thus normal strain ϵ_z and shear strain γ_{xz} and γ_{yz} are assumed to be zero, while the plane stress condition is a biaxial stress state which applies stresses only in a plane (x - y plane) perpendicular to the thickness direction (z -direction) and thus the normal stress σ_z and the shear stress τ_{xz} and τ_{yz} are assumed to be zero (Bruch, J. C. & Boeriu, S., n.d.). The plane strain condition refers to high constraints and usually occurs in a thick specimen with a deep crack, while the plain stress condition refers to low constraints and usually occurs in a thin specimen with a shallow crack (Barson and Rolfe, 1999). For most ductile steel materials, the effect

of specimen thickness on the fracture behavior can be determined by the relative portions of flat fracture and shear fracture. As shown in Fig. 2.28, a thick specimen is dominated by flat fracture shown by large percentage of fibrous and flat central regions, while a thin specimen is dominated by shear fracture, shown by large percentage of 45° shear lips on the edges.

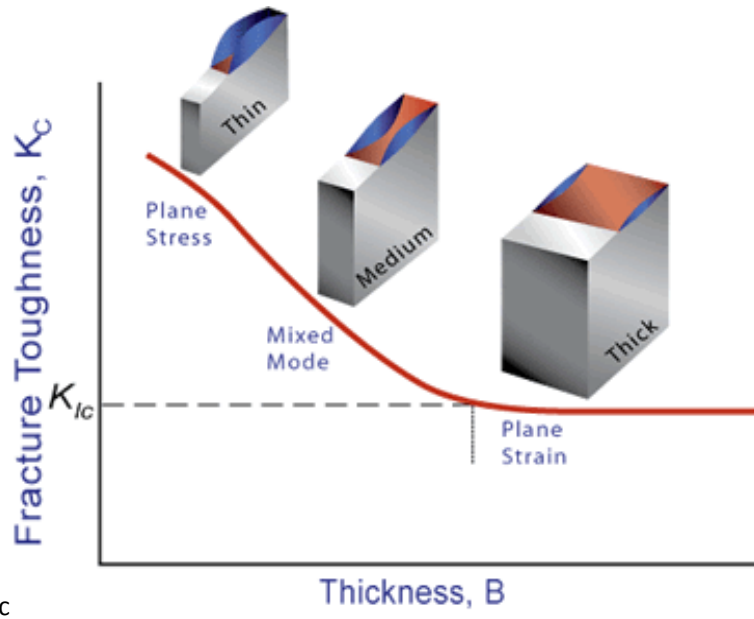


Fig. 2.27 Effects of specimen thickness on fracture toughness K (From Nondestructive Testing (NDT) Resource Centre, “fracture toughness”)

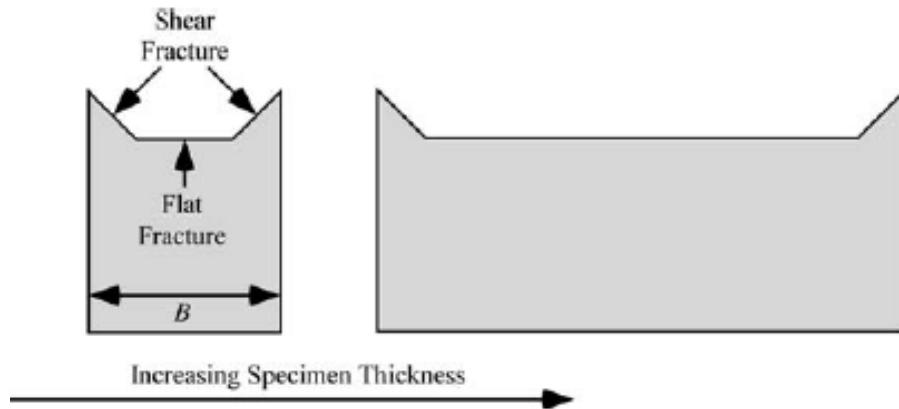


Fig. 2.28 Effects of specimen thickness on fracture surface (From Anderson, 2005, pp.76)

Test temperature plays a significant role in determining material fracture behaviors. As shown in Fig. 2.29, a schematic CTOD (δ) versus temperature transition curve for

structural steels was studied by Barson and Rolfe (1999) and Wellman and Rolfe (1985). The transition curve can be generally divided into four regions, including (I) lower shelf, (II) lower transition, (III) upper transition, and (IV) upper shelf. In the region I, there is almost no or little increase in toughness characterized by CTOD as temperature increases. The brittle fracture behavior and linear elastic deformation behavior are predominant when crack initiates and propagates. K_{Ic} is used to measure fracture toughness at brittle fracture initiation under the linear elastic plain strain condition in the lower shelf region. A valid K_{Ic} is obtained at a very low temperature about more than 150°C below the nil-ductility temperature (NDT) of the studied steels. NDT temperature is designed for a test temperature when the specimen shows approximately 100% brittleness but 0% ductility. The high strength A517 steel was tested at -200°C to obtain a valid K_{Ic} according to ASTM E 399-12 (Wellman & Rolfe, 1985). However, due to a very strict requirement for the specimen size is established in ASTM E 399-12, many steels cannot be tested to directly obtain a valid value of K_{Ic} . In the II region, no prior stable cracking is observed as the crack propagates in a brittle manner. As the temperature increases, toughness increases. For A131, A516, A533, A508 steels studied by Wellman & Rolfe (1985), the CTOD values increases from about 0.005mm to 0.25mm in a temperature range of 100 to 150 °C in the lower transition. Based on a finite element analysis conducted by Wellman, Rolfe & Dodds (1985), a plastic hinge develops in the three-point bend test specimen with CTOD ranging from 0.05 to 0.18mm (variation is due to the yield strength and specimen size) and indicates that the elastic-plastic fracture behavior is shown in the lower transition region. δ_c and J_c are used to measure fracture toughness at brittle fracture initiation under the elastic-plastic plane stress condition. Although the plastic zone develops, there is no stable crack extension. Final fracture is still the rapid unstable brittle fracture. In the III region, a large amount of plastic zone develops and stable ductile tearing occurs, shown by a visible coarse fibrous thumbnail. The ductile tearing is followed by unstable brittle fracture or mixed mode of fast fracture. As mentioned earlier, the upper transition region starts when CTOD is about 0.25mm for A131, A516, A533, A508 steels. J_{Ic} is used to measure the fracture toughness at the onset of the slow stable crack extension under the elastic-plastic plane strain condition. In the VI region, the specimen is yielding and the fibrous ductile tearing is shown in the entire fracture surface. The upper shelf region starts at the temperature

when specimen shows 100% ductility. δ_u and J_u are used to measure fracture toughness at the fracture instability after the onset of considerable stable tearing crack extension under the elastic-plastic plane stress condition.

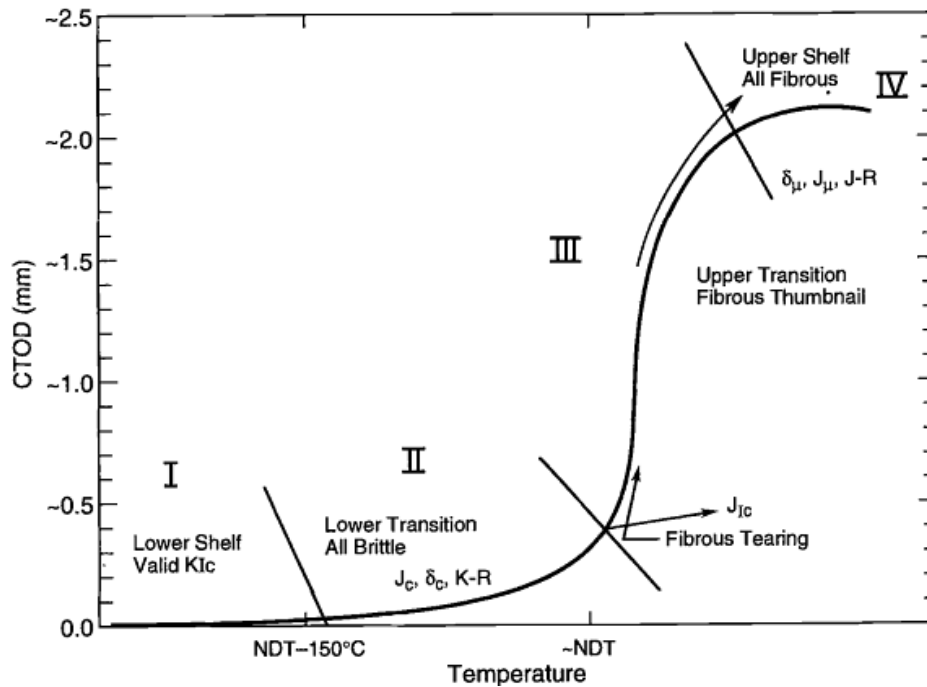


Fig. 2.29 Schematic CTOD versus temperature transition curve showing four regions of fracture behavior for structural steels (Adapted from Barson & Rolfe 1999, pp.77)

2.5.2.5 Variables to Fracture Toughness

The fracture toughness characterized by resistance curves (J - R and $CTOD$ - R) is dependent on the crack tip constraints against the plastic deformation, and the high level of constraints usually produce low toughness resistance curve and vice versa (Yuan & Brocks, 1998; Wang et al., 2012). Conventional and standardized fracture toughness tests require high constraint levels at the crack tip and use deep-cracked specimens such as compact tension (CT) specimens and single edge notch bend (SENB) specimens, as described in ASTM E 1820-11, and shown in Fig. 2.30. It is a generalized fracture toughness test method that combines three toughness parameters K , J , $CTOD$ in a single test. The electrical discharge machining (EDM) is conducted to machine the notch with the initial length of a_0 and the fatigue pre-cracking in a three-point bend fixture is conducted to sharpen the notch tip with the final length of a (Drexler et al., 2010).

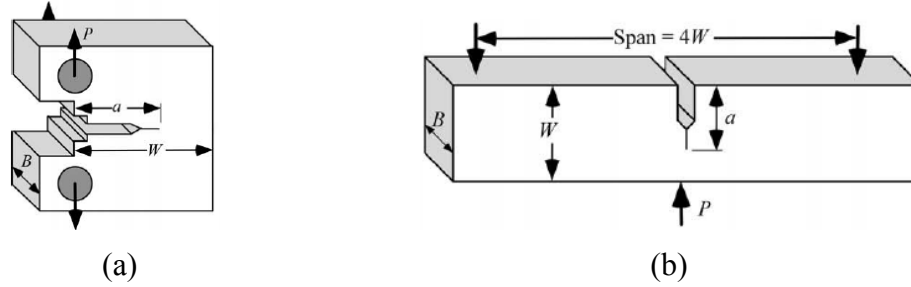


Fig. 2.30 Fracture toughness test specimens (a) compact tension specimens; (b) single edge notch bend specimens (From Anderson, 2005, pp.300)

With the high crack tip constraints, the measured fracture toughness represents the lower bound toughness (K_{Ic}) and is independent of the loading and geometric conditions (Wang et al., 2012). ASTM E399-12 was the first standardized test method for K_{Ic} testing and published in 1970. It puts stringent restrictions for specimen size to ensure the small scale yielding and predominantly plane strain conditions at the crack tip. To obtain a valid K_{Ic} , test specimen must be very brittle or thick. To avoid the invalidity of the fracture toughness results, the preliminary validity check of specimen size is suggested based on following requirements (Anderson, 2005).

$$B \geq 2.5 \left(\frac{K_{Ic}}{\sigma_{YS}} \right)^2, a \geq 2.5 \left(\frac{K_{Ic}}{\sigma_{YS}} \right)^2, 0.45 \leq a/w \leq 0.55$$

where

B, w, a are specimen thickness, specimen width, and crack length (mm)

σ_{YS} is 0.2% offset yield strength (MPa)

K_{Ic} is the critical plane strain stress-intensity factor ($MPa\sqrt{m}$)

The resistance curve test method in ASTM E1820-11 requires sophisticated instrumentation to monitor the ductile tearing resistance against crack extension. The method also puts restrictions for specimen size, and maximum capacity of J -integral and crack extension, which are given by (Anderson, 2005):

$$B \geq \frac{25J_{Ic}}{\sigma_Y}, b_0 \geq \frac{25J_{Ic}}{\sigma_Y}, 0.50 \leq \frac{a}{w} \leq 0.70$$

$$J_{max} \leq \frac{B\sigma_Y}{10}, J_{max} \leq \frac{b_0\sigma_Y}{10}, \Delta a_{max} \leq 0.25b_0$$

where

B , w , a are specimen thickness, specimen width, and crack length (mm)

b_0 is original remaining ligament, which is equal to $w - a_0$ (mm)

σ_Y is effective yield strength or flow strength, which is equal to $\frac{\sigma_{YS} + \sigma_{TS}}{2}$ (MPa)

J_{IC} is plain strain fracture toughness characterized by J -integral (kJ/m^2)

J_{max} is maximum value of J -integral (kJ/m^2)

Δa_{max} is maximum value of crack extension Δa (mm)

Due to the above restrictions, invalid fracture toughness results are usually obtained for pipelines with thin wall thickness and relatively high toughness. This is due to the loss of crack tip constraints. An example was shown by Shen et al. (2008) who conducted SENB tests for high strength steel X80 and X100 steel pipeline. They did not obtain a valid $J - R$ curve from the deep-cracked SENB specimens because most of their test data exceeded the limit of J_{max} as described in ASTM E1820-11. In fact, high level of constraints and deep-cracked specimens are too conservative in the study of thin-walled high-toughness steel pipeline (Zhang et al., 2010; Wang et al., 2012; Billingham et al., 2003). The actual field cracks on the pipe wall are usually shallow and may experience low levels of crack tip constraints, which result in the apparent toughness significantly higher than K_{IC} . In addition, Wang et al. (2012) mentioned that the tensile strain capacity of the cracked pipeline based on the fracture toughness measured from the high constraint specimens may be overly conservative compared to that from low constraint specimens with large plasticity.

In recent years, fracture toughness tests requiring low constraint levels at the crack tip and using shallow-cracked specimens have been developed (Wang, et al. 2001; Verstraete et al., 2012). Common specimens are shallow-cracked single edge notched bend (SENB) specimens and single-edge-notched tension (SENT) specimens (clamped or pin-loaded) (Shen et al., 2008; Wang et al., 2012). Wang et al. (2012) conducted fracture toughness for X80 steel pipeline using both SENT and SENB specimens. The measured $J - R$ and $CTOD - R$ curves of shallow-cracked SENT specimens ($a/w=0.25$) are higher than those of shallow-cracked SENB specimens ($a/w=0.25$) and deep-cracked SENT specimens ($a/w=0.5$) based on the same nominal initial crack length (a). The results show that the crack tip constraints are lower for shallow cracks than deep cracks, and are lower in tension

than in bending. As shown in Fig. 2.31, the ratio of span between load points to width of SENT specimens is recommend to $H/W=10$, and width and thickness of SENT specimens are recommend to be equal $W=B$ (Shen et al., 2008; Drexler, 2010; Wang et al., 2012). In the study of SENT methodology, Zhang et al. (2010) stated that the cracked pipeline is essentially low constraint structures because the whole ligament where crack is in tension even the pipe is subjected to global bending. They also discovered that the crack depth is not critical to fracture resistance of SENT specimens for pipeline with small wall thickness and high toughness. Even though SENT test method has been developed and accepted, it has not been standardized and concluded by any standards.

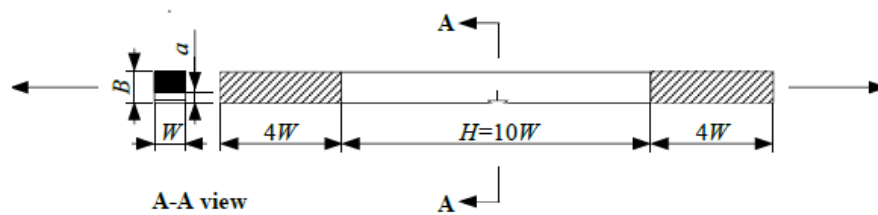


Fig. 2.31 Clamped single edge notch tension specimens (From Wang et al., 2012)

Compared to the above fracture toughness tests which can be used to directly measure the fracture toughness, Charpy V-notch impact test is regarded as a convenient and economical test to provide satisfactory but comparative fracture toughness results. This test was named after George Charpy and developed in 1901, before the formal fracture mechanics theory was introduced (Anderson, 2005). The test methodology, experimental set up, specimens design, and results analysis are further discussed in Chapter 4.

3. Tension Test

In the previous chapter, the most important material properties of structural steel are reviewed. This chapter discusses the experimental setup and the analysis of the results of the tensile properties of Enbridge Norman Wells X52 pipelines along with their girth welds. A series of standard tension tests were conducted to obtain the material properties in the circumferential and longitudinal direction for both the base metal and the girth weld. The tests were designed to accommodate the small thickness of the pipe and were conducted at the University of Alberta. The obtained properties are used to analyze the expected behavior of the pipes and the girth welds.

3.1 Introduction to Tension Test

In accordance with ASTM E8/E8M-11, a total of 25 tension specimens machined from different locations of the provided X52 pipe were designed and tested to obtain the uniaxial tensile stress-strain curves to investigate the tensile properties. As mentioned in Chapter 1, the pipe has a wall thickness of 6.86 mm (0.27 inch) and an outer diameter of 324 mm (12.75 in) (NPS 12) with a girth weld that was manufactured in 1980s, and the other that was manufactured in 2013 (Fig. 1.1). To distinguish these two girth weld, the former weld is called “old weld” and its ambient HAZ is called “old HAZ”, while the latter weld is called “new weld” and its ambient HAZ is called “new HAZ”.

3.2 Objective

A series of standard tension coupon tests were conducted to obtain and compare engineering stress-strain curve and true stress-strain curve of the provided X52 material at a room temperature. The main objectives of the studying of the stress-strain curves are summarized as follow:

- (1) To determine the important tensile properties: elastic deformation properties (elasticity modulus), strength properties (yield strength and ultimate tensile strength), ductility properties (elongation and reduction of area), and other characteristics (strain-hardening and necking)

- (2) To understand the difference in behavior between the different parts of the pipe: the girth weld (new and old), the location from which specimens were cut (base metal, weld metal, and heat-affected zone) and the orientation from which specimens were cut (longitudinal and transverse/circumferential direction)
- (3) To characterize large amount of experimental data by simpler representative curves, and particularly to describe the strain-hardening region of the true stress-strain curves by empirical mathematical equations
- (4) To compare the tensile properties of X52 pipe obtained in this research with other higher grades of pipes obtained from past research by University of Alberta, by comparing their stress-strain curves

3.3 Test Methodology

In accordance with ASTM E8/E8M-11, a standard test specimen is subjected to a uniaxial tensile force that is produced by the test loading machine to deform until fracture. Its force and deformation data over the time are monitored and recorded by the force-measuring device and the extensometer respectively. By converting the force and deformation data to stress and strain data, both engineering stress-strain curves and true stress-strain curves are plotted for further analysis. The loading is applied with a low rate to decrease the dynamic loading rate effect on the material. Due to the material's time dependence and sensitivity to the test speed, the yield strength and the tensile strength both increase as the applied loading rate increases (Davis, 2004). During the test, manually taking regular stoppages at yielding and strain hardening ranges of the stress-strain curve is employed to determine the static strength. The recorded stress-strain data on stoppages contributes to producing a quasi-static stress-strain curve, which better represents the material behavior. Before conducting the tests, many important preparation works should be done, which include the design of specimens and grips, the selection of loading range and extensometer, the determination of the loading rate, and the calibration of the test machine and devices. These preparations are further explained below in following sections.

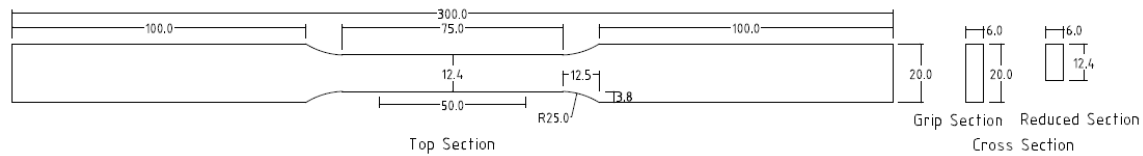
3.4 Test Specimens and Grips

3.4.1 Design of Specimens

Two typical types of specimens are designed for performing a standard tension test in accordance with ASTM Standard E8/E8M-11.

- (1) The standard rectangular tension test specimens with a gauge length of 50 mm (2 inch), a reduced width of 12.5 mm (1/2 inch), and a pair of enlarged ends. (Fig. 3.1)
- (2) The small-size round tension test specimen with a gauge length of 10 mm (0.45 inch), a nominal diameter of 2.5 mm (0.113 inch) and a pair of M4×0.7 threaded ends. (Fig. 3.2)

The reduced cross section is designed to ensure the failure and deformation occurs within the gauge length region, while the pair of enlarged ends are designed to safely grip with test grips. The commonly used ISO metric screw threads are specially designed for small-size round specimens to stably fit the grips. The selected M4×0.7 screws has a 4mm nominal outer diameter and a 0.7mm pitch.

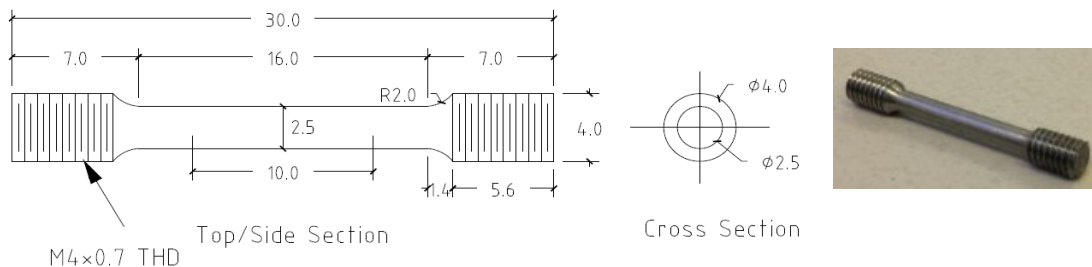


(a)



(b)

Fig. 3.1 A rectangular tension test specimen (a) design (unit: mm); (b) photo



(a)



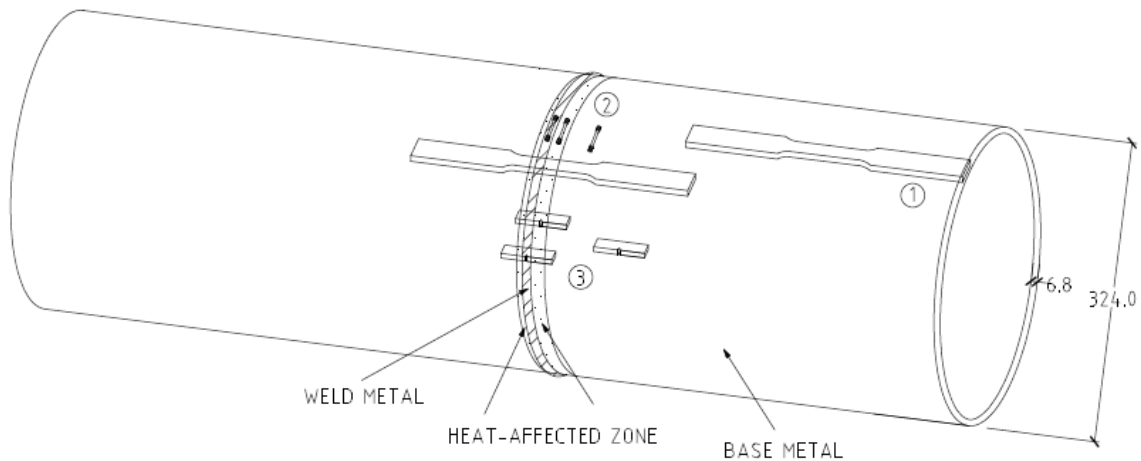
(b)

Fig. 3.2 A round tension test specimen (a) design (unit: mm); (b) photo

The rectangular specimens were cut from the longitudinal direction of the base metal and HAZ, while the round specimens were cut from the circumferential direction of the weld metal, the base metal and the HAZ. The numbers of required specimens and their location and orientation are summarized in table 3.1 and illustrated in Fig. 3.3.

Table 3.1 Numbers of tension test specimens

Specimens Location	Longitudinal Rectangular Specimens	Circumferential Round Specimens
Base metal	6	3
New weld metal		3
New HAZ	3	3
Old weld metal		2
Old HAZ	3	2
Total	12	13



SPECIMEN NO.	SPECIMEN TYPES
①	Tension Test Specimen in Longitudinal Direction
②	Tension Test Specimen in Circumferential Direction
③	Charpy V-Notch Impact Test Specimen

Fig. 3.3 Location and orientation of specimens machined from the pipe ①longitudinal rectangular tension test specimen, ②circumferential round tension test specimen, and ③ Charpy V-notched impact test specimen (introduced in Chapter 4)

3.4.2 Design of Grips

Gripping is designed to guarantee that the specimen are stably mounted, without failing or slipping when resisting the ultimate tensile force in the test. Therefore, grips should not only properly fit the specimens but also have sufficient force capacity to resist damage. Common ways of gripping include wedge grips, threaded grips, and some others types. Wedge grips work for most geometry of the specimens and wedge blocks should be designed and installed into the machines with proper alignment to ensure axial loading and avoid bending, while threaded grips work only for round specimens (Davis, 2004). During this test, the rectangular specimen was directly placed into the MTS grips and fixtures with correct alignment (Fig.3.5). However, a set of MTS end tab threaded grips that fit both designed round specimens and available MTS fixtures were specially designed and manufactured for this test. Each end of a round bar specimen was properly screwed into the threaded grips (Fig. 3.4). Since every round bar specimen was machined with one right-hand threaded end and the other left-hand threaded end, a pair of test grips were specially designed with reverse hand threads as well to fit the specimen. The specific dimension of the threaded grips are shown in Appendix B

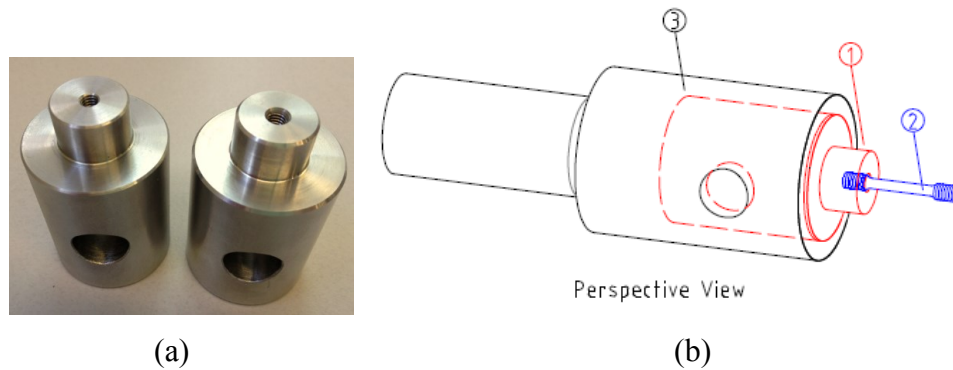


Fig.3.4 Design of grips (a) photo of grips; (b) perspective view assembly of single ① grip, ②round tension test specimen and ③MTS fixture

3.5 Test Equipment and Setup

The University of Alberta MTS Criterion Universal Testing Systems is used to perform the standard tension tests in this research, which consists of following components (“Universal testing machine”, n.d.):

- (1) Load frame: two strong supports
- (2) Load cell: a transducer to convert forces into electrical signals
- (3) Cross head: to move up and down for testing specimen.
- (4) MTS fixtures: to hold grips and test specimen

Other important devices for the test includes:

- (1) Extensometer: a device to measure the extension of the specimen
- (2) Strain gauge: to measure the lateral strains, but were not required for this research
- (3) Output device: to record the force and extension data
- (4) Caliper: to measure the dimension of cross sectional area and gauge length of each specimen before and after the test

3.5.1 Selection of Loading Range

Selection of the appropriate loading range for testing specimen is important prior to the test. The load capacity of testing machine should be sufficient to break the test specimens, but should not far exceed the force that is required for breaking. The prediction of how much force will be required is usually determined by past experiences of similar tests. The yield strength and ultimate tensile strength for X52 material was expected to be about 440 MPa and 520 MPa prior to the tests. For the rectangular specimen with a reduced sectional area of $A = 12.4 \times 6 = 74.4 \text{ mm}^2$, its predicted yield load and ultimate load were calculated as $YL = 74.4 \times 420 = 32.7 \text{ kN}$ and $UL = 74.4 \times 520 = 38.7 \text{ kN}$ respectively. For the round specimen with a reduced sectional area of $A = \pi \cdot 2.5^2/4 = 4.91 \text{ mm}^2$, its predicted yield load and ultimate load were calculated as $YL = 4.91 \times 440 = 2.2 \text{ kN}$, $UL = 4.91 \times 520 = 2.6 \text{ kN}$ respectively. Obviously, these two sizes of specimens may require two ranges of load capacity for acquiring better results. In this research, a loading machine with a capacity of 1000 kN (Fig. 3.5) is selected to test the rectangular specimen, while another loading machine with a capacity of 40kN (Fig. 3.6) is selected to test the round specimen.

3.5.2 Selection of Extensometer

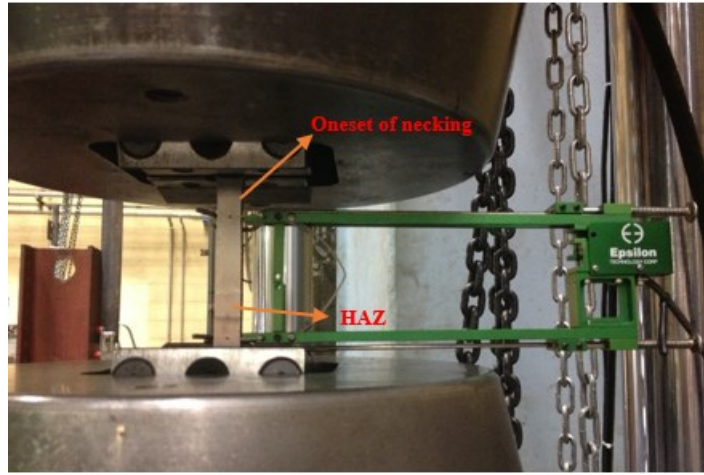
In order to measure strains in a uniaxial test, the most common way is to use an extensometer to measure axial change in length from which the strains is calculated. If lateral strains are also required, strain gauges are often used. In this particular test, only clip-on epsilon extensometer is selected to measure the localized strains of the specimen over its gauge length. The gauge length were marked by a scribe or a permanent marker on the reduced section of each rectangular or round specimen respectively prior to the test. The extensometer was zeroed and stably installed on the gauge length of the specimen to automatically record the change of the length between two gauge marks. Selection of an appropriate extensometer for specimens depends on whether the gauge length of the extensometer and the specimen match. In this research, an epsilon extensometer of 50mm gage length (Fig. 3.5) with a travel range of +25mm (+50%) and -5mm (-10%) is selected for testing the rectangular specimens, while another epsilon extensometer of 10mm gage length (Fig. 3.6) with a travel range of ± 2 mm ($\pm 20\%$) is selected for testing round specimens. It is noted that when testing a very ductile specimen with a large amount of elongation, the extensometer should better be safely removed from the test specimen during the necking before the fracture is completed, because a completed necking and fracture may damage the extensometer over its travel range (Davis, 2004). In this research, the 50mm extensometer was removed during the necking of the rectangular specimen for protection, while the 10mm extensometer was used until the final fracture of the round specimen.

3.5.3 Calibration and Alignment

All test machine and devices were calibrated prior to the test, to ensure the load and displacement measuring machines start from zero without making an error of the magnitude of the stress and the strain. In addition, the specimen was placed into the machine between the grips with proper alignment. All of the axis of loading frame, MTS fixtures grip and specimen should be coincident. The off-center force generated by misalignment may induce incorrect measurement because of the presence of bending moment and bending stresses (Davis, 2004).

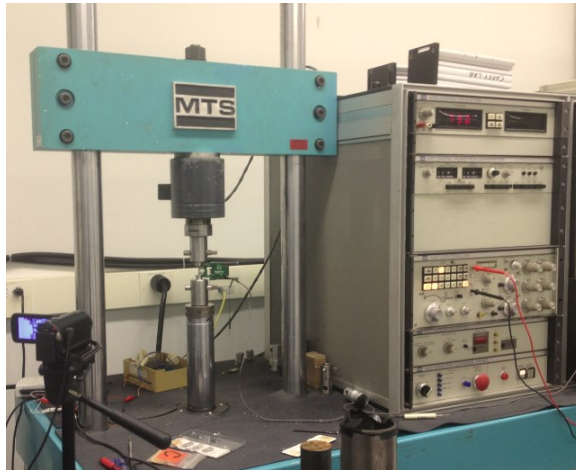


(a)



(b)

Fig. 3.5 (a) MTS test machine (1000kN capacity) and (b) an epsilon extensometer (50mm gage length)



(a)



(b)

Fig. 3.6 (a) MTS test machine (40kN capacity) and (b) an epsilon extensometer (10mm gage length) and assembly of specimen, grips, and MTS fixtures

3.6 Test Procedures

The general test procedures for a completed tension test including preparation and result analysis are summarized in the following steps.

- (1) Design specimens and grips and measure the dimension
- (2) Select loading range and extensometer
- (3) Calibrate test machine and devices, and set up the tension test
- (4) Control loading rate and time to start and stop for recording static data during the test
- (5) Measure the dimension of fracture specimens after the test
- (6) Analyze the experimental raw data to plot engineering and true stress-strain curves
- (7) Determine important tensile parameters on each stress-strain curve
- (8) Characterize experimental curves of every specimen set to single representative curve
- (9) Compare curves and conclude the result

During the test, manual control of test speed and recording the static values when the loading stopped is extremely important. These static values are valuable because the measured strength is increased by higher loading rate. The slower the force is applied to the specimen, the more the result represents the “static” material behavior. For every rectangular test specimen, an initial loading rate of 0.1mm per minute was employed until it passed the yielding range, then the loading rate was set to 1.5 mm per minute until the specimen fractured into two pieces. Increasing the loading rate at the onset of the strain-hardening was only aimed to speed up the test and save time. For every small round specimen, the loading rate of 0.1mm per minute was employed during the whole test until final fracture because it required less amount of time to fail compared to that for the longer rectangular specimen. By observing the force-deformation curve on the displacement screen during the test, the loading was manually stopped 2-3 times at the yielding range, stopped 2-3 times at strain hardening range, and stopped once when the curve reached around the peak value. All these static points were recorded and converted into static stress and strain to produce the quasi-static stress-strain curve.

3.7 Test Result and Analysis

The 25 tension specimens mentioned before were tested and studied in this research. 6 specimens (0A, 0B, 0C, 0D, 0E and 0F) were machined and tested by Qualimet Inc., and the remaining 19 specimens were machined by Rejent Tool and Manufacturing Co. Ltd, and tested at the University of Alberta. The engineering stress-strain curves and true stress-strain curves were produced for all specimens, and the quasi-static stress-strain curves were produced for most specimens. The engineering stress-strain curves were converted into the true stress-strain curves as described in section 2.3.2. The quasi-static stress-strain curves were extrapolated from the data recorded when loading was stopped during the test. All curves are included in Appendix C, and the important tensile properties of every specimen determined from the experimental stress-strain curves are shown in table 3.2.

The most important material properties include the Young's modulus, the yield strength, the tensile strength and the uniform strain, the fracture strength, and the ductility expressed by the final elongation and the reduction of area at fracture. Their determination methods are summarized below (Davis, 2004; ASTM E8/E8M-11):

- (a) The Young's modulus (E) can be measured by the slope of the initial linear stress-strain curve up to the proportional limit.
- (b) The yield strength can be determined by the offset method (offset=0.2%) or the extension-under-load method (EUL=0.5%) for a specimen showing gradual yielding, while the yield strength can be determined by the upper yield strength (UYS), the lower yield strength (LYS), and the mean yield strength during the yield point elongation (YPE) for a specimen exhibits yielding plateau.
- (c) The tensile strength determined by the engineering or true stress-strain curves are quite different, because the two curves begin to diverge greatly after yielding. The engineering tensile strength is calculated by dividing the maximum tensile force by the original cross sectional area, while the true tensile strength is converted from the engineering tensile strength when the maximum tensile force is reached. The corresponding true strain at the true tensile strength is termed the true uniform strain, and is converted from the engineering uniform strain.

(d) The fracture strength is the failure stress at fracture, which should be clarified based on either the engineering or true stress-strain curve. The engineering fracture strength is calculated by dividing the actual fracture force by the original cross sectional area. The true fracture strength should be calculated by dividing the fracture load by the final cross sectional area at fracture. However, this calculation requires correction for the effect of the triaxial state of stress produced by specimen's necking. In the lack of sufficient information to determine such effect, the calculated true fracture strength will be very erroneous. Therefore, only the values of the engineering fracture strength are shown in table 3.2.

(e) The ductility is measured by the elongation ($El\%$) or the reduction of area ($RA\%$) at fracture location and both of them are expressed as the percentage. After fracture, the final distance between two gauge marks (L_f) and the cross-sectional area at fracture location (A_f) are measured. The reduction of area is obtained by dividing the reduction of cross-sectional area (ΔA) by the original cross-sectional area (A_0). The elongation is equal to the engineering strain at fracture. It can be manually measured after fracture by dividing the change in gauge length (ΔL) by the original gauge length (L_0), which was used for the longitudinal rectangular specimens. Alternatively, it can be directly measured by the extensometer by taking the value of the engineering fracture strain, which was used for the circumferential small round specimens.

$$El\% = \frac{\Delta L}{L_0} = \frac{L_f - L_0}{L_0}$$

$$RA\% = \frac{\Delta A}{A_0} = \frac{A_0 - A_f}{A_0}$$

3.7.1 Summary of Experimental Tensile Properties

Some important tensile properties obtained for each specimen are summarized below in table 3.2, and several abnormal values are analyzed and the possible reasons are given. All specimens exhibited ductile failure with apparent necking. Since the loading was applied with a very slow rate to each specimen, the test results are acceptable because there are less than 6% difference between the test and the quasi-static results.

Table 3.2 Tensile properties obtained from the standard tension tests

Properties Specimen Set		Stiffness		Strength										Strain Hardening		Ductility				
		E (GPa)	Promotional limit (MPa)	Yield Strength (True) (MPa)						Quasi- Static	Tensile Strength (MPa)				Fracture strength (Eng)	Y/T Ratio		Uniform Strain (True)	Total Elongation	Reduction of Area
Gradual Yielding				Yielding Plateau			Test	Quasi-Static			Test									
0.2% Offset	0.5% Strain			UYS	LYS	Mean Stress		YPE	Eng		True	Eng	True	Eng		True				
Location	#																			
<p>Specimens cut from the longitudinal direction of the pipe Gauge length is 50 mm, and total elongation was manually measured after fracture Loading rate was 0.1mm/min upto yielding, and 1.5mm/min upto failure during the test</p>																				
Base Metal	1A	200	260	417	422					415	496	571	475	539	331	85%	74%	14.1%	29.3%	70.0%
	1B	193	251	406	411					403	492	572	468	543	315	84%	72%	15.0%	33.0%	66.6%
	1C	205	385	421	421	440	421	423	1.4%	413	500	575	473	544	327	85%	74%	14.1%	32.7%	66.6%
	0A			402	412						504					81%			39.1%	
	0B			415	424						505					84%			40.7%	
	0C			407	415						509					81%			35.9%	
	Ave	199	299	411	418					410	501	573	472	542	325	83%	73%	14.4%	35.1%	67.7%
<p>(1) All base metal specimens showed smooth gradual yielding except specimen 1C showing a small range of yielding plateau.</p>																				
New HAZ	1D	200	300				427	435	1.3%	422	503	551	478	528	343	86%	79%	8.9%		64.6%
	1E	207	310			444	427	433	1.7%	422	503	563	478	535	334	86%	77%	11.4%	25.2%	61.1%
	1F	175	350				429	430	1.3%	423	499	547	474	525	324	85%	77%	9.1%		66.9%
	Ave	194	320				428	433		423	502	554	477	529	334	86%	78%	9.8%		64.2%
Old HAZ	0D	215		424	433						514					84%			24.0%	
	0E	190		430	435						511					85%			23.9%	
	0F	209		431	435						503					86%			25.1%	
	Ave	205		428	434						509					85%			24.3%	
<p>(1) New HAZ specimens showed yielding plateau while old HAZ specimens showed gradual yielding. (2) All specimens fractured at the base metal rather than the HAZ (Fig. 3.8).</p>																				

- (3) Specimen 1D and 1F fractured beyond the effective 50 mm gauge length marks (Fig.3.8), thus the final elongation cannot be manually measured by a 50mm gauge length. Alternative measurement with longer gauge length (center 100mm between shoulders of the specimen) was included in Appendix A for reference only.
- (4) New HAZ specimens exhibited similar strength and ductility with old HAZ specimens.
- (5) Specimen 1F had a low value of elasticity of modulus. It might be softened when it was machined or it might cut from a location of the HAZ that was softened for a reason, and thus this location would be easier to deform plastically.

Specimens cut from the circumferential direction of the pipe
 Gauge length is 10 mm, and total elongation was determined by engineering fracture strain measured by extensometer
 Loading rate is 0.1mm/min upto failure during the test

Base Metal	2G	231	420			465	442	455	1.1%		521	568			156	87%	80%	8.5%		80.0%
	2H	223	400			445	433	440	1.6%		520	592			146	85%	74%	12.9%	27.9%	76.0%
	2I	224	400			455	437	444	1.6%		520	577			119	85%	77%	10.4%		79.3%
	Ave	226	407			455	437	446			520	579			140	86%	77%	10.6%		78.4%

- (1) Specimen 2G and 2I fractured beyond the effective measure range of the extensometer. When it happened, the extensometer stopped to measure the necking range, but still measured the center non-necking gauge length range. The strain at fracture determined by extensometer could not represent the total elongation any more. The reason for this phenomenon was that the extensometer was not installed stably on specimens by rubber bands during the test (Fig.3.9). Alternative manual elongation measurement with longer gauge length (centre 16mm between shoulders) was included in Appendix A for reference only to calculate the final elongation of these specimens.

New Weld Metal	2A	Nonlinear			377						543	608			154	69%	62%	11.3%	28.3%	85.9%
	2B	220	444			450	425	445	3.2%	421	533	612	504	589	291	83%	73%	13.9%	29.6%	86.6%
	2C	210	425			485	430	450	3.7%	417	528	601	497	583	156	86%	75%	13.9%	29.4%	86.4%
	Ave	215	435				428	448		419	531	607	501	586	224	85%	74%	13.9%	29.5%	86.5%
Old Weld Metal	3A	217	405				438	443	1.4%	418	518	561	487	522	146	86%	79%	7.5%		85.6%
	3B	200	320				464	475	2.2%	456	569	633	537	592	262	84%	76%	10.7%		83.5%
	Ave	209	363				451	459	1.8%	437	544	597	510	557	204	85%	78%	9.1%		84.6%

- (1) Specimen 2A was tested initially and it was deformed before it was truly tested. The test frame was slightly misaligned, and the test machine and load output had not been calibrated well. The initial machine setup work and practice test on specimen 2A made it deformed and softened before the

actual test. Therefore, almost no linear portion was observed in the initial region of stress-strain curve. Due to the loss of stiffness, the specimen became easier to deform plastically, and contributed to a lower yield strength (measured at 0.5% total strain).

- (2) For the new weld metal specimens, the average value of every tensile property obtained from the test was calculated based on specimen 2B and 2C, eliminating 2A.
- (3) Values of the properties obtained from the two old weld metal specimens varied significantly, and had about 10% difference in strength. This is because the old girth weld was manufactured in 1980s and the weld metal is different compared to the new weld metal manufactured in 2013. It was conservative to use the lower properties obtained from specimen 3A rather than the average properties of specimen 3A and 3B as the material properties of the old weld metal.

New HAZ	2D	217	435				460	470	2.6%		537	608			197	88%	77%	12.3%	25.0%	80.0%
	2E	173	345				517	517	0.6%	489	519	540	485	513	165	100%	96%	4.0%		80.2%
	2F	220	430			505	463	470	2.3%	450	522	581	491	551	152	90%	81%	11.5%		79.5%
	Ave	203	433				462	470		450	530	595	491	551	175	85%	79%	11.9%		79.8%
Old HAZ	3C	223	445			466	446	455	3.1%	424	515	584	486	552	202	87%	79%	12.5%		81.8%
	3D	207	430				455	480	2.7%	436	560	606	531	574	230	88%	81%	7.8%		75.4%
	Ave	215	438				451	468	2.9%	430	538	595	509	563	216	88%	80%	10.2%		78.6%

- (1) Specimen 2E had a very small amount of uniform elongation (4.0%), apparent higher yield strength, and very high Y/T ratio (over the specified maximum ratio 0.93). It might have been cut from a location of the HAZ that was bent. The prior-plastic history before the test would generate residual strains of the specimen, decrease the ductility, and increase the chance to fail in a brittle rather than ductile behavior. It was conservative to use the properties obtained from specimen 2D and 2F (eliminating 2E) to represent the new HAZ.
- (2) Values of the properties obtained from two old HAZ specimens varied significantly, and had about 10% difference in strength. The great variation in HAZ is affected by the field girth weld manufactured in 1980s. It was conservative to use the lower resistance obtained from specimen 3C (eliminating 3D) as the material properties of old HAZ. The average value of every tensile property was conservatively taken as the value obtained from the specimen 3C.

The obtained strength properties of every specimen satisfy the requirement of X52 in accordance with API Spec 5L. All yield strength are higher than the specified minimum yield strength of 360 MPa and lower than the specified maximum yield strength of 530 MPa. All obtained tensile strength are higher than the specified minimum tensile strength of 460 MPa and lower than the specified maximum tensile strength of 760 MPa. Except for the specimen 2E, all Y/T ratio are lower than the specified maximum Y/T ratio of 0.93. The maximum limit 0.93 is designed as the margin of safety against fracture. A higher ratio results in a rapid fracture at a small plastic deformation, just like the specimen 2E. Conversely, a lower ratio provides more protection to resist fracture, due to the observable and substantial plastic deformation.

All specimens fractured after a considerable amount of plastic deformation and necking, shown by a localized reduction in the cross-sectional area, which indicates X52 pipe is made from a ductile steel material and will fail in a ductile manner. As further explained in section 2.5.1, the ductile fracture occurs by a slow tearing of the material accompanied by the consumption of a considerable amount of energy. The tearing starts with the initiation of the voids and cracks at the central inner surface areas, and followed by the slow propagation of cracks due to the normal fracture. The central irregular and fibrous flat region is produced at this stage. The tearing ends at the shear lips around the outer perimeter of necking due to the shear fracture. The rapid formation of the shear lips results in the cup-and cone fracture, with one fracture surface in the form of a cup, and the other fracture surface in the form of a cone (Askeland & Phule, 2006). Both rectangular and round specimens during the tension tests displaced the dimpled cup-and cone fracture appearances after appreciable necking, which are shown in Fig.3.7 (a) and 3.8 (a).

All three rectangular HAZ specimens 1D, 1E, 1F fractured at the base metal rather than HAZ itself during the test, which are shown in Fig.3.7 (b). This is an indication that the HAZ is much stronger than the base metal for the research X52 pipe. Furthermore, it is noted that a few rectangular specimens fractured beyond the effective 50 mm gauge length marks, such as the specimen 1D and 1F, so that the final elongation cannot be measured by the standard 50mm gauge length. Alternative manual measurements with a longer gauge length of the center 100 mm between the shoulders of the specimen are

used for reference only to compare each specimen's total elongation, and included in Appendix A. In addition, a few round specimens fractured beyond the effective 10mm measure which is the range of the extensometer. When it happened, the extensometer stopped to measure the necking range, but still measured the center non-necking gauge length range, because it was not installed stably on specimens by rubber bands during the test. The specimen 2G is such an example, and shown in Fig.3.8 (b). Therefore, the engineering strain at fracture determined by the extensometer cannot represent the elongation any more. Alternative manual measurements with a longer gauge length of the center 16mm between the shoulders of the specimen are used for reference only to compare each specimen's total elongation, and included in Appendix A.

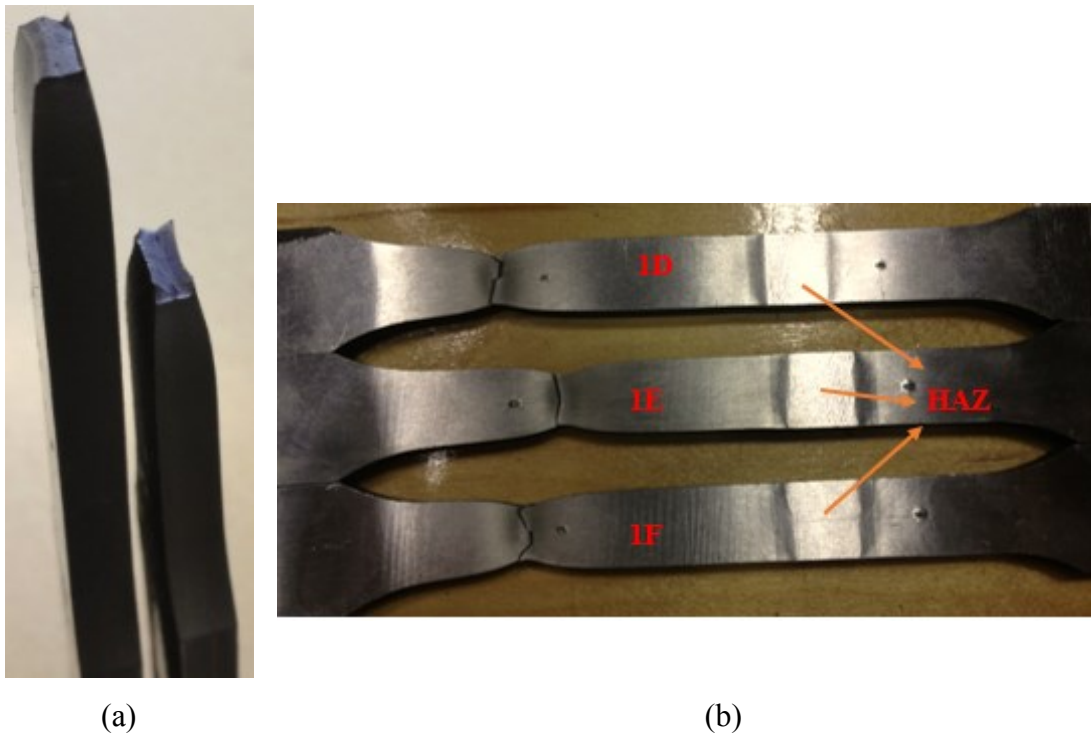


Fig. 3.7 Photos of fracture of a rectangular specimen (a) fracture appearance; (b) fracture occurs at the base metal within (Specimen 1E) or beyond the effective 50mm gauge length (Specimen 1D and 1F)

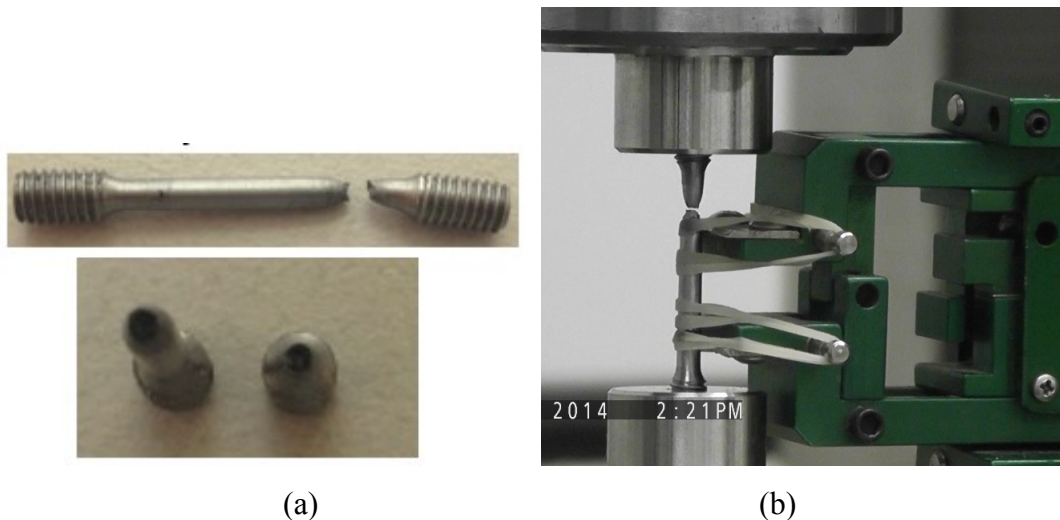


Fig. 3.8 Photos of fracture of a round specimen (a) fracture appearance; (b) fractures occur beyond the effective 10mm measure range of the extensometer (Specimen 2G)

3.7.2 Representative Curves

In this research, 7 specimen sets were tested at the University of Alberta. The specimen sets are classified by the longitudinal base metal, the circumferential base metal, the circumferential new weld metal, the circumferential old weld metal, the longitudinal new HAZ, the circumferential new HAZ, and the circumferential old HAZ. The individual stress-strain curve of each specimen varies in every specimens set. However, a representative stress-strain curve is necessary to distinguish different specimen sets for easier comparison. To model a representative quasi-static true stress-strain curve, a curve was plotted manually to fit all the static stress-strain points recorded for all specimens in a specimens set. All recorded static stress-strain points and quasi-static stress-strain curves are included in the Appendix C. To analyze test results and model a representative true stress-strain curve for every specimens set, two method are used.

3.7.2.1 Average Curve

The first method is described by taking the average of the true stress corresponding to the selected same true strain for all curves in a specimen set, and then combining these “average true stress-strain points” to create a new representative curve up to the average uniform elongation. These representative curves are included in Appendix C and used to compare each specimens set in the next section. One example of how to determine an average curve using this method is illustrated in Fig. 3.9. The points are average

values of the base metal specimens 1A, 1B, and 1C, and the representative curves are produced by connecting these average points.

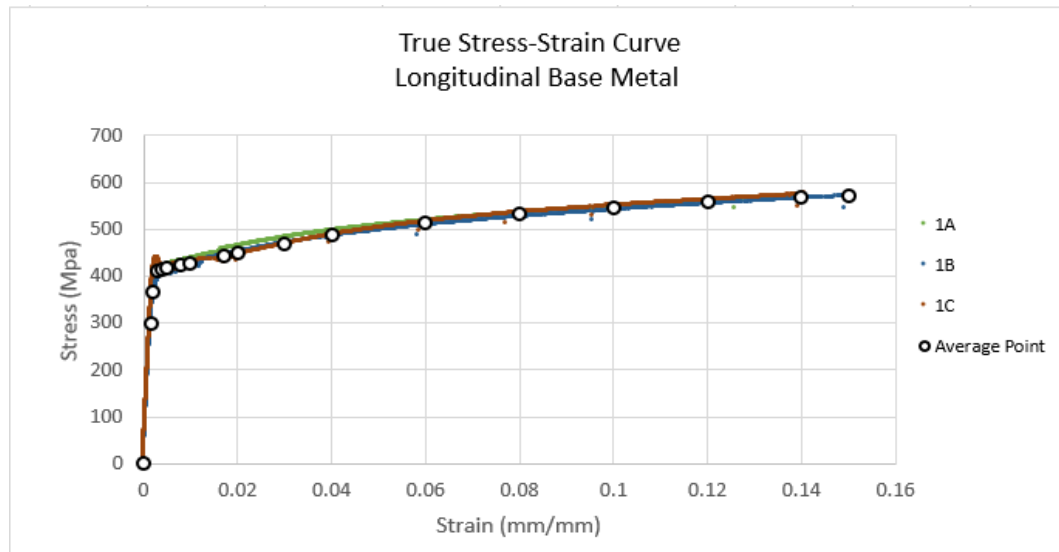


Fig. 3.9 Average points to create a representative curve of longitudinal base metal

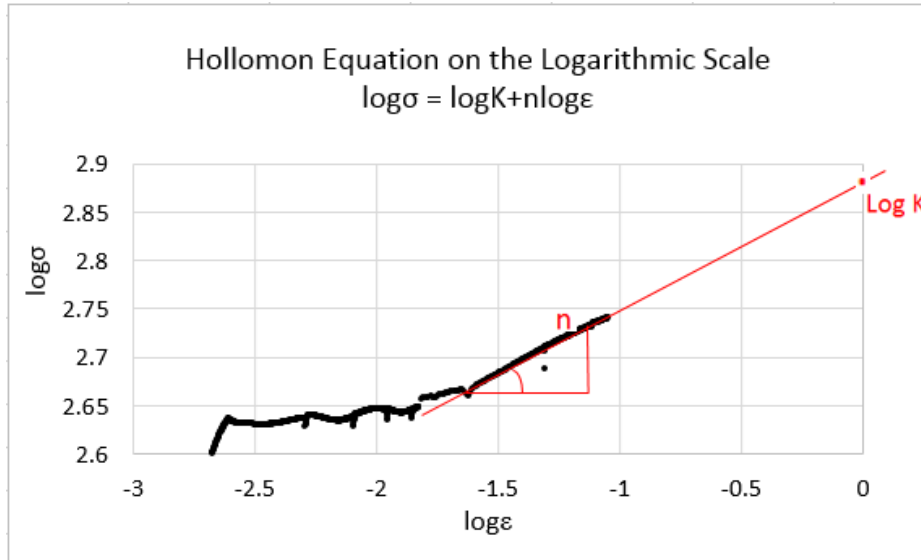
3.7.2.2 Mathematical Equations

The second method is described by using an empirical mathematical equation to model the curve in the strain-hardening region. Many equations were developed in the past. The most two well-known equations are Hollomon equation (1945) and Ramberg-Osgood equation (1943) and are used to characterize the strain-hardening phenomenon in this thesis. The Hollomon equation (1945) is a power law function of stress and strain after yielding, and is expressed by $\sigma = K\varepsilon^n$, where n is termed strain-hardening exponent and K is termed the strength coefficient. The value of n indicates the increase in strength and hardens due to the plastic deformation (ASTM E646-07). In other words, it also indicates the resistance of a material to be stretched, which means a higher value of n represents a better stretch-formability (Kleemola & Nieminen, 1974; Moosbrugger, 2002). In addition, if a Hollomon equation is valid, n is equal to the uniform strain (ε_u) (Kleemola & Nieminen, 1974). K is determined from the fit of experimental data to Hollomon equation, and is numerically equal to the value of true stress at unit true strain ($\varepsilon=1$) (Moosbrugger, 2002; ASTM E646-07). Hollomon equation is included in ASTM E646-07, and the true plastic strain (ε_p) is particularly indicated to replace true strain (ε) and the equation is shown by $\sigma = K\varepsilon_p^n$. Ramberg-Osgood equation (1943) is expressed by $\varepsilon = \frac{\sigma}{E} + K_{RO} \left(\frac{\sigma}{E}\right)^{n_{RO}}$, where σ , ε , σ_y , E , K_{RO} , n_{RO} , , represents true stress,

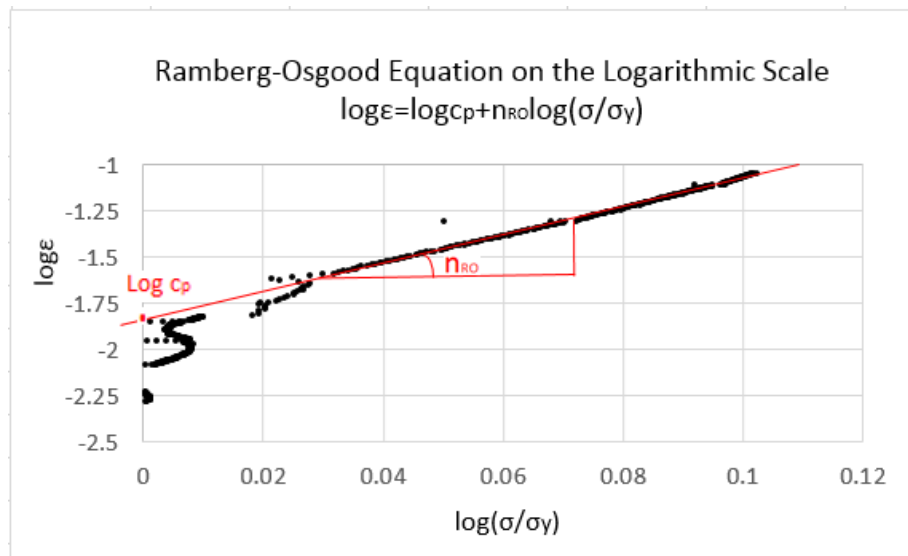
true strain, yield strength, Young's modulus, Ramberg-Osgood strength coefficient, and Ramberg-Osgood strain-hardening exponent respectively. In the equation, $\frac{\sigma}{E}$ is equal to the elastic strain (ε_e), while $K_{RO} \left(\frac{\sigma}{E}\right)^{n_{RO}}$ is equal to the plastic strain (ε_p). A new coefficient α is defined by $\alpha = K_{RO} \left(\frac{\sigma_y}{E}\right)^{n_{RO}-1}$, and therefore $\varepsilon = \frac{\sigma}{E} + \alpha \frac{\sigma_y}{E} \left(\frac{\sigma}{\sigma_y}\right)^{n_{RO}}$. By adding another coefficient $c_p = \alpha \frac{\sigma_y}{E}$, the Ramberg-Osgood equation is converted to $\varepsilon = \frac{\sigma}{E} + c_p \left(\frac{\sigma}{\sigma_y}\right)^{n_{RO}}$, then $\varepsilon_p = c_p \left(\frac{\sigma}{\sigma_y}\right)^{n_{RO}}$. c_p is determined from the fit of experimental data to Ramberg-Osgood equation and is numerically equal to the true plastic strain ε_p at the start of strain hardening ($\sigma = \sigma_y$) (Ahmed, 2010). The value of $c_p = \alpha \frac{\sigma_y}{E}$ is usually taken by the yield offset which is equivalent to 0.002 in the stress-strain curve showing the gradual yielding (Wang et al., 2011). However, this is not appropriate for the measured stress-strain curves of X52 steel pipe because most specimens showed yielding plateau and the yield strength was not determined by the 0.2% offset method. The primary advantage of above two empirical mathematical equations is to describe the stress-strain relationships by certain parameters.

In order to determine the constant parameters n and K , both sides of equations are converted into base 10 logarithmic form, and then equations are linearized (Kleemola & Nieminen, 1974; ASTM E646-07). Hollomon equation is converted to $\log \sigma = \log K + n \log \varepsilon_p$. If $\log \sigma$ versus $\log \varepsilon_p$ curve is plotted, the slope of the straight line on the curve is equal to the strain hardening exponent (n), and the extrapolated value of $\log \sigma$ at $\log \varepsilon = 0$ ($\varepsilon = 1$) is equal to $\log K$. n and K can be thus determined. Similarly, the Ramberg-Osgood equation is converted to $\log \varepsilon_p = \log c_p + n_{RO} \log \left(\frac{\sigma}{\sigma_y}\right)$. If $\log \varepsilon_p$ versus $\log \left(\frac{\sigma}{\sigma_y}\right)$ curve is plotted, the slope of the straight line on the curve is equal to n_{RO} , and the extrapolated value of $\log \varepsilon_p$ at $\log \left(\frac{\sigma}{\sigma_y}\right) = 0$ ($\sigma = \sigma_y$) is equal to $\log c_p$. n_{RO} and K_{RO} can be thus determined. For convenience, the small value of ε_e can be often neglected and thus ε_p in the above equations can be reasonably replaced by the total strain ε to plot the stress versus strain curve in logarithmical scale. Such omission is acceptable in ASTM E646-07. All experimental stress-strain data in strain-hardening region were used to seek a well-fit power curve described by Hollomon or Ramberg-

Osgood equation. An example of how to determine the important parameters in the Hollomon and Ramberg-Osgood equations on the logarithmic scale is shown in Fig. 3.10. The experimental true stress and true strain data were obtained from the testing specimen 1D.



(a)



(b)

Fig. 3.10 An example of how to determine parameters in Hollomon and Ramberg-Osgood equations (specimen 1D)

All true stress-strain curves of specimens were characterized by both Hollomon and Ramberg-Osgood equations, and strain hardening exponent n , strength coefficient K , and other related parameters are summarized in table 3.3. The yield strength used in

the Ramberg-Osgood equation was taken from the mean stress during then yield point elongation or stress by 0.2% offset. The average of each parameters is calculated and used to determine the representative power law equation of every specimen set in the strain hardening region.

Table 3.3 Assumed properties from power law equations

Power Law Equations			Hollomon $\sigma = K\varepsilon_p^n$		Ramberg-Osgood $\varepsilon = \frac{\sigma}{E} + c_p \left(\frac{\sigma}{\sigma_y}\right)^{n_{RO}} = \frac{\sigma}{E} + \alpha \frac{\sigma_y}{E} \left(\frac{\sigma}{\sigma_y}\right)^{n_{RO}} = \frac{\sigma}{E} + K_{RO} \left(\frac{\sigma}{E}\right)^{n_{RO}}$						
Orientation	Location	#	n	K	σ_{YT} (MPa)	E (GPa)	n_{RO}	c_p	α	K_{RO}	
Longitudinal	Base Metal	1A	0.106	700	417	200	9.385	0.00794	3.808	1.148E+23	
		1B	0.120	716	406	193	8.286	0.00912	4.335	1.386E+20	
		1C	0.133	747	421	205	7.692	0.13183	64.193	6.195E+19	
		Ave	0.119	721	415	199	8.454	0.01008	4.842	4.711E+20	
	New HAZ	1D	0.128	750	435	200	7.0	0.01445	6.644	6.276E+16	
		1E	0.143	771	433	207	6.727	0.19055	91.094	2.018E+17	
		1F	0.150	789	430	175	7.1	0.0166	6.756	5.598E+16	
		Ave	0.140	770	433	194	7.176	0.0167	7.482	1.772E+17	
Circumferential	Base Metal	2G	0.111	749	455	231	8.947	0.01259	6.392	2.028E+22	
		2H	0.131	777	440	223	7.36	0.01380	6.994	1.116E+18	
		2I	0.140	794	444	224	6.909	0.01660	8.375	7.838E+16	
		Ave	0.128	773	446	226	7.739	0.01433	7.261	1.226E+19	
	New Weld Metal (eliminate 2A)	2A	0.124	794	377		8.095	0.00282			
		2B	0.182	883	445	220	5.571	0.02188	10.817	2.232E+13	
		2C	0.181	868	450	210	5.538	0.02570	11.993	1.552E+13	
		Ave	0.181	876	448	215	5.555	0.02379	11.417	1.863E+13	
	Old Weld Metal (eliminate 3B)	3A	0.143	811	443	217	7.2	0.01445	7.078	3.375E+17	
		3B	0.176	945	475	200	6.0	0.01905	8.021	1.061E+14	
	New HAZ (eliminate 2E)	2D	0.145	826	470	217	6.909	0.01995	9.211	5.105E+16	
		2E	0.030	594	517	173	28.333	0.01122	3.754	3.786E+69	
		2F	0.128	776	470	220	8.7	0.01698	7.948	2.896E+21	
		Ave	0.137	801	470	203	7.8	0.01847	7.977	6.646E+18	
	Old HAZ (eliminate 3D)	3C	0.153	804	455	223	6.6	0.02399	11.758	1.368E+16	
		3D	0.180	968	480	207	5.6	0.02089	9.009	1.187E+13	

Both equations described the nonlinear relationship between the true stress and true strain in the hardening range very well. In the Hollomon equation, it is noted that each measured strain hardening exponent (n) is not equal to the uniform strain (ε_u) measured directly from the test. This difference is normal because the empirical equations cannot accurately describe the stress-strain curve, they are just a good fit to the experimental

data (Kleemola & Nieminen, 1974). In addition, the neglected elastic strain in the equation and individual measurement difference may also result in the difference between n and ϵ_u . In the Ramberg-Osgood equation, all values of $c_p = \alpha \frac{\sigma_y}{E}$ are higher than 0.002. This is because the specimens showed yielding plateau, and the yield strength was determined by the mean stress during the yield point elongation, rather than the 0.2% offset method.

3.7.2.3 Comparison of the Representative Curves

A typical comparison of the average curve, the Hollomon power curve, the Ramberg-Osgood power curve and the quasi-static curve for the longitudinal base metal specimens sets starting from 400Mpa stress is illustrated in Fig. 3.11. The average true stress-strain curve of three test specimens 1A, 1B, and 1C matches the Hollomon power curve with $n = 0.119$ and $K = 721$ and the Ramberg-Osgood power curve with $n_{RO} = 8.454$ and $c_p = 0.01008$ well in the strain hardening region after a true strain of 0.016. The actual test curve points are higher than the quasi-static curve points because of the dynamic loading rate effect. The actual test stress is about 1% higher than the quasi-static stress up to yielding (loading rate is 0.1mm/min), and is about 5% higher in the strain hardening region (loading rate is 1.5mm/min). As the difference is small, the actual test stress-strain curve can be reasonably used to characterize and compare the specimens.

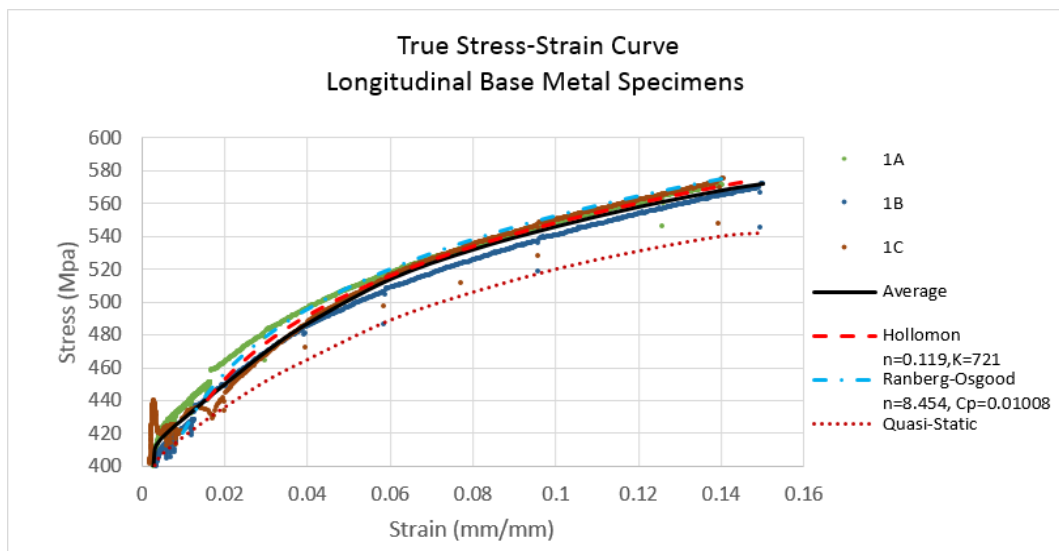


Fig. 3.11 Comparison of average curve, two power curves, and quasi-static curve of longitudinal base metal

The figures that describe the true stress-strain curves for all 7 specimen sets starting from 0 or 400Mpa stress are compared and included in Appendix C. A brief classification of these specimen sets and the descriptions of their true stress-strain curves are summarized below.

(1) Base metal specimens sets (Appendix C.1)

- (a) Longitudinal base metal: The average curve develops linearly with a slope of E which is equal to 199 GPa, then yields at 411Mpa by 0.2% offset and yields at 418 MPa at a true strain of 0.005, and lastly reaches to the ultimate true tensile strength of 573 MPa at a true uniform strain of 0.015. It matches the Hollomon power curve with $n = 0.119$ and $K = 721$ and the Ramberg-Osgood power curve with $n_{RO} = 8.454$ and $c_p = 0.01008$ well in the strain hardening region after a true strain of 0.016.
- (b) Circumferential base metal: The average curve develops linearly with a slope of E which is equal to 226 GPa, then discontinuously yields at a mean stress of 446 MPa during the yield point elongation ranging from 0.002 to 0.014 true strain, and lastly reaches to the ultimate true tensile strength of 579 MPa at a true uniform strain of 0.11. It matches the Hollomon power curve with $n = 0.128$ and $K = 773$ and the Ramberg-Osgood power curve with $n_{RO} = 7.739$ and $c_p = 0.01433$ well in the strain hardening region after a true strain of 0.014.

(2) Weld metal specimens sets (Appendix C.2)

- (a) Circumferential new weld metal: The average curve develops linearly with a slope of E which is equal to 215 GPa, then discontinuously yields at a mean stress of 448 MPa during the yield point elongation ranging from 0.0023 to 0.034 true strain, and lastly reaches to the ultimate true tensile strength of 607 MPa at a true uniform strain of 0.14. It matches the Hollomon power curve with $n = 0.181$ and $K = 876$ and the Ramberg-Osgood power curve with $n_{RO} = 5.555$ and $c_p = 0.02379$ well in strain hardening region after a true strain of 0.04.
- (b) Circumferential old weld metal: The average curve develops linearly with a slope of E which is equal to 217 GPa, then discontinuously yields at a mean stress of 443 MPa during the yield point elongation ranging from 0.002 to 0.016 true strain, and lastly reaches to the ultimate true tensile strength of 561 MPa at a true uniform strain of 0.075. It matches the Hollomon power curve with $n =$

0.143 and $K = 811$ and the Ramberg-Osgood power curve with $n_{RO} = 7.2$ and $c_p = 0.01445$ well in the strain hardening region after a true strain of 0.016.

(3) HAZ specimens sets (Appendix C.3)

(a) Longitudinal new HAZ: The average curve develops linearly with a slope of E which is equal to 194 GPa, then discontinuously yields at a mean stress of 433 MPa during the yield point elongation ranging from 0.0025 to 0.015 true strain, and lastly reaches to the ultimate true tensile strength of 554 MPa at a true uniform strain of 0.1. It matches the Hollomon power curve with $n = 0.14$ and $K = 770$ and the Ramberg-Osgood power curve with $n_{RO} = 7.176$ and $c_p = 0.0167$ well in the strain hardening region after a true strain of 0.018.

(b) Circumferential new HAZ: The average curve develops linearly with a slope of E which is equal to 203 GPa, then discontinuously yields at a mean stress of 470 MPa during the yield point elongation ranging from 0.0023 to 0.025 true strain, and lastly reaches to the ultimate true tensile strength of 595 MPa at a true uniform strain of 0.075. It matches the Hollomon power curve with $n = 0.137$ and $K = 801$ and the Ramberg-Osgood power curve with $n_{RO} = 7.8$ and $c_p = 0.01847$ well in the strain hardening region after a true strain of 0.036.

(c) Circumferential old HAZ: The average curve develops linearly with a slope of E which is equal to 223 GPa, then discontinuously yields at a mean stress of 455 MPa during the yield point elongation ranging from 0.0022 to 0.033 true strain, and lastly reaches to the ultimate true tensile strength of 585 MPa at a true uniform strain of 0.125. It matches the Hollomon power curve with $n = 0.153$ and $K = 804$ and the Ramberg-Osgood power curve with $n_{RO} = 5.6$ and $c_p = 0.02089$ well in the strain hardening region after a true strain of 0.04.

3.7.3 Comparison between the Curves

The representative curves obtained in the last section are used to summarize the difference between the tensile true stress-strain curves of the various locations of the X52 pipe (base metal, weld metal, and HAZ), the two orientations (longitudinal and circumferential), and the two girth weld conditions (new and old).

(1) Base Metal vs. Weld Metal vs. HAZ

In the longitudinal direction, the HAZ around the new and old girth weld both have higher yield strength but less ductility than the base metal. The base metal has very good ductility shown by 10% higher fracture strain and 5% higher uniform strain compared to the HAZ. In addition, large difference is found in the yielding region. Base metal showed gradual yielding while the HAZ showed yielding plateau. (Table 3.1 and Fig. 3.12). In the circumferential direction, the girth weld and its HAZ have higher yield strength than the base metal (Fig. 3.13). One old girth weld specimen has lower yield strength than the base metal (Fig. 3.14), while another one has a higher yield strength than the base metal (Table 3.1). In general, the girth weld metal and its HAZ are stronger than the base metal in both directions, but the old girth weld is an exception because of the great variation of the measurement. This shows the great difference between the field girth weld manufactured in 1980s and the new girth weld manufacture in 2013. The new girth weld was machined in the machine shop in a well-controlled environment. The base metal has an obvious higher ductility in the longitudinal direction, but slightly lower ductility in the circumferential direction than the weld metal and HAZ. The axial stiffness measured by Young's modulus does not show a direct relationship with the different locations.

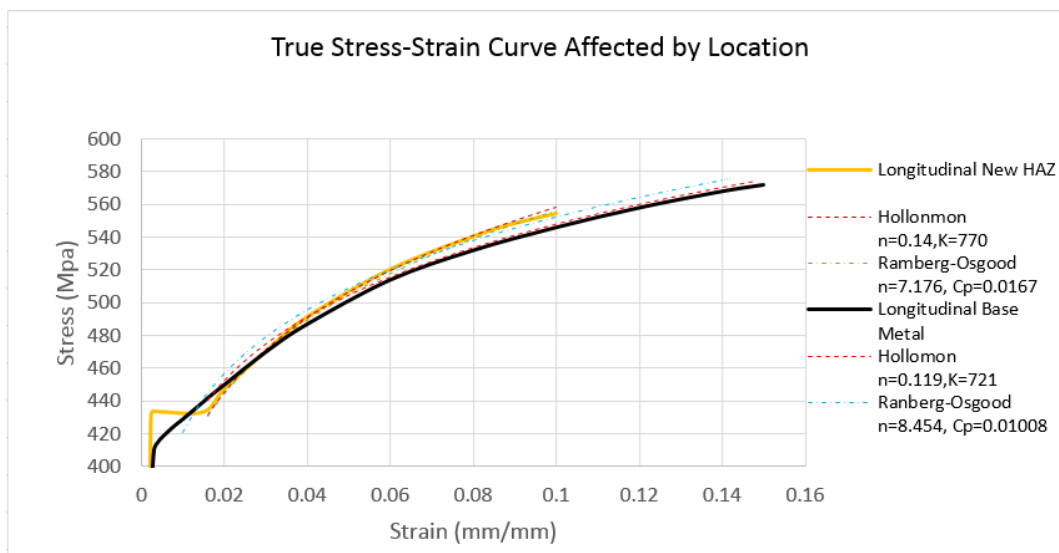


Fig. 3.12 Comparison of the longitudinal new HAZ and base metal

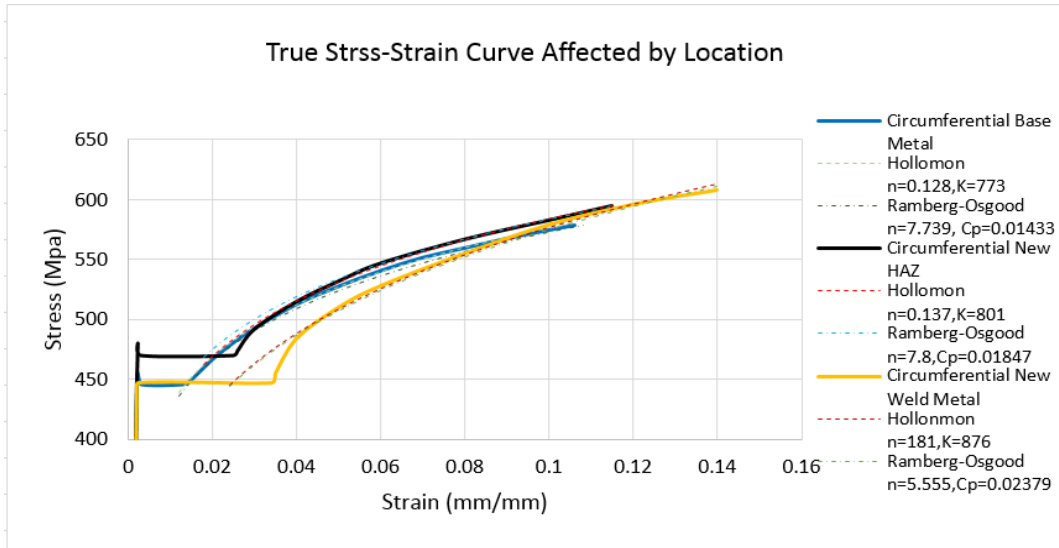


Fig. 3.13 Comparison of the circumferential new weld, HAZ and base metal

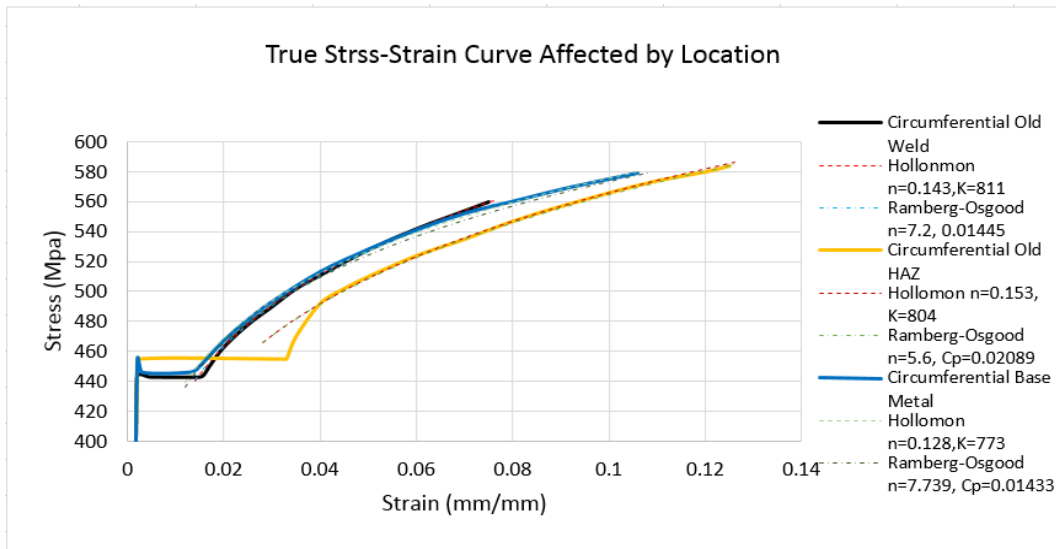


Fig. 3.14 Comparison of the circumferential old weld, HAZ and base metal

(2) New vs. Old Girth Weld

New and old girth weld exhibits similar strength and ductility in both direction, same as their HAZ (Table 3.1). However, two old weld metal specimens have great variation of measurement, same as two old HAZ. The curves of the old weld metal and the old HAZ in Fig. 3.15 and 3.16 were conservatively taken from the lower resistance measured from the two specimens of each set. Obviously, the old field girth weld manufactured in 1980s was quite different compared to the new girth weld manufactured in 2013. The new girth weld was manufactured in the machine shop in a

well-controlled environment.

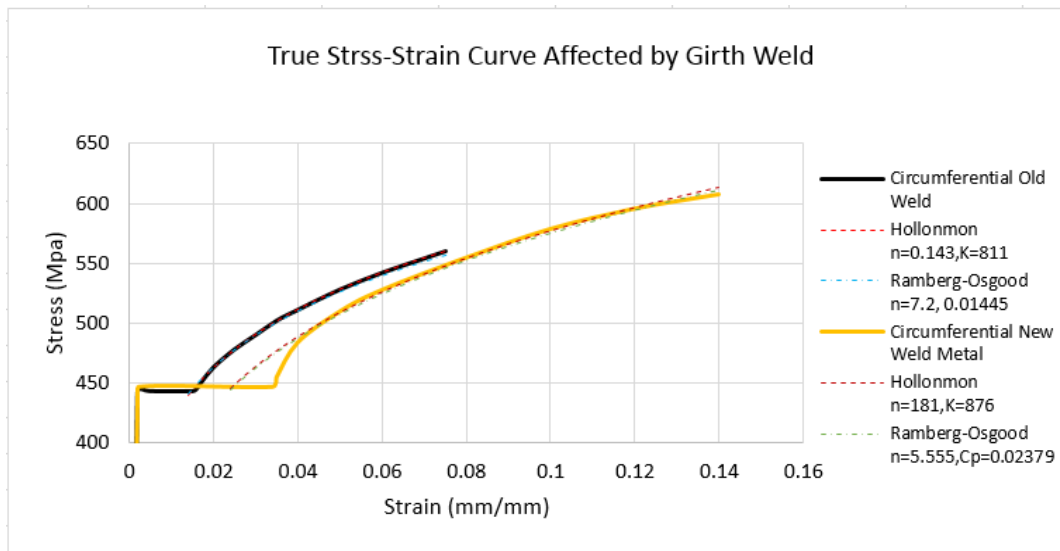


Fig. 3.15 Comparison of the circumferential new and old girth weld metal

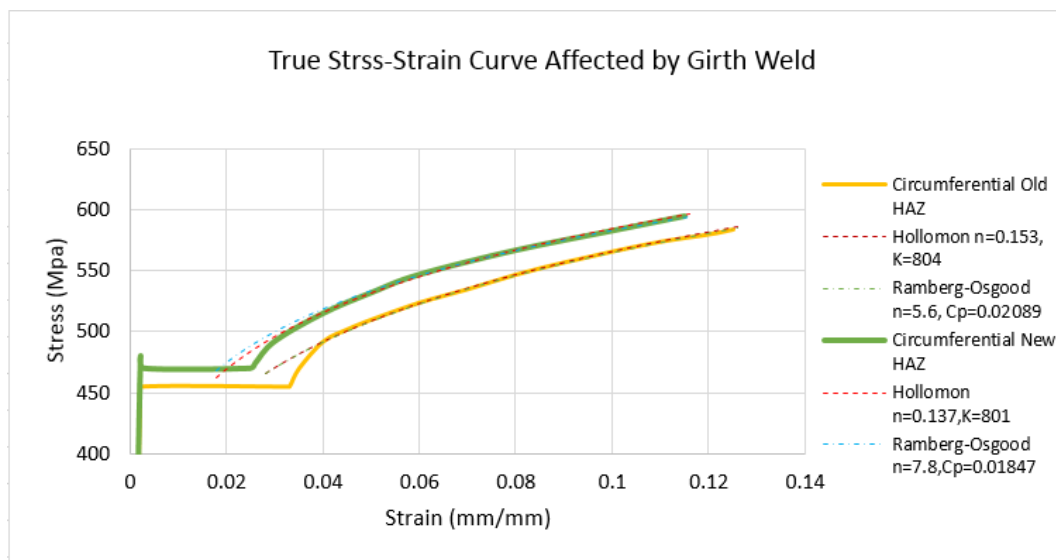


Fig. 3.16 Comparison of the circumferential new and old HAZ

(3) Longitudinal vs. Circumferential Direction

The specimens from both the base metal and the HAZ in the circumferential direction are stronger and stiffer than those in the longitudinal direction. The base metal specimens are much more ductile in longitudinal direction, while the HAZ specimens are similar in ductility in both directions (Fig. 3.17 and 3.18, table 3.1). Apparently, the tensile strength, axial stiffness and ductility varies in various direction. The strength and stiffness are better in the circumferential direction, but the ductility is better in

longitudinal direction. In addition, the base metal shows gradual yielding in the longitudinal direction, while it shows a well-defined yield point followed by yielding plateau in the circumferential direction.

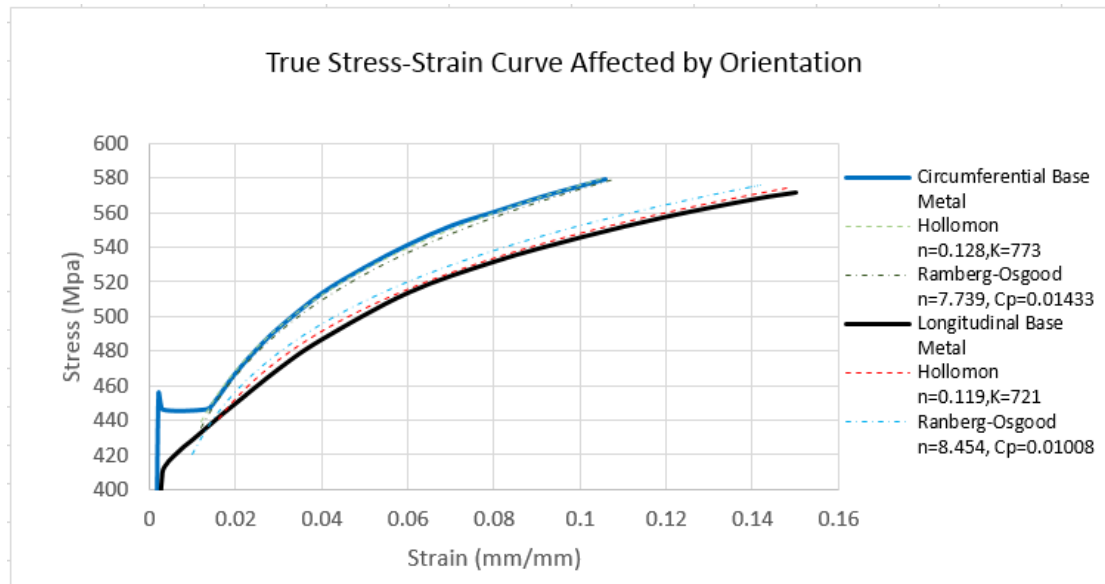


Fig. 3.17 Comparison of the longitudinal and circumferential base metal

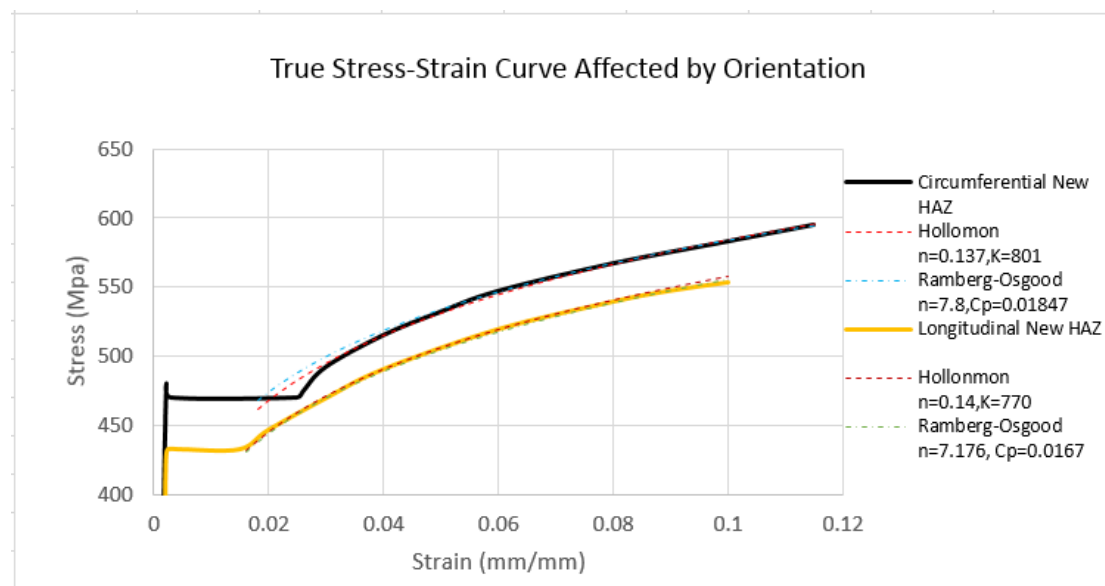


Fig. 3.18 Comparison of the longitudinal and circumferential new HAZ

3.8 Conclusion of Tests

A comprehensive and rigorous investigation for the material properties of research X52 pipe has been done by performing a series of tension tests, and five important significant discoveries are summarized. First of all, by testing specimens machined from different location of the pipe, it is shown that the girth weld and its ambient HAZ are stronger than the base pipe. The results also show that the base metal exhibits higher ductility in the longitudinal direction but slightly lower ductility in the circumferential direction compared to the girth weld and HAZ. However, the axial toughness measured by Young's modulus is not affected much by locations. Secondly, by testing specimens machined from the longitudinal and circumferential directions of the pipe, the anisotropic behavior is shown by the difference of the stress-strain curves. The yield strength, tensile strength and Young's modulus are all higher in the circumferential direction, while the ductility determined from uniform strain is similar in both directions. The ductility measured by elongation and reduction of cross sectional area for both directions cannot be compared because the test specimens have different dimensions and gauge length. In addition, the pipe base shows gradual yielding in the longitudinal direction of the pipe, while it shows a well-defined yield point followed by the yielding plateau in the circumferential direction of the pipe. The anisotropic behaviors have great influence on compressive strain capacity and buckling response. Thirdly, by testing specimens machined from the old girth weld manufactured in 1980s and new girth weld manufactured in 2013, the great differences between them were discovered. The field girth weld has less strength than the new weld, and a great difference in strength and ductility were measured from the two old weld metal specimens and two old HAZ specimens. Due to the fact that the pipe obtained from Enbridge Pipeline Inc. has only one original girth weld, it was not possible to manufacture more specimens from more field girth welds to accurately determine their mechanical properties. Fourthly, by taking regular stoppages during the tension test, the quasi-static strength is determined. The obtained tensile strength properties from the test are higher than the recorded quasi-static strength because of the loading rate effect. The lower the loading rate is applied on the specimen, the more accurate the static properties of the material. Since a very low loading rate is set for the whole tests, the differences between the actual test results and the quasi-static curve are well controlled below 6%. Lastly, by modelling simpler representative stress-strain curves to conclude

the large amount of experimental stress-strain data, the comparison of the test results of different specimen sets become much easier. The average method and the two power-law equation methods (Hollomon and Ramberg-Osgood) are used, and the latter two successfully characterize the curves for the strain hardening region into mathematical expressions.

The most important tensile properties of X52 pipe obtained in the tension test are summarized in table 3.4 and 3.5. The values of properties in the tables are the average of the test data. The tables also include the results of empirical characterization of strain-hardening regions determined in the tests. It is noted that the tensile properties are determined from two types of test specimens whose shape and size are significantly different, and specimens are machined from the various location and orientation of the pipe. All the above variables contribute to different values of the tensile properties. As a result, it is conservative to take the average test results obtained from rectangular specimens machined from the base metal in the longitudinal direction of the pipe as the final values of the tensile properties of Enbridge Norman Well X52 pipes in this research. The Young's modulus (E) is about 200 GPa, the yield strength (σ_{YT}) is about 410 MPa, the tensile strength (σ_{TS}) is about 570 MPa at the uniform strain (ϵ_u) of 14%. The elongation is about 35% based on 50mm gauge length, and the reduction of cross sectional area is about 68%. The strain hardening region characterized by the Hollomon relation has the strain hardening exponent (n) about 0.12 and the strength coefficient (K) about 720. The strain hardening region characterized by the Ramberg-Osgood relation has the strain hardening exponent (n_{RO}) about 8.45, strength coefficient (K_{RO}) about 4.71×10^{20} , and another coefficient (α) about 4.84.

Table 3.4 Tensile properties of X52 pipe (longitudinal direction)

Sets of Rectangular Specimens	Young's Modulus (GPa)	Promotional Limit (MPa)	Yield Strength (MPa)		Tensile Strength MPa			Uniform Strain	Elongation (Gauge Length 50mpamm)	Reduction of Area	Strain-hardening Region (Empirical Characterization)					
			Test (loading rate 0.1mm/min)	Quasi-Static	Test (loading rate 1.5mm/min)	Quasi-Static	Hollomon $\sigma = K\varepsilon_P^n$				Ramberg-Osgood $\varepsilon = \frac{\sigma}{E} + c_p \left(\frac{\sigma}{\sigma_y}\right)^{n_{RO}} = \frac{\sigma}{E} + \alpha \frac{\sigma_y}{E} \left(\frac{\sigma}{\sigma_y}\right)^{n_{RO}} = \frac{\sigma}{E} + K_{RO} \left(\frac{\sigma}{E}\right)^{n_{RO}}$					
							True				True	Eng	True	True	True	n
Base Metal	199	299	411		501	573	542	14.4%	35.1%	67.7%	0.119	721	8.454	0.0100	4.842	4.71E+20
New HAZ	194	320	428	423	502	554	529	9.8%	25.2%	64.2%	0.140	770	7.176	0.0167	7.482	1.77E+17
Old HAZ	205		428		509				24.3%							

Table 3.5 Tensile properties of X52 pipe (circumferential direction)

Sets of Round Specimens	Young's Modulus (GPa)	Promotional Limit MPa	Yield Strength MPa		Tensile Strength MPa			Uniform Strain	Elongation (Gauge Length 10mm)	Reduction of Area	Strain-hardening Region (Empirical Characterization)					
			Test (loading rate 0.1mm/min)	Quasi-Static	Test (loading rate 0.1mm/min)	Quasi-Static	Hollomon $\sigma = K\varepsilon_P^n$				Ramberg-Osgood $\varepsilon = \frac{\sigma}{E} + c_p \left(\frac{\sigma}{\sigma_y}\right)^{n_{RO}} = \frac{\sigma}{E} + \alpha \frac{\sigma_y}{E} \left(\frac{\sigma}{\sigma_y}\right)^{n_{RO}} = \frac{\sigma}{E} + K_{RO} \left(\frac{\sigma}{E}\right)^{n_{RO}}$					
							True				True	Eng	True	True	True	n
Base Metal	226	407	437		520	579		10.6%	27.9%	78.4%	0.128	773	7.739	0.0143	7.26	1.22E+19
New HAZ	203	433	462	450	530	595	551	11.9%		79.8%	0.137	801	7.8	0.0185	7.98	6.65E+18
Old HAZ	223	445	446	424	515	584	552	12.5%		81.8%	0.153	804	6.6	0.024	11.76	1.37E+16
New Weld Metal	215	435	428	419	531	607	586	13.9%	29.5%	86.5%	0.181	876	5.555	0.0238	11.42	1.86E+13
Old Weld Metal	217	405	438	418	518	561	522	7.5%		85.6%	0.143	811	7.2	0.0145	7.08	3.36E+17

3.9 Variability of Test Results

Even though all the tests were carefully conducted, the obtained stress-strain curves for the X52 pipe differed from each other even in the same specimen set under the same design and conditions. The magnitude and shape of the curves are affected by many variables, which are caused by the materials, methodology, equipment, ambient conditions, and other human factors (Davis, 2004). To be more specific, each particular test specimen may result in various material properties. The specimens may have different design (rectangular or round shape), may be machined from various locations (base or weld or HAZ) and orientation (longitudinal or circumferential direction), may have any unknown prior plastic deformation or heat treatment, and may exhibit actual material inhomogeneities that affect the results of the test. The different methodologies used in the test also affect the results, such as the gripping method (wedge or threaded grips), and the speed of loading. The appropriate grips guarantee the specimen are stably mounted, without failing or slipping when resisting the ultimate tensile force in the test. The lower speed of the loading reduces the loading rate effect, and increases the accuracy to obtain the static material properties. The accuracy and sensitivity of the test equipment such as the loading machine and the extensometer play an important role in achieving the correct results. The loading machine should be calibrated prior to the test to ensure the load and displacement measuring apparatus start from zero to reduce the error of the magnitude of the stress and the strain. All of the axis of the loading frame, MTS fixtures grip and the specimen should be coincident to reduce the incorrect measurement induced by the off-center force which might generate the bending moments and additional bending stresses. In addition, the ambient conditions in the laboratory are critical to the test result consistency. The difference of the test temperature, or any external interference like noise disturbance could lead to inconsistent test results. Lastly, human factors should be considered. The individual doing the test varies in their experience, judgment, and measurement difference. All above possible variables are considered in the analysis of the obtained test results in this research, and they contribute to explaining some of the variability of the test data. However, with all these sources of variability and except for the old girth weld specimens, the samples of each specimen set exhibited the same behavior strengthening the conclusions of this work.

4. Charpy V-notch Impact Test

The Charpy V-notch impact (CVN) test is selected in this research to understand the fracture behavior of Enbridge Norman Well X52 pipelines along with their girth weld. A series of sub-size Charpy V-notch specimens were designed to accommodate the small thickness of the pipe, machined from the base metal, girth weld, and heat-affected zone (HAZ) of the pipe, and tested by a pendulum-testing machine at the University of Alberta. The obtained CVN energy indicates the resistance of the material against fracture by impact loading. This chapter discusses the experimental setup and the results of CVN test and the empirical correlation between the experimental CVN energy values and the fracture toughness values.

4.1 Introduction to CVN Test

The Charpy impact test was named after George Charpy and developed in 1901, before the formal fracture mechanics theory was introduced (Anderson, 2005). In comparison with formal fracture toughness tests which require precracking and more sophisticated instrumentation to monitor crack extension, the Charpy impact test is considered as a convenient and economical test to provide a comparative rather than direct fracture toughness result. In accordance with ASTM Standard E23-07, a dynamic high loading rate pendulum-testing machine is used to measure the energy to fracture of a small notched bar specimen, and to indicate the resistance of the material against fracture. Due to its easiness and cheapness to perform and obtain qualitative results of the fracture energy, the CVN impact test is commonly utilized as a quality control method to measure the toughness, and determine the ductility of the material which can be observed by its fracture appearance.

Test temperature plays a significant role in determining the CVN energy, ductility and impact toughness. By cooling or heating specimens into various temperatures, the obtained CVN energy or CVN impact toughness versus temperature can be plotted. The curve is divided by the lower shelf region, the transition region, and the upper shelf region (Barsom & Rolfe, 1999). A material has more ductility and impact toughness as the temperature increases, while it has less ductility and impact toughness as the temperature decreases. A shifting point from brittle to ductile behavior is called the

“ductile to brittle transition temperature” (DBTT), which is an important indication in determining the suitable service temperature and selecting the appropriate material. DBTT is also called “fracture appearance transition temperature (FATT)” where the percentage of brittle fracture is equal to the percentage of ductile fracture (Udomphol ,n.d.). DBTT can be determined by the temperature that corresponds to the average value of the lower shelf energy and the upper shelf energy. The temperature that corresponds to the upper shelf energy and 100% ductility fracture is called “fracture transition plastic (FTP)”, while the temperature corresponds to the lower shelf energy and 100% brittle fracture is called “nil-ductility temperature (NDT)”. A typical CVN impact energy and cleavage (brittle) fracture versus temperature curve is shown in Fig. 4.1, where three energy regions and important transition temperature DBTT, FTP, and NDT are marked. API Spec 5L (2012) provides the basic requirement of CVN energy on pipelines to avoid unstable brittle fracture. The minimum average (of a set of three specimens) CVN absorbed energy shall be more than 20 ft-lb (27 Joules) and the percentage of shear fracture shall be more than 85% (or the percentage of cleavage fracture shall be less than 15%). These values are obtained based on the standard CVN specimens machined from the base metal, weld metal or HAZ on a pipe whose grade is smaller than X60 and outside diameter is less than 508mm at a test temperature lower than 0 °C. The temperature that corresponds to 20ft-lb or 85% shear fracture should be higher than the DBTT.

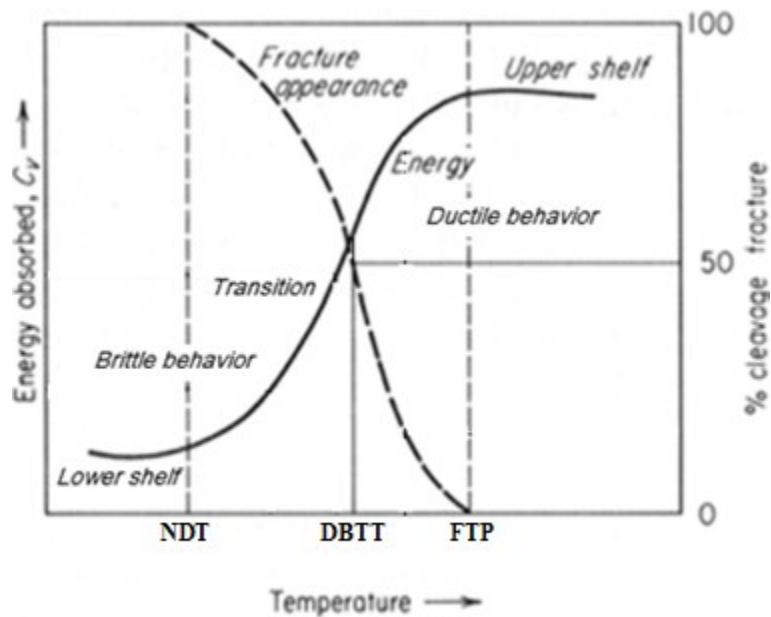


Fig. 4.1 Charpy impact energy and cleavage fracture versus temperature curve (Adapted from Udomphol ,n.d., pp.7)

4.2 Objective

A series of Charpy V-notch impact tests were conducted to determine the impact toughness and estimate the fracture toughness of the provided X52 material at a specific temperature. The main objectives of analyzing the results of the tests are summarized as follow:

- (1) To measure the CVN energy values and fracture appearance of sub-size CVN specimens at room temperature and lower temperature to determine impact toughness and ductility
- (2) To convert CVN energy values of the experimental sub-size specimens to that of the standard full-size specimens and compare the energy difference affected by the location that the notch is machined from: base metal, new weld metal, new HAZ, old weld metal, Old HAZ
- (3) To correlate CVN energy values with the toughness parameters, such as plane strain fracture toughness characterized by the stress intensity factor (K_{Ic}), J -integral (J_{Ic}) or critical crack-tip opening displacement (δ_{Ic})
- (4) To understand the difference between CVN impact test and fracture toughness test in determining fracture toughness of the material
- (5) To investigate tensile strain capacity of pipelines with a selected defect according to CSA Z662-11

4.3 Test Specimens and Test Temperature

In accordance with ASTM A370-12a and E23-07, the design of a typical subsize Charpy V-notch impact test specimen is shown in Figure 4.2. All CVN specimens had constant overall length of 55 mm, depth of 10 mm, and a standard centered v-notch with depth of 2 mm, angle of 45° and radius of 0.25 mm. However, the width of each specimen varies due to the manufacturing requirements. 6 specimens were manufactured with a width of 5.3 mm, 6 specimens were manufactured with a width of 5.7 mm, and the rest 12 specimens were manufactured with a width of 5.0 mm. The correct notch tip radius was carefully machined to ensure consistent results.

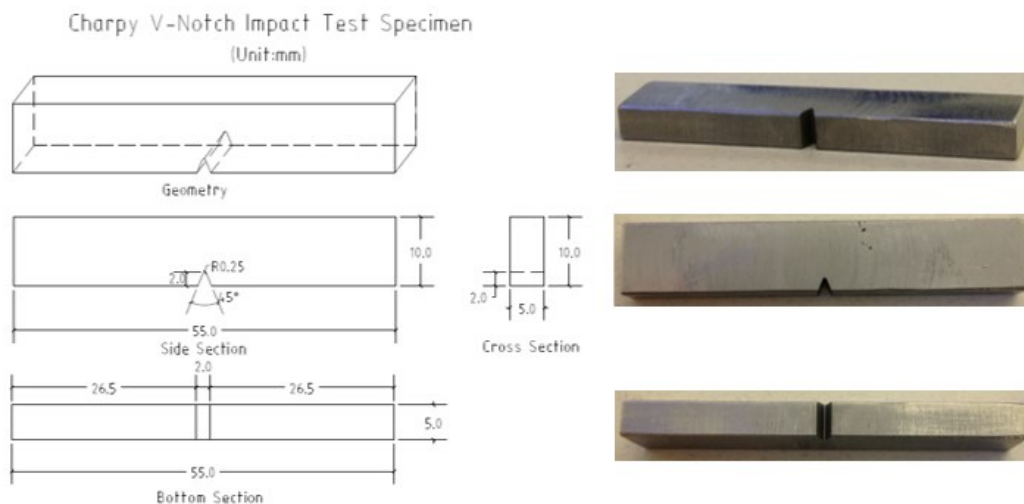


Fig. 4.2 Design and photos of a subsize Charpy V-notch impact test specimen

It is recommended to test specimens at various specific temperature to plot CVN impact toughness versus temperature curve, and determine the ductile-brittle transition of a material (Fig.4.1). However, in the absence of the large numbers of available test specimens in this research, only the room temperature of about 22 Celsius degree (°C) and a lower temperature of about -21 Celsius degree (°C) were selected to test the specimens. The difference of the results from the two selected temperature contributes to the understanding of the temperature effect on the Charpy impact toughness. Overall 13 specimens that were machined from the base metal, weld metal, or HAZ were tested at room temperature. Out of those, 10 specimens were tested at 22°C, and 3 specimens were tested at 19°C because of a different test day. Overall 11 specimens were cooled to a lower temperature and tested. Out of those, 7 specimens were cooled in a freezer to -21°C, and 3 specimens were cooled to -29°C. It is noted that one specimen was particularly cooled by dry ice to -78°C, which was achieved by surrounding the

specimen by a quantity of dry ice as the solid form of carbon dioxide. -78°C was expected as an approximate temperature at which brittle fracture of the research X52 material would be observed, and it was supported by the result of this specimen showing a 5% shear fracture appearance. The number of test Charpy V-notch test specimens and their notch locations are summarized in Table 4.1 and illustrated in Fig 3.4.

Table 4.1 Numbers of Charpy V-notch impact test specimens

Notch Location \ Specimens	Specimens at the Room Temperature	Specimens at a Lower Temperature
New weld metal	2 (22°C)	2 (-21°C)
New HAZ	2 (22°C)	2 (-21°C)
Old weld metal	3 (22°C)	1 (-21°C); 1 (-78°C)
Old HAZ	3 (22°C)	2 (-21°C)
Base metal	3 (19°C)	3 (-29°C)
Total	13	11

4.4 Test Methodology

4.4.1 Test Methodology and Test Machine

In accordance with standard ASTM E 23-07, a CVN specimen with a standardized and machined notch is struck and broken by a single impact blow from a freely swinging heavy pendulum. The test specimen, V-notched in the center, is placed on two supports at the bottom of the test machine, and is considered as a simple notched beam impacted in three-point bending. The principle of this specially designed Charpy testing machine is generally summarized below and illustrated in Fig 4.3: the heavy pendulum (hammer) is concentrically released from a fixed height (h_1) and has sufficient energy to break the CVN specimen and swings to a height (h_2). The weight of the pendulum times the difference in height before and after impact ($mgh_1 - mgh_2$) is equal to the absorbed energy by the specimen (NDT Resource Centre). The value of the energy is directly recorded on the scale. The absorbed energy (in foot-pounds or Joules) is an indication of the material resistance to fracture under impact loading.



(a)



(b)



(c)

Fig. 4. 3 Charpy impact test machine (a) pendulum device; (b) Charpy energy scale (in foot-pounds); (c) simple beam impacted in three-point bending

4.4.2 Measurement of Ductility

In addition to the absorbed energy, the measurement of the percentage of shear fracture and lateral expansion on the fracture surfaces are required to determine the ductility of the material, according to the methods provided in ASTM E 23-07.

4.4.2.1 Percentage of Shear Fracture

The relative amount of shear fracture to brittle fracture on the fracture surfaces is observed and estimated following the guidance provided in the ASTM E23-07. A typical fracture appearance is illustrated in Fig. 4.4, and displays a clear separation of the inner flat fracture area and the outer shear-lip fracture areas. The bright and granular flat fracture area is formed by brittle fast and unstable crack propagation (cleavage). The outer rough shear fracture areas including fracture initiation, two shear lips and the final fracture are formed by ductile slow and stable crack growth. The percentage of shear fracture is calculated as the ratio of the shear ductile fracture areas to the total fracture areas and can be determined based on the guide charts provided in ASTM E 23-07.

4.4.2.2 Lateral Expansion

Lateral expansion also indicates the relative amount of ductile shear fracture during fracture. It is described as the expansion of width of the broken specimen over that of original unbroken specimen. A brittle fracture is not associated with a noticeable increase in width, while a ductile shear fracture is associated with a significant increase in width due to the tearing at two sides (shear lips). The lateral expansion is calculated as the sum of the maximum width expansions on both sides of both half broken specimens. For example, it is the sum of A_1 and A_4 if A_1 is greater than A_2 , and A_4 is greater than A_3 (Fig. 4.4).

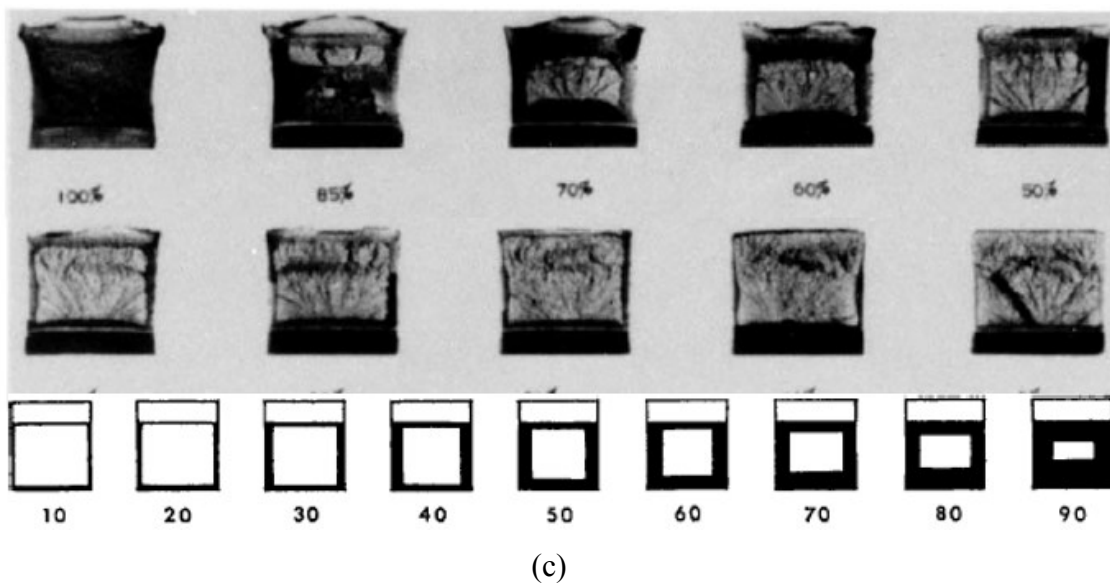
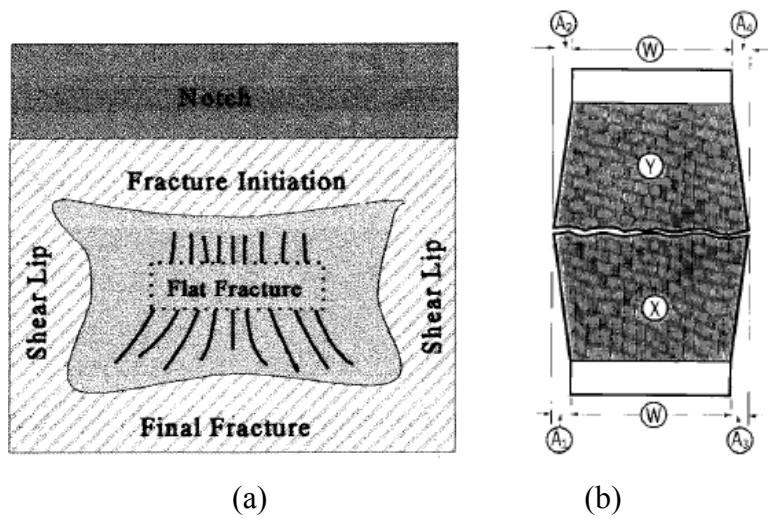


Fig. 4.4 Examples of fracture appearance (a) typical fracture appearance; (b) lateral expansion of two half broken specimens; (c) percentage of shear fracture guide charts (From AMTM E23-07, p.7,9,24)

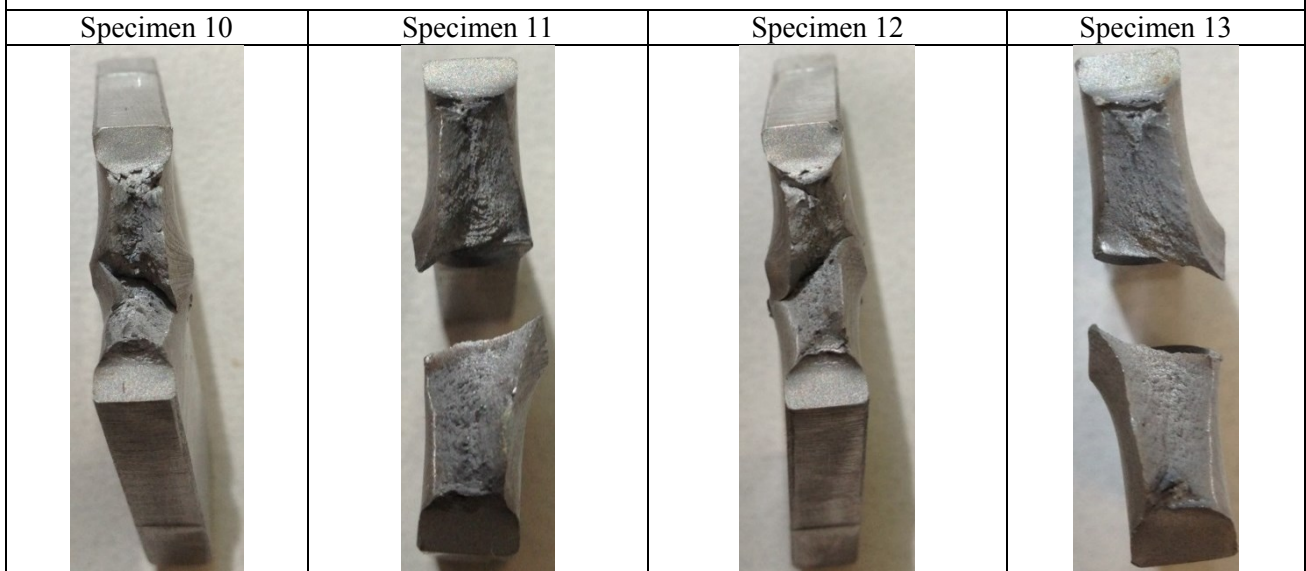
4.5 Test Results and Analysis

The total 24 CVN specimens were machined and tested at room temperature or a lower temperature below -21°C. A set of two or three specimens were tested for each notch location, including the base metal, weld metal and HAZ. Specimens 1-9 and A-C were machined and tested by Qualimet Inc., while other specimens were machined by Rejent Tool and Manufacturing Co. Ltd, and tested at the University of Albert. The resultant CVN impact energy values and fracture appearance measurement are all summarized in Table 4.2 and Table 4.3. In order to compare each subsize specimen with the constant thickness of 10mm but various width ranging from 5.0 mm to 5.7 mm, their measured actual values of energy were converted to their corresponding values of energy for a standard full size specimen with constant thickness of 10 mm and constant width of 10 mm. The converted “full size impact energy” is approximately calculated by the “actual impact energy” multiplied the ratio of the width of the full-size specimen to the width of the sub-size specimen (API 579-1, 2007).

Table 4.2 Results obtained from CVN impact tests at room temperature

Specimen Set	Specimen #	Specimen Width (mm)	Test Temperature (°C)	Actual Impact Energy (ft-lb) (size: width×10mm)	Full Size Impact Energy (ft-lb) (size: 10mm×10mm)	Fracture Appearance	
						Percent Shear Fracture	Lateral Expansion (mm)
Base Metal	1	5.3	19	64	121 (164 J)	100%	2.2
	2	5.3	19	67	126 (171 J)	100%	2.4
	3	5.3	19	64	121 (164 J)	100%	2.3
	Average	5.3	19	65	123 (167 J)	100%	2.3
Old Weld Metal	4	5.7	22	42	74 (100 J)	100%	1.8
	5	5.7	22	33	58 (79 J)	100%	1.4
	6	5.7	22	43	75 (102 J)	100%	1.5
	Average	5.7	22	39	69 (94 J)	100%	1.6
Old HAZ	7	5.7	22	94	165 (224 J)	Did not break	
	8	5.7	22	73	128 (174 J)	Did not break	
	9	5.7	22	87	153 (207 J)	Did not break	
	Average	5.7	22	85	149 (202 J)	Did not break	
New Weld Metal	10	5.0	22	71	142 (193 J)	Did not break	
	11	5.0	22	61	122 (165 J)	100%	2.2
	Average	5.0	22	66	132 (179 J)		
New HAZ	12	5.0	22	84	168 (228 J)	Did not break	
	13	5.0	22	78	156 (212 J)	100%	2.5
	Average	5.0	22	81	162 (220J)		

Photos of Fracture Appearance

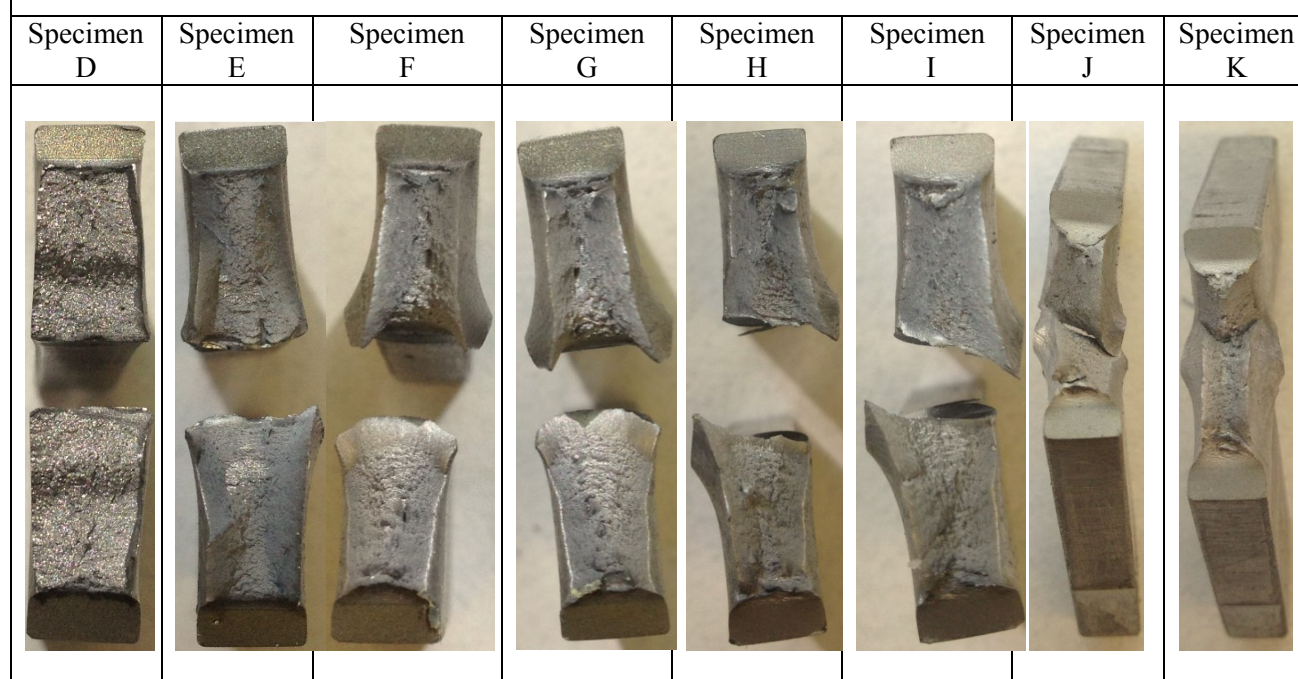


In the set of the two new weld metal specimens, specimen 10 did not break in to two pieces but specimen 11 did. The broken specimen 11 is caused by the eccentric impact rather than the supposed concentric impact. The heavy pendulum might be released imperfectly by the test operator, so that the hammer struck the specimen eccentrically. Since the eccentric loading is more critical than the concentric loading, the obtained value of CVN energy from specimen 11 is smaller than that from specimen 10. The smaller value of the absorbed energy indicates the lower impact toughness. The two new HAZ specimens 12 and 13 show similar results.

Table 4.3 Results obtained from CVN Impact tests at lower temperature

Specimen Set	Specimen #	Specimen Width (mm)	Test Temperature (°C)	Test Impact Energy (ft-lb) (size: width×10mm)	Full Size Impact Energy (ft-lb) (size: 10mm×10mm)	Fracture appearance	
						Percent Shear Fracture	Lateral Expansion (mm)
Base metal	A	5.3	-29	58	109 (148 J)	100%	2.3
	B	5.3	-29	56	106 (144 J)	100%	2.2
	C	5.3	-29	63	119 (161 J)	100%	2.2
	Average	5.3	-29	59	111 (150 J)	100%	2.2
Old weld metal	D	5.0	-78	16	32 (43 J)	5%	0.2
	E	5.0	-21	34	68 (92 J)	90%	1.2
	Average						
Old HAZ	F	5.0	-21	72	144 (195 J)	100%	2.3
	G	5.0	-21	70	140 (190 J)	100%	2.3
	Average	5.0	-21	71	142(193 J)	100%	2.3
New weld metal	H	5.0	-21	68	136 (184 J)	100%	2.3
	I	5.0	-21	66	132 (179 J)	100%	2.3
	Average	5.0	-21	67	134 (182 J)	100%	2.3
New HAZ	J	5.0	-21	78	156 (212 J)	Did not break	
	K	5.0	-21	81	162 (220 J)	Did not break	
	Average	5.0	-21	80	159 (216 J)	Did not break	

Photos of Fractured Appearance



The specimen D was cooled by dry ice and tested at -78°C. The very low temperature resulted in brittle fracture rather than ductile fracture. The fracture surface of specimen D is predominated by bright and granular flat zone due to cleavage fracture (roughly 95%). All other specimens were cooled in a fridge and tested at either -21°C or -29°C and displayed gray and fibrous fracture surfaces due to shear fracture and large percentage of shear lips. Except for specimen E showing a small region of bright and granular flat zone in the center (roughly 10%), all other specimens show roughly 100% shear fracture surface.

4.6 Conclusion of Tests

The results obtained from the Charpy V-notch impact tests contributes to the following five conclusions. The first conclusion is that the girth weld and its ambient HAZ are tougher than the base metal for the research X52 pipe material. This is supported by the absorbed CVN energy values and the HAZ around new weld showed the highest impact toughness, followed by the new weld metal and the base metal. Similarly, the HAZ around the old weld showed highest impact toughness, followed by the base metal and the old weld metal. Obviously, the old girth weld showing a significant lower toughness is an exception of this statement. The second conclusion is that the research X52 pipe experience stable ductile fracture even at a temperature as low as -21°C . All specimens displayed about 100% shear fracture at room temperature 22°C or lower temperature -21°C , except an old weld metal specimen which displayed about 90% shear fracture at -21°C . This is the basis of good operation and function when pipeline is buried beneath the ground below 0°C . The third conclusion is that the field girth weld that manufactured in 1980s is very different than the new girth weld that manufactured in 2013 in a machine shop. The old girth weld specimen showed lower toughness and ductility than other specimens. The fourth conclusion is related to the temperature effect to the absorbed energy and material impact toughness. Based on test data obtained from all specimens, the converted CVN energy values for the standard CVN specimen ($10\text{ mm}\times 10\text{ mm}\times 55\text{ mm}$) as a function of temperature is shown in Fig. 4.5. As temperature decreases, the absorbed CVN energy and material impact toughness decreases. Due to the fact that the CVN energy values measured at -21°C is similar to those measured at 22°C , a temperature range from -20°C upwards should be in the upper shelf region of the CVN energy versus temperature curve. In addition, all measured energy are higher than 27 Joules, which is the specified minimum average CVN energy according to API Spec 5L (2012). The minimum 85% shear fracture is ensured for all specimens tested at temperature higher than -30°C . The fifth conclusion is related to the transition temperature from ductile to brittle fracture. One old weld metal specimen is particularly tested at -78°C , showing lower toughness and 5% shear fracture (or 95% brittle fracture). It is hard to say this brittle fracture behavior is largely caused by the low temperature (-78°C) or the old weld metal itself. Although in the lack of large quantity of specimens to determine the accurate ductile-brittle transition temperature, it should be within the range from -78°C to -21°C .

In addition, the energy converting method from subsize specimens to full specimens requires further discussion. Due to the small difference in every subsize specimen's width, all measured CVN energy values were multiplied by the ratio of the width of the full size specimen to the width of the subsize specimen and then compared. Although this converting method is supported by API 579-1 (2007), the converted values should be higher than the direct test values from the standard specimens. This is because the value of the energy increases but not necessarily in a linear fashion as the specimen width increases. In addition, the fracture mode transition may occur at lower temperatures in the subsize specimens than the standard full size specimens, because subsize specimens tend to reduce tri-axial crack tip constraints and increase the possibility of ductile fracture when they are both tested at the same temperature.

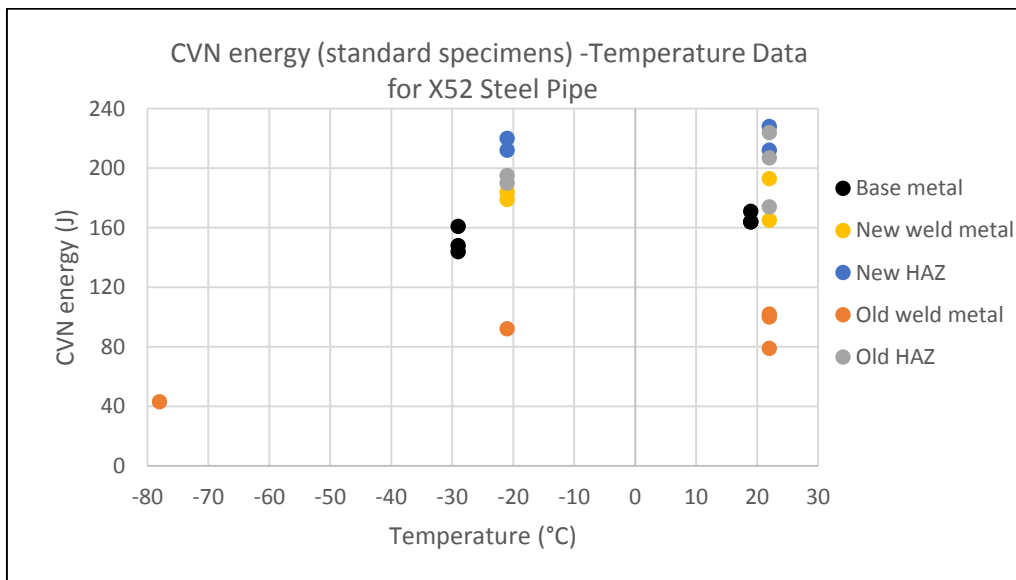


Fig. 4.5. CVN energy (based on standard CVN specimen) versus temperature data for X52 steel pipe

4.7 Variability of Test Results

Even though the Charpy V-notched impact tests were easier to be performed, the obtained test results may also be affected by many reasons, such as the individual difference on test operation and measurement, difference on test temperature, and difference of specimen sizes. First of all, most values of test CVN energy in a specimen set were close, but some were different with a relatively obvious variation. As mentioned earlier, some specimens broke into two pieces and absorbed lower value of CVN energy while other specimen did not break into two pieces and absorbed higher value of CVN energy, even they were in the same specimen set. The reason might be that the heavy pendulum was released imperfectly by the test operator, so that the hammer struck the specimens eccentrically. Therefore, more test specimens are recommended in a specimen set to minimize the variation caused by the discrete values of CVN energy and determine the average. Secondly, there were differences in the values of CVN energy but no obvious differences in the percentage of shear fracture area between the specimens tested at room temperature 22°C and at a low temperature -21°C in a specimen set. This means even lower temperatures are required to increase the probability of brittle fracture. If possible, various temperatures in a large temperature range are suggested to test specimens and understand the change of fracture behavior due to the temperature. Lastly, all test values of CVN energy for subsize specimens were approximately converted to those for full size specimens to compare the results, because test specimens were machined with various specimen widths by different machine shops and manufacturing requirements. The converted values were used for further discussion in the following sections. However, it is worth noting that these converted values should be higher than the actual values if full size specimens are directly tested. This is because the increase of specimen thickness increases the probability of brittle fracture behavior, decreases the impact toughness of material, and thus reduces the value of obtained CVN energy. With all the above analysis of variability, the samples of each specimen set exhibited the same fracture behavior strengthening the conclusion of this work.

4.8 Comparison with Higher Grades of Steel Pipes for CVN Tests Results

In order to have a better understanding of the values of the obtained CVN energy for X52 steel pipes in this research, some other researches about CVN tests for higher grades of API X-grade steel pipes were discussed in this section. All comparisons are shown in Table.4.4. In general, higher grade of steel pipes have higher strength but it is also accompanied by a reduction in the ductility and toughness. In extremely cold regions, the ductile-brittle transition temperature (DBTT) and low-temperature fracture toughness are very important for the structural design and material selection. Even though DBTT was not obtained for the research X52 pipe, it may be lower than $-70\text{ }^{\circ}\text{C}$ because the DBTT usually decreases as the strength decreases (Shin et al., 2009). This temperature value is significantly lower than the service temperature that the pipe will experience. In addition, the DBTT measured by CVN tests should be higher than the actual DBTT measured by direct fracture toughness tests because the loading rate of CVN tests is extremely higher than the actual loading rate in the process of the pipeline operation.

Chapelle et al. (2013) investigated API X65 steel pipes. The standard CVN specimens ($w \times t \times L = 10 \times 10 \times 55\text{ mm}$) were machined from the pipe base and tested in the temperature range from -196°C to 20°C , The obtained CVN energy values versus temperature (Kelvin) was plotted and shown in Fig.4.6. The relationship between the Celsius temperature scale and Kelvin temperature scale is $K = ^{\circ}\text{C} + 273.15$. The ductile-brittle transition temperature (DBTT) or called fracture appearance transition temperature (FATT) was measured and this is the temperature corresponds to the 50-50% brittle and ductile fracture and the average value of the lower shelf energy and the upper shelf energy (USE). The temperature that corresponds to the USE and 100% ductile fracture was called fracture transition plastic (FTP). In addition, a temperature T_{27J} that corresponds to the average energy value of 27 J was measured. Table 4.4 summarizes all above values from the CVN tests and includes some tensile properties determined at room temperature 20°C from base metal specimens.

Gomes et al. (2004) investigated API X65 (OD=508mm) and X70 (OD=660mm) steel pipes. The CVN specimens ($w \times t \times L = 7.5 \times 10 \times 55\text{ mm}$) were machined from the

pipe base and tested in the temperatures range from -70°C to 20°C . The obtained average CVN energy values for the subsize specimens were converted to those for the standard specimens, and shown in Fig.4.7. In this research, X65 and X70 steels have similar toughness at the upper shelf region indicated by similar USE about 230 J , but X70 steel has higher FTP about -20°C compared to X65 steel whose FTP was about -40°C . Table 4.4 summarizes all above values from the CVN tests and includes some tensile properties determined at room temperature 20°C from base metal specimens.

Shin et al. (2009) investigated X70 and X80 steel pipes. The standard CVN specimens were machined from the pipe base tested in the temperature range from -196°C to 20°C , and the obtained CVN energy values versus temperature curve were plotted and shown in Fig.4.8. The values of USE for both pipes and their important temperature such as DBTT and FTP were measured. In addition, T_{28J} , T_{41J} and T_{68J} which correspond to the average energy value of 28 J , 41 J and 68 J respectively were measured to better understand the lower transition region. These three values were selected according to API Spec 5L (2012): the absorbed CVN energy should be more than 27 J ($\text{OD} \leq 30\text{ in.}$), more than 40 J ($30\text{ in.} < \text{OD} \leq 48\text{ in.}$), more than 54 J ($48\text{ in.} < \text{OD} \leq 56\text{ in.}$) and more than 68 J ($56\text{ in.} < \text{OD} \leq 84\text{ in.}$) for X70 steel; the absorbed CVN energy should be more than 40 J ($\text{OD} \leq 48\text{ in.}$), more than 54 J ($48\text{ in.} < \text{OD} \leq 56\text{ in.}$) and more than 68 J ($56\text{ in.} < \text{OD} \leq 84\text{ in.}$) for X80 steel. Table 4.4 summarizes all above values from the CVN tests and includes some tensile properties determined at room temperature 20°C from base metal specimens. In this research, X70 and X80 steels had similar toughness at the upper shelf region indicated by similar USE values, but X70 steel exhibited higher transition temperature FATT compared to X80 steel. The transition temperature usually decreases as the strength decreases and effective grain size decreases. Even though X80 steel has higher strength, it had lower effective grain size in this research. The average effective grain measured was $9\ \mu\text{m}$ for X70 steel, but $6\ \mu\text{m}$ for X80 steel.

Table 4.4 CVN and tension tests results of API X52, X65, X70 and X80 pipe steels

Pipeline steel (base metal)	Tensile properties (room temperature)			CVN results						Reference
	σ_{YS} (MPa)	σ_{TS} (MPa)	Elongation	T_{27J} (°C)	T_{41J} (°C)	T_{68J} (°C)	DBTT (°C)	FTP (°C)	USE (J)	
X52	437 (C) 411 (L)	579 (C) 573 (L)	10.6% (10mm G.L.; C) 35.1% (50 mm G.L.; L)					-20	167	This research
X65	465.5	588.6	10.94%	-99			-94	-81	277	Chapelle et al. (2013)
X65	522.5 (C) 541.0 (L)	608.5 (C) 608.5 (L)	44.4% (C) 43.5% (L)					-40	230	Gomes et al. (2004)
X70	528.5 (C) 538.0 (L)	650.5 (C) 614.0 (L)	44.5% (C) 46.5% (L)					-20	230	
X70	504	616	28% (30 mm G.L.)	-103 (T_{28J})	-100	-88	-69	0	280	Shin et al. (2009)
X80	574	737	23% (30 mm G.L.)	-118 (T_{28J})	-116	-106	-87	-10	286	

C: circumferential or transverse direction

L: longitudinal direction

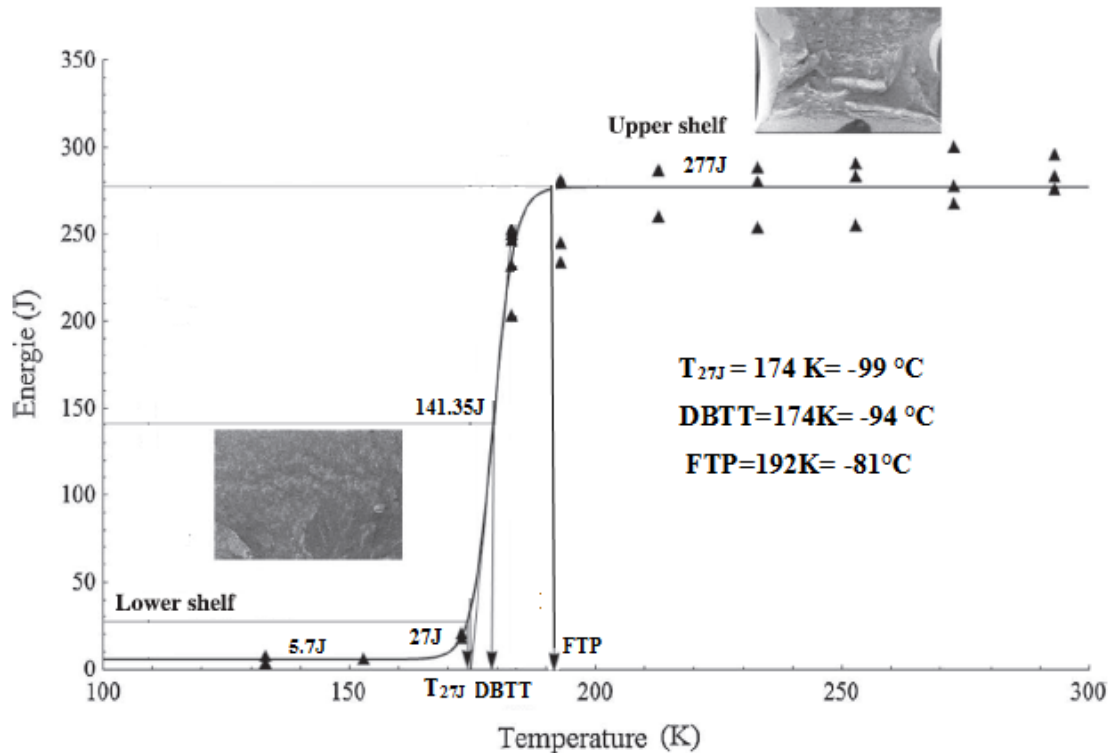


Fig. 4.6 CVN energy versus temperature curve for API X65 steel pipe (Adapted from Chapelle et al.; 2013)

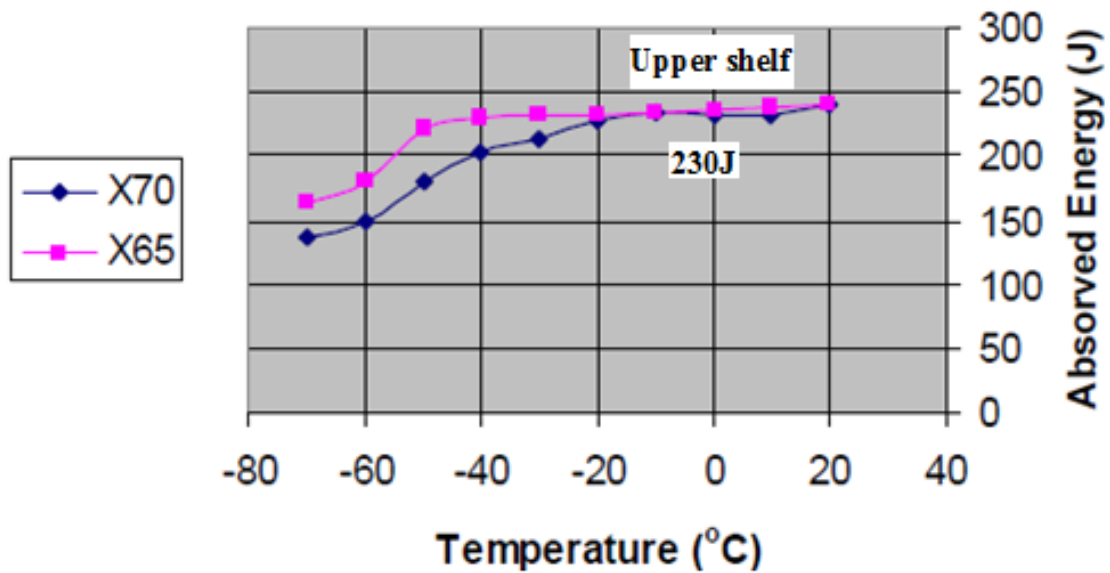
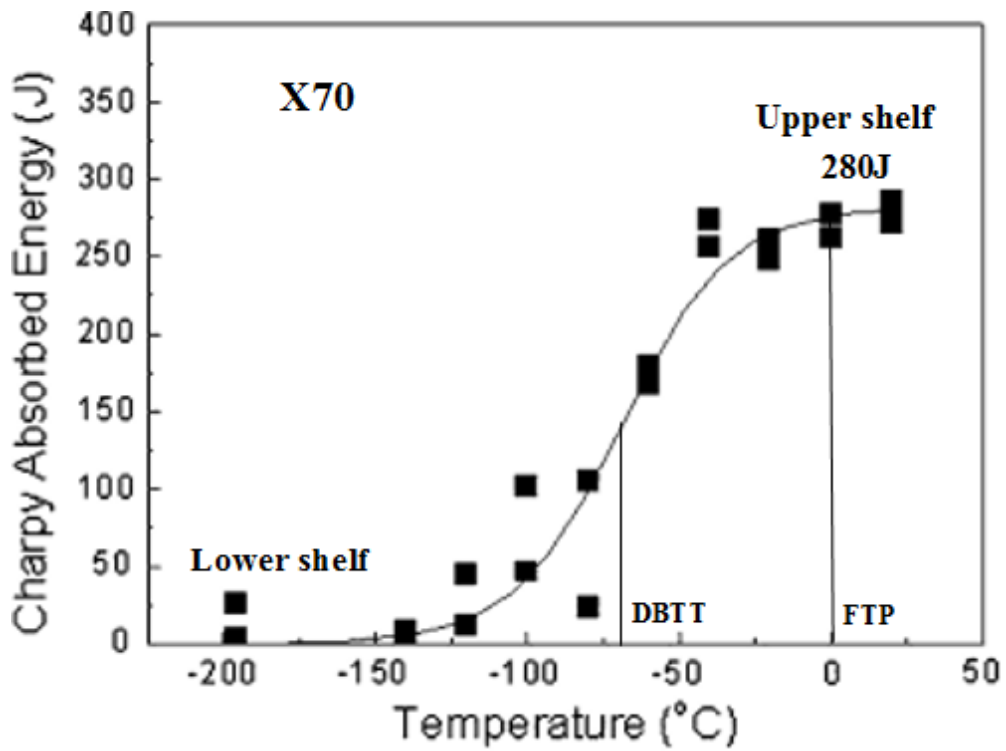
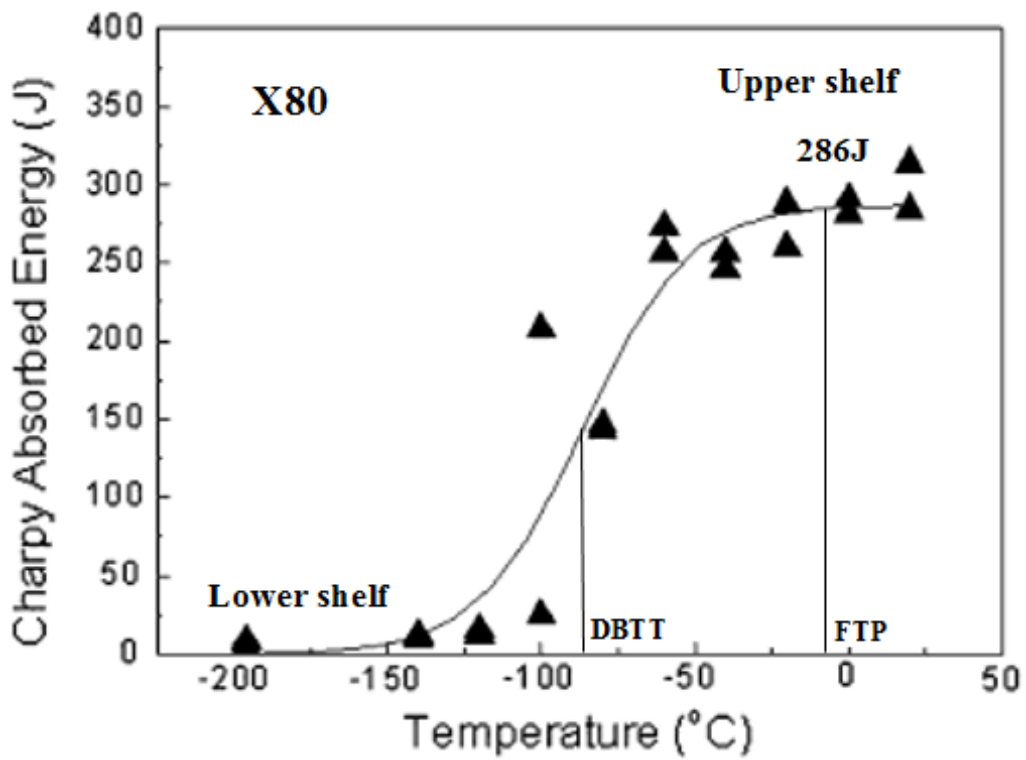


Fig.4.7 CVN energy versus temperature curve for API X65 and X70 steel pipes (Adapted from Gomes et al.; 2004)



(a)



(b)

Fig. 4.8 CVN energy versus temperature curve for (a) API X70 and X80 steel pipes (Adapted from Shin et al.; 2009)

4.9 Correlation with Fracture Toughness

The fracture toughness measures the ability of a material to resist the propagation of a preexisting crack. Structural engineers believe that cracks have great possibility to be formed in the process of the manufacture or service of a material, and thus they usually assume a preexisting crack with a selected size on a material and further analyze it by an appropriate fracture mechanics approach, either linear elastic fracture mechanics approach or elastic-plastic fracture mechanics approach. The magnitude and distribution of the stress field surrounding the crack-tip is emphasized (NDT Resource Centre). The fracture toughness can be directly measured by a fracture toughness test as a form of a fracture toughness parameter to resist crack propagation, or indirectly measured by a Charpy V-notch impact test as a form of the required energy to impact and break a notched specimen.

4.9.1 Fracture Toughness Parameters

In this section, the relevant fracture toughness parameters that have been mentioned earlier in section 2.5.2.3 are repeated. Fracture toughness can be characterized by a fracture toughness parameter in a fracture toughness test, such as stress-intensity factor (K), energy release rate (G), J integral (J), and crack-tip opening displacement ($CTOD$ or δ). They can be measured by a single point value of fracture toughness under plain strain conditions, such as K_{Ic} , G_{Ic} , J_{Ic} and δ_{Ic} , or an entire resistance curve (R -curve) where one of the parameters (K , G , J , δ) is plotted against the crack extension (Anderson,2005). It is significant to determine an appropriate fracture toughness parameter to characterize material fracture toughness.

Linear elastic fracture mechanics applies to materials whose crack tip is surrounded and dominated by linear elastic deformation or with small scale plastic deformation (small scale yielding). The crack grows rapidly and unstable brittle fracture occurs when a critical stress is reached. Fracture toughness is determined at this point of instability near the crack initiation and characterized by critical plain strain stress-intensity factor (K_{Ic}) or critical energy release rate (G_{Ic}). The material resistance beyond the crack initiation is small and thus the measurement is not required (Zhu & Joyce, 2012). Elastic-plastic fracture mechanics applies to materials whose crack tip is surrounded by large scale plastic deformation (large scale yielding). The crack fractures in a ductile

manner after initial crack blunting. The fracture resistance increases as the crack grows due to material strain hardening. The fracture toughness is determined by an entire R -curve, such as J - R curve or δ - R curve, which describes the continuous process of slow and stable crack tearing. Due to the requirement of a single point value of the fracture toughness in many methods and applications, J_{Ic} or δ_{Ic} is usually deduced from the R -curve at the onset of ductile crack growth, which is shown at a point on curve whose slope changes dramatically (Zhu & Joyce, 2012). J_{Ic} or δ_{Ic} indicates elastic-plastic initiation toughness under plane strain conditions.

In the linear elastic regime, there are important theoretical relationships between fracture toughness parameters. J -integral is a measure of the energy required to grow the crack, and its elastic component is equal to elastic energy release rate: $J_{el} = G$. The relationship between K and G , and J and δ are dependent on the crack tip constraints: $G = \frac{K^2}{E'}$ where $E' = E$ for plane stress but $E' = \frac{E}{(1-\nu)^2}$ for plane strain (Anderson, 2005); $J = m \cdot \sigma_Y \cdot \delta$ where σ_Y is the effective yield strength and m is a constraint factor and is approximately taken as 1.4 in the absence of more detailed information (API 579-1/ASME FFS-1, 2007). As a result, an “equivalent K_{Ic} ” value can be derived from J_{Ic} or δ_{Ic} value in the limit of small scale yielding under plane strain conditions, which are shown as follow (API 579-1/ASME FFS-1, 2007):

$$K_{Ic} = \sqrt{\frac{J_{Ic} \cdot E}{1-\nu^2}} = \sqrt{\frac{1.4 \cdot \sigma_Y \cdot \delta_{Ic} \cdot E}{1-\nu^2}}$$

where

K_{Ic} , J_{Ic} , and δ_{Ic} are plane strain fracture toughness characterized by stress-intensity factor K ($MPa\sqrt{m}$), J integral (kJ/m^2), and by crack-tip opening displacement (mm)

E is young’s modulus at the temperature of interest (MPa)

ν is poisson’s ratio in the elastic range and is normally taken as 0.3 for steels

σ_Y is effective yield strength or flow strength, which is equal to $\frac{\sigma_{YS} + \sigma_{TS}}{2}$ (MPa)

4.9.2 Restrictions of Fracture Toughness Test

In this section, the restrictions of conventional and standardized fracture toughness tests that have been mentioned earlier in section 2.5.2.5 are repeated. ASTM standards provide standardized methods and procedures for measuring the fracture toughness, such as ASTM E399-12 and ASTM E1820-11. ASTM E399 was the first standardized test method for K_{Ic} testing, and ASTM E 1820 is a generalized fracture toughness test method that combines three toughness parameters K , J , $CTOD$ in a single test. The Model I fracture is specified in both tests, which is an opening mode in which the tensile stress is normal to the plane of the crack. The common used deep-cracked specimens, are compact tension (CT) specimens and single edge notch bend (SENB) specimens containing a sharp fatigue crack with a selected size (Fig. 2.28). ASTM E399-11 requires high crack tip constraints to insure the small scale yielding and predominant plane strain conditions at the crack tip. To obtain a valid K_{Ic} , test specimen must be very brittle or thick. The specimen geometric dimensions are restricted as follows.

$$B \geq 2.5 \left(\frac{K_{Ic}}{\sigma_{YS}} \right)^2, a \geq 2.5 \left(\frac{K_{Ic}}{\sigma_{YS}} \right)^2, 0.45 \leq a/w \leq 0.55$$

where

B , w , a are specimen thickness, specimen width, and crack length (mm)

σ_{YS} is 0.2% offset yield strength (MPa)

K_{Ic} is the critical plane strain stress-intensity factor ($MPa\sqrt{m}$)

The fracture toughness measured by the J -integral or δ is used to characterize the relatively ductile or thin specimens. In this case, the crack tip is surrounded by a large zone of plastic deformation, and the crack grows in a ductile manner after initial crack blunting. The ductile tearing resistance against crack extension should be carefully monitored by sophisticated instrumentation, and single point value of plane strain fracture toughness are determined from the resistance curves near the onset of ductile crack growth. Both J and δ can be separated into elastic and plastic components. Their elastic components are equal to J_{Ic} and δ_{Ic} . The specimen geometric dimensions and limits on J -integral and crack extension are restricted by ASTM E1820-11 as follow.

$$B \geq \frac{25J_{Ic}}{\sigma_Y}, b_0 \geq \frac{25J_{Ic}}{\sigma_Y}, 0.50 \leq \frac{a}{w} \leq 0.70$$

$$J_{max} \leq \frac{B\sigma_Y}{10}, J_{max} \leq \frac{b_0\sigma_Y}{10}, \Delta a_{max} \leq 0.25b_0$$

where

B , w , a are specimen thickness, specimen width, and crack length (mm)
 b_0 is original remaining ligament, which is equal to $w - a_0$ (mm)
 σ_Y is effective yield strength or flow strength, which is equal to $\frac{\sigma_{YS} + \sigma_{TS}}{2}$ (MPa)
 J_{Ic} is plain strain fracture toughness characterized by J -integral (kJ/m^2)
 J_{max} is maximum value of J -integral (kJ/m^2)
 Δa_{max} is maximum value of crack extension Δa (mm)

The preliminary validity check of specimen geometric dimensions is required prior to the test to avoid the invalidity of the fracture toughness results. The required specimen thickness is calculated based on the yield strength obtained in tension test and K_{Ic} and J_{Ic} values estimated from CVN energy. As shown in Table 4.5, σ_{YS} is $436 MPa$, σ_Y is $507 MPa$, K_{Ic} is $219 MPa\sqrt{m}$, and J_{Ic} is $213.19 kJ/m^2$. As a result, the minimum specimen thickness for a valid K_{Ic} is $630 mm$, while it is $10.5 mm$ for a valid J_{Ic} . It is obvious that the specimen geometric restrictions for J_{Ic} is much more lenient than that for K_{Ic} . However, both of them exceed the thickness $6.86 mm$ of the research X52 pipe. As the pipe is very ductile and thin, it runs the risk of invalid plane strain fracture toughness values in the fracture toughness test due to the strict requirements. As a result, SENB or CT tests were not performed in this research.

In recent years, alternative methods for testing fracture toughness of thin walled cracked pipelines with relatively high toughness use shallow-cracked single edge notch tension (SENT) specimens. The low levels of crack tip constraints is more close to the actual conditions of the cracked pipeline. Although many researches have been successfully conducted SENT tests on pipelines, the test method has not been standardized and concluded in any standards. Therefore, SENT was not performed in this research either. In addition, the current tests in the literature require sophisticated instrumentation and currently are not available in the laboratory of University of Alberta.

Considering all above reasons, Charpy V-notch impact test was selected to perform in this research and it is deemed satisfactory for the comparative description of the fracture toughness of the various locations of the research pipe.

4.9.3 Correlation between CVN Energy and Fracture Toughness

Many structural engineers have attempted to investigate the possibility to correlate the CVN impact energy with the plane strain fracture toughness K_{Ic} . The primary concern is the difference that CVN has fast impact loading rate while K_{Ic} is obtained in a slow bend loading rate. Structural materials are usually very sensitive to loading rate. As shown in Fig. 4.9, as the loading rate increases, the transition region occurs at higher temperature and the fracture toughness to impact loading (absorbed energy) is higher in the upper shelf region.

A good correlation between CVN- K_{Ic} is defined by Barsom and Rolfe (1999). Both the lower shelf and upper shelf regions are estimated by particular equations, while the transition region is estimated by interpolation. At the lower shelf and lower transition regions, the CVN- K_{Id} - K_{Ic} correlation is described by converting the CVN at every lower temperature to K_{Id} , and then shifting the fracture toughness from the dynamic loading rates (K_{Id}) to the slow loading rates (K_{Ic}) by the empirically derived temperature shift (T_s). The correlations are shown as follows (Barsom & Rolfe, 1999; US Army Corps of Engineers, 2001):

$$T_s = 102 - 0.12\sigma_{YS}, \text{ for } 250 \text{ MPa} < \sigma_{YS} < 965 \text{ MPa}; T_s = 0, \text{ for } \sigma_{YS} > 965 \text{ MPa}$$

$$K_{Id} = \sqrt{0.64 \cdot CVN \cdot E}$$

$$K_{Ic}(T_0) = K_{Id}(T_0 + T_s)$$

where

K_{Id} and K_{Ic} are plain strain stress-intensity factor at dynamic loading rate and slow loading rate ($kPa\sqrt{m}$)

CVN is standard Charpy V-notch impact energy at lower temperature in the lower shelf and lower transition regions (J)

E and σ_{YS} are Young's modulus and static yield strength (kPa)

T_s and T_0 are temperature shift and every lower temperature ($^{\circ}C$)

At the upper shelf, the CVN- K_{Ic} correlation is described by converting the CVN at every higher temperature to K_{Ic} . Barsom and Rolfe (1999) discovered that the loading rate effect is significant for steels with yield strength less than 100ksi (690 MPa) while it is small for steels with yield strength more than 100ksi (690 MPa). The following CVN- K_{Ic} correlation using the static yield strength works well for steels with higher yield

strength, but replacing the static yield strength by the dynamic yield strength works better for steels with lower yield strength.

$$\left(\frac{K_{Ic}}{\sigma_{YS}}\right)^2 = 0.64 \left(\frac{CVN}{\sigma_{YS}} - 0.01\right)$$

where

K_{Ic} is plane strain stress-intensity factor at slow loading rate ($MPa\sqrt{m}$)

σ_{YS} is yield strength (MPa), $\sigma_y = \sigma_{YS}$ if $\sigma_y \geq 100ksi$ and $\sigma_y = \sigma_{Ysd}$ if

$\sigma_{YS} < 100ksi$

CVN is standard Charpy V-notch impact energy at higher temperature in the upper shelf region (J)

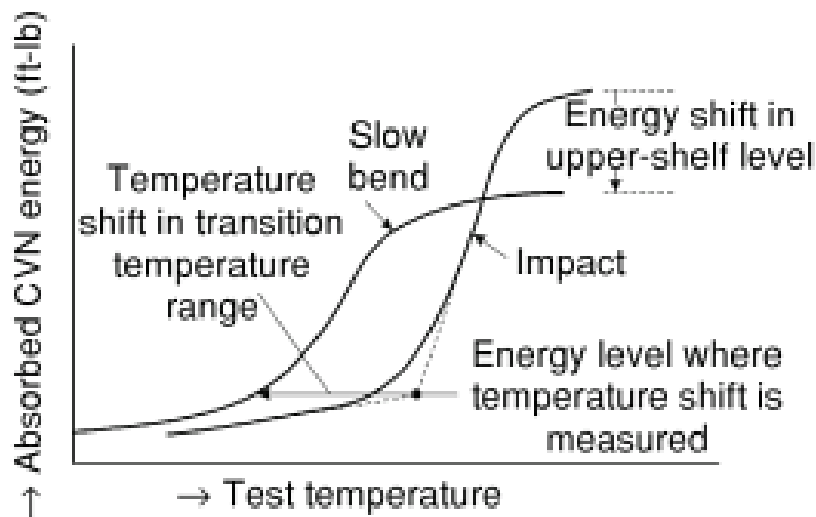


Fig. 4.9 Charpy impact energy versus temperature curve for impact loading and slow bend loading (Barsom and Rolfe, 1999, p.99)

Due to the fact that the CVN specimens tested at 22°C and -21°C displayed extremely higher percent of shear fracture, the obtained CVN values at both temperature should be in the upper shelf region. The converted CVN data for standard full size specimens at 22 °C are used to empirically correlate with K_{Ic} by using the equation $\left(\frac{K_{Ic}}{\sigma_{YS}}\right)^2 = 0.64 \left(\frac{CVN}{\sigma_{YS}} - 0.01\right)$, where σ_{YS} is the test yield strength obtained from the tension test at room temperature. In addition, based on the linear elastic plane strain assumptions, the corresponding J_{Ic} and δ_{Ic} values at the initiation of crack growth are derived from the correlated K_{Ic} .

$$J_{Ic} = \frac{K_{Ic}^2(1 - \nu^2)}{E}$$

$$\delta_{Ic} = \frac{K_{Ic}^2(1 - \nu^2)}{1.4\sigma_Y E}$$

where

K_{Ic} , J_{Ic} , and δ_{Ic} are plane strain fracture toughness characterized by stress-intensity factor K ($MPa\sqrt{m}$), J integral (kJ/m^2), and by crack-tip opening displacement (mm)

E is young's modulus obtained from tension test at 22 °C (MPa)

ν is poisson's ratio in the elastic range and is normally taken as 0.3 for steels

σ_Y is effective yield strength, which is equal to $\frac{\sigma_{YS} + \sigma_{TS}}{2}$ (MPa)

Table 4.5 summarizes all measured tensile properties and CVN energy values as well as the converted values of plane strain fracture toughness K_{Ic} , J_{Ic} and δ_{Ic} . Taking into account all results of the specimens from base metal, weld metal and HAZ, the average of the standard Charpy V-notch impact energy is 178 Joule. Correspondingly, the empirical estimated plane-strain stress intensity factor K_{Ic} is $219MPa \cdot \sqrt{m}$. Based on the liner elastic plane strain assumption, plane strain fracture toughness J_{Ic} is $213 kJ/m^2$ and δ_{Ic} is 0.3 mm at the onset of slow, stable and ductile crack growth. Any of these three toughness parameters are able to characterize the fracture toughness of the research X52 pipe. However, these values may be maybe conservative because they were converted from CVN energy and CVN conversion equations are lower bounds. The accurate values should be measured by fracture toughness tests. The entire resistance curve, such as J - R curve or δ - R curve would be favorable than the single values of fracture toughness as it describes the continuous process of the slow and stable crack tearing. In the absence of direct measurements of fracture toughness, the current converted values of plane strain fracture toughness do provided a good reference for understanding the research X52 pipe.

Table 4.5 Correlations between CVN and K_{Ic} , J_{Ic} , δ_{Ic}

Specimen sets		σ_{YS} (MPa)	σ_{TS} (MPa)	σ_Y (MPa)	E (MPa)	CVN_{avg} (J)	CVN_{min} (J)	K_{Ic} (MPa · \sqrt{m})	J_{Ic} (kJ/m ²)	δ_{Ic} (mm)	δ_{max} (mm)
Location	Orientation										
Base metal	Longitudinal	411	573	492	199000	167	164	207	195.93	0.2845	0.7422
	Circumferential	437	579	508	226000			213	183.14	0.2575	0.7422
New HAZ	Longitudinal	428	554	491	194000	220	212	243	277.17	0.4032	0.9778
	Circumferential	462	595	529	203000			252	285.48	0.3858	0.9778
Old HAZ	Circumferential	446	584	515	215000	202	174	237	238.66	0.3310	0.8978
New weld	Circumferential	428	607	518	215000	179	165	219	202.57	0.2796	0.7956
Old weld	Circumferential	438	561	500	209000	94	79	159	109.38	0.1564	0.4178
Average		436	579	507	208714	178	167	219	213.19	0.2997	0.7930

The calculated δ_{Ic} value should be checked against the CVN test values according to CSA Z662-11(2011). The maximum value of δ_{Ic} should be smaller than both δ_{max1} and δ_{max2} .

$$\delta_{max1} = \frac{0.2}{30} CVN_{min} \text{ and } \delta_{max2} = \frac{0.2}{45} CVN_{avg}$$

where

CVN_{min} is the minimum standard CVN impact energy (J)

CVN_{avg} is the average standard CVN impact energy (J)

4.9.4 Comparison with Higher Grades of Steel Pipes for Fracture Toughness Tests Results

In order to have a better understanding of the estimated or converted values of plane strain fracture toughness K_{Ic} , J_{Ic} and δ_{Ic} for X52 steel pipes in this research, some other researches about fracture toughness tests for higher grades of API 5L X-grade steel pipes were discussed in this section. All comparisons are shown in Table. 4.6. It shows that the lower grade of steel pipes usually have higher fracture toughness (K_{Ic} , J_{Ic} and δ_{Ic}) at room temperature because of the higher ductility and toughness. For this reason, the X52 pipe should have higher fracture toughness than other higher grades of pipes. However, current estimated fracture toughness values were very small because they were converted from the CVN energy and CVN conversion equations were lower bounds. The direct measurements from the fracture toughness tests would be favorable. It is worth noting that the measured K_{Ic} value for the weld API 5L X52 steel pipe in Angeles-Herrera et al. research is very small. This is because K_{Ic} measured in ASTM E399-12 is the plane strain fracture toughness at the initiation of the rapid and unstable brittle fracture with little or no deformation. Other converted K_{Ic} values for higher grades of steel pipe are comparatively higher because they were converted from J_{Ic} . J_{Ic} measured in ASTM E1820-11 is the plane strain fracture toughness at the onset of slow, stable and ductile crack extension, and is deduced from the resistance curve (J - R curve) near the transition from initial crack blunting to crack tearing.

Angeles-Herrera et al. (2014) investigated the weld API 5L X52 steel. The sample pipe (OD=36 in., t=1 in.) was welded by a submerged arc-welding (SAW) longitudinal seam weld. They measured the fracture toughness K in the circumferential-longitudinal (CL) and circumferential-radial (CR) directions of the weld metal, by means of standard compact tension CT specimens and nonstandard curved SENB specimens according to ASTM E399-12. Fig. 4.10 shows how the test specimens were machined. At the room temperature (25°C), the measured average value of K_{Ic} from the longitudinal weld metal was $75.43 \pm 3.22 \text{ MPa}\sqrt{\text{m}}$ in the CL direction and $56.29 \pm 2.93 \text{ MPa}\sqrt{\text{m}}$ in the CR direction. The difference was attributed to the anisotropy of the longitudinal weld metal, shown by the microconstituent distribution of predominant ferrite grains (ductile) in the CL direction or predominant acicular ferrite grains (brittle) in the CR direction. The predominant brittle behavior explained the lower fracture toughness values in the

CR direction. It is worth noting that the measured value of K_{IC} is very small and it is the lower bound fracture toughness of X52 longitudinal weld metal, and it is independent of the loading rate and geometric conditions. In addition, the tensile properties of the longitudinal weld metal were determined by tensile tests according to ASTM E8/E8M-11. In the longitudinal direction, $\sigma_{YS}=384$ MPa, $\sigma_{TS}=453$ MPa and $\epsilon_{ult}=30\%$; however, in the circumferential direction, $\sigma_{YS}=345$ MPa, $\sigma_{TS}=415$ MPa, and $\epsilon_{ult}=25\%$. Based on the relationship between K , J , and CTOD (δ) in linear elastic fracture mechanics, J_{IC} and δ_{IC} can be calculated following the equation $K_{IC} = \sqrt{\frac{J_{IC} \cdot E}{1-\nu^2}} = \sqrt{\frac{m \cdot \sigma_Y \cdot \delta_{IC} \cdot E}{1-\nu^2}}$, where $\sigma_Y = \frac{\sigma_{YS} + \sigma_{TS}}{2}$. E and ν were assumed to be 210 GPa and 0.3 respectively because their accurate values were not mentioned in the literature. m was taken as 1.4, which is recommended in API 579-1/ASME FFS-1 (2007). All measured and converted values are summarized in Table 4.6. It is worth noting that the converted value J_{IC} is very small and δ_{IC} is closed to zero. This is because K_{IC} measured in ASTM E399-12 is the plane strain fracture toughness at the initiation of the rapid and unstable brittle fracture with little or no deformation.

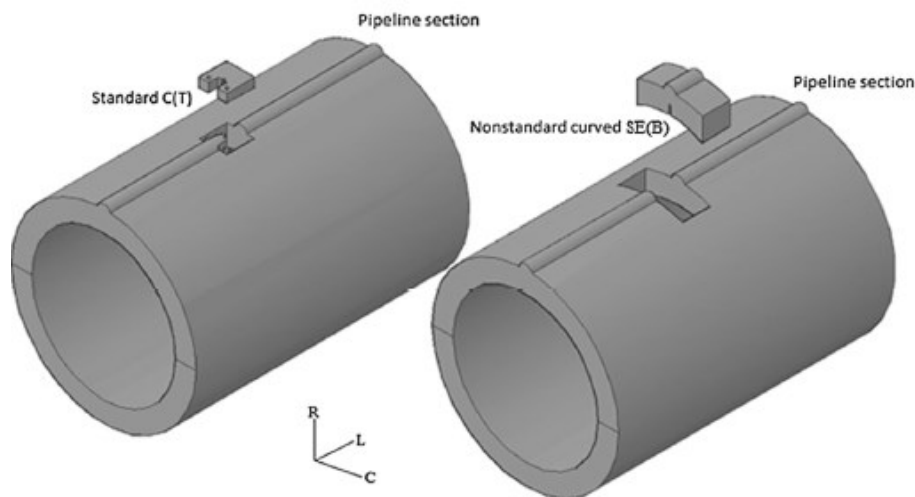


Fig. 4.10 (a) Standard CT specimen in the CL direction and (b) nonstandard curved SENB specimen in the CR direction (From Angeles-Herrera et al., 2014)

Drexler et al. (2010) investigated API 5L X65 steel pipe welds. The sample pipe (OD=12.75 in., t=0.5 in.) was welded by an electric resistance welding (ERW) girth seam weld. They performed single edge notch tension (SENT) tests and plotted the J

versus crack extension Δa curve (J - R curve). The value of J_Q was determined at the intersection of a 0.2 mm offset construction line and the J - R curve according to ASTM E1820-11. A blunting construction line was plotted in accordance with the equation $J = 2\sigma_Y\Delta a$, whose slope 2 can be larger to fit the initial test data (Zhu & Joyce, 2012). Then another line was plotted parallel to the construction line with an offset of $\Delta a = 0.2$ mm. If all qualification requirements defined in ASTM E1820-11 are met ($B \geq \frac{25J_Q}{\sigma_Y}$ and $b_0 \geq \frac{25J_Q}{\sigma_Y}$), J_Q is J_{IC} . At the room temperature (20°C), the measured average value of J_{IC} was $942 \pm 43 \text{ kJ/m}^2$ for the base metal, and $499 \pm 37 \text{ kJ/m}^2$ for the weld metal. Table 4.6 summarizes all measured values and their converted values K_{IC} and δ_{IC} as well as σ_{YS} and σ_{TS} determined at room temperature from base metal and weld metal specimens.

Chen (2009) investigated API X70, X80 and X100 steel pipes by testing specimens in standard three-point-bending tests according to GB 4161-84 (corresponding to ASTM E399-12) and GB 2038-91 (corresponding to ASTM E1820-11). For X70 and X80 steels, most obtained test data J failed to meet the validation criteria, because the test specimens were too thin and ductile to meet the plane strain condition. However, for X100 pipe, most test data were valid, and the measured crack initiation toughness value $J_{0.2}$ at $\Delta a = 0.2\text{mm}$ was 304.9 kJ/m^2 . For the plastic X70 and X80 steels, Chen separated the elastic and plastic component of J data, and obtained $J_{0.2}$, which were 318.6 kJ/m^2 for X70 pipe and 258.7 kJ/m^2 for X80 pipe. Based on $K_c = \sqrt{J_c \cdot E}$, and $E=210 \text{ GPa}$, the converted plane stress fracture toughness K_c was $258.9 \text{ MPa} \cdot \sqrt{\text{m}}$ for X70 pipe and $233.1 \text{ MPa} \cdot \sqrt{\text{m}}$ for X80 pipe. In order to ensure the plane-strain condition for ductile specimens, Chen included a new side-cut three-point bending method to obtain the brittle fracture curve. The obtained fracture toughness J_{IC} was $423.7 \pm 38.0 \text{ kJ/m}^2$ for X70 pipe, was $430.1 \pm 33.7 \text{ kJ/m}^2$ for X80 pipe, and was $332.9 \pm 26.1 \text{ kJ/m}^2$ for X100 pipe. Table 4.6 summarizes all measured values and their converted values K_{IC} and δ_{IC} as well as σ_{YS} and σ_{TS} determined at room temperature from the base metal specimens.

Table 4.6 Fracture toughness test and tension test results of API X52, X65, X70, X80 and X100 pipe steels

Pipeline steel	Specimens	Tensile properties (measured)			Fracture toughness (at room temperate)			Reference
		σ_{YS} (MPa)	σ_{TS} (MPa)	E (GPa)	K_{Ic} (MPa $\cdot\sqrt{m}$)	J_{Ic} (kJ/m ²)	δ_{Ic} (mm)	
X52	Base metal	411 (L)	573 (L)	199 (L)	207 (converted from CVN=167 J)	196 (converted)	0.285 (converted)	This research
	Girth weld metal (new)	428	607	215	219 (converted from CVN=179 J)	203 (converted)	0.280 (converted)	
	Girth weld metal (old)	438	561	209	159 (converted from CVN=94 J)	109 (converted)	0.156 (converted)	
X52	Longitudinal weld metal (CL)	384 (L) 345 (C)	453 (L) 415 (C)		75.43 \pm 3.22 (measured)	24.66 (converted)	0.00004 (converted)	Angeles-Herrera et al.(2014)
	Longitudinal weld metal (CR)				56.29 \pm 2.93 (measured)	13.73 (converted)	0.00002 (converted)	
X65	Base metal	420.5	478.9		466.2 (converted)	942 \pm 43 (measured)	1.496 (converted)	Drexler et al. (2010)
	Girth weld metal	456.4	570.6		339.3 (converted)	499 \pm 37 (measured)	0.694 (converted)	
X70	Base metal	604	753		312.4 (converted)	423.7 \pm 38.0 (measured)	0.446 (converted)	Chen (2009)
X80	Base metal	611	721		314.8 (converted)	430.1 \pm 33.7 (measured)	0.461 (converted)	
X100	Base metal	650	805		277.0 (converted)	332.9 \pm 26.1(measured)	0.327 (converted)	

CL: circumferential-longitudinal direction; CR: circumferential-radial direction; C: circumferential direction; L: longitudinal direction

Conversion equation: $K_{Ic} = \sqrt{\frac{J_{Ic} \cdot E}{1-\nu^2}} = \sqrt{\frac{m \cdot \sigma_Y \cdot \delta_{Ic} \cdot E}{1-\nu^2}}$, where $\sigma_Y = \frac{\sigma_{YS} + \sigma_{TS}}{2}$, $E=210$ GPa (if E was not mentioned in the reference), $\nu=0.3$, and $m=1.4$

5. Prediction of Tensile Strain Capacity

Strain-based design has been developed in recent years in the assessment of cracked pipelines. It studies the stress-strain behaviors and strain limits, and guarantees the applied strain does not exceed strain limits. In this Chapter, the tensile strain capacity of X52 steel pipes is predicted according the empirical formula provided in CSA Z662-11. Prior to these calculations, the stress-strain curves of X52 steel pipes are compared to higher grades of steel pipes to better understand the stress-strain behaviors of different grades of steel pipes.

5.1 Introduction to Strain-based Design

Traditional stress-based design requires the maximum stress of the material in response to the applied loads to not exceed the allowable stress, and does not consider the stress-strain behaviors. However, the strain-based design requires the maximum applied strain to not exceed the allowable strain (Gao et al., 2010). Since the most important design of pipelines is their resistance to the large plastic deformation due to soil movements, such as slope instability, frost heave and thaw settlement, and seismic activities, the strain based-design is more appropriate than the stress-based design in the engineering critical assessment of pipelines (Gao et al., 2010; Wang, et al. 2012). According to CSA Z662-11, there are two main strain limits, which are compressive strain limit and tensile strain limit. Both of them are affected by many variables, such as the material properties of pipe body, girth weld, and HAZ, weld flaws, pipe geometry, and loading (Wang et al., 2011). In CSA Z662-11, empirical formulae are provided to calculate the strain limits, but accurate values have to be obtained from the experiments. The compressive strain capacity of the pipeline is the limit state for compressive buckling, and it is greatly influence by the stress-strain curve (Gao et al., 2010). Material anisotropy is very important in affecting the buckling response (Neupane, 2012; Fathi, 2012). In addition, as the thickness decreases, the ratio of D/t increases, and thus the compressive strain capacity decreases (Baker, 2008). The tensile strain capacity of the pipeline is the limit state for tensile rupture, and it is the ultimate limit state in pipeline design (Wang et al., 2011). In general, it increases as the wall thickness (t) of the pipe increases, hardening exponent (n) increases, uniform elongation increases, but the ratio of yield strength to tensile strength (Y/T) decreases (Gao et al., 2010). In addition, it is

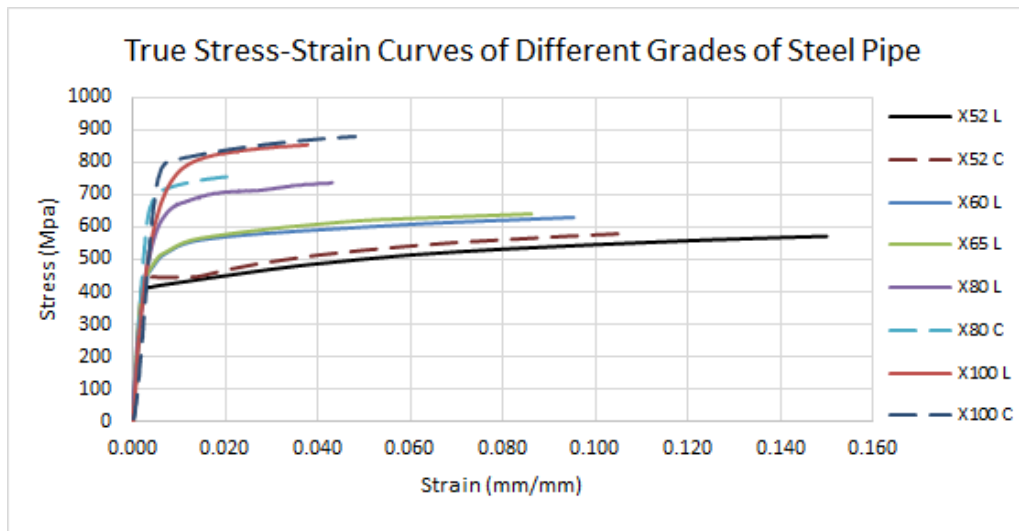
also affected by mismatch level of girth weld, toughness and softening of HAZ, and location, orientation, and dimension of weld flaws (Wang et al., 2011). It is worth noting that the fracture toughness (CTOD) is an essential element in the assessment of the tensile strain capacity of pipelines (Wang, et al. 2012).

5.2 Comparison of X52 to Higher Grades of Steel Pipes

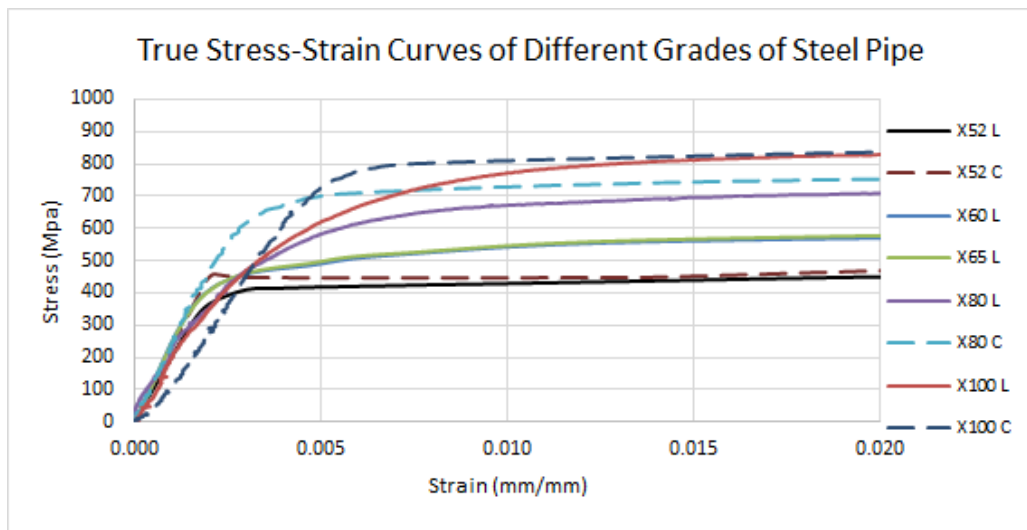
The research vintage X52 pipes are made of relatively low strength steels. Normal strength and high strength steels ranging from X60 to X100 are often used for pipelines today. A brief comparison between the research X52 steel pipes to higher grades of steel pipes is shown in Table 5.1, and their true stress-strain curves from small scale tension tests are compared in Fig. 5.1. Both curves of the base metal specimens machined in the longitudinal and circumferential directions of the pipe are taken as the final stress-strain curve of X52 steel pipe. The curves of higher grades of steel pipes are obtained in the past researches by the University of Alberta. The stress-strain curves of normal strength steel pipes (X60 and X65) were reported by Ahmed (2010), and high strength steel pipes (X80 and X100) were reported by Fathi (2012). Strip specimens were machined from each grade of the pipe in the longitudinal direction, and round specimens were machined from X52, X80 and X100 steel pipe in the circumferential direction. Some important tensile properties are obtained from their stress-strain curve and compared in table 5.1 and Fig.5.1.

Although the results may be affected by many variables, such as the different ratio of nominal outside diameter to nominal thickness, and various specimen shapes and sizes, the main differences in the tensile strength and ductility properties from low strength to high strength steel pipes are still obvious. In general, as the grade of steel increases, both the yield strength and tensile strength increase, but the ductility decreases. The higher yield strength contributes to resisting the higher forces without permanent plastic deformation, and the higher tensile strength contributes to resisting the higher forces without fracture. Even though the X52 steel pipe has the lowest strength, it has very desirable ductility, which makes the pipe deform substantially without fracture and provides a useful warning of safety. Furthermore, due to its high ductility, the material toughness of X52 steel pipe is higher than high strength steel pipes. As mentioned in Chapter 2, the high material toughness requires a good combination of high strength and high ductility, and can be measured by the areas under the stress-strain curve. In the comparison of the magnitude and shape of the stress-strain curves obtained from specimens machined in the longitudinal and circumferential direction, the anisotropic behaviors can be clearly seen. The circumferential stress-strain curve generally lies over the longitudinal stress-strain curve. Fig. 5.1 (b) enlarges the yielding region of the

stress-strain curves and shows that the circumferential yielding is more flat and tend to have a distinct yield point while the longitudinal yielding is gradual. The anisotropic behavior is more significant in high strength steel pipes than low strength steel pipes. The anisotropic behavior is the reason that there is a high discrepancy between the buckling experimental results and buckling models of the high strength steel (Neupane, 2012; Fathi, 2012).



(a)



(b)

Fig. 5.1 Comparison of true stress-strain curves of different grades of pipe (a) up to ultimate tensile strength at uniform strain; (b) up to strain value of 0.02

Table 5.1 Comparison of different grades of steel pipes

Steel Pipes		Test Pipe Dimensions			Material properties					
Grades	Specimen	Nominal Outside Diameter (mm)	Nominal Wall Thickness (mm)	D/t Ratio	Modulus of Elasticity (GPa)	Yield Strength		Ultimate tensile strength (MPa)	Y/T Ratio	Uniform Strain
						Measured at 0.5% strain (MPa)	Measure at 0.2% offset			
X100	Longitudinal Strip	762	12.7	60	170	620	633	855	73%	3.8%
	Circumferential Round				168	735	790	880	82%	4.8%
X80	Longitudinal Strip	762	12.7	60	170	580	602	738	79%	4.3%
	Circumferential Round				232	702	700	757	93%	2.2%
X65	Longitudinal Strip			34	210	497		641	78%	8.6%
X60	Longitudinal Strip			79	208	490		630	78%	9.5%
X52	Longitudinal Strip	324	6.9	47	199	418	411	573	72%	14.4%
	Circumferential Round				226	446	446	579	77%	7.3%

5.3 Prediction of the Tensile Strain Capacity

The tensile strain capacity of pressurized pipelines is reduced in the presence of girth weld defects under axial tensile and bending stresses. Many studies in the literature tried to experimentally and numerically investigate this reduction as a function of the material properties of the pipe and defect geometries.

5.3.1 Introduction of CSA Z662-11 Equations

CSA Z662-11 provides a set of equations for predicting the tensile strain capacity of flawed pipes. Two possible weld defects are specified, which are surface-breaking defects and buried defects in the pipe wall (Fig. 5.2). The surface-breaking defects are connected to the surface of the pipe while buried defects are not. The relationship between the longitudinal tensile strain capacity and the possible weld defects have been further studied. Their relationships are summarized as a form of generally conservative equations. They are derived from extensive experimental results of modern steel pipelines with high toughness on curved wide plates with particular prefabricated defects, and the pressure effects are excluded. The equation of determining longitudinal tensile strain capacity ε_t^{crit} is a function of apparent crack-tip opening displacement, surface-breaking or buried defect size, and strength properties of the material. CSA Z662-11 stipulates that a valid value of ε_t^{crit} should not exceed one third of the uniform strain ε_u from the standard tension test.

For surface-breaking defects:

$$\varepsilon_t^{crit} = \delta^{(2.36-1.58\lambda-0.101\xi\eta)} (1 + 16.1\lambda^{-4.45}) (-0.157 + 0.239\xi^{-0.241}\eta^{-0.315})$$

For buried defects:

$$\begin{aligned} \varepsilon_t^{crit} = & \delta^{(1.08-0.612\eta-0.0735\xi+0.364\psi)} (12.3 - 4.65\sqrt{t} + 0.495t)(11.8 - 10.6\lambda)(-5.14 \\ & + \frac{0.992}{\psi} + 20.1\psi)(-3.64 + 11.0\sqrt{\eta} - 8.44\eta)(-0.836 + 0.733\eta \\ & + 0.0483\xi + \frac{3.49 - 14.6\eta - 12.9\psi}{1 + \xi^{1.84}}) \end{aligned}$$

where

δ is the apparent crack-tip opening displacement toughness (mm), $0.1 \leq \delta \leq 0.3$

λ is the ratio of the yield strength to tensile strength, shown by Y/T , $0.7 \leq \lambda \leq 0.95$

ξ is the ratio of defect length to pipe wall thickness ($2c/t$), $1 \leq \xi \leq 10$

η is the ratio of defect height to pipe wall thickness (a/t for surface breaking defects or $2a/t$ for buried defects), $\eta \leq 0.5$

ψ is the ratio of defect depth to pipe wall thickness (d/t)

t is the pipe wall thickness (mm)

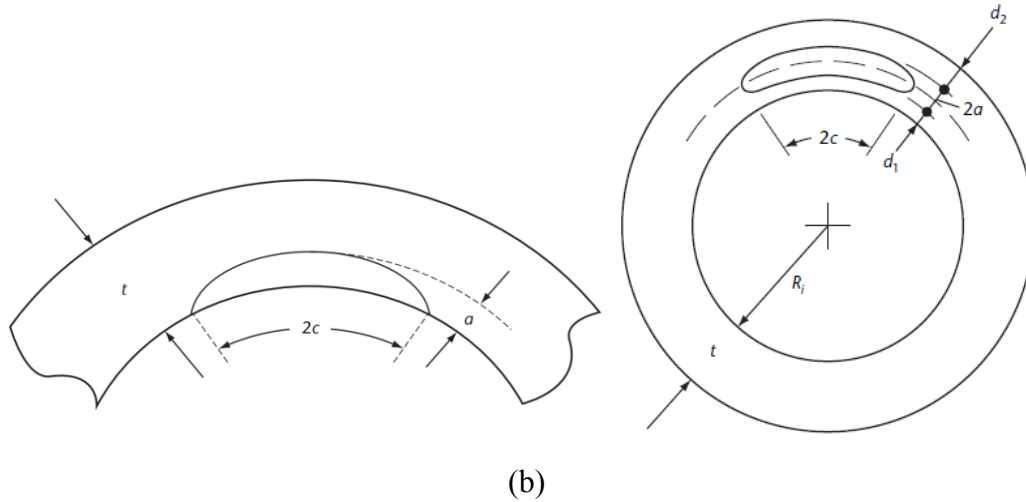


Fig. 5.2 A planar defect in the pipe wall (a) surface-breaking defect; (b) buried defect (From Z662-11, pp. 379)

According to CSA Z662-11, the apparent crack-tip opening displacement toughness δ should be measured in a low-constraint condition from the test, which is the common loading condition of pipelines subjected to the longitudinal strains. If δ is measured in a high-constraint condition from standard three-point CTOD tests, the value must be checked against the maximum valid high-constraint crack-tip opening displacement toughness δ_{max}^{HC} , which is a function of the minimum value of the specimen thickness and ligament χ and strain hardening exponent n in the Ramberg-Osgood stress strain relation, and given by $\delta_{max}^{HC} \leq 0.04\chi \left[3.69 \left(\frac{1}{n} \right)^2 - 3.19 \left(\frac{1}{n} \right) + 0.882 \right]$. A valid δ_{max}^{HC} is limited to less than $\frac{0.2}{30} CVN_{min}$ and $\frac{0.2}{45} CVN_{avg}$. In the absence of test data from CTOD test, δ is taken as 0.3mm which is an estimated value from Charpy V-notch impact test (Table 4.5). This value is in the range of $0.1 \leq \delta \leq 0.3$ and can be used in the CSA equations.

5.3.2 Calculation of Tensile Strain Capacity

In order to calculate the tensile strain capacity of X52 pipes, the strength properties such as the yield strength and the tensile strength and the uniform strain in the longitudinal direction are directly obtained from the tension tests described in Chapter 3 and summarized in table 5.2. The defect size to be used in the equations should be limited in a possible range. Although the lower limit of η and a possible range of ψ are not indicated in CSA Z662-11, they are particularly limited in a reasonable range in this research to calculate ε_f^{crit} . The selected range of defect size over the pipe wall thickness are $1 \leq \xi \leq 10$, $0.1 \leq \eta \leq 0.5$ and $0.1 \leq \psi \leq 0.5$. Based on the upper limit, lower limit and medium point of each defect size parameters, 9 defect sizes are selected for a surface-breaking defect and 27 defect sizes are selected for buried defects to investigate the reduction caused by defects in the longitudinal tensile strain capacity of the pipe. The dimension of each defect size, and its calculated longitudinal tensile strain capacity using CSA equations are summarized in table 5.3 and 5.4.

Table 5.2 Results from tension test

Longitudinal specimens	Uniform Strain ε_u	Yield Strength (MPa)	Tensile Strength (MPa)	Y/T Ratio
Base metal	14.4%	411	573	0.72
New HAZ	9.8%	428	554	0.77
Average	12.1%	420	564	0.75

Table 5.3 Determination of ε_t^{crit} for a surface-breaking defect

Surface-breaking Defect #	Wall Thickness t (mm)	CTOD δ (mm)	Y/T Ratio λ	2c/t ξ	a/t η	Defect Length 2c (mm)	Defect Height a (mm)	ε_t^{crit}	Valid ε_t^{crit} ($\leq 1/3\varepsilon_u = 4.03\%$)
1	6.86	0.3	0.75	10	0.5	70	3.5	0.36%	0.36%
2					0.3		2	0.90%	0.90%
3					0.1		0.7	2.04%	2.04%
4				6	0.5	40	3.5	0.74%	0.74%
5					0.3		2	1.24%	1.24%
6					0.1		0.7	2.52%	2.52%
7				1	0.5	7	3.5	2.13%	2.13%
8					0.3		2	2.86%	2.86%
9					0.1		0.7	4.88%	4.03%

Table 5.4 Determination of ε_t^{crit} for a buried defect

Buried Defect #	Wall Thickness t (mm)	CTOD δ (mm)	Y/T Ratio λ	2c/t ξ	2a/t η	d/t ψ	Defect Length 2c (mm)	Defect Height 2a (mm)	Defect Depth d (mm)	ε_t^{crit}	Valid ε_t^{crit} ($\leq 1/3\varepsilon_u = 4.03\%$)	
1			0.75	10	0.5	0.5	70	3.5	3.5	0.78%	0.78%	
2									0.3	2	0.37%	0.37%
3									0.1	0.7	0.41%	0.41%
4					0.3	0.5		2	3.5	2.16%	2.16%	
5						0.3			2	1.21%	1.21%	

6	6.86	0.3			0.1		0.7	0.7	1.75%	1.75%				
7								0.1	0.5	3.5	18.4%	4.03%		
8											0.3	2	10.4%	4.03%
9				0.1	0.7	10.9%	4.03%							
10				6	0.5	40	3.5	3.5	2.24%	2.24%				
11								2	1.24%	1.24%				
12								0.7	1.74%	1.74%				
13								0.3	0.5	2	3.5	3.75%	3.75%	
14											0.3	2	2.10%	2.10%
15											0.1	0.7	3.02%	3.02%
16				0.1	0.5	0.7	3.5	23.7%	4.03%					
17							0.3	2	13.5%	4.03%				
18							0.1	0.7	19.7%	4.03%				
19				1	0.5	7	3.5	3.5	14.7%	4.03%				
20								2	7.5%	4.03%				
21								0.7	9.2%	4.03%				
22					0.3		0.5	2	3.5	17.4%	4.03%			
23									0.3	2	8.0%	4.03%		
24									0.1	0.7	8.0%	4.03%		
25					0.1		0.5	0.7	3.5	70.7%	4.03%			
26									0.3	2	26.2%	4.03%		
27									0.1	0.7	9.8%	4.03%		

For very small defects, CSA equations result in high values of longitudinal tensile strain capacity ε_t^{crit} , which is unreasonable for pipes. Therefore the upper limit value of ε_t^{crit} is indicated to be $1/3\varepsilon_u$, which is 4.03% for the research X52 pipe.

5.3.3 Effects of Defect Size on the Tensile Strain Capacity

The value of ε_t^{crit} as a function of the defect size to pipe wall thickness ratios are plotted and shown in Fig. 5.3 and Fig. 5.4. The calculated values of ε_t^{crit} using the CSA equation are coloured in blue and the upper limit 4.03% value is coloured in black. For a surface-breaking defect, Fig. 5.3 clearly shows that ε_t^{crit} reduces as ξ (or $2c/t$) or η (or a/t) increases. For a buried defect, two variable defect parameters with an assumed constant defect parameter are used to investigate the relationship between ε_t^{crit} and the buried defect size. The relationship based on a constant ξ (or $2c/t$) = 6, η (or $2a/t$) = 0.3, or ψ (or d/t) = 0.3 is shown in Fig 5.4, while those based on other constant parameters corresponding to the lower or upper limit in the possible range are shown in Appendix D, which are $\xi=1$, $\xi=10$, $\eta=0.1$, $\eta=0.5$, $\psi=0.1$, and $\psi=0.5$. Fig.4.9 (c) clearly shows that ε_t^{crit} reduces as ξ or η increases, while Fig.5.3 (a) and (b) show that ε_t^{crit} reduces as ψ increases to a value around 0.22 and then surprisingly increases. The variable decrement and increment are the calculations from the empirical CSA equation, which is unreasonable for pipes. The equation may be more appropriate to determine ε_t^{crit} with a small buried defect depth to wall thickness ratio (less than 0.22). In addition, the buried defect width is more critical than its depth in reducing the longitudinal tensile strain capacity of the pipe. This is supported by ε_t^{crit} calculated from $\eta=0.5$ and $\psi=0.3$ smaller than that calculated from $\eta=0.3$ and $\psi=0.5$ based on a constant $\xi=10$ or 6 in the Table 5.3. In conclusion, the reduction of ε_t^{crit} is caused by the growth of the defect and the upper limit value of the longitudinal tensile strain capacity (ε_t^{crit}) of the test welded X52 steel pipe is predicted to 4.03% according to CSA Z662-11.

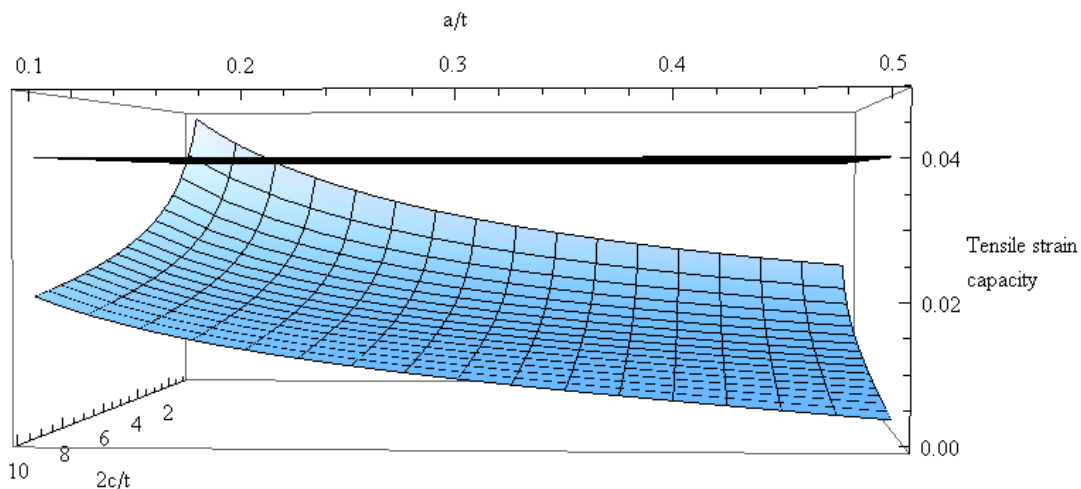


Fig. 5.3 Longitudinal tensile strain capacity as a function of two surface-breaking defect parameters ξ or $2c/t$ and η or a/t

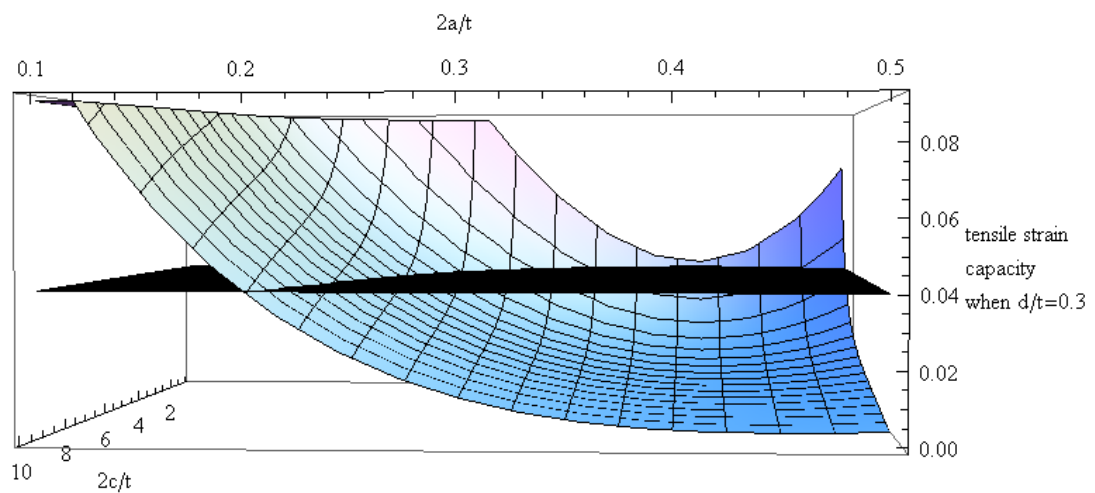
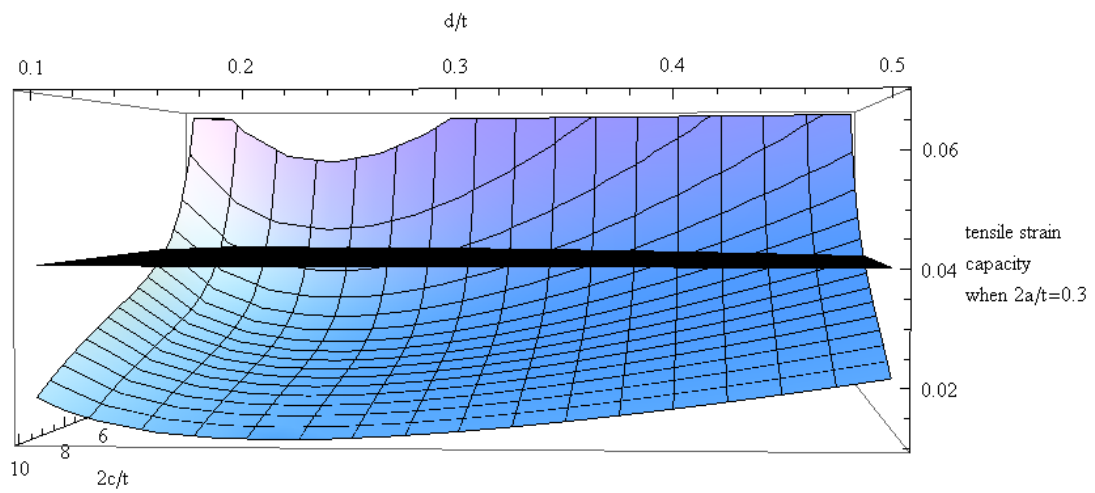
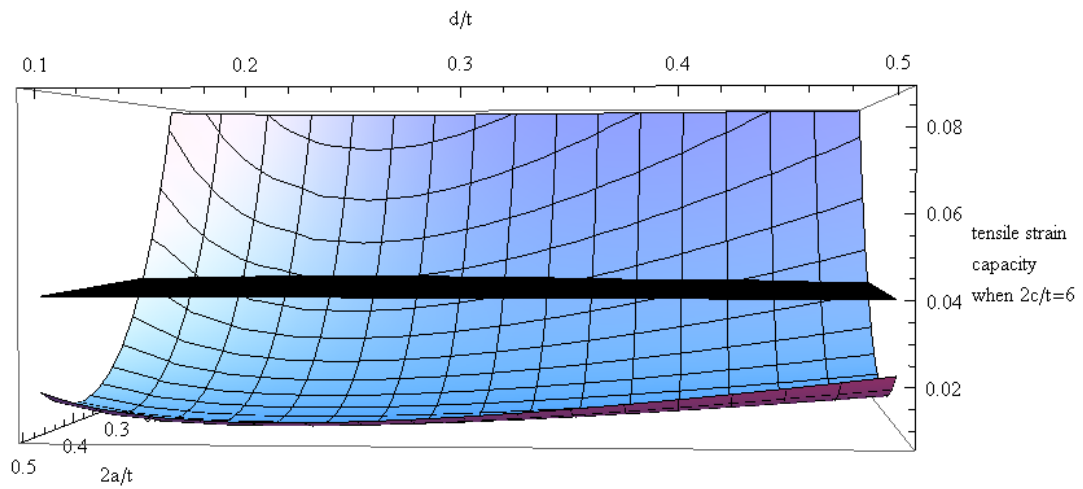


Fig. 5.4 Longitudinal tensile strain capacity as a function of two buried defect parameters and a constant buried defect parameter (a) ξ or $2c/t = 6$; (b) η or $2a/t = 0.3$; (c) ψ or $d/t = 0.3$

5.3.4 Limitation of CSA Z662-11 Equations

The limitation of the equations should be carefully studied. The equations were developed from high strength steel pipes (X80 or higher) and determined based on curved wide plate tests (CWP) without the pressure effect. Extensive full scales tests on curved wide plate with prefabricated defects in a possible range were conducted by Wang et al. (2004) and Glover et al. (1980). Numerical finite element analysis (FEA) were studied by Wang et al. (2002). ABAQUS was utilized to model various defect size, pipe toughness and weld strength mismatch level for calculating the strain capacity of girth welds. The conclusion of their studies is that the defect size plays a predominant role in determining the strain capacity.

However, in recent years, full scale tests on pressurized pipes were required to measure the accurate ε_t^{crit} of pipelines. In a FEA modelling of a pressurized pipe test, Minnar et al. (2007) discovered that the crack growth driving force was strengthened by the internal pressure while the material resistance to crack growth was not. This discovery was supported by Sakimoto et al. (2009) through their experimental and FEA studies. The effective opening displacement and cleavage increased as the driving force increased due to the internal pressure. The Single Edge Notch Tensile (SENT) test was suggested by Cheng et al. (2009) to measure the toughness material curves (R-curve), which are similar to those measured from full scale tests. A comparison of full scale tension tests on pressurized pipes and wide plates were carefully studied in many research. Igi et al. (2010) conducted full scale tension tests on X80 pipes and discovered that the ε_t^{crit} measured in the wide place tests were approximately two times higher than that measured in pressurized pipe tests. Stephens et al. (2010) conducted full scale tension tests with high internal pressure or low internal pressure on X65 pipes and discovered that the ε_t^{crit} was reduced considerably by high internal pressure, and the reduction was related to the yield to tensile ratio and the defect location at body pipe or heat-affected zone. Gioielli et al. (2007) and Qstby et al. (2007) obtained similar results from their experimental studies as well. Based on FEA studies on welded pipelines, the closed form, simplified strain capacity equations were developed by Kibey et al. (2010). The equations were related to various defect size, pipe geometry and pipe grades of X65 and X80, and were validated by experimental tests on pressurized pipelines. A pressure effect factor in the range of 1.5 to 2.5 was introduced by Wang et al. (2011)

based on their extensive experiments and numerical analysis on high strength steel pipes. The ε_t^{crit} measured without internal pressure were 1.5 to 2.5 times higher than that measured with internal pressure. All above research were based on pipes with defects, while Zhu and Leis (2010) did research on plain pipes and concluded that the internal pressure would reduce the ε_t^{crit} of plain pipes as well.

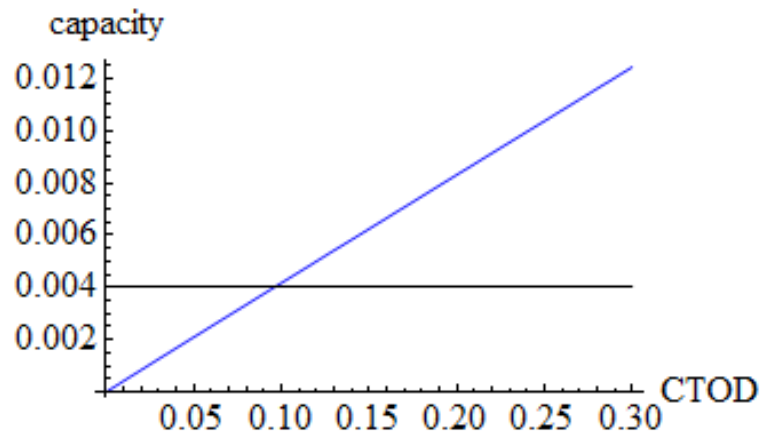
Based on above review of recent research, the reduction in the ε_t^{crit} caused by the internal pressure was examined for steel pipe of grades X65 and X80. A reasonable prediction can be made that the ε_t^{crit} measured without internal pressure should be higher than that measured with internal pressure. For this reason, the current CSA equations may over predict the longitudinal tensile strain capacity of X52 welded pipeline if the internal pressure effect is considered.

In addition, current CSA equations were validated for high strength steel pipes, but were not validated for X52 steel pipes. Even though X52 pipes have lower tensile strength, it have high ductility and toughness which were measured in previous chapters. As shown in Fig. 5.1, in comparison with higher grades of steel pipes, X52 steel pipe has highest material toughness, shown by the areas under the stress-strain curve. The relationship of longitudinal ε_t^{crit} and *CTOD* toughness based on a constant defect parameters ($\xi=6$, $\eta=0.3$, $\psi=0.3$) and a constant yield to tensile ratio ($\lambda=0.75$) is illustrated in Fig. 5.5. The value of ε_t^{crit} is increased by the increases of *CTOD* toughness. For this reason, the current CSA equations may result in conservative value of longitudinal tensile strain capacity of welded X52 pipeline because of its high ductility and toughness.

As a result, the current CSA equations may not be able to determine the accurate longitudinal tensile strain capacity of welded X52 pipes. Full scale pressurized tests on X52 steel pipes are necessary to check the validity of the current CSA equations.

Surface-breaking Defect:

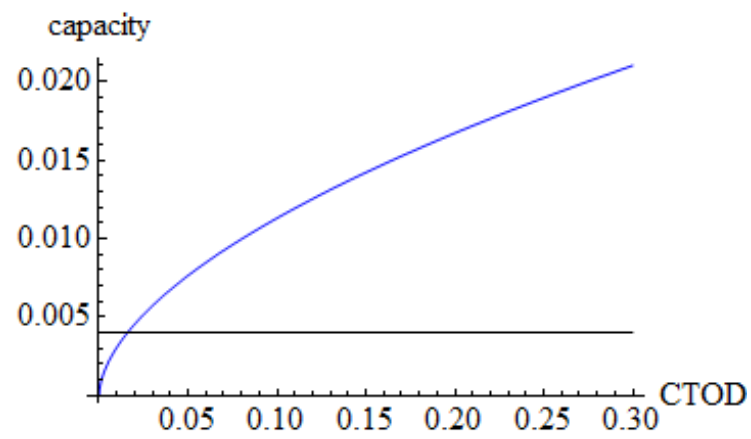
Tensile strain



(a)

Buried Defect:

Tensile strain



(b)

Fig. 5.5 Longitudinal tensile strain capacity as a function of crack-tip opening displacement toughness based on constant $\lambda=0.75$, $\xi=6$, $\eta=0.3$, $\psi=0.3$ (a) surface-breaking defect; (b) buried defect

6. Summary, Conclusion, and Future Direction

6.1 Summary

Enbridge vintage X52 steel pipeline has been used to transport crude oil from Norman Wells, Northwest Territories (NWT) to places of consumption to fuel the lives of people since 1980s. The harsh climate and difficult terrain in Norman Wells result in potential threats to pipelines buried out of sight beneath the ground, as a form of imposing substantial external stresses and strains caused by impact and displacement from geotechnical instability. Therefore, it is significant to investigate the resistance of the pressurized pipeline in response to the external loadings. In addition, Enbridge integrity personnel need to understand the tensile strain capacity of their vintage pipes in case of the discovery of any weld defects. Currently, they don't have a clear understanding of how applicable the equations are to their pipes and this study is a part of a large study where the tensile strain capacity of these pipes are tested. This thesis investigated the tensile and fracture behaviors of vintage X52 steel pipes and focused on the small scale material tests. The pipe for the use of the research was provided by Enbridge Pipelines Inc., and has a wall thickness of 6.86 mm (0.27 inch) and an outer diameter of 324 mm (12.75 inch) (NPS 12). It has a girth weld which was manufactured in 1980s (labeled as "old") and another girth weld which was manufactured in 2013 (labeled as "new"). A series of tension tests and Charpy V-notch impact tests were conducted at the University of Alberta to accurately measure the tensile and fracture properties of the base pipe and two girth welds. The stress-strain curves obtained from X52 steel pipe in tension test were used to compare with those obtained from other higher grades of steel pipes, such as X60, X65, X80, and X100. The comparison contributed to understanding the difference between low and high strength of API X-grade steel pipes. Based on the test results, the longitudinal tensile strain capacity (ϵ_t^{crit}) of X52 steel pipe based on a selected defect or crack size was predicted using the empirical equation provided by CSA Z662-11. The tensile strain capacity is a function of apparent crack-tip opening displacement, surface-breaking or buried defect geometry, and strength properties of the material, and should not exceed one third of the uniform strain (ϵ_u).

In the tension tests, a total of 25 specimens were machined from the base metal, the

weld metal, and the heat-affected zone (HAZ) and tested at room temperature and compared through both engineering and true stress-strain curves. 12 standard rectangular specimens and 13 small-size round specimens were designed in accordance with ASTM E8/E8M-11 and machined from the longitudinal direction and circumferential direction of the pipe respectively. Young's modulus, yield strength, and tensile strength were measured from the experimental true stress-strain curves. Ductility was determined by elongation at fracture or reduction of cross-sectional area at necking. Strain-hardening and necking were observed by plotting the stress-strain curves. Strain-hardening region of the curve were particularly characterized into the empirical mathematical expressions known as the Hollomon equation and the Ramberg-Osgood equation. The necking and ductile fracture were observed during the tests and shown by the final fracture appearance. All produced stress-strain curves and important tensile properties were compared in the specimens machined from different locations of the pipe, such as the base metal/weld metal/HAZ, the old weld metal/new weld metal, or the longitudinal direction/circumferential direction of the pipe. In order to eliminate the dynamic loading effects, all tests were conducted in a relative low loading rate, and some test were even manually stopped several times to record quasi-static data.

In the Charpy V-notch impact tests, a total of 24 sub-size specimens were machined with a V-notch from the base metal, the weld metal, and the heat-affected zone (HAZ) and tested at room temperature or a lower temperature. All specimens were designed in accordance with ASTM 23-07 and machined from the longitudinal direction of the pipe. 13 specimens were tested at a room temperature ranging from 19°C~23°C, 10 specimens were tested at a lower temperature ranging from -21°C~-29°C, and 1 old weld metal specimen was particularly tested at -78°C. The impact toughness were measured by the energy required to fracture the specimen. The ductility was determined by fracture appearance. By testing specimens at different temperature, the temperature effects on material resistance were studied through CVN energy values and shear-lips regions. All experimental results were compared in specimens with notch machined from different locations of the pipe, such as the base metal/weld metal HAZ and the old/new weld metal. Fracture mechanics were particularly studied and the unavailability of conducting a fracture toughness test was explained because of the relatively strict requirements to specimen thickness. Alternatively, an empirical

correlation between experimental CVN energy data and fracture toughness parameters, such as plane-strain stress intensity factor (K_{Ic}), J - integral value (J_{Ic}), or critical crack-tip opening displacement (δ_{Ic}) were investigated. A comparison with higher grade of API X-grade steel pipes for fracture toughness were discussed to better understand the results of X52 research pipe.

6.2 Conclusion

By conducting a series of tension tests, three important conclusions about the tensile properties of X52 steel pipes are given. Firstly, the girth weld and its ambient HAZ have higher tensile strength than the pipe base no matter specimens are machined in the longitudinal or circumferential direction of the pipe. The pipe base shows an obvious higher ductility in the longitudinal direction, but slightly less ductility in the circumferential direction than the weld metal and the HAZ. The axial toughness measured by Young's modulus is not affected much by different locations. Secondly, the pipe shows anisotropic behaviors because the measured strength, ductility, and axial stiffness vary in the various direction. When comparing the longitudinal direction with the circumferential direction, the yield strength, tensile strength and axial stiffness are all higher in the circumferential direction of the pipe, while the ductility is higher in the longitudinal direction. In addition, the pipe base shows gradual yielding in the longitudinal direction of pipe, while it shows a well-defined yield point followed by the yielding plateau in the circumferential direction of the pipe. The anisotropic behaviors have great influence on the compressive strain capacity and buckling response. Thirdly, the field girth weld that manufactured in 1980s has less strength and toughness compared to the new girth weld that manufactured in 2013. In addition, a great variation in strength and ductility were measured from the two old weld metal specimens and two old HAZ specimens in tension tests. The new girth weld was manufactured in the machine shop and it had a well-controlled welding environment than the field girth welding. By comparing stress-strain curves between X52 steel pipes and other higher grades of steel pipes (X60, X65, X80, and X100), X52 steel pipe is able to resist higher deformation but lower yield and tensile strength. Good ductility makes X52 steel pipes deform considerably without fracture and provides a useful warning of safety. It is worth noting that the tensile properties are determined from two types of test specimens whose shape and size are significantly different, and specimens are machined from the

various location and orientation of the pipe. All the above variables contribute to different values of the tensile properties. As a result, it is conservative to take the average test results obtained from rectangular specimens machined from the base metal in the longitudinal direction of the pipe as the final values of the tensile properties of Enbridge Norman Well X52 pipes in this research. The Young's modulus is about 200 MPa, the yield strength is about 420 MPa, and the tensile strength is about 570 MPa at the uniform strain of 14%. The elongation is about 35% based on 50mm gauge length, and the reduction of cross sectional area is about 68%. The strain hardening of the true stress-strain curve is characterized by the Hollomon equation $\sigma = K \varepsilon_p^n$, where the strain hardening exponent $n=0.12$ and the strength coefficient $K=720$, and characterized by the Ramberg-Osgood equation $\varepsilon = \frac{\sigma}{E} + K_{RO} \left(\frac{\sigma}{E}\right)^{n_{RO}} = \frac{\sigma}{E} + \alpha \frac{\sigma_y}{E} \left(\frac{\sigma}{\sigma_y}\right)^{n_{RO}}$, where the strain hardening exponent $n_{RO}=8.45$, strength coefficient $K_{RO}=4.7 \times 10^{20}$, and another important coefficient $\alpha=4.84$.

By conducting a series of Charpy V-notch impact tests, four important conclusions about the impact toughness of X52 steel pipes measured at room temperature are given. Firstly, the girth weld and its ambient HAZ have higher impact toughness than the pipe base in general. Secondly, the old girth weld than manufactured in 1980s has lower impact toughness than the new girth weld that manufactured in 2013 and their pipe base. Thirdly, the pipe material is very tough and ductile and the failure is predominated by stable shear fracture against impact loading at room temperature or even at a temperature as low as -21°C . By testing specimens at different temperature, the effects of temperature on impact toughness is analyzed. The material impact toughness decreases as the temperature decreases. If a curve of CVN energy as a function of temperature is plotted, the temperature range from -20°C upwards should be in the upper shelf region of the curve which corresponds to 100% shear fracture. This is the basis of good operation and function when pipeline is buried beneath the ground below 0°C . The last conclusion is the estimation of CVN ductile-brittle transition temperature (DBTT). One weld metal specimen fractured in brittle manner at -78°C , and showed significantly lower toughness and 95% brittle fracture. In the lack of large quantity of specimens, the accurate DBTT cannot be measured, but it may be within the range from -78°C to -21°C . Since DBTT of higher grade of steel pipes (X65, X70 and X80) were measured below -70°C in CVN tests from other researches. The DBTT of X52 pipe

can be estimated below $-70\text{ }^{\circ}\text{C}$ as well because of its higher toughness and ductility, and DBTT usually decreases as the strength decreases. For the research X52 steel pipe, the average of standard Charpy V-notch impact energy is about 178 Joule. Based on empirical correlations identified by Barsom and Rolfe, the fracture toughness characterized by plane-strain stress intensity factor (K_{Ic}) is estimated about $219\text{MPa} \cdot \sqrt{\text{m}}$. Based on linear elastic plane strain assumption, the fracture toughness characterized by J -integral (J_{Ic}) is estimated about 213 kJ/m^2 and characterized by critical crack-tip opening displacement (δ_{Ic}) is estimated about 0.3mm. These values indicate the fracture toughness of X52 steel pipe at the onset of ductile crack growth.

Based on obtained strength properties and crack-tip opening displacement toughness, the longitudinal tensile strain capacity (ε_t^{crit}) of X52 steel pipe was calculated as a function of the geometry of either the surface-breaking defect or buried defect according to CSA Z662-11. The upper limit value of ε_t^{crit} stipulated as one third of the uniform strain was about 4%. The presence of the defect or crack on the pipe wall would reduce the ε_t^{crit} of the pipe, and this reduction was increased by crack growth. However, the current CSA equations were not validated for the X52 steel pipe. It may over predict the longitudinal tensile strain capacity if the internal pressure effect is considered, and it may also result in conservative value of longitudinal tensile strain capacity because of the high ductility and toughness of welded X52 steel pipeline. Full scale pressurized tests on X52 steel pipes would be necessary to check the validity of the current CSA equations and modify the code equations based on the actual experimental results if possible.

6.3 Future Directions

Based on the current results and discussion of this thesis, several directions for future work are recommended. Firstly, more specimens could be manufactured from additional field girth welds to accurately determine the mechanical properties of welded X52 steel pipes in 1980s. The obtained properties from this thesis only investigating one field girth weld are not supported by large amount of test data. Secondly, Charpy V-notch impact tests could be conducted at various temperature in a large temperature range to determine the important “ductile to brittle transition temperature” shifting from predominant brittle to ductile fracture behavior. This temperature would provide a significant guideline for the selection of the material. Thirdly, low-constraint toughness tests, such as single edge notched tension (SENT) test, could be conducted to directly determine the ductile tearing resistance against to the crack extension for X52 steel pipes. This method using the shallow-cracked SENT specimens is appropriate for pipelines with thin wall thickness and relatively high toughness (Verstraete et al., 2012; Wang, et al. 2001). The conventional and standardized methods using the deep-cracked CT or SENB specimens require high levels of crack tip constraints and measure the lower bound of fracture toughness. This will lead to overly conservative estimation of the tensile strain capacity of the cracked pipeline. The critical value of J_{IC} and δ_{IC} can be determined from the measured resistance curves at the onset of ductile crack growth and can be used to check the estimated values from CVN test in this thesis. Lastly, the current prediction of the longitudinal tensile strain capacity of flawed X52 steel pipe in this thesis would be compared to the real test value in the future, thanks to the ongoing full-scale tests of X52 pipes with and without internal pressure at the University of Alberta.

References

1. Adeeb, S. (2011). *Introduction to solid mechanics and finite element analysis using Mathematica*. Dubuque, IA: Kendall Hunt Publishing Company.
2. Adeeb, S. (2012). *Plasticity*. Class lecture for course CivE664: Solid mechanics, University of Alberta, AB.
3. Adeeb, S., Zhou, J., & Horsley, D. (2006) Investigating the effect of UOE forming processes on the buckling of line pipes using finite element modeling. *ASME Proceedings of 2006 International Pipeline Conference, Volume 1* (pp. 169-174). doi:10.1115/IPC2006-10175.
4. Ahmed, A. U. (2010). *Failure criteria for tearing of telescoping wrinkles* (PhD Dissertation). Structural Engineering, University of Alberta, Edmonton, AB, Canada.
5. Alberta Energy Regulator (2013, August). *Report 2013-B: Pipeline Performance in Alberta, 1990-2012*. Retrieved from: <http://www.aer.ca/documents/reports/R2013-B.pdf>
6. Anderson, T. L. (2005). *Fracture mechanics: fundamentals and applications* (3rd ed). Boca Raton, FL: Taylor & Francis Group.
7. Angeles-Herrera, D., Albiter-Hernández, A., Cuamatzi-Meléndez, R., & González-Velázquez, J. L. (2014). Fracture toughness in the circumferential–longitudinal and circumferential–radial directions of longitudinal weld API 5L X52 pipeline using standard C(T) and nonstandard curved SE(B) specimens. *International Journal of Fracture*, 188 (2), 251-256. doi: 10.1007/s10704-014-9949-1
8. Askeland, D. R. & Phule, P. P. (2006). *The science and engineering of materials*. (5th ed). Toronto, ON: Nelson.
9. API Specification 5L (2012). *Specification for line pipe* (45th ed.). Washington, DC: American Petroleum Institute (API).
10. API 579-1/ASME FFS-1 (2007). *Fitness-for-service* (2nd ed). Washington, DC: American Petroleum Institute (API)/American Society of Mechanical Engineers (ASME).

11. Arya, A. K, Shingan, B. & Vara Prasad, Ch. (n.d.). Seismic design of continuous buried pipeline. *Research Inventy: International Journal of Engineering and Science*, India, 1(1), 6-17. Retrieved from <http://www.researchinventy.com/documents/Research%20inventy%202.pdf>
12. Askeland, D. R., & Phule, P. P. (2006). *The science and engineering of materials* (5th ed.). Toronro, ON: Nelson.
13. ASTM A370-12a (2012). *Standard test methods and definitions for mechanical testing of steel products*. West Conshohocken, PA: American Society of Testing and Materials.
14. ASTM E1290-08 (2008). *Standard test methods for crack-tip opening displacement (CTOD) fracture toughness measurement*. West Conshohocken, PA: American Society of Testing and Materials.
15. ASTM E1820-11 (2011). *Standard test methods for measurement of fracture toughness*. West Conshohocken, PA: American Society of Testing and Materials.
16. ASTM E23-07 (2007). *Standard test methods for notched bar impact testing of metallic materials*. West Conshohocken, PA: American Society of Testing and Materials.
17. ASTM E399-12 (2012). *Standard test methods for linear elastic plane-strain fracture toughness K_{Ic} of metallic materials*. West Conshohocken, PA: American Society of Testing and Materials.
18. ASTM E646-07 (2007). *Standard test methods for tensile strain-hardening exponents (n -values) of metallic sheet materials*. West Conshohocken, PA: American Society of Testing and Materials.
19. ASTM E8/E8M-11 (2011). *Standard test methods for tension testing of metallic materials*. West Conshohocken, PA: American Society of Testing and Materials.
20. AWWA. (2004). *AWWA Manual of water supply practices-Manual M11 Steel pipe-A guide for design and installation* (4th ed.). Denver, CO: American Water Works Association (AWWA).
21. Bai, Q., & Bai, Y. (2014). *Subsea pipeline design, analysis, and installation*. Waltham, MA: Gulf Professional Publishing/Elsevier.

22. Baird, J.D. (1963). Strain aging steel-A critical review. *Iron and Steel*, Vol. 36 (pp. 186-192, 400-405).
23. Baker, M. Jr. Inc. (2008). *Comparison of US and Canadian transmission pipeline consensus standards*. Prepared for US Department of Transportation Pipeline and Hazardous Materials Safety Administration Office of Pipeline Safety. Retrieved from http://primis.phmsa.dot.gov/gasimp/docs/FinalReport_TransborderStandards.pdf
24. Barsom, J. M., & Rolfe, S. T. (1999). *Fracture and fatigue control in structures* (3rd ed). Woburn, MA: Butterworth-Heinemann.
25. Baum, R. L., Galloway, D. L., & Harp, E. L. (2008). *Landslide and land subsidence hazards to pipelines*. U.S Geological Survey, Reston, Virginia. Retrieved from http://pubs.usgs.gov/of/2008/1164/pdf/OF08-1164_508.pdf
26. Baumgart, F. (2000). Stiffness - an unknown world of mechanical science? *Injury*, Vol. 31, Suppl. 2 (pp. 14-23). Elsevier. doi:10.1016/S0020-1383(00)80040-6. Retrieved from <http://www.sciencedirect.com/science/journal/00201383/31/supp/S2>
27. Bhushan, B. (2013). *Principles and applications of tribology* (2nd ed.). New York, NY: Wiley.
28. Billingham, J., Sharp J. V., Spurrier, J., & Kilgallon, P. J. (2003). Review of the performance of high strength steels used offshore. Cranfield University, Cranfield, Bedfordshire, UK. Retrieved from <http://www.hse.gov.uk/research/rrpdf/rr105.pdf>
29. Bridigum, T. (2008). *How to weld*. Minneapolis, MN: Motorbooks.
30. Brockenbrough, R. L., & Johnston, B. G. (1981). *USS steel design manual*. Pittsburgh, PA: United States Corporation.
31. Bruch, J. C. & Boeriu, S. (n.d.). *Module for plane stress and plane strain analysis. Lecture for Research: High Performance Scientific Computing*. University of California Santa Barbara, Santa Barbara, CA, USA. Retrieved from <http://www.engineering.ucsb.edu/~hpscicom/projects/stress/introge.pdf>
32. Burgess, M. M., Oswell, J., & Smith, S.L. (2010). Government-industry collaborative monitoring of a pipeline in permafrost - the Norman Wells Pipeline experience, Canada. In *GEO 2010, 63rd Canadian Geotechnical Conference and the*

- 6th Canadian Permafrost Conference* (pp. 579-586). Retrieved from <http://pubs.aina.ucalgary.ca/cpc/CPC6-579.pdf>
33. Cakiroglu, C., Adeeb, S., Cheng, J. J. R., & Sen, M. (2014). Numerical analysis of pressurized cold bend pipes under bending to investigate the transition from compression to tension side failures. *ASCE Proceedings of Structures Congress 2014* (pp. 1990-2001). doi:10.1061/9780784413357.175
 34. Cakiroglu, C., Adeeb, S., Cheng, J. J. R., & Sen, M. (2014). Design of the full scale experiments for the testing of the tensile strain capacity of X52 pipes with girth weld flaws under internal pressure and tensile displacement. *ASME Proceedings of 2014 10th International Pipeline Conference, Vol. 4*. doi:10.1115/IPC2014-33225
 35. Cakiroglu, C., Komeili A., Adeeb S., Cheng J. J. R., & Sen, M. (2012). Numerical analysis of high pressure cold bend pipe to investigate the behaviour of tension side fracture. *ASME Proceedings of 2012 9th International Pipeline Conference, Vol. 4* (pp. 273-278). doi:10.1115/IPC2012-90381
 36. Cheng, J. J. R., Sen, M., Behbahanifard, M., & Murray, D. W. (2004). *Local buckling behavior and design of cold bend pipes*. Pipeline Technology Report No. 2004-1. Structural Engineering, University of Alberta, Edmonton, AB, Canada.
 37. Cakiroglu C., Duke, K., El-Rich, M., Adeeb, S., Cheng, J. J. R., Sen, M. (2012). Influence of girth weld flaw and pipe parameters on the critical longitudinal strain of steel pipes. *ASME Proceedings of 2012 9th International Pipeline Conference, Vol. 3* (pp. 671-678). doi:10.1115/IPC2012-90736
 38. Cao, H. (2009). *Research on fracture toughness of high-grade pipeline steel for gas and oil* (MSc thesis in Chinese). Structural Engineering Wuhan University of technology, Wuhan, Hubei, China.
 39. Capelle, J., Furtado, J., Azari, Z., Jallais, S., & Pluvinage, G. (2013). Design based on Design based on ductile – brittle transition temperature for API 5L X65 steel used for dense CO₂ transport. *Engineering Fracture Mechanics 110*, 270-280. doi: 10.1016/j.engfracmech.2013.08.009
 40. Cassa, A. M. (2005). *A numerical investigation into the behavior of leak openings in pipes under pressure* (MSc thesis). University of Johannesburg, South Africa. Retrieved from <https://ujdigispace.uj.ac.za/handle/10210/464>

41. Cheng, W., Tang, H, Gioielli, P. C, Minnaar, K, and Macia, M. L. (2009). Test methods for characterization of strain capacity - comparison of R-curves from SENT/CWP/FS tests. *Proceedings of the 5th Pipeline Technology Conference*, Ostend, Belgium.
42. Chandra, N. (2001). *Fracture mechanics* [ppt]. Class lecture for course EML 3004C: Introduction to Mechanical Engineering. Florida A&M University-Florida State University (FAMU-FSU) College of Engineering, Tallahassee, FL, United States. Retrieved from <http://www.eng.fsu.edu/~chandra/courses/eml3004c/Fracturemechanics-ppt/>
43. Chen, S. (2009). *Study on test methods of fracture toughness of high grade pipeline steel* (Master thesis in Chinese). Materials Science and engineering, Xi'an Jiaotong University, Xian, Shanxi, China.
44. Clemens, K. (2005). CET 1: *Stress analysis & pressure vessels*. Class lecture for course, University of Cambridge, England. Retrieved from <http://laser.cheng.cam.ac.uk/wiki/images/2/2b/SAPV.pdf>
45. CSA Z245.1-14 (2014). *Steel Pipe* (9th ed.). Canadian Standards Association (CSA).
46. CSA Z662-11 (2011). *Oil and gas pipeline systems*. Canadian Standards Association (CSA).
47. Czicho, H., Saito, T., & Smith, L. (Eds.) (2006). *Springer handbook of materials measurement methods*. German: Springer.
48. Chan P. D. S. (1999). *Soil-pipeline interaction in slopes* (MSc Thesis). The University of Calgary.
Retrieved from <http://dspace.ucalgary.ca/bitstream/1880/42245/1/49672Chan.pdf>
49. Das, S. (2003). *Fracture of wrinkled energy pipelines* (PhD Dissertation). Structural Engineering, University of Alberta, Edmonton, AB, Canada.
50. Davis, J. R. (Eds.) (2004). *Tensile testing* (2nd ed). Materials Park, OH: American Society for Metals (ASM International).
51. Dieter, G. E. (2000). Mechanical behavior under tensile and compressive loads. In H. Kuhn & D. Medlin (Eds.), *ASM Handbook, Volume 8: Mechanical Testing and Evaluation* (pp.99-108). Materials Park, OH: American Society for Metals (ASM International).

52. Drexler, E., Wang, Y.-Y., Sowards, J. W., & Dvorak, M. D. (2010). SE(T) Testing of Pipeline Welds. *Proceedings of the 2010 8th International Pipeline Conference, Vol. 4* (pp. 149-158). New York, NY: American Society of Mechanical Engineers (ASME). doi:10.1115/IPC2010-31325
53. Drive, R. G. (2013). *Steel: Production, properties, and shapes*. Class lecture for Behavior and Design of Steel Members course, University of Alberta.
54. Enbridge Inc. (2014). *Map library*. Retrieved from <http://www.enbridge.com/MediaCentre/AssetMap.aspx>
55. Fatemi, A., Kenny, S., Sen, M., Zhou, J., Taheri, F., & Paulin, M. (2008) Investigations on the local buckling response of high strength line pipe. *ASME Proceedings of 2008 7th International Pipeline Conference, Vol. 3* (pp.649-656). doi:10.1115/IPC2008-64407.
56. Fathi, A. (2012). *Effects of material anisotropy on the buckling resistance of high strength steel pipelines* (PhD Dissertation). Structural Engineering, University of Alberta, Edmonton, AB, Canada.
57. Gao, H., Yu, Z., Zhang, Z., & Shi, H. (2010). The concepts for pipeline strain-based design. *Proceedings of the 2010 20th International Offshore and Polar Engineering Conference*. Cupertino, CA: International Society of Offshore and Polar Engineers (ISOPE).
58. GB 2038-91 (1991). *Metallic materials - Standard test method for J_{IC} , a measure of ductile fracture toughness* (in Chinese). Standardization Administration of China.
59. GB 4161-84 (1984). *Standard Test Method for Plane-Strain Fracture Toughness of Metallic Materials* (in Chinese). Standardization Administration of China.
60. Gere, J. M. & Goodno, B. J. (2012). *Mechanics of materials* (8th eds.) Stamford, CT: Cengage Learning.
61. Gioielli, P. C., Minnaar, K., Macia, M. L. & Kan, W. C. (2007). Large-scale testing methodology to measure the influence of pressure on tensile strain capacity of a pipeline.” *Proceedings of the 17th International Offshore and Polar Engineering Conference, Vol. 4* (pp. 3023-3027). Cupertino, CA: International Society of Offshore and Polar Engineers (ISOPE).

62. Glover, A. G. & Coote, R. I. (1984). Full-scale fracture tests of pipeline girth welds. In G.M. Wilkowski (Eds.), *Circumferential Cracks in Pressure Vessels and Piping – Vol. II* (pp.107-121). New York, NY: American Society of Mechanical Engineers (ASME).
63. Glover, A. G., Coote, R. I. and Pick, R. J. (1982). Engineering critical assessment of pipeline girth welds. R.W. Nichols (Eds.), *Proceedings of Conference on Fitness for Purpose Validation of Welded Construction*. Cambridge, England: Welding Institute.
64. Gomes, R.V., Aidar, C.H., & Kojima, S.S. (2004). Study of the mechanics fracture in API 5L X70 and X70 steel pipes. *Proceeding of 2004 SEM X International Congress & Exposition on Experimental & Applied Mechanics*. Retrieved from <http://sem-proceedings.com/04s/sem.org-SEM-X-Int-Cong-s049p01-Studey-Mechanics-Fracture-API-5L-X70-X70-Steel-Pipes.pdf>
65. Guo, Y. W., You, W. Y. & Tronskar, J. P. (2008). *Development of fracture toughness using SENT specimens and validation tests on large strained pipeline weldment*. Beijing, China: International Committee of Analysis for Steel and Iron Industry (ICASI). Retrieved from http://www.analysis-training.org.cn/icas/UploadFiles_4056/200811/2008111411415179.pdf
66. Hillenbrand, H-G., & Kalwa, C. (2002). High strength line pipe for project cost reduction. *World Pipelines*, 2 (1), 1-10.
67. Hollomon, J. H. (1945). Tensile Deformation. *Transaction of the American Institute of Mining, Metallurgical and Petroleum Engineers*, Vol. 162 (pp.268-290).
68. Holt, J.M. (2000). Uniaxial tension testing. In H. Kuhn & D. Medlin (Eds.), *ASM Handbook, Volume 8: Mechanical Testing and Evaluation* (pp.124-142). Materials Park, OH: American Society for Metals (ASM International).
69. House, J.W., & Gillis, P.P. (2000). Testing machines and strain sensors. In H. Kuhn & D. Medlin (Eds.), *ASM Handbook, Vol. 8: Mechanical Testing and Evaluation* (pp. 79-92). Materials Park, OH: American Society for Metals (ASM International).
70. Igi, S., Sakimoto, T., and Endo, S. (2010). Tensile strain capacity of X80 pipeline under tensile loading with internal pressure. *Proceeding of the ASME 2010 8th International Pipeline Conference, Vol.4* (pp. 91-100).doi:10.1115/IPC2010-31281.

71. Igi, S., Sakimoto, T., and Endo, S. (2011). Effect of internal pressure on tensile strain capacity of X80 Pipeline. *Procedia Engineering*, 10, 1451-1456.
doi: 10.1016/j.proeng.2011.04.241.
72. ISO 3183 (2012). *Petroleum and natural gas industries-Steel pipe for pipeline transportation systems* (3rd ed.). International Organization for Standardization (ISO).
73. Johnson, M. R., Woodward, H., & Campbell, K. (Eds.). (2008). Best Practices. *Inspection Trends*, 11(3), 30-31. Retrieved from <http://www.aws.org/itrends/2008/07/it200807/it0708-30.pdf>
74. Juneja, B.L. (2010). *Fundamentals of metal forming process*. New Delhim India: New Age International Publisher.
75. Kailas, S.V. (n.d.). *Mechanical properties of metals*. Class lecture for course Material Science. Indian Institute of Science, Bangalore, India. Retrieved from <http://nptel.ac.in/courses/112108150/4>
76. Kailas, S.V. (n.d.). *Failure*. Class lecture for course Material Science. Indian Institute of Science, Bangalore, India. Retrieved from <http://nptel.ac.in/courses/112108150/8>
77. Kalpakjian, S., & Schmid, S. (2009). *Manufacturing engineering and technology* (6th ed.). Prentice Hall.
78. Kerlins, V., & Phillips, A. (1987). Modes of fracture. In K. Mills, J.R. Davis & J.D. Destefani (Eds.), *ASM Handbook, Volume 12: Fractography* (pp.99-108). Materials Park, OH: American Society for Metals (ASM International).
79. Khoo, H. A., Cheng, J. J. R., & Hrudey, T. M. (2000). Ductile fracture of steel. Structural Engineering Report No. 232, University of Alberta, Edmonton, AB, Canada.
80. Kibey, S., Lele, S.P., Tang, H., Macia, M.L., Fairchild, D.P., Cheng, W., Noecker, R., Woktulewicz, P.J., Newbury, B., Kan, W.C., Cook, M.F. & Hukle, M. (2011). Full-scale test observations for measurement of tensile strain capacity of welded pipelines. *Proceedings of the 21th International Offshore and Polar Engineering Conference, Vol.4*, (pp. 660-667). Cupertino, CA: International Society of Offshore and Polar Engineers (ISOPE).

81. Kibey, S., Wang, X., Minnaar, K., Macia, M.L., Fairchild, D.P., Kan, W.C., Ford, S.J., & Newbury, B. (2010). Tensile strain capacity equations for strain-based design of welded pipelines. *Proceeding of the ASME 2010 8th International Pipeline Conference, Vol. 4*, (pp. 355-363). doi: 10.1115/IPC2010-31661.
82. Kleemola, H.J., Nieminen, M.A. (1974, August). On the strain-hardening parameters of metals. *Metallurgical Transactions*, 5(8), 1863-1866. doi: 10.1007/BF02644152
83. Kocak, M., Webster, S., Janosch, J. J., Anisworth, R. A., & Koers, R. (Eds.). (2006). *FINET Fitness-for service procedure final draft MK7*. European fitness-for service thematic network – FITNET, Germany.
84. Kulak, G.L., & Grondin, G.Y. (2010). *Limit states design in structural steel* (9th ed). Markham, ON: Canadian Institute of Steel Construction.
85. Lee, J., Rainey, W., & Brunner, M. (1998, January 3). Determining wall thickness for deepwater pipelines. *Offshore*, 58 (3). Retrieved from <http://www.offshore-mag.com/articles/print/volume-58/issue-3/news/pipeline/determining-wall-thickness-for-deepwater-pipelines.html>
86. Leppin, C., Shercliff, H., Robson, J., & Humphreys, J. (n.d.) Property Definitions. In *aluMatter*. Retrieved from <http://aluminium.matter.org.uk/content/html/eng/default.asp?catid=150&pageid=2144416422>
87. Lubahn, J. D., & Felgar, R. P. (1961). *Plasticity and Creep of Metals*. Wiley, New York.
88. Lubliner, J. (2008). *Plasticity theory*. Mineola, NY: Dover Publications.
89. Lu, J.P. (1990). *Influence of strain hardening, strain aging and the Bauschinger effect on steel tubular strut load capacity* (PhD Dissertation). University of Wollongong, Wollongong, New South Wales, Australia. Retrieved from <http://ro.uow.edu.au/cgi/viewcontent.cgi?article=2248&context=theses>
90. Makar, J.M., Desnoyers, R., & McDonald, S.E. (2001). Failure modes and mechanisms in gray cast iron pipe. *Underground Infrastructure Research 2001* (pp. 1-10), Waterloo, Ontario. Retrieved from <http://www.puretechltd.com/events/2012/miami-workshop/failure%20modes%20of%20Gray%20Cast%20iron%20pipesl.pdf>

91. Wenham, M. (2001). Stiffness and flexibility. *200 science investigations for young students*, pp. 126.
92. Menon, E.S. (2005). *Gas pipeline hydraulics*. Boca Raton, FL: CRC Press/Taylor & Francis Group.
93. Minnaar, K., Gioielli, P.C., Macia, M.L., Bardi, F., & Biery, N.E. (2007). Predictive FEA modeling of pressurized full-scale tests. *Proceedings of the 17th International Offshore and Polar Engineering Conference, Vol. 4* (pp. 3114-3120). Cupertino, CA: International Society of Offshore and Polar Engineers (ISOPE).
94. Moosbrugger, C. (2002). Representation of stress-strain behavior. In Y. Tamarin (Eds.), *Atlas of stress-strain curves* (2nd ed., pp. 1-19). Materials Park, OH: American Society for Metals (ASM International).
95. Morgan, P.R., & Schmidt, L.C. (1985). *The Influence of Material Effects on Tubular Steel Strut Capacity*. Report RR/STRUCT/11/1985 (pp.1-56), University of Melbourne, Parkville, Victoria, Australia.
96. Muhlbauer, W.K. (2004). *Pipeline risk management manual: Ideas, techniques, and resources* (3rd ed). Burlington, MA: Gulf Professional Publishing/Elsevier.
97. Natural Resources Canada (2014). *Energy market fact book 2014-2015*. Retrieved from http://www.nrcan.gc.ca/sites/www.nrcan.gc.ca/files/energy/files/pdf/2014/14-0173EnergyMarketFacts_e.pdf
98. Neupane, S. (2012). *Material characterization of HSS pipes and its effects on the deformation response* (MSc Thesis). Structural Engineering, University of Alberta, Edmonton, AB, Canada.
99. Nixon, J. F., & Sortland, K. A., & James, D. A. (1990). Geotechnical aspects of northern gas pipeline design. *Proceedings of 5th Canadian Permafrost Conference, Collection Nordicana No. 54* (pp. 299-307). Laval University, Montreal, Quebec, Canada. Retrieved from <http://pubs.aina.ucalgary.ca/cpc/CPC5-299.pdf>
100. Okatsu, M., Shikanai, N., & Kondo, J. (2008). Development of a high-deformability linepipe with resistance to strain-aged hardening by HOP (Heat-treatment on-line process). *JFE GIHO* No. 17 (pp. 20-25). Retrieved from <http://www.jfe-steel.co.jp/en/research/report/012/pdf/012-03.pdf>

101. Palmer, A.C. & King, R.A. (2008). *Subsea pipeline engineering* (2nd ed.). Tulsa, Oklahoma: PennWell Books.
102. Pederson, I., Sen, M., Bidwell, A., & Yoosef-Ghods, N. (2010). Enbridge Northern pipeline: 25 years of operations, success and challenges. *ASME Proceedings of 2010 8th International Pipeline Conference, Vol. 3* (pp. 703-710). doi:10.1115/IPC2010-31611.
103. Pick, R.J., Glover, A. G. and Coote, R.I. 1980. Full Scale Testing of Large Diameter Pipelines. *Proceedings of Conference on Pipeline and Energy Plant Piping*. Pergamon Press.
104. Qstby, E. and Hellesvik, A.O. (2007). Fracture control –Offshore pipelines JIP: results from large scale testing of the effect of biaxial loading on the strain capacity of pipes with defects.” *Proceedings of the 17th International Offshore and Polar Engineering Conference, Vol.4*, (pp. 3231-3237). Cupertino, CA: International Society of Offshore and Polar Engineers (ISOPE).
105. Ramberg, W. and Osgood, W. R. (1943). *Description of stress-strain curves by three parameters*. Technical Note No. 902, National Advisory Committee for Aeronautics, Washington, DC, United States.
106. Roylance, D. (2008). *Mechanical properties of materials*. Course lecture for course. Retrieved from <http://web.mit.edu/course/3/3.225/book.pdf>
107. Schmidt, L.C., Lu, J.P., & Morgan, P.R. (1989). The influence on steel tubular strut load capacity of strain hardening, strain aging and the Bauschinger effect. *Journal of Constructional Steel Research, 14*(2), 107-119. doi: 10.1016/0143-974X(89)90018-7
108. Sharma, S.C. (n.d). *Strength of Materials*. Class lecture for course. Indian Institute of Technology Roorkee, India. Retrieved from http://nptel.ac.in/Aeronautical/Strength%20of%20Materials/course_strength%20of%20materials.pdf
109. Sen, M. (2006). *Behavior of cold bend pipes under combined loads* (PhD Dissertation). Structural Engineering, University of Alberta, Edmonton, AB, Canada.

110. Sen M., Cheng, J. J. R., & Zhou, J. (2011, May). Behaviour of cold bend pipes under bending loads. *Journal of Structural Engineering*, 137(5), 571-578.
doi:10.1061/(ASCE)ST.1943-541X.0000219.
111. Sharpy, W.N. (Eds.) (2008). *Springer handbook of experimental solid mechanics*. New York, NY: Springer Science+Business Media.
112. Shen, G., Bouchard, R., Gianetto, J. A., & Tyson, W. R. (2008). Fracture toughness evaluation of high strength steel pipe. *Proceedings of ASME 2008 Pressure Vessel and Piping Division Conference, Vol. 5* (pp. 1275-1282). Her Majesty the Queen in Right of Canada. doi:10.1115/PVP2008-61100
113. Shin, S. Y., Woo K. J., Hwang, B., Kim, S., & Lee, S. (2009). Fracture-toughness analysis in transition-temperature region of three American Petroleum Institute X70 and X80 pipeline steels. *Metallurgical and Materials Transactions A*, 40 (4), 867-876. doi: 10.1007/s11661-008-9764
114. Simonen, F.A. (n.d.). *Pressure vessels and piping systems: Reliability, risk and safety assessment*. Encyclopedia of Desalination and Water Resources (DESWARE). Retrieved from <http://www.desware.net/sample-chapters/d09/e6-165-07-00.pdf>
115. Toughness. (n.d.) In *Nondestructive Testing (NDT) Resource Centre*. Retrieved from <https://www.nde-ed.org/EducationResources/CommunityCollege/Materials/Mechanical/Toughness.htm>
116. Udomphol. T. (n.d.). *Mechanical metallurgy laboratory 6: Impact testing*. Class lecture for course. Retrieved from http://eng.sut.ac.th/metal/images/stories/pdf/Lab_6Impact_Eng.pdf
117. Universal testing machine. (n.d.). In *Wikipedia*. Retrieved from http://en.wikipedia.org/wiki/Universal_testing_machine
118. USACE EM 1110-2-6054 (2001). *Inspection, evaluation, and repair of hydraulic steel structures*. Washington, DC: US Army Corps of Engineers (USACE). Retrieved from http://www.publications.usace.army.mil/Portals/76/Publications/EngineerManuals/EM_1110-2-6054.pdf

119. Verstraete, M., Hertele, S., Waele, W. D., Denys, R., & Minnebruggen, K. V. (2012). Measurement of ductile crack extension in single edge notch tensile specimens. *Proceedings of 15th International Conference on Experimental Mechanics (ICEM 15)*. Retrieved from http://paginas.fe.up.pt/clme/icem15/ICEM15_CD/data/papers/2876.pdf
120. Wang, E., Zhou, W., Shen, Guo, & Duan, D. (2012). An experimental study on $J(CTOD)$ -R curves of single edge tension specimens for X80 steel. *Proceedings of the 2012 9th International Pipeline Conference, Vol.4* (pp. 241-248). New York, NY: American Society of Mechanical Engineers (ASME).
doi:10.1115/IPC2012-90323
121. Wang X., Kibley S., Tang H., Cheng W., Minnaar K., Macia M.L., Kan W.C., Ford S.J. & Newbury B. (2010, June). Strain-based design - Advances in prediction method of tensile strain capacity. *Proceedings of the 20th International Offshore and Polar Engineering Conference, Vol.4* (pp. 376-382). Cupertino, CA: International Society of Offshore and Polar Engineers (ISOPE).
122. Wang, Y.-Y., Liu, M., & Song, Y. (2011). *Second generation models for strain-based design*. PRCI Project ABD-1, Final report. Pipeline Research Council International (PRCI). Retrieved from <http://primis.phmsa.dot.gov/matrix/PrjHome.rdm?prj=201>
123. Water Services Association of Australia. (2012, August 28). *Failure modes in pressurized pipeline systems*. Australia: Water Services Association of Australia Limited. Retrieved from <https://www.wsaa.asn.au/Codes/Documents/Failure%20Mode%20Table%202012%20V8.pdf>
124. Welding. (n.d.) In *SteelConstruction.info*. Retrieved from <http://www.steelconstruction.info/Welding>
125. Wellman, G. W. & Rolfe, S. T. (1985). Engineering aspects of crack-tip opening displacement of fracture toughness test. In E.T. Wessel & F.J. Loss (Eds.), *Elastic-plastic fracture toughness test methods: The user's experience, ASTM STP 856* (pp. 230-262). Philadelphia, PA: American Society for Testing and Materials (ASTM).
126. Wellman, G. W., Rolfe, S. T., and Dodds, R. H. (1985). Two and three dimensional

- finite element analysis of standard three-point bend specimens. *Fracture mechanics: Sixteenth symposium, ASTM STP 868*. Philadelphia, PA: American Society for Testing and Material (ASTM).
127. White, B. (2013, July 30). *Buried Alaska gas line could face powerful bending forces*. Office of the Federal Coordinator (OFC). Retrieved from <http://www.arcticgas.gov/buried-alaska-gas-line-could-face-powerful-bending-forces>
 128. Yoo, J.-Y., Seo, D.-H., Ahn, S.-S., & Kang, K.-B. (2008). Development of X80/X100 linepipe steels with high strain aging resistance. *Proceedings of the 2008 18th International Offshore and Polar Engineering Conference, Vol.19* (pp.61-66). Cupertino, CA: International Society of Offshore and Polar Engineers (ISOPE).
 129. Yuan, H., & Brocks, W. (1998). Quantification of constraint effects in elastic-plastic crack front fields. *Journal of the Mechanics and Physics of Solids*, 46(2), 219-242.
 130. Zhang, Z., Xu, J., Nyhus, B., & Østby, E. (2010). SENT (Single edge notch tension) methodology for pipeline applications. *Proceeding of the 18th European Conference on Fracture, Vol 18* (pp.1-8). Retrieved from <http://www.gruppofrattura.it/ocs/index.php/esis/ECF18/paper/viewFile/6314/2182>
 131. Zhu, X. K., & Joyce, J. A. (2012). Review of fracture toughness (G, K, J, CTOD, CTOA) testing and standardization. *Engineering Fracture Mechanics*, 85, 1-46. doi:10.1016/j.engfracmech.2012.02.001

Appendix A - Measurement of Ductility

Table A.1 includes the measurement of reduction of cross-sectional area and elongation of for longitudinal rectangular tension specimens and Table A.2 includes the measurement of reduction of cross-sectional area and elongation of for circumferential round tension specimens. The specimens 0A, 0B, 0C, 0D, 0E and 0F were machined and tested by Qualimet Inc., while all other specimens were machined by Rejent Tool and Manufacturing Co. Ltd according to the design drawings shown in Appendix B and tested at the University of Alberta. In the table A.1, the reduction of area of every specimen was obtained by dividing the reduction of cross-sectional area by original cross-sectional area. The elongation of every specimen was manually measured after fracture, by dividing the change in gauge length by the original 50mm gauge length. For specimen 1D and 1F which fractured beyond the effective 50mm gauge length marks (Fig.3.8), alternative measurement with a longer gauge length (center 100mm between shoulders of the specimen) were used for reference only to compare each specimen's total elongation. In the table A.2, the reduction of area of every specimen was obtained by dividing the reduction of cross-sectional area by original cross-sectional area. The elongation of every specimen was directly taken as the values of engineering fracture strain recorded by the extensometer. It is noted that the specimen 2G, 2I, 3A, 3B, 2E, 2F, 3C, and 3D fractured beyond the effective 10mm measure range of the extensometer. When it happened, the extensometer stopped to measure the necking range, but still measured the center non-necking gauge length range. The strain at fracture determined by extensometer could not represent the total elongation any more. The reason for this phenomenon is that the extensometer was not installed stably on specimens by rubber bands during the test (Fig.3.9). Alternative manual elongation measurement with longer gauge length (centre 16mm between shoulders) was used for reference only to compare each specimen's total elongation.

Table A.1 Measurement of reduction of area and elongation for longitudinal rectangular tension specimens

Specimen Set	Specimen #	Reduction of Area Measurement							Total Elongation Measurement					
		Dimension of Reduced Section						Reduction of Area	Elongation (50mm Gauge Length)			Elongation (100mm Measurement)		
		Original			Final				Distance between two Marks		Elongation	Distance between two Marks		Elongation
		<i>w</i>	<i>t</i>	<i>A</i>	<i>w</i>	<i>t</i>	<i>A</i>		Original	Final		Original	Final	
		(mm)	(mm)	(mm ²)	(mm)	(mm)	(mm ²)		<i>l</i>	<i>l</i>		<i>l</i>	<i>l</i>	
						(mm)	(mm)	(mm)	(mm)					
New Base Metal	1A	12.428	6.736	83.72	7.95	3.16	25.1	70.0%	48.70	62.97	29.3%		116.61	
	1B	12.674	6.778	85.90	7.96	3.60	28.7	66.6%	48.70	64.75	33.0%		119.87	
	1C	12.644	6.820	86.23	7.85	3.67	28.8	66.6%	48.26	64.05	32.7%		119.73	
	Ave			85.3			27.5	67.7%			31.7%			
Old Base Metal	0A	37.135	6.629	246.18							39.1%			
	0B	37.440	6.604	247.25							40.7%			
	0C	37.821	6.731	254.47							35.9%			
	Ave			249.3							38.6%			
New HAZ	1D	12.478	6.024	75.17	8.15	3.27	26.7	64.6%				100	113.39	13.4%
	1E	12.476	6.006	74.93	8.10	3.26	29.2	61.1%	48.97	61.30	25.2%	100	115.16	15.2%
	1F	12.462	6.008	74.87	8.01	3.10	24.8	66.9%				100	113.69	13.7%
	Ave			75.0			26.9	64.2%						
Old HAZ	0D	19.075	6.452	123.07							24.0%			
	0E	18.898	6.528	123.36							23.9%			
	0F	18.974	6.528	123.86							25.1%			
	Ave			123.4							24.3%			

Table A.2 Measurement of reduction of area and elongation for circumferential round tension specimens

Specimen Set	Specimen #	Reduction of Area Measurement				Total Elongation Measurement				
		Dimension of Reduced Section				Reduction of Area	Elongation (10mm Gauge Length)	Elongation (16mm Measurement)		
		Original		Final			Elongation determined by Extensometer (engineering fracture strain)	Distance between two marks		Elongation
		<i>D</i> (mm)	<i>A</i> (mm ²)	<i>D</i> (mm)	<i>A</i> (mm ²)			Original	Final	
					<i>l</i> (mm)	<i>l</i> (mm)				
New Base Metal	2G	2.39	4.486	1.07	0.899	80.0%		16	18.12	13.3%
	2H	2.43	4.638	1.19	1.112	76.0%	27.9%	16	18.45	15.3%
	2I	2.44	4.676	1.11	0.968	79.3%		16	19.21	20.1%
	Average		4.600		0.993	78.4%				16.2%
New Weld Metal	2A	2.40	4.524	0.90	0.636	85.9%	28.3%	16	18.67	16.7%
	2B	2.40	4.524	0.88	0.608	86.6%	29.6%	16	19.75	23.4%
	2C	2.39	4.486	0.88	0.608	86.4%	29.4%	16	19.72	23.3%
	Average		4.511		0.617	86.3%	29.1%			21.1%
Old Weld Metal	3A	2.48	4.831	0.94	0.694	85.6%		16	18.80	18.6%
	3B	2.46	4.753	1.00	0.785	83.5%		16	18.66	16.6%
	Average		4.792		0.740	84.6%				17.6%
New HAZ	2D	2.39	4.486	1.07	0.899	80.0%	25.0%	16	19.36	21.0%
	2E	2.38	4.449	1.06	0.882	80.2%		16	18.96	18.5%
	2F	2.43	4.638	1.10	0.950	79.5%		16	19.33	20.8%
	Average		4.524		0.910	79.8%				20.1%
Old HAZ	3C	2.44	4.676	1.04	0.849	81.8%		16	19.50	21.9%
	3D	2.44	4.676	1.21	1.150	75.4%		16	18.31	14.4%
	Average		4.676		1.000	78.6%				18.2%

Appendix B - Design of test specimens

Tension test Specimens shown in Fig. B.1 and Fig. B.2 were designed according to ASTM E8/E8M-11 for tension tests. A pair of specially designed grips is shown in Fig. B.4 for testing small round specimens in Fig. B.2. The assembly of the round test specimens, designed grips and available fixtures is shown in Fig.B.5. CVN Specimens shown in Fig. B.3 were design according ASTM E23-07.

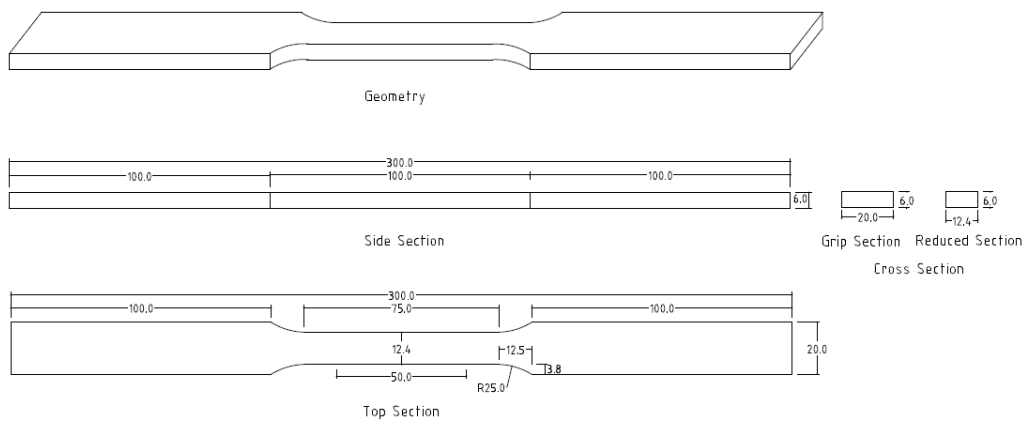


Fig. B.1 Design of rectangular tension test specimen (unit: mm)

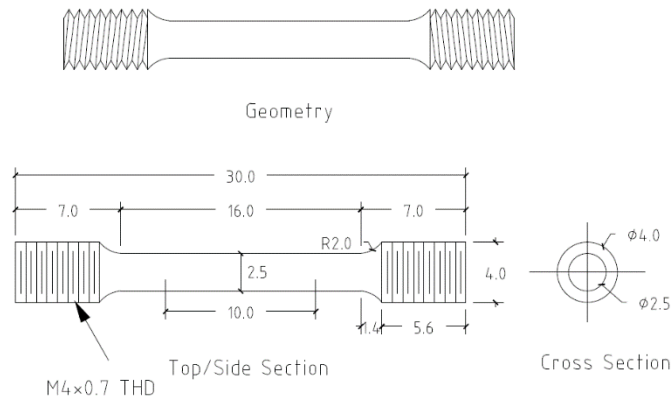


Fig. B.2 Design of round tension test specimen (unit: mm)

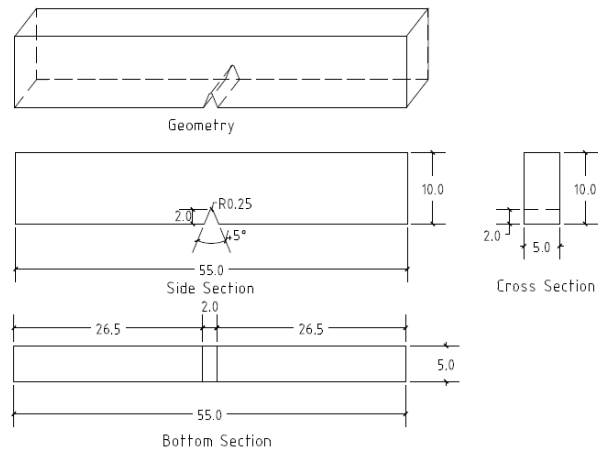


Fig. B.3 Design of subsize CVN test specimen (unit: mm)

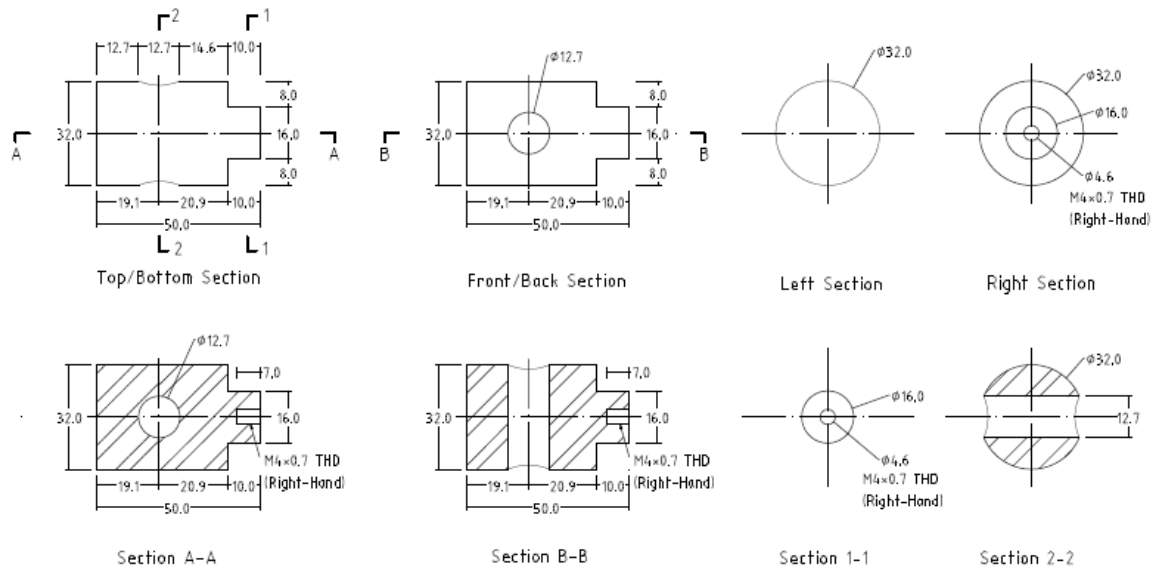


Fig. B.4 MTS end tab grip with right-hand thread (left-hand thread uses same design) (unit: mm)

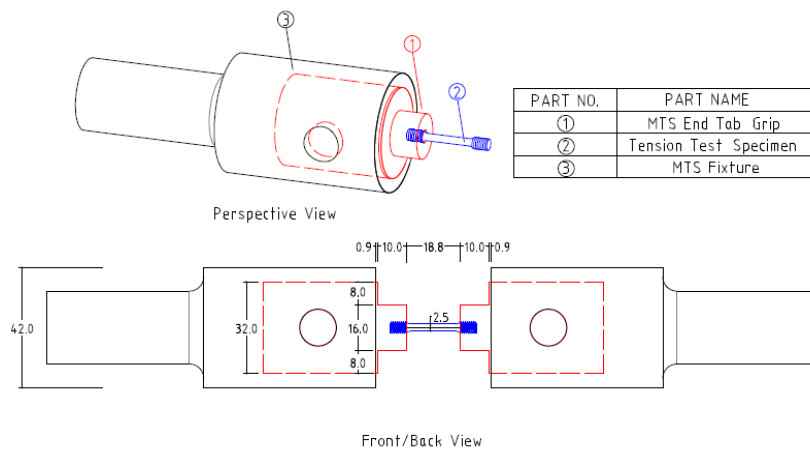


Fig. B.5 Assembly of tension test specimen, grips and fixtures (unit: mm)

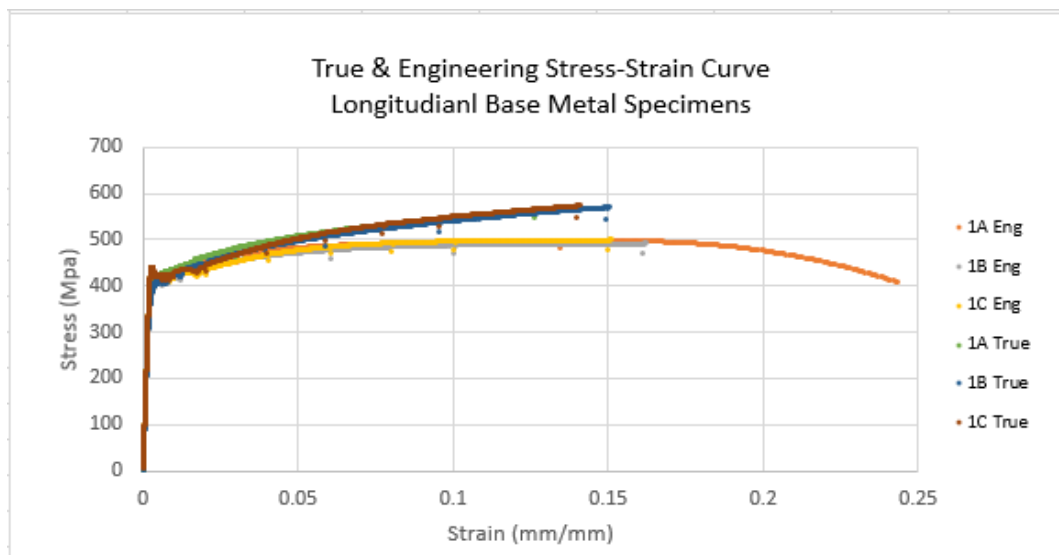
Appendix C - Test Stress-Strain Curves

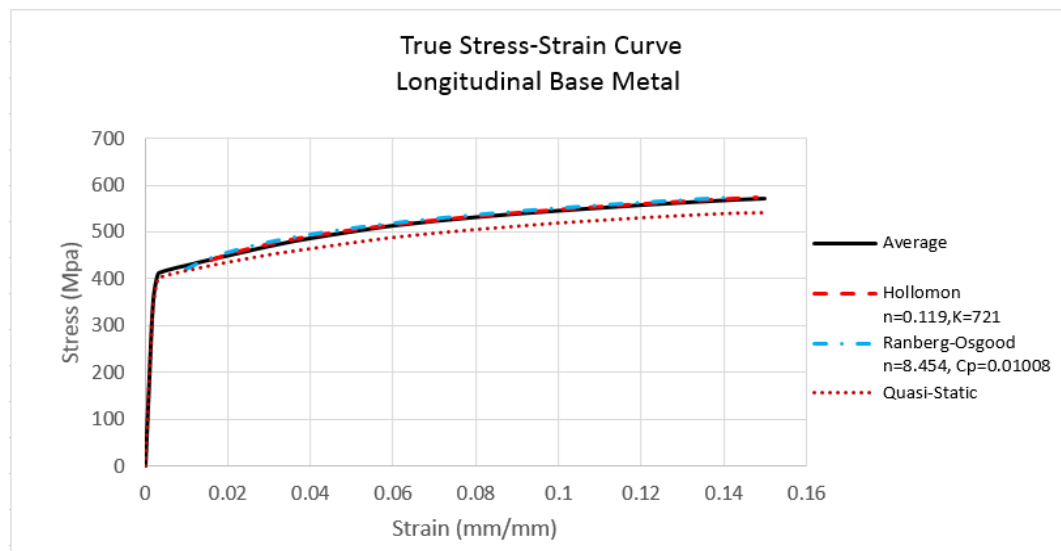
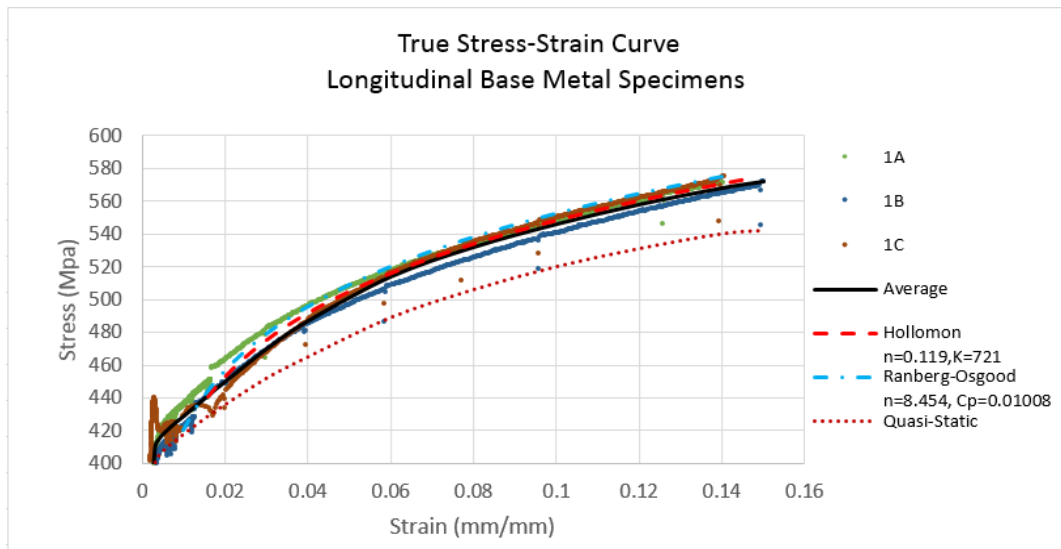
All stress-strain curves from the experimental data and the representative curves of each set of specimens are included below. Curves include the true stress-strain curves, the engineering stress-strain curves, quasi-static stress-strain curves, Hollomon power curves, and Ramberg-Osgood power curves

C.1 Stress-strain curves of Base metal (in the longitudinal or the circumferential direction)

C.1.1 Longitudinal base metal

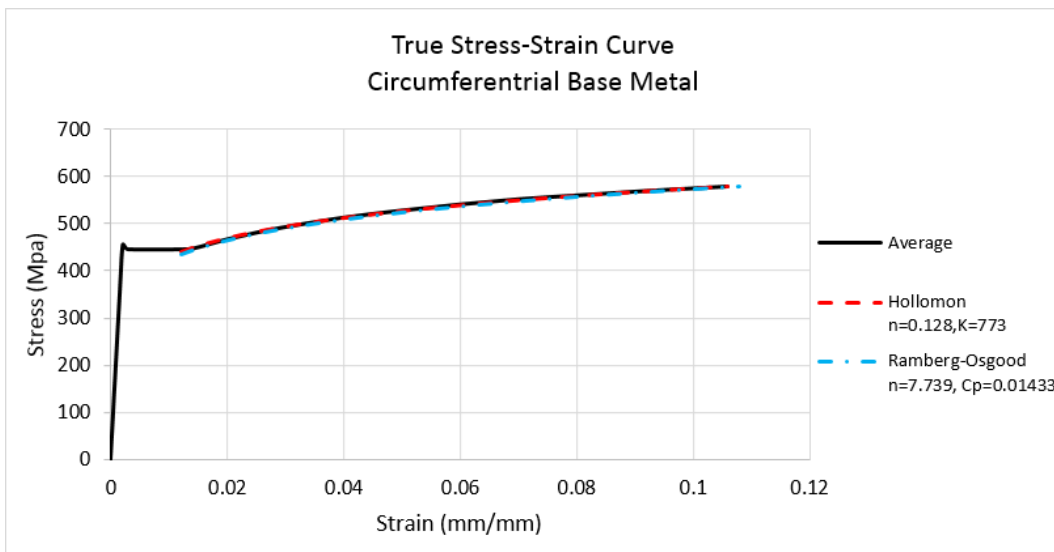
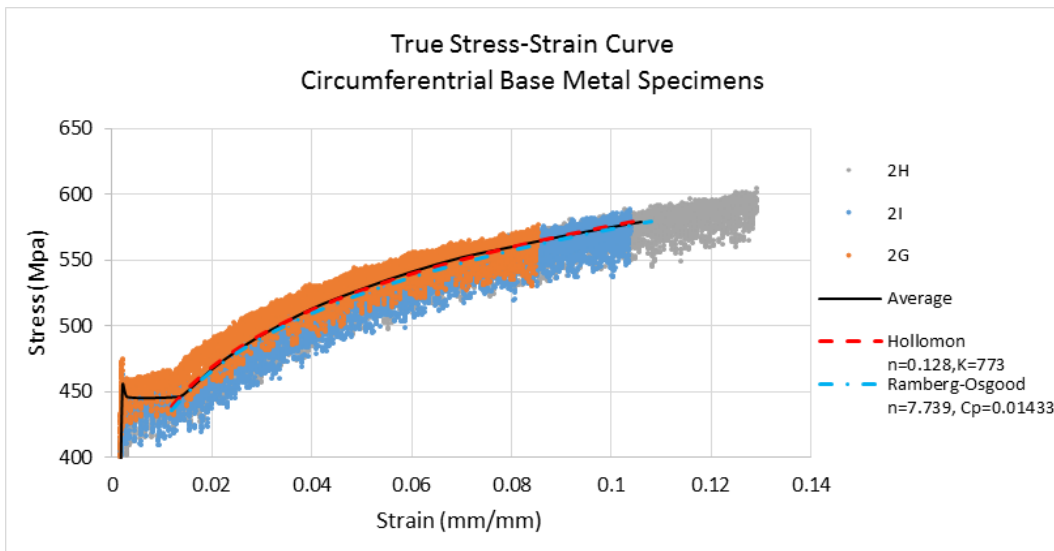
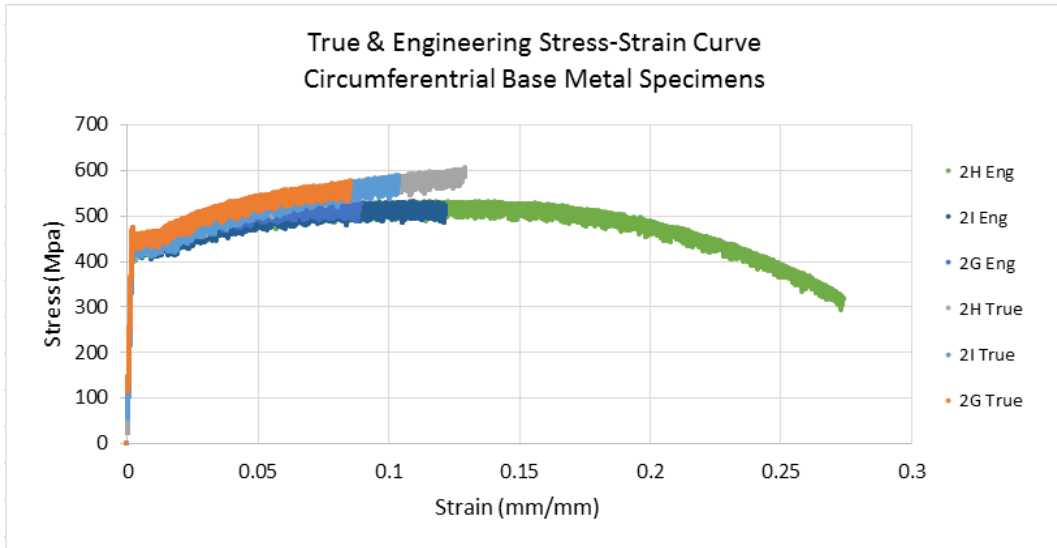
The average true stress-strain curve of three test specimens 1A, 1B, and 1C develops linearly with a slope of E which is equal to 199 GPa, then yields at 411 MPa by 0.2% offset and yields at 418 MPa at a true strain of 0.005, and lastly reaches to the ultimate true tensile strength of 573 MPa at a true uniform strain of 0.015. It matches the Hollomon power curve with $n = 0.119$ and $K = 721$ and the Ramberg-Osgood power curve with $n_{RO} = 8.454$ and $c_p = 0.01008$ well in strain hardening region after a true strain of 0.016.





C.1.1 Circumferential base metal

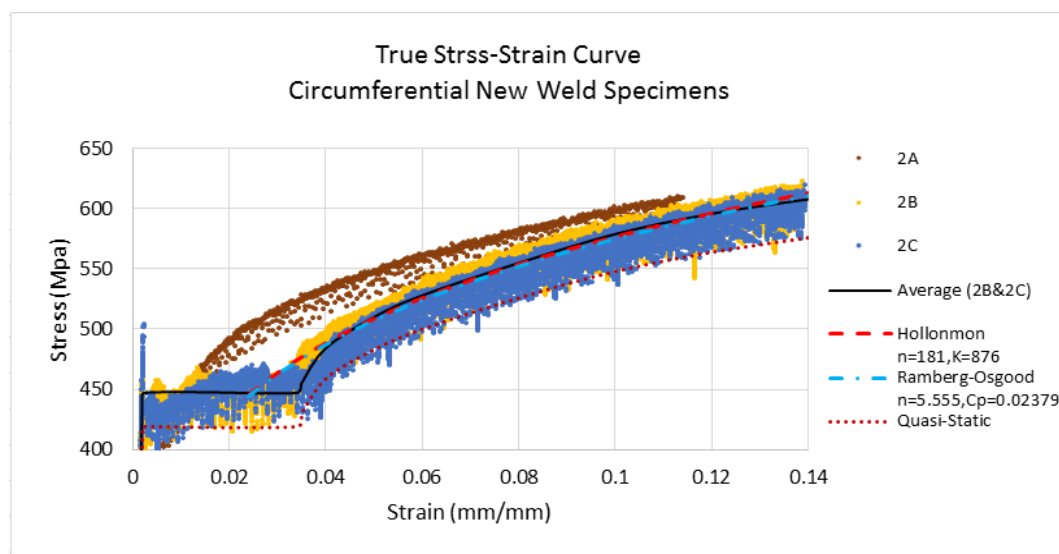
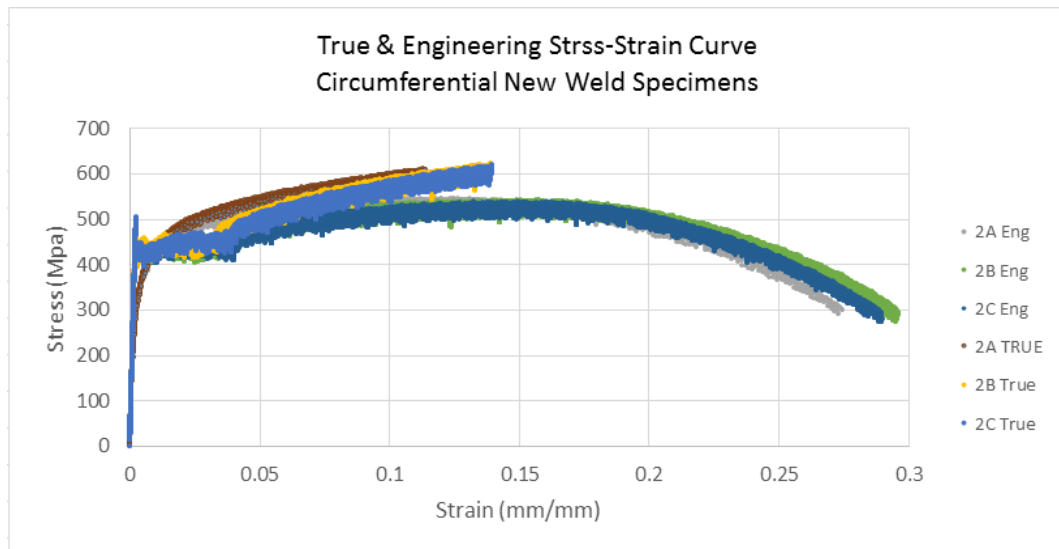
The average true stress-strain curve of three test specimens 2G, 2H, and 2I develops linearly with a slope of E which is equal to 226 GPa, then discontinuously yields at a mean stress of 446 MPa during the yield point elongation ranging from 0.002 to 0.014 true strain, and lastly reaches to the ultimate true tensile strength of 579 MPa at a true uniform strain of 0.11. It matches the Hollomon power curve with $n = 0.128$ and $K = 773$ and the Ramberg-Osgood power curve with $n_{RO} = 7.739$ and $c_p = 0.01433$ well in strain hardening region after a true strain of 0.014.

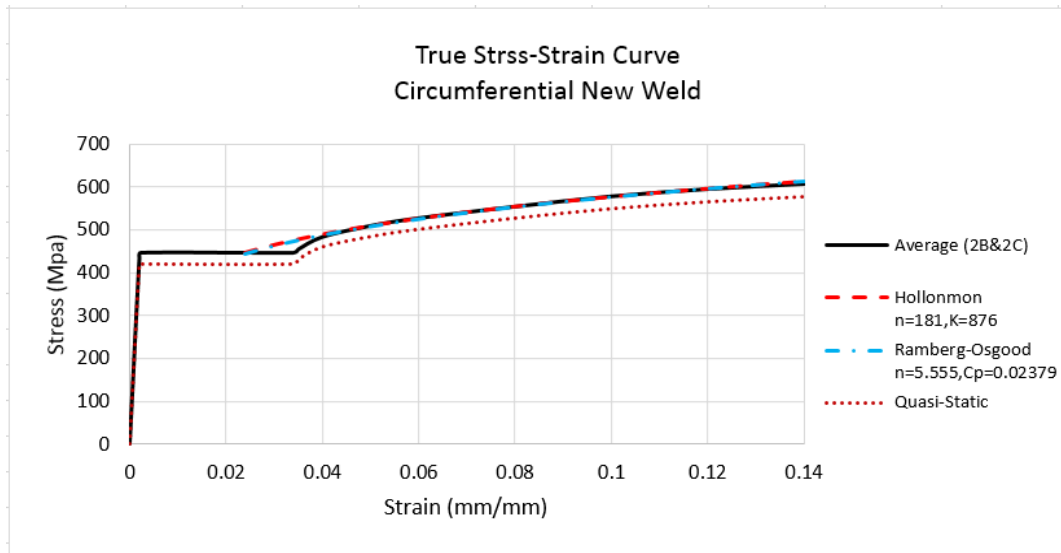


C.2 Stress-strain curves of weld metal (new and old weld metal in the circumferential direction)

C.2.1 Circumferential new weld metal

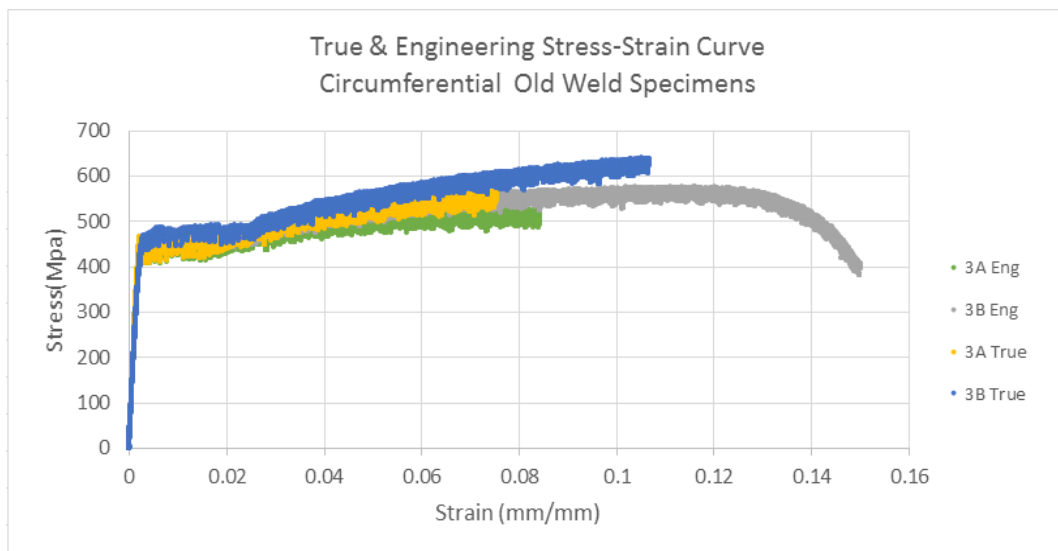
The test specimen 2A exhibits initial nonlinear elasticity range and lower yield strength due to the prior deformation caused by initial setup and calibration work. The average true stress-strain curve of two test specimens 2B and 2C (eliminating 2A) develops linearly with a slope of E which is equal to 215 GPa, then discontinuously yields at a mean stress of 448 MPa during the yield point elongation ranging from 0.0023 to 0.034 true strain, and lastly reaches to the ultimate true tensile strength of 607 MPa at a true uniform strain of 0.14. It matches the Hollomon power curve with $n = 0.181$ and $K = 876$ and the Ramberg-Osgood power curve with $n_{RO} = 5.555$ and $c_p = 0.02379$ well in strain hardening region after a true strain of 0.04.

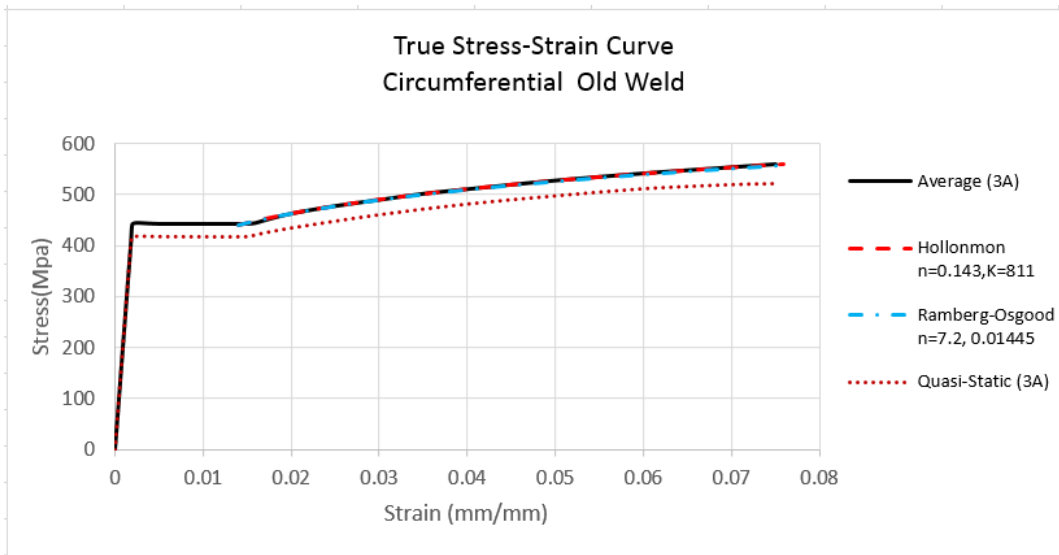
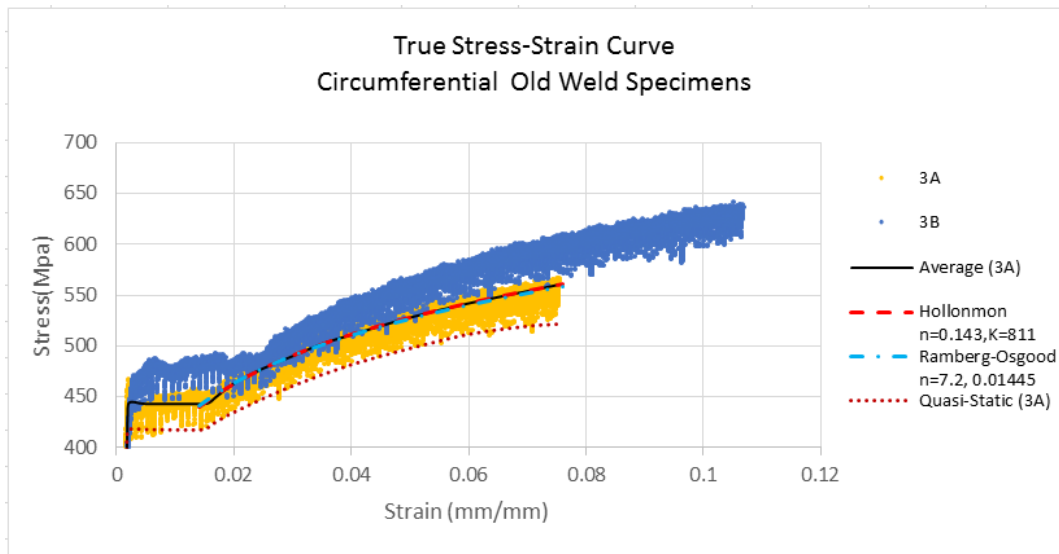




C.2.2 Circumferential old weld metal

The test specimen 3B exhibits 10% higher strength than the test specimen 3A. The average true stress-strain curve is conservatively taken as the curve obtained from the specimen 3A (eliminating 3B). It develops linearly with a slope of E which is equal to 217 GPa, then discontinuously yields at a mean stress of 443 MPa during the yield point elongation ranging from 0.002 to 0.016 true strain, and lastly reaches to the ultimate true tensile strength of 561 MPa at a true uniform strain of 0.075. It matches the Hollomon power curve with $n = 0.143$ and $K = 811$ and the Ramberg-Osgood power curve with $n_{RO} = 7.2$ and $c_p = 0.01445$ well in strain hardening region after a true strain of 0.016.



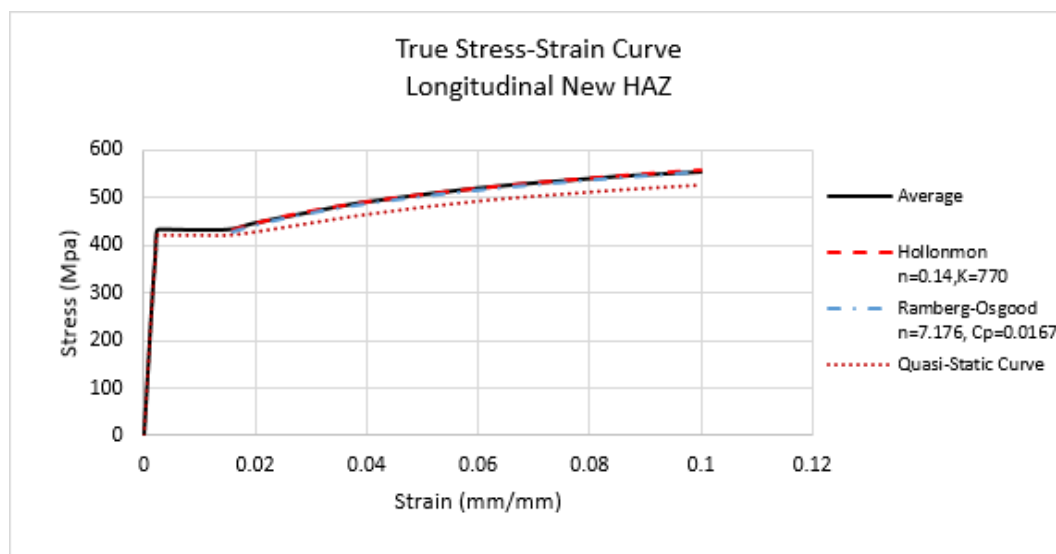
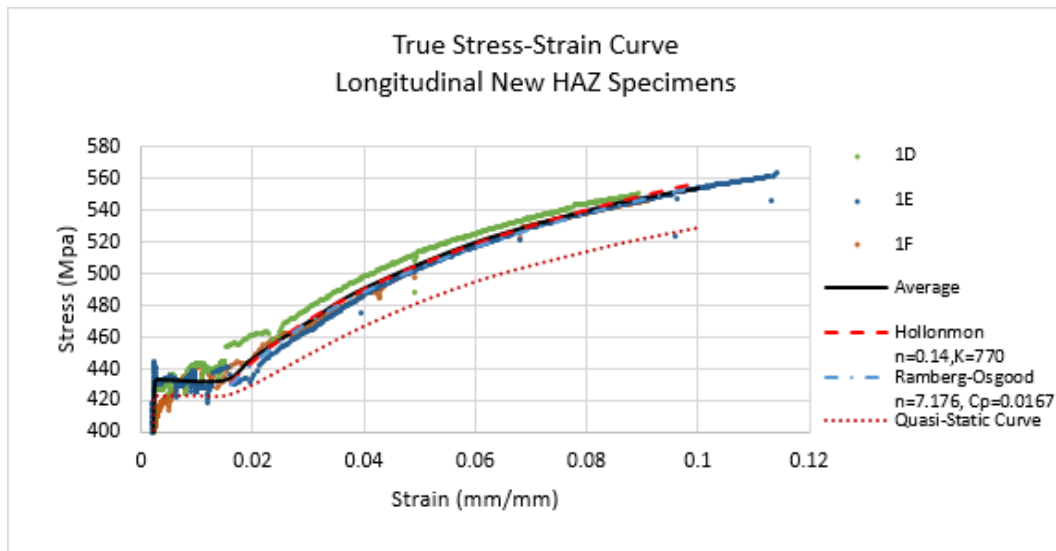
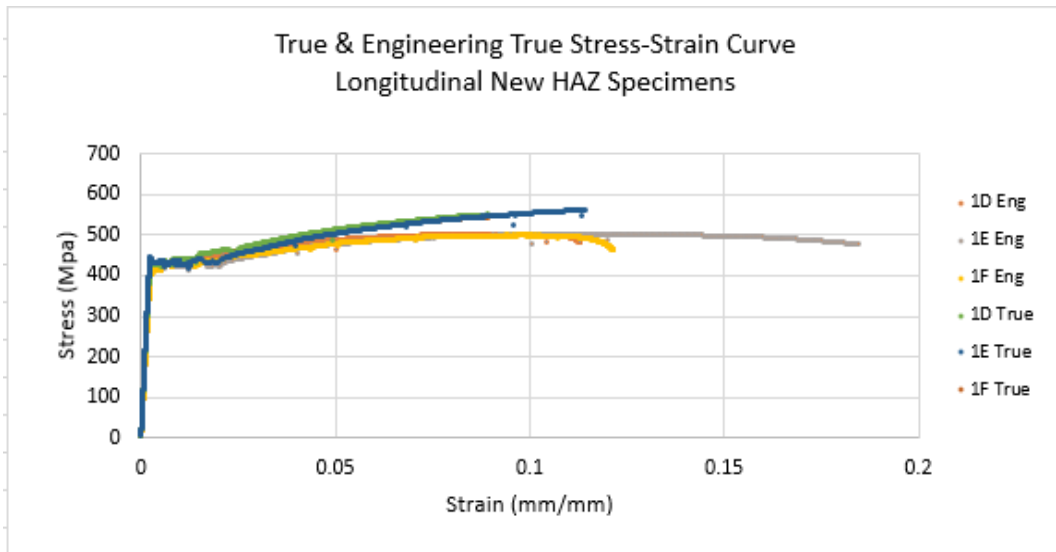


C.3 Stress-strain curves of HAZ (new and old HAZ in the longitudinal and the circumferential direction)

C.3.1 Longitudinal New HAZ

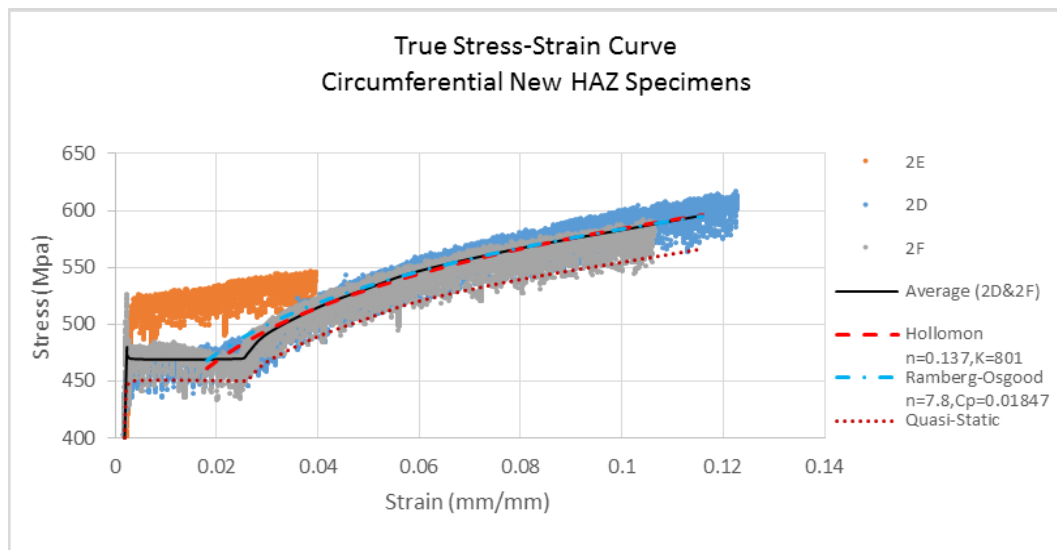
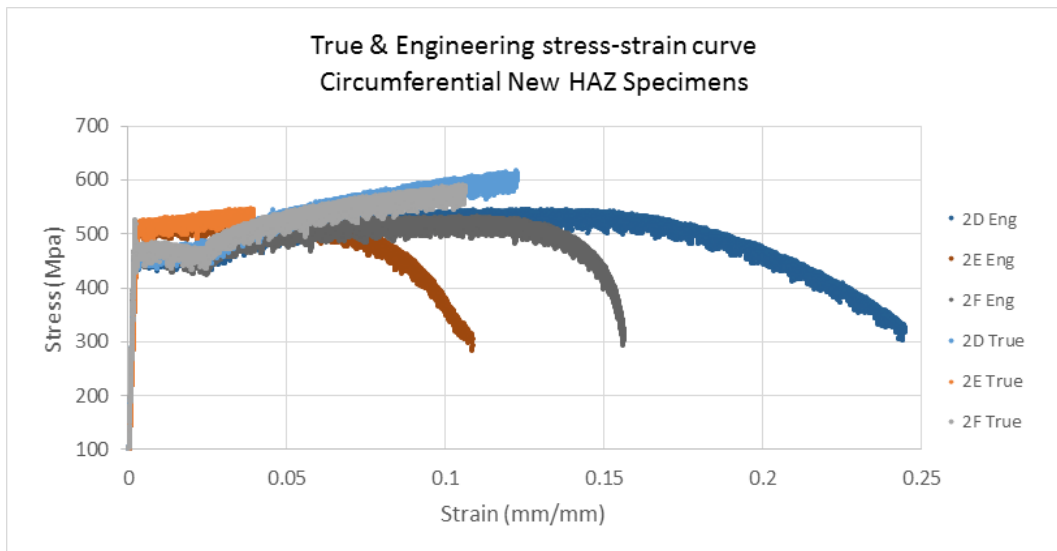
The average true stress-strain curve of three test specimens 1D, 1E and 1F develops linearly with a slope of E which is equal to 194 GPa, then discontinuously yields at a mean stress of 433 MPa during the yield point elongation ranging from 0.0025 to 0.015 true strain, and lastly reaches to the ultimate true tensile strength of 554 MPa at a true uniform strain of 0.1. It matches the Hollomon power curve with $n = 0.14$ and $K = 770$ and the Ramberg-Osgood power curve with $n_{RO} = 7.176$ and $c_p = 0.0167$ well in strain

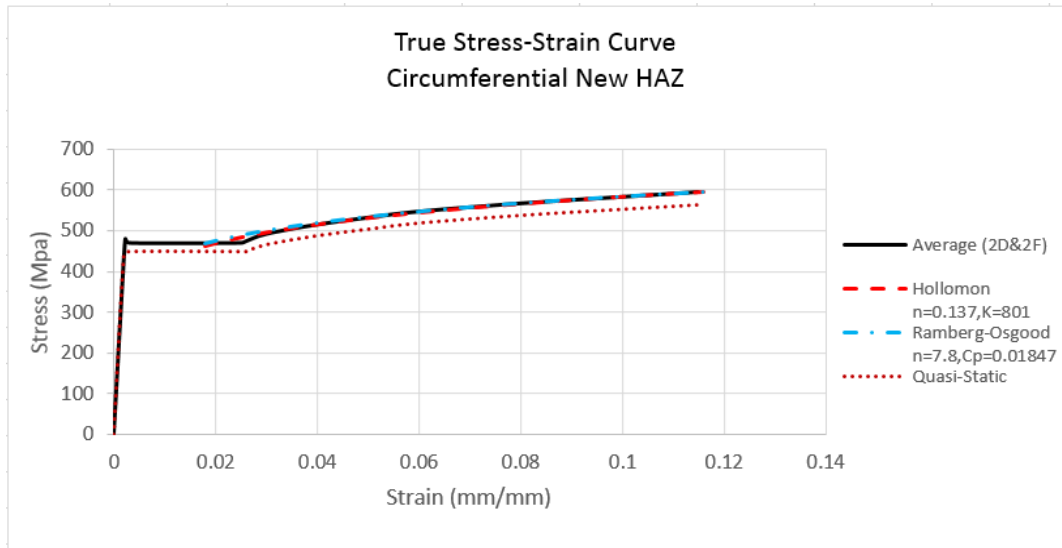
hardening region after a true strain of 0.018.



C.3.2 Circumferential New HAZ

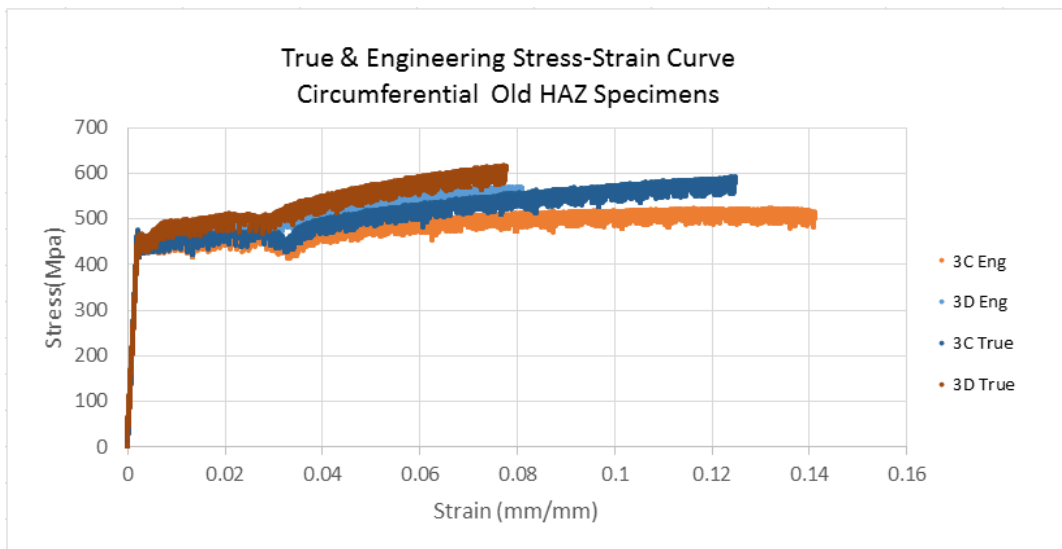
The test specimen 2E exhibits higher yield strength but smaller amount of plasticity than other two specimens 2D and 2F. The specimen 2E might cut from a location of the HAZ that was bended. The average true stress-strain curve of two test specimen 2D and 2F (eliminating 2E) develops linearly with a slope of E which is equal to 203 GPa, then discontinuously yields at a mean stress of 470 MPa during the yield point elongation ranging from 0.0023 to 0.025 true strain, and lastly reaches to the ultimate true tensile strength of 595 MPa at a true uniform strain of 0.075. It matches the Hollomon power curve with $n = 0.137$ and $K = 801$ and the Ramberg-Osgood power curve with $n_{RO} = 7.8$ and $c_p = 0.01847$ well in strain hardening region after a true strain of 0.036.

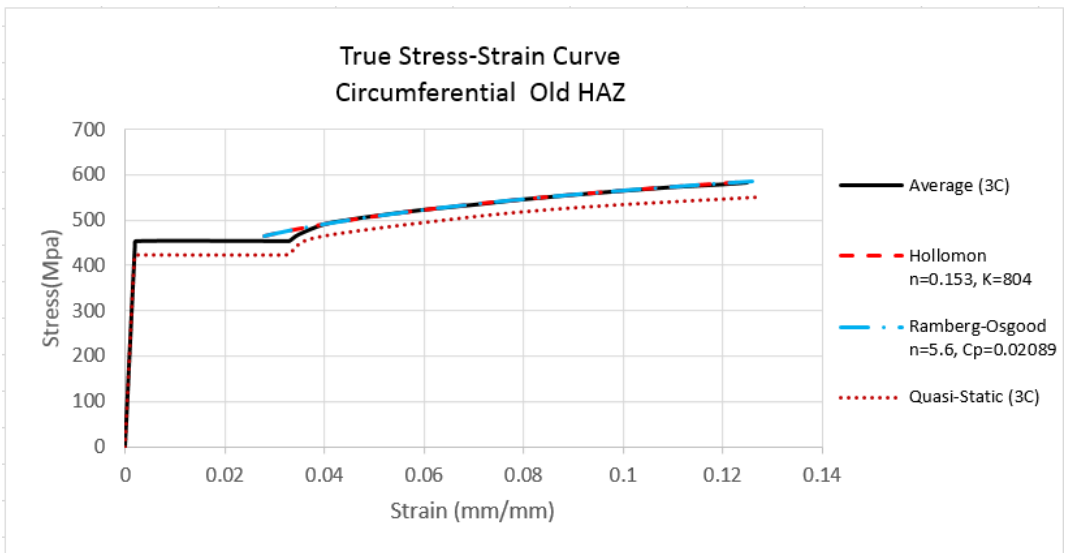
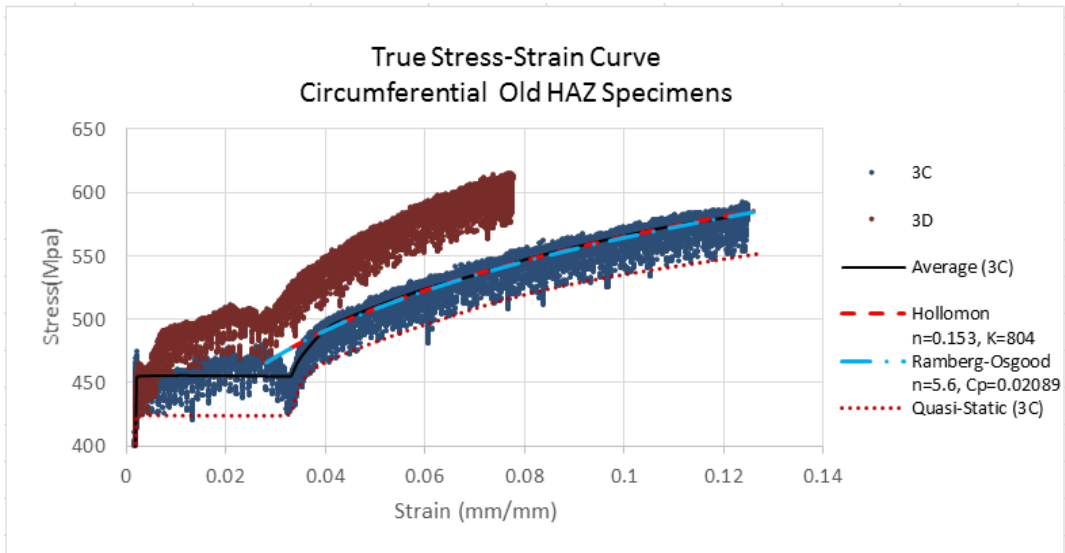




C.3.3 Circumferential Old HAZ

The test specimen 3D exhibits about 10% higher strength than the test specimen 3C. The average true stress-strain curve is conservatively taken as the curve obtained from the specimen 3C (eliminating 3D). It develops linearly with a slope of E which is equal to 223 GPa, then discontinuously yields at a mean stress of 455 MPa during the yield point elongation ranging from 0.0022 to 0.033 true strain, and lastly reaches to the ultimate true tensile strength of 585 MPa at a true uniform strain of 0.125. It matches the Hollomon power curve with $n = 0.153$ and $K = 804$ and the Ramberg-Osgood power curve with $n_{RO} = 5.6$ and $c_p = 0.02089$ well in strain hardening region after a true strain of 0.04.

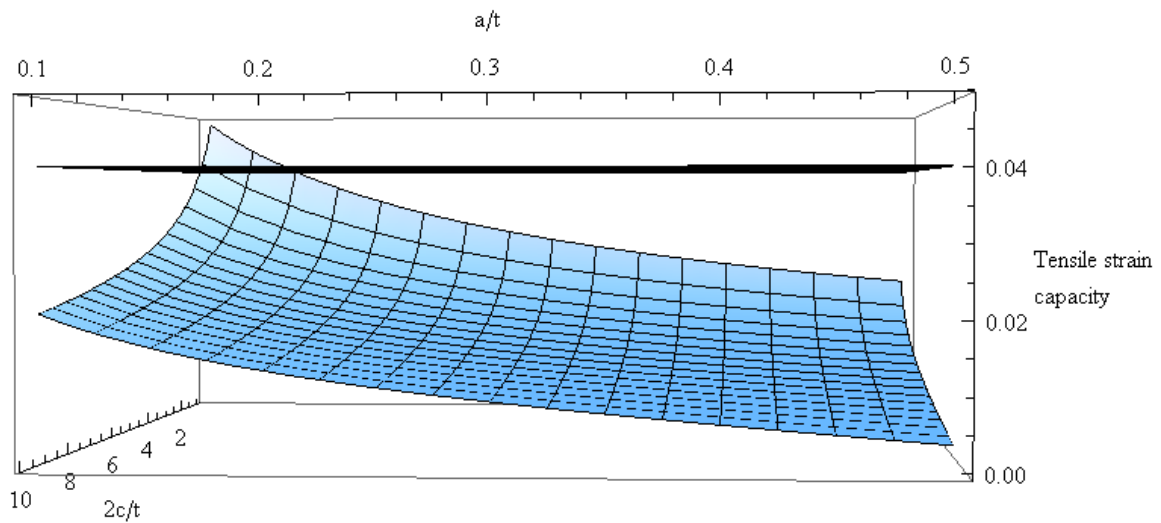




Appendix D – ε_t^{crit} affected by Defect Size

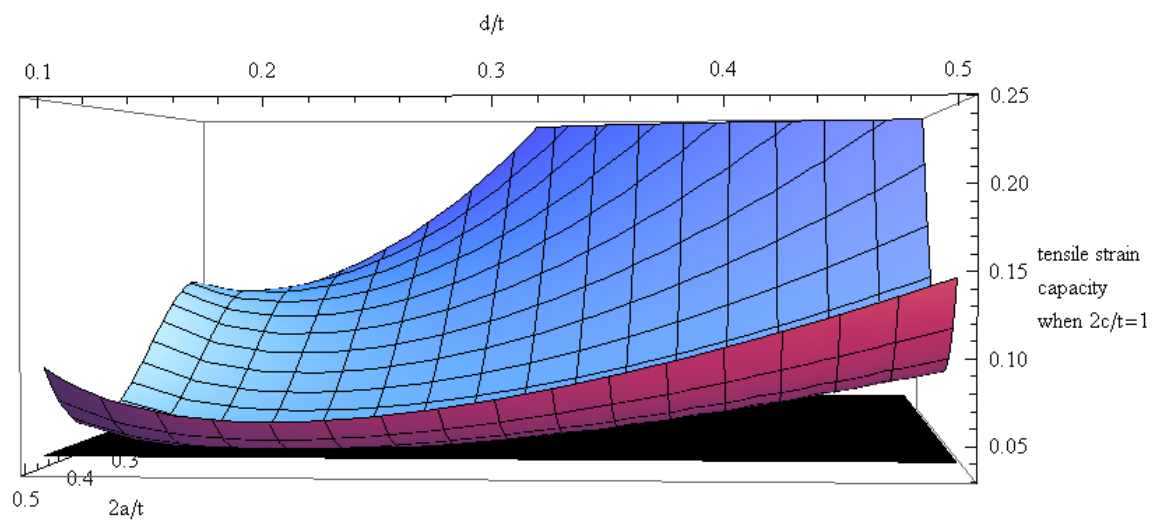
According to CSA Z662-11, the longitudinal tensile strain capacity ε_t^{crit} can be calculated as a function of surface-breaking defect size or buried defect size, and are plotted by Mathematica. The calculated values of ε_t^{crit} are coloured in blue and the upper limit capacity value 4.03% ($1/3\varepsilon_u$) is coloured in black.

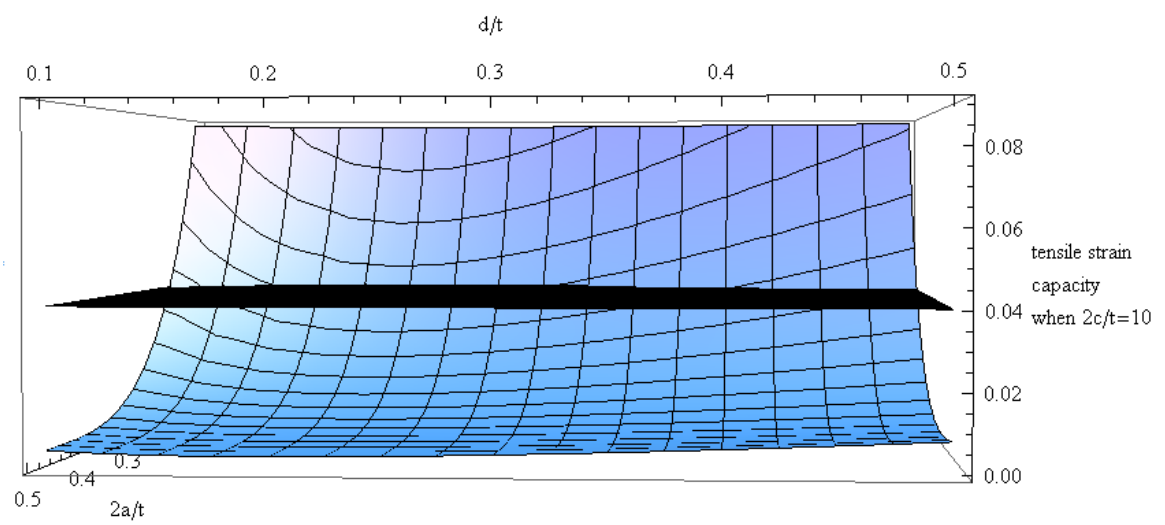
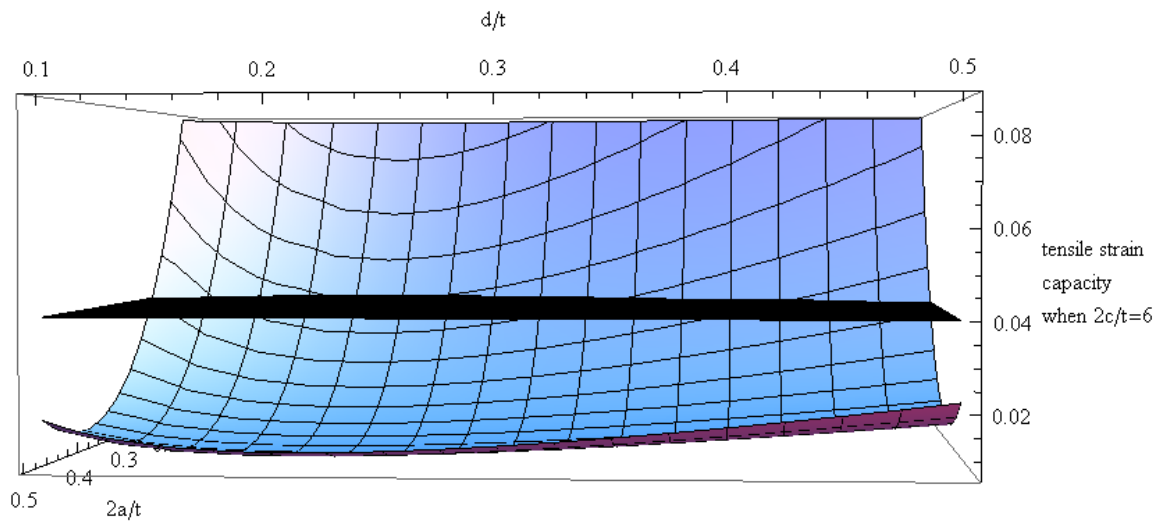
D.1 ε_t^{crit} for surface-breaking defects



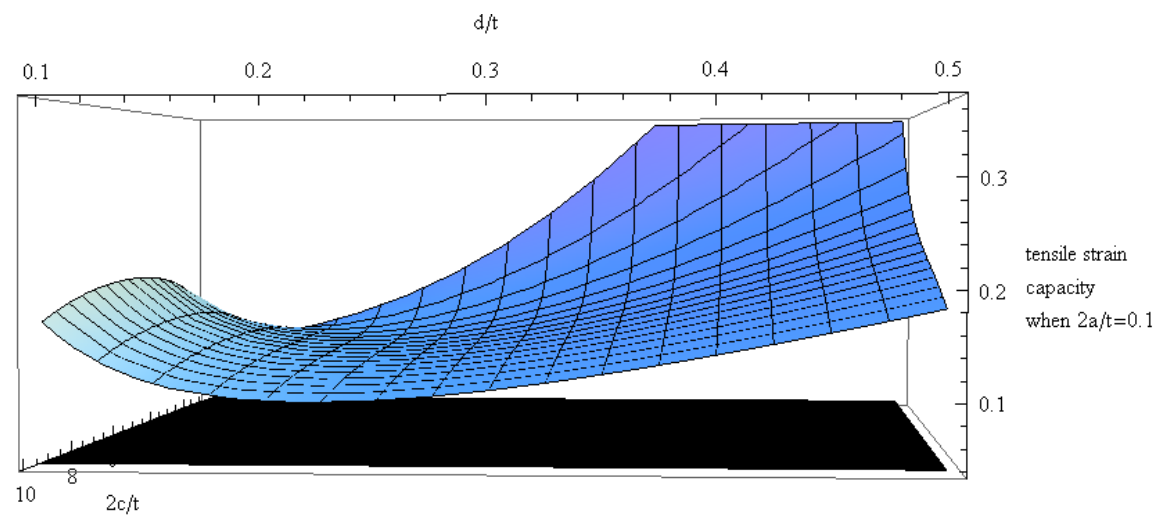
D.2 ε_t^{crit} for buried defects

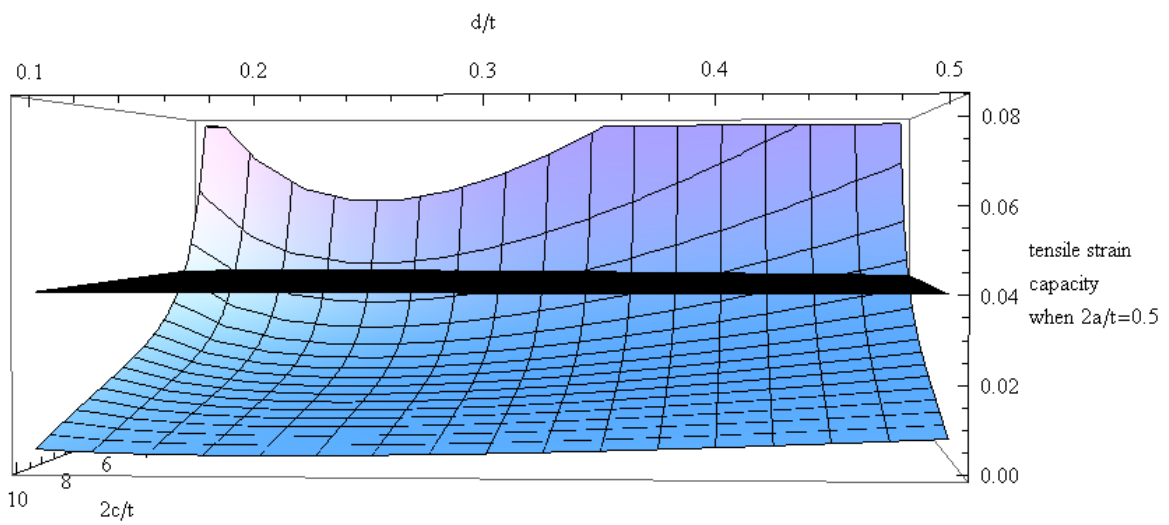
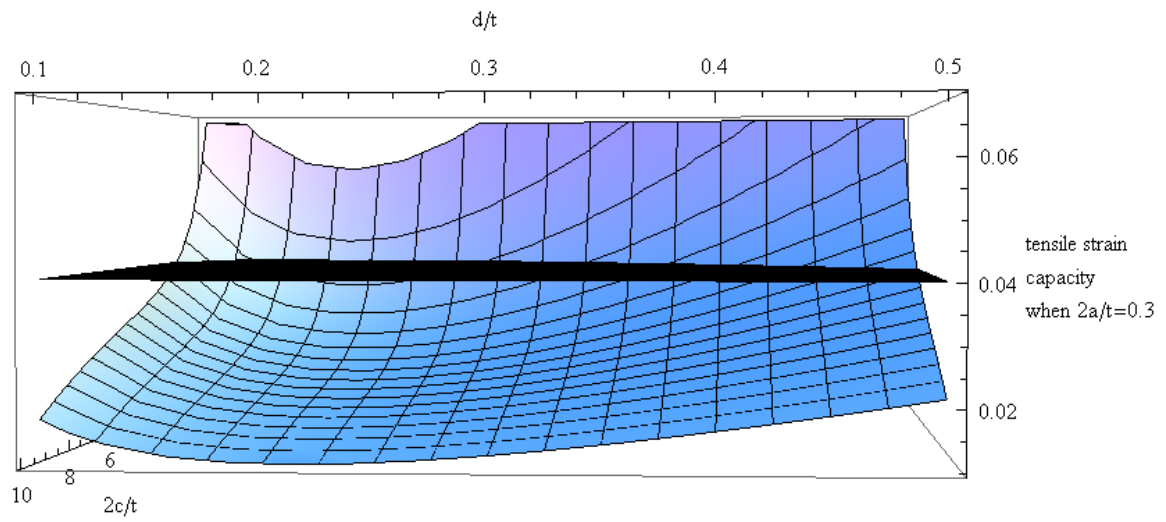
D.2.1 Constant defect length





D.2.2 Constant defect height





D.2.3 Constant defect depth

